

Award Number: W81XWH-16-1-0005

TITLE: Lymph Node Metastases Optical Molecular Diagnostic and Radiation Therapy

PRINCIPAL INVESTIGATOR: Lesley A. Jarvis

CONTRACTING ORGANIZATION: Dartmouth-Hitchcock Medical Center
Hanover NH 03755

REPORT DATE: June 2019

TYPE OF REPORT: Final

PREPARED FOR: U.S. Army Medical Research and Materiel Command
Fort Detrick, Maryland 21702-5012

DISTRIBUTION STATEMENT: Approved for Public Release;
Distribution Unlimited

The views, opinions and/or findings contained in this report are those of the author(s) and should not be construed as an official Department of the Army position, policy or decision unless so designated by other documentation.

REPORT DOCUMENTATION PAGE

Form Approved
OMB No. 0704-0188

Public reporting burden for this collection of information is estimated to average 1 hour per response, including the time for reviewing instructions, searching existing data sources, gathering and maintaining the data needed, and completing and reviewing this collection of information. Send comments regarding this burden estimate or any other aspect of this collection of information, including suggestions for reducing this burden to Department of Defense, Washington Headquarters Services, Directorate for Information Operations and Reports (0704-0188), 1215 Jefferson Davis Highway, Suite 1204, Arlington, VA 22202-4302. Respondents should be aware that notwithstanding any other provision of law, no person shall be subject to any penalty for failing to comply with a collection of information if it does not display a currently valid OMB control number. **PLEASE DO NOT RETURN YOUR FORM TO THE ABOVE ADDRESS.**

1. REPORT DATE June 2019		2. REPORT TYPE Final		3. DATES COVERED 1Mar2016 - 28Feb2019	
4. TITLE AND SUBTITLE Lymph Node Metastases Optical Molecular Diagnostic and Radiation Therapy				5a. CONTRACT NUMBER W81XWH-16-1 -0005	
				5b. GRANT NUMBER	
				5c. PROGRAM ELEMENT NUMBER	
6. AUTHOR(S) Brian W Pogue & Lesley A Jarvis E-Mail: brian.w.pogue@dartmouth.edu				5d. PROJECT NUMBER	
				5e. TASK NUMBER	
				5f. WORK UNIT NUMBER	
7. PERFORMING ORGANIZATION NAME(S) AND ADDRESS(ES) Dartmouth-Hitchcock Medical Center Hanover NH 03755				8. PERFORMING ORGANIZATION REPORT NUMBER	
9. SPONSORING / MONITORING AGENCY NAME(S) AND ADDRESS(ES) U.S. Army Medical Research and Material Command Fort Detrick, Maryland 21702-5012				10. SPONSOR/MONITOR'S ACRONYM(S)	
				11. SPONSOR/MONITOR'S REPORT NUMBER(S)	
12. DISTRIBUTION / AVAILABILITY STATEMENT Approved for Public Release; Distribution Unlimited					
13. SUPPLEMENTARY NOTES					
14. ABSTRACT Breast cancer metastases detection, imaging and management is limited by a key technical problem fundamental to the nature of imaging, which is that micro metastases cannot be visualized at a relevant stage, largely because most imaging is based upon structures and not molecular functions. Surgical dissection is commonly done, as a result of the fact that there is no molecular imaging tool today which can routinely sense the presence of cancer cells in lymph nodes or organs at the micro-metastases stage. The needed probe sensitivity would be in the microMolar to nanoMolar range with sub mm spatial resolution throughout the body. In this proposal, we develop a completely unique hybrid modality which will have high resolution capability through several centimeters of tissue, and all the molecular specificity of standard optical luminescence tracers, with sensitivity down to the sub microMolar level and spatial resolution below 1mm. The new approach uses high energy x-rays from a linear accelerator, LINAC, used in radiation therapy, allowing metabolic imaging and treatment in the same setting. The LINAC radiation induces Cherenkov light in the tissue, and this light can excite luminescence for molecular imaging. This study on metastatic cancer will have shown the value in a single detection paradigm of metastatic cancer in lymph nodes.					
15. SUBJECT TERMS Radiotherapy, Cherenkov, imaging, tomography, metastases					
16. SECURITY CLASSIFICATION OF: U			17. LIMITATION OF ABSTRACT Unclassified	18. NUMBER OF PAGES 106	19a. NAME OF RESPONSIBLE PERSON USAMRMC
a. REPORT Unclassified	b. ABSTRACT Unclassified	c. THIS PAGE Unclassified			19b. TELEPHONE NUMBER (include area code)

Table of Contents

	<u>Page</u>
1. Introduction.....	3
2. Keywords.....	3
3. Accomplishments.....	3
4. Impact.....	9
5. Changes/Problems.....	9
6. Products.....	10
7. Participants & Other Collaborating Organizations.....	11
8. Special Reporting Requirements.....	12
9. Appendices.....	13

Addressing overlap with recently funded NIH grant R01EB024498-01 (page 14)

Specific Aims page for R01EB024498-01 (page 15)

Publications & pending publications (pages 16-69)

- 1) Dsouza A, Lin H, Gunn JR, Gladstone DJ, Jarvis LA, Pogue BW. Cherenkov-excited Multi-Fluorophore Sensing in Tissue-Simulating Phantoms and In Vivo from External Beam Radiotherapy. **Radiation Research** 189(2):197-204 (2018). (9 pgs)
- 2) S. R. Ahmed, J. M. Jia, P. Bruza, S. Vinogradov, S. Jiang, D. J. Gladstone, L. A. Jarvis, B. W. Pogue, "Radiotherapy-induced Cherenkov Luminescence Imaging in a Human Body Phantom" *Journal of Biomedical Optics* 23(3) 1-4 (2018) (4 pages)
- 3) J. R. Shell, E. P. LaRochelle, P. Bruza, J. R. Gunn, S. A. Vinogradov, L. A. Jarvis, D. J. Gladstone, B. W. Pogue "Comparison of Phosphorescent Agents for Noninvasive Detection Imaging of Tumor Oxygenation via Cherenkov Excited Luminescence Imaging" **J. Biomedical Optics** 24(3) 1-8 (2018) (8 pages)
- 4) M. Jia, P. Bruza, D. J. Gladstone, B. W. Pogue, "Multi-point and linescan excitation from a linac for improved lateral resolution in Cherenkov-excited molecular luminescence imaging", **Medical Physics** 46(7) 3067-77 (2019) (7 pages)
- 5) B. W. Pogue, J. Feng, E. P. LaRochelle, P. Bruza, H. Lin, R. Zhang, J. R. Shell, H. Dehghani, S. C. Davis, S. A. Vinogradov, D. J. Gladstone, L. A. Jarvis "Maps of in vivo oxygen pressure with submillimetre resolution and nanomolar sensitivity enabled by Cherenkov-excited luminescence scanned imaging" **Nature Biomedical Engineering** 2(4) 254-264 (2019) (14 pages)
- 6) Jia MJ, Cao X, Gunn JR, Bruza P, Jiang S, Pogue BW. "Tomographic Cherenkov-excited luminescence scanned imaging with multiple pinhole beams recovered via back-projection reconstruction." **Optics Letters** 44(7):1552-1555.(2019).

- 7) Jia MJ, Bruza P, Jarvis LA, Gladstone DJ, Pogue BW. "Multi-beam scan analysis with a clinical LINAC for high resolution Cherenkov-excited molecular luminescence imaging in tissue." **Biomedical Optics Express**. 9(9):4217-4234 (2018)
- 8) X. Cao, S. R. Allu, S. Jiang, M. Jia, J. R. Gunn, C. Yao, E. P. LaRochelle, J. R. Shell, P. Bruza, D. J. Gladstone, L. A. Jarvis, J. Tian, S. A. Vinogradov, B. W. Pogue, "Tissue pO₂ Distribution Changes Monitored During Fractionated Radiation Therapy by Cherenkov-Excited Phosphorescence Lifetime Imaging" (**accepted into peer-review, Nature Communications, 2019**)

1. **INTRODUCTION:**

Breast cancer metastases detection, imaging and management is limited by a key technical problem fundamental to the nature of imaging, which is that micro metastases cannot be visualized at a relevant stage., largely because most imaging is based upon structures and not molecular functions. But there are no tools to effectively sense early metastases, and this lack of high spatial resolution molecular imaging is a key factor inhibiting breast metastases research and treatment. In this proposal, we develop a completely unique hybrid modality which will have high resolution capability through several centimeters of tissue, and all the molecular specificity of standard optical luminescence tracers, with sensitivity down to the sub uM level and spatial resolution below 1mm. The new approach uses high energy x-rays from a linear accelerator, LINAC, used in radiation therapy, allowing metabolic imaging and treatment in the same setting. The LINAC radiation induces Cerenkov light in the tissue, and this light can excite luminescence for molecular imaging. This Cerenkov-excited luminescence scanned imaging approach is referred to as CELSI throughout this work. We proposed to develop the two unique parts to this tool, and test it as combined with multi-probe imaging, to quantify the molecular microenvironment of cancer tumors in vivo.

The individual aims in this overall goal are (1) to optimize the setup and design of a dedicated system to sense signals. (2) To design and build a dedicated system suitable for imaging signals from in small animals on the standard radiation therapy tools. (3) To evaluate the limits on structural, metabolic and immunologic probes for molecular imaging, and (4) to complete studies on metastatic breast cancer with MeV photon imaging and treatment.

CELSI has been demonstrated at the initial in vivo feasibility stage in a lymph node imaging study and should be evaluated as a fundamentally new molecular imaging modality. We anticipate the as the ability to sense molecular concentrations at low radiation dose gets established that human use possibilities will be discovered, either as a therapy/diagnosis tool in Radiation Oncology or purely as a low dose diagnostic.

2. **KEYWORDS:**

Radiotherapy, Cerenkov, Cherenkov, imaging, tomography, sentinel, lymph node, metastases, detection, staging, therapy.

3. **ACCOMPLISHMENTS:**

- **What were the major goals of the project?**

Tasks	Timeline	Site 1 (PI Pogue)	Site 2 (PI Jarvis & Gladstone)
Major Task 1: Development of a high-resolution molecular imaging system	Months	Engineering	Radiation Oncology
Subtask 1: Evaluate components for optimal CELSI system <ul style="list-style-type: none"> • oversee system development, detector choice & evaluation • Monte Carlo modeling of detection & geometry 	1-6 3-6	Bruza & Pogue	
Subtask 2: Determine the limits to detection for CELSI <ul style="list-style-type: none"> • Dr Pogue’s lab: testing limits, SNR, CBR, for relevant targets • Dr. Gladstone’s lab: evaluate the performance in linac use, testing dose requirements. • Dr. Jarvis’s lab: estimate limits for lymph node detection in animals & humans 	7-10 11-12		Dr Gladstone & Gollub Gunn & Jarvis
Milestones: <i>quantify possible tradeoffs on: depth, ii) radiation dose, and iii) probe concentration</i> <i>identify realistic limits for radiation dose & probe concentration for lymph node imaging</i> <i>identify realistic limits for tumor imaging with intravascular & interstitial delivery</i> <i>Publication on limits and potential for CELSI imaging (Phys. Med. Biol.)</i>			
Major Task 2: Design and build a dedicated system for CELSI imaging in small animals, to allow imaging of molecular probes in a manner which has maximal spatial, temporal and contrast resolution.		Engineering	Radiation Oncology

Subtask 1: Completion of an optimized system for delivery to Radiation Oncology	13-18	Jia & Pogue	
Subtask 2: Implementation in radiation oncology & initial animal testing.	19-21		Shell, Gladstone & Gunn
Milestones: <i>Delivery of completed system capable of 200 micron resolution & imaging 2 cm deep into tissue</i> <i>Co-author manuscript on system and construction (Optics Letters)</i>			
Major Task 3: Evaluate the quantitative limits on structural, metabolic and immunologic probes for metastatic breast cancer molecular imaging with CELSI and establishing Standard Uptake Values (SUV).		Engineering	Radiation Oncology
Subtask 1: Evaluating molecular probes for use	22-24	Pogue & Shell	Gunn, Shell & Jarvis
Subtask 2: Establish SUV value in vivo	25-28	Pogue & Shell	Gunn, Shell & Jarvis
Milestones: <i>Demonstrated limits to detection for metabolic & immunologic probes.</i> <i>Publication on CELSI & SUV of different molecular probes (Science Translational Medicine)</i>			
Major Task 4: Complete metastatic breast cancer detection & treatment with MeV photon treatment		Engineering	Radiation Oncology
Subtask 1: complete metastatic & non-metastatic imaging studies in vivo	29-34	Pogue	Gunn & Jarvis
Subtask 2: complete radiation treatment study on involved nodes	34-36		Gunn & Jarvis
Milestone #4: <i>demonstration of in vivo detection and limits to numbers of cells detectable in lymph nodes</i> <i>Publication on in vivo detection & treatment using CELSI and radiation therapy (Int. J. Rad. Oncol. Biol. Phys.).</i>			

What was accomplished under these goals?

In year 1, the Major Task 1 was largely completed, as described in the year 1 report. What remained as the last goal of subtask 2, to examine how this approach to imaging could be optimally deployed in animal and human lymph nodes. So, in this past year we completed a series of studies in which this goal was definitively completed for the potential for translation to human use.

In Major Task 1, Subtask 2, For human lymph node assessment, this work was largely completed in year 2. The feasibility of sensing luminescence from a tissue molecular oxygen sensor from within a human body phantom was examined using the geometry of the axillary lymph node region. Radiation sheet scanning in an epi-illumination geometry provided optimal coverage, and maximum intensity projection images provided illustration of the concept. In summary, detection of regions down to 30 mm deep was feasible with sub-millimeter spatial resolution with the total quantity of the phosphorescent sensor PtG4 near 1 nanomole. This work provided the preliminary information needed to attempt this type of imaging in vivo.

The work included a set of experiments initially focused on determining the optimum positioning of the body phantom, couch, gantry and camera for maximal sensitivity. Three orientations were investigated: i) vertical with the gantry directly above the body phantom on the couch at 180° reference angle and the camera placed directly facing the left side of the body phantom; ii) horizontal with the gantry directly facing the left side of the body phantom at 90° reference angle and a 45° front-surface mirror placed above the top surface of the body phantom, allowing horizontal mounting of the ICCD directly facing the mirror; and iii) angled with the gantry at 145° reference angle with ICCD on the same side. The angular orientation in an epi-illumination configuration was determined to be optimum and used for all subsequent experiments. In this orientation, a Cherenkov sheet was clearly visible translating through the body phantom (see Figure 2 below). The recovery of intensity was highly modulated by the depth of tissue overlying the tubes, and it was apparent that the signal was not linear with concentration because of this effect. However, with skin thickness measured by the CT scan and geometry, it is feasible to quantify these values based on depth-dependent attenuation correction.

In order to pursue a minimum radiation dose scan design, a sparse illumination was also investigated, i.e. the number of radiation sheets used was desired to be as few as possible. Here, a total of 25, 50, 100 and 250 light sheets were

used with equal spacing, i.e. with spaces 2mm, 1mm, 0.5mm, and 0.2mm, respectively. It can be seen that the image quality was substantially equivalent, even for 25 light sheets.

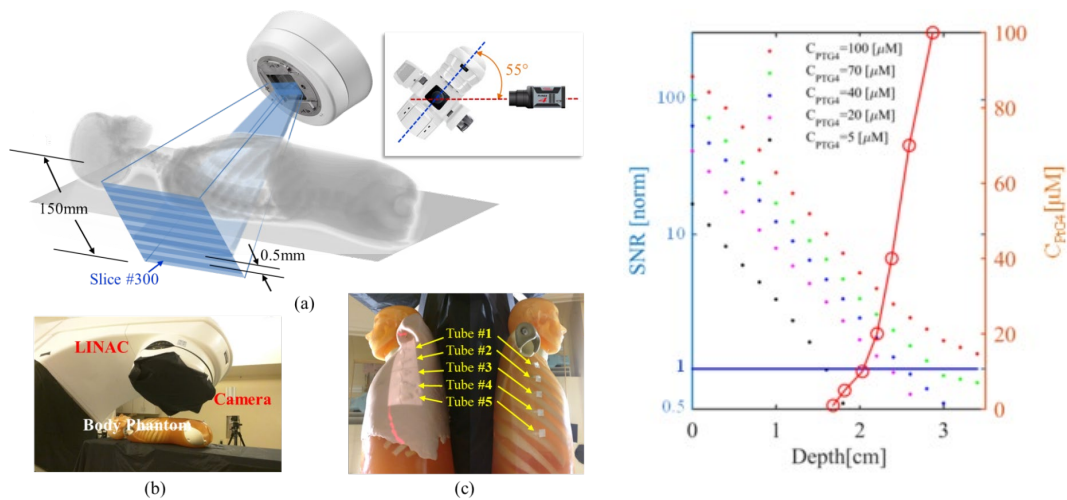


Figure 1. The measurement geometry for a body phantom is shown with (a) a schematic of the geometry, (b) a photograph of the setup, and (c) the body phantom with skin on (left) and without skin (right) as shown with five tubes fixed onto the lateral rib area. In the graph at right, a series of depth studies for CELSI recovery were done with the tubes used here, to show that imaging with sufficient Signal to noise ratio (SNR) was possible down to 2-3cm, but that the minimum detectable concentration necessarily had to increase as the depth grew (red line data & right vertical axis).

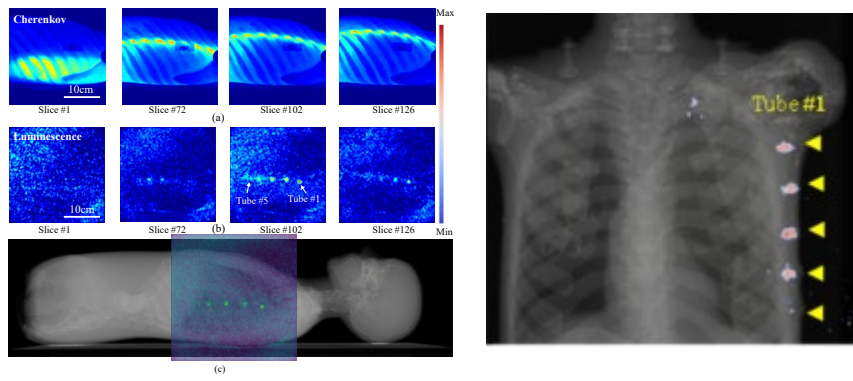


Figure 2. The imaging of the human body phantom shown in Figure 1 was completed with modeling clay skin overlying the 5 tubes of PtG4, and in the top row, 4 static time images of the linac line scan are shown at points during the vertical sweep, showing the Cherenkov emission intensity. The recovered CELSI luminescence in the middle row at each timepoint, and then in the bottom row the Maximum intensity projection is overlaid on the x-ray CT scan. The thresholded image data is shown more clearly in the image at right.

Deliverable for Major Task 1, Subtask 2: In summary, this work was largely done in year 2. For human assessment, our conclusion was that for human imaging, we can image lymph node sized objects down to 2cm depth with as low as 10 uM concentration of PtG4 in the node, and down to 3cm depth with 100 uM concentration, and this can be done for radiation doses near 0.1 Gy, characteristic of a diagnostic x-ray CT scan.

Major Task 2, Subtask 1: Completion of an optimized system for delivery to Radiation Oncology
 We have finished this goal, designing a way to optimize scan time and optimize image quality. The scan time is optimized by using multiple beams from the same linac head, by designing a multi-point or multi-line scan approach, similar to a scanning pinhole confocal microscope. The set up and sequence of studies are shown below in the figures. Briefly, the linac Multi-leaf colimator (MLC) was set to scan a spot, in phantoms and a small luminescent test object placed inside (Figure 3(a)). The scanning of the beam in smaller and smaller blocks illustrates that the Signal to Background Ratio (SBR) is better with smaller spots, because the rejection of outside light is better.

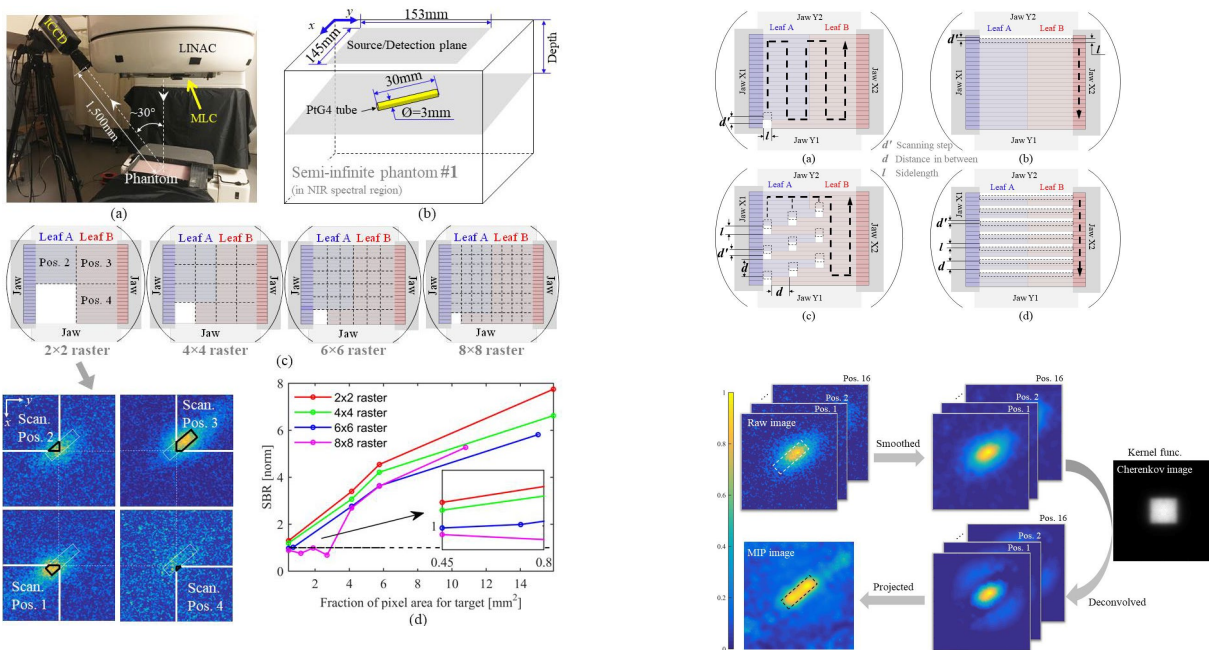


Figure 3. Experiments on the effective radiation beam size shown at left (a) the experimental setup for Cherenkov light sheet luminescence imaging; (b) the phantom geometry; (c) square-raster scanning with different pixel areas, and CELSI images from a 2x2 raster illumination, and (d) the calculated Signal to Background ratio (SBR) versus target area within an illumination square for different square size, indicating smaller is usually better. In the scanning approaches the range of scans from points or lines are illustrated at top right. Then finally in the bottom right images, the sequence of image processing to go from raw data to smoothed, to deconvolved is shown.

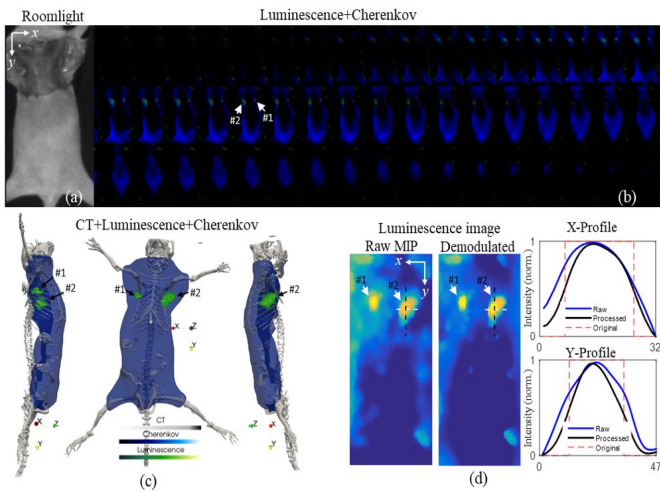


Figure 4. In-vivo mouse expt for 3D CELSI: (a) photograph of mouse with one MDA-MB-231 tumor on the upper limb flank injected with 50 ml of 25 μ M PtG4, (b) merged Cherenkov and demodulated luminescence images, (c) 3D perspective views of combined CT, Cherenkov and luminescence images, and (d) comparisons of luminescence MIP image before and after demodulation and their X-profiles across tumor center. Arrows #1 & #2 show non-tumor and tumor regions, respectively.

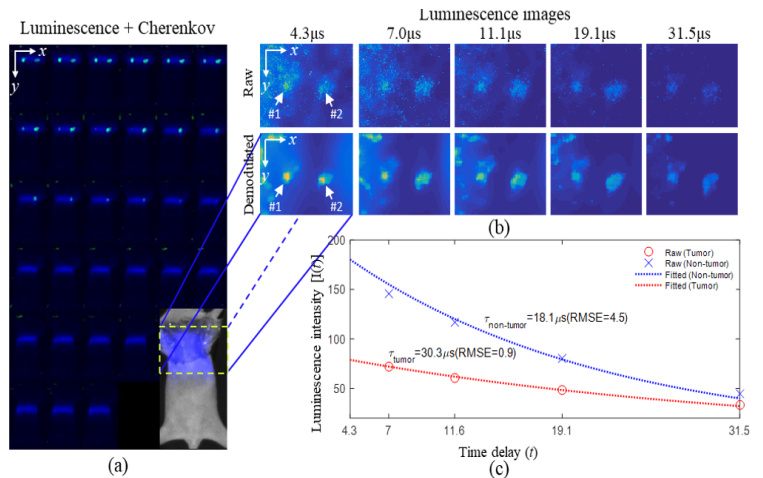


Figure 5. pO_2 sensing demonstration: (a) merged Cherenkov and demodulated luminescence images, (b) luminescence images of the scanned region before and after demodulation at different post-excitation time points, and (c) raw and fitted luminescence decay curves for the tumor and non-tumor regions. A photograph overlaid with Cherenkov MIP image is shown at the last position of (a). Arrows labeled with #1 and #2 point to the non-tumor and tumor regions, respectively.

Deliverable for Major Task 2, Subtask 1: We defined our preferred approach to multipoint scanning of tissues, which optimizes for speed while providing independent sampling of the tissue at each point, and allows scanning with the same radiation dose and spatial resolution achieved as for a single point or line. This methodology is ready to be deployed in our preclinical testing.

Major Task 2, Subtask 2: Implementation in radiation oncology & initial animal testing.

A series of animal studies were carried out to verify that sufficient signal to background was obtainable for line-scan approaches. We carried out individual scans of mice injected with PtG4 and Iridium complex, to assess signal to background ratio (SBR). The optimization of the acquisition parameters were provided by a related ongoing study, and the focus here was to demonstrate sufficient SBR values to carry on with larger cohorts of mice. As shown in the Figure 6 below, both agents were imaged well (a), and the linescan approach illustrated in (b) provided SBR values near 2, for these minimal concentrations of 10 μ M probe used and near 1 cGy of radiation dose. These represent true lower limits of use, and SBR will increase nearly linearly with increases of either input parameter. Finally, in a pilot study of 8 tumors, we showed that with PtG4, the tumor pO₂ could be measured from the lifetime decay change (c).

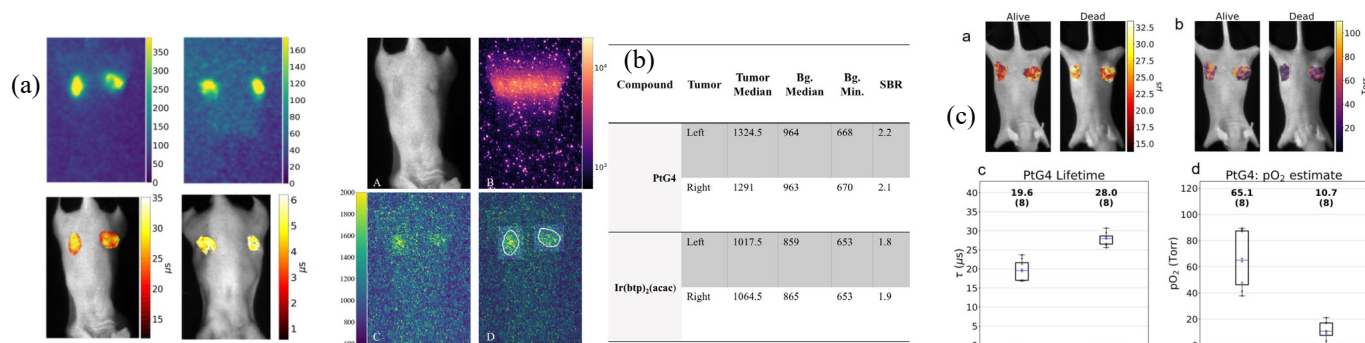


Figure 6. Images of mice in (a) show PtG4 (left) and Ir complex (right) for CELSI images (top row) and luminescence lifetimes overlaid on the white light mouse images. The linescan sequence is illustrated in (b) with lower limits on detection assessed for both PtG4 and Ir complex, with numerical data tabulated beside it to calculate the signal to background ratio (SBR). In (c) PtG4 was used with linescan sequences of CELSI to show that the luminescence lifetimes (left) with mice alive and dead show good representation of the expected values of pO₂ (65 mmHg alive and 5 mmHg dead).

Deliverable for Major Task 2, subtask 2: The scan sequences developed for phantom imaging work well in preliminary in vivo settings. Using the lower limits on PtG4 concentration (10 μ M) in small volumes, and minimal radiation dose (1 cGy), Signal to Background is above 2 for PtG4. This is the lower limit, and increases in either radiation dose, PtG4 concentration will improve this. However, we also recognize that increases in depth must be accompanied by nearly linear increases in either PtG4 concentration or radiation dose in order to achieve the same SBR value.

Major Task 3, Subtask 1: Evaluating molecular probes for use: Metabolic & Immunologic

This subtask was advanced considerably in the final year by Dr Shell. We completed a comparison study of all possible biocompatible **metabolic oxygen sensing luminescent agents**. We also began work on a next generation approach to imaging immune binding CELSI agents, by identifying Europium Chelate Microspheres as the ideal platform for luminescent activity and compatible with biological protein labeling. Both of these advances are described below.

Briefly, the oxygen sensing probes were chosen from a survey of the literature, and in communication with those who produce them. We identified 4 possible commercially available candidates that have claimed biological compatibility and in situ oxygen sensing with lifetimes in the range of microseconds. These were PtG4 (S. Vinogradov U Penn), Iridium complex Ir(bt_p)₂(acac) (Lumtec Corp), MM2 nanoparticles (Ibidi USA) and MitoID (Enzo Lifesciences). These were each compared for their efficiency i) in solution ii) in cells in vitro, and iii) in vivo (summarized in a paper in review, Shell et al, attached in appendix). In the end, only PtG4 and Ir(bt_p)₂(acac) were viable in vivo, which narrowed down the choice. The signal strengths were strong, and preliminary in vivo studies (Shown below) illustrated that the could both be detected with sufficient signal to background.

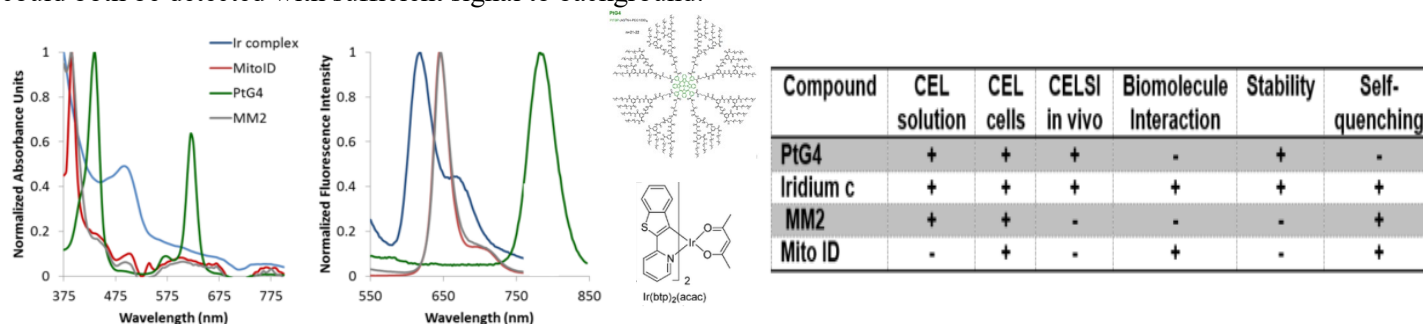


Figure 7. The 4 agents tested have their absorption and emission spectra shown (left) and the molecular structures of PtG4 and Ir(otp)2(acac) are shown, in the middle. The summary of the testing is listed in the table at right, showing phantom, in vitro and in vivo results with interaction, stability and quenching effects. In the end, the in vivo results showed that only PtG4 and I(otp)2(acac) would be viable.

Additionally, we have initiated a comparison study of different ways to image *molecular tracers for immunology*. Initial studies that were done with fluorescent tracers, with fast lifetime, have not proven useful, because the temporal kinetics are too fast (1-20ns) for the comparatively slower linac pulse (3-4 us) and they could not be separated by time-gating. Spectral separation of the signals has been shown in a recent work by our group, published by Dsouza et al, (Radiation Research, 2017), but the inability to spectrally image with sufficient signal to background makes this approach unattractive. After initial screening to compare different luminescent agents, Europium chelate microspheres were found to be an optimal solution for immune sensing with CELSI, because they are highly luminescent upon UV excitation, emitting in red wavelengths, as shown in Figure 9(a). These agents were chosen for their ability to be imaged in vivo (Figure 9(d&e)), as well as be labeled with proteins such as Erbitux (Figure 9(b&c)). The signal strength has been examined and it shows the ability to image signals at the nmol concentration level, at varying sizes down to 10^{-15} moles. Given a receptor concentrations of 10 nMolar, this would indicate that we could image tumors down to $vol = 10^{-15}/10^{-8} = 10^{-7}$ L or 0.1 microliters. This is sufficient to be able to image small metastases, which is the primary goal of this work.

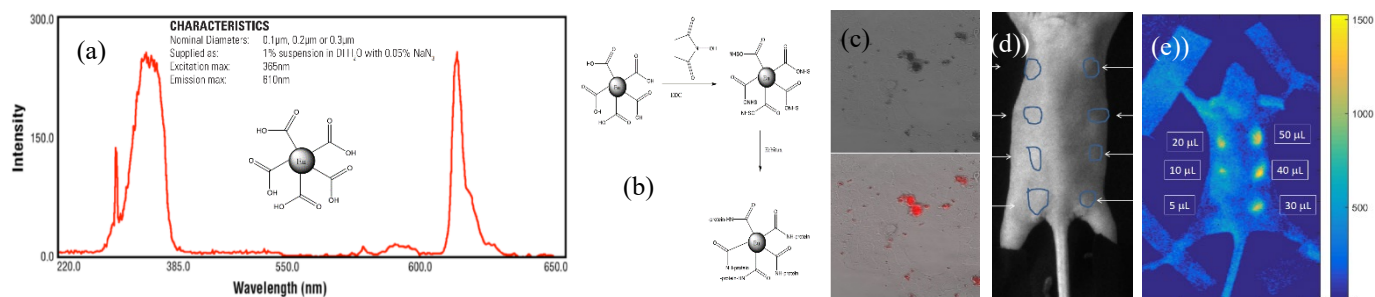


Figure 8. The Eu Chelate microsphere absorption and emission spectra are shown (a), with the chemistry produced to label them with proteins (b). After labeling with Erbitux, and purification, MCF7 cells were incubated with them to show positive uptake with EGFR expression (c). Imaging of the luminescence from CELSI excitation is shown in vivo (d) with image emission data (e). This will likely become our platform technology for immune sensing with CELSI probes in Aim 3.

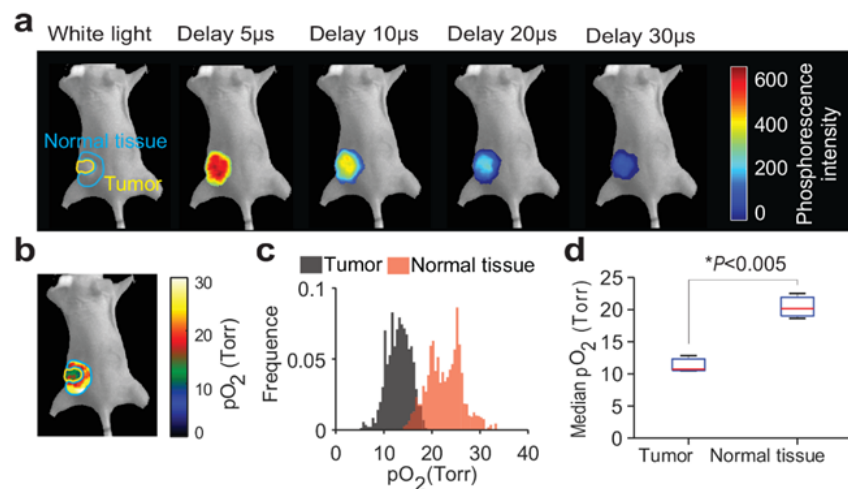
Deliverables for Major Task 3, subtask 1: We have clearly identified our lead candidate molecules for Metabolic Sensing (PtG4 for pO₂) and Immunologic sensing (Eu Chelate microspheres conjugated with antibodies). These can be used in concentrations that are viable for molecular sensing in vivo (10 uM for PtG4 and nM level for Eu Chelate microspheres), and at radiation doses compatible with diagnostic imaging (near 1 cGy).

Major Task 3, Subtask 1: Estimating a quantitative metric SUV

We wound up focusing this subtask on the pO₂ estimates, as this became more reliable than uptake of the nanoparticles. Basically the nanoparticles were not biologically distributed well in the tumors, whereas the PtG4 Oxyphor was found to remain in the tumors for days after injection. We developed a histogram approach to reporting CELSI data which

provided an analogy to Eppendorf histograms of pO₂, which are the most comprehensive way to present the heterogeneity of pO₂ present in a tumor. So while this was not an SUV metric, it provided the quantitative basis to carry on with Task 4. Examples of the histogram approach to interpreting the data are shown in figure 9 below.

Figure 9: Images of the delay images of CELSI phosphorescence lifetime fitting to estimate maps of pO₂ across the tumor and surrounding normal tissue, and the histograms (c), and mean values for 5 mice (d).



Deliverables for Major Task 3, subtask 2: We have developed a histogram approach to quantifying pO₂ throughout the surface of the tumor imaged with CELSI, and use this to track daily pO₂ ranges for normal and tumor tissues (pending publication Xu et al, Nat Comm (in review)).

Major Task 4: Subtask 1: We completed a large study of pO₂ measurements in metastatic and non-metastatic tumor lines in vivo (summary of work submitted in review at Nature Communications). The animals were used in cohorts of 6, with two tumor lines each, and irradiated with hypofractionated radiotherapy 5Gy/day x 5 days, and the pO₂ was imaged daily during treatments from CELSI. The tumor volumes were tracked and the resulting data is in figure 10. The responsive tumor line (MDA-MB-231) responded with increased pO₂ value, and less hypoxia, while the tumor swelled in response. Eventually after a few days the tumors shrunk in size and disappeared. The known non-responsive tumor (non-metastatic) did not change in pO₂ and the hypoxic fraction stayed the same.

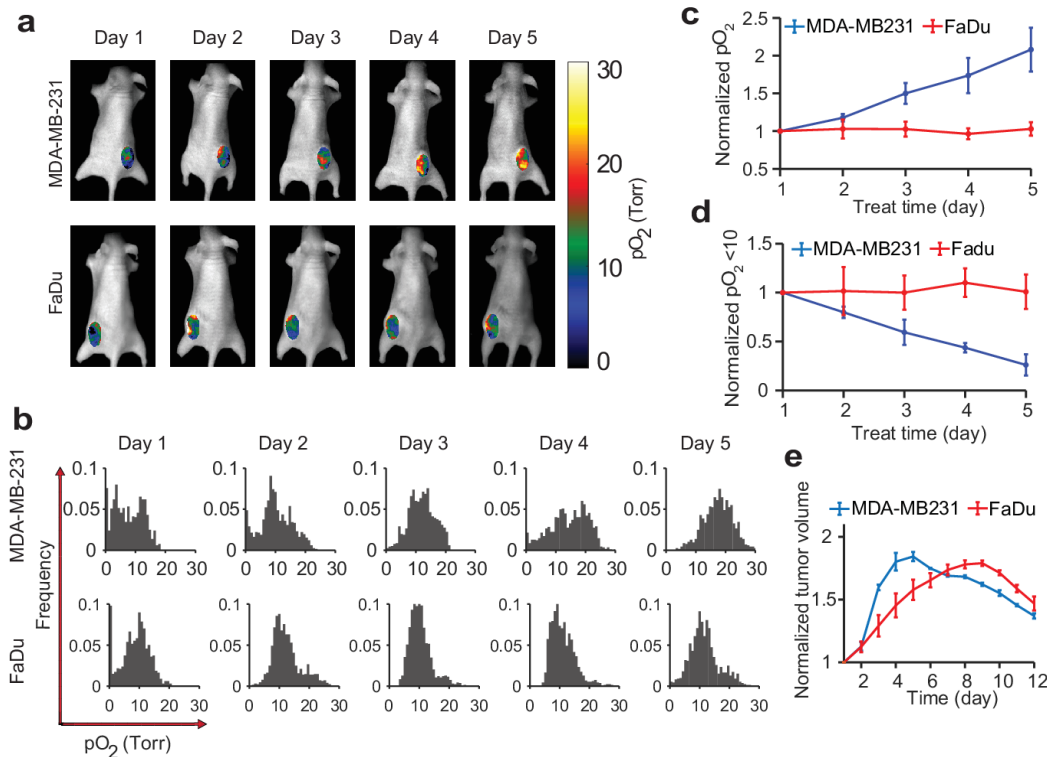


Figure 10. Images of mice getting fractionated radiotherapy (5Gy) daily for 5 days are shown for two tumor lines, MDA-MB-231 metastatic line responsive to radiotherapy, and FaDu non-metastatic and weakly responsive to radiotherapy. The treatments were complete on 6 mice per group and histograms of oxygen are shown below each day (b). The normalized pO₂ per day show increasing values for the responsive line (MDA-MB-231) and not for the FaDu, while the increase in oxygen matches the rapid response by tumor swelling to radiation (e).

Deliverables for Major Task 4, subtasks 1&2: We completed an extensive study of tumor responses to radiotherapy, using two tumor models as proposed. We tracked response to radiotherapy for 12 days outcome, and correlated for how pO₂ was predictive of response. (pending publication Xu et al, Nat Comm (in review)).

What opportunities for training and professional development has the project provided?

Mengyu Jian (post doc) obtained knowledge and mentoring about how to run the linear accelerators, how to acquire data with the cameras, and how to process the data. Jennifer Shell (Research Scientist) has been exposed to the Radiation Therapy world and trained in how to use these systems. Xu Cao was an exchange scientist who was able to participate in the work and also gained radiation therapy experience.

How were the results disseminated to communities of interest?

Our publication efforts have been quite productive these 3 years, with 8 published, and one more being reviewed in Nature Communications now. Dr Pogue had over 10 invited/plenary conference presentations on this work (see below).

What do you plan to do during the next reporting period to accomplish the goals?

The project is completed now.

4. **IMPACT:**

What was the impact on the development of the principal discipline(s) of the project? - Nothing to report

What was the impact on other disciplines?

We demonstrated for the first time that recovery of luminescent objects could be recovered from depths near 3cm in tissue simulating media in a human body phantom. This is being published in our paper Ahmed et al, J. Biomed Optics (2018) and Jia et al, Medical Physics (2019), and showed that by Cherenkov excitation and data collection, can be used in a human geometry. This is a paradigm shift in how to think about molecular sensing in human tissue, and in particular if we could interrogate lymph nodes in patients with potential metastases. These proof of concept studies allow us to consider planning for human studies. The idea is quite forward looking and so while it has not penetrated any clinical practice yet, there is considerable interest in the idea, as indicated by our paper published in Nature Biomedical Engineering (see appendix).

What was the impact on technology transfer? - Nothing to report to date.

What was the impact on society beyond science and technology?

The capabilities of CELSI will allow more useful detection of small objects inside tissue, such as lymph nodes involved with breast cancer. This could have wide ranging implications on how metastatic breast cancer is managed. It is hoped that this high-resolution imaging at the 0 – 3 cm depth range will provide the tool needed to interrogate lymph nodes and help surgeons make a decision about whether to resect them or not. If this works, it would reduce the number of patients with morbidity associated with lymphedema.

5. **CHANGES/PROBLEMS:**

Changes in approach and reasons for change - Nothing to report.

Actual or anticipated problems or delays and actions or plans to resolve them - Nothing to report.

Changes that had a significant impact on expenditures - Nothing to report

Significant changes in use or care of human subjects, vertebrate animals, biohazards, and/or select agents - Nothing to report

Significant changes in use or care of human subjects – Nothing to report.

Significant changes in use or care of vertebrate animals. – Nothing to report.

Significant changes in use of biohazards and/or select agents – Nothing to report.

6. **PRODUCTS:**

Journal publications published :

- 1) Dsouza A, Lin H, Gunn JR, Gladstone DJ, Jarvis LA, Pogue BW. Cherenkov-excited Multi-Fluorophore Sensing in Tissue-Simulating Phantoms and In Vivo from External Beam Radiotherapy. **Radiation Research** 189(2):197-204 (2018). (9 pgs)
- 2) S. R. Ahmed, J. M. Jia, P. Bruza, S. Vinogradov, S. Jiang, D. J. Gladstone, L. A. Jarvis, B. W. Pogue, "Radiotherapy-induced Cherenkov Luminescence Imaging in a Human Body Phantom" *Journal of Biomedical Optics* 23(3) 1-4 (2018) (4 pages)
- 3) J. R. Shell, E. P. LaRochelle, P. Bruza, J. R. Gunn, S. A. Vinogradov, L. A. Jarvis, D. J. Gladstone, B. W. Pogue "Comparison of Phosphorescent Agents for Noninvasive Detection Imaging of Tumor Oxygenation via Cherenkov Excited Luminescence Imaging" **J. Biomedical Optics** 24(3) 1-8 (2018) (8 pages)
- 4) M. Jia, P. Bruza, D. J. Gladstone, B. W. Pogue, "Multi-point and linescan excitation from a linac for improved lateral resolution in Cherenkov-excited molecular luminescence imaging", **Medical Physics** 46(7) 3067-77 (2019) (7 pages)
- 5) B. W. Pogue, J. Feng, E. P. LaRochelle, P. Bruza, H. Lin, R. Zhang, J. R. Shell, H. Dehghani, S. C. Davis, S. A. Vinogradov, D. J. Gladstone, L. A. Jarvis "Maps of in vivo oxygen pressure with submillimetre resolution and nanomolar sensitivity enabled by Cherenkov-excited luminescence scanned imaging" **Nature Biomedical Engineering** 2(4) 254-264 (2019) (14 pages)

- 6) Jia MJ, Cao X, Gunn JR, Bruza P, Jiang S, Pogue BW. "Tomographic Cherenkov-excited luminescence scanned imaging with multiple pinhole beams recovered via back-projection reconstruction." **Optics Letters** 44(7):1552-1555.(2019).
- 7) Jia MJ, Bruza P, Jarvis LA, Gladstone DJ, Pogue BW. "Multi-beam scan analysis with a clinical LINAC for high resolution Cherenkov-excited molecular luminescence imaging in tissue." **Biomedical Optics Express**. 9(9):4217-4234 (2018)

Journal publications in submission/review:

X. Cao, S. R. Allu, S. Jiang, M. Jia, J. R. Gunn, C. Yao, E. P. LaRochelle, J. R. Shell, P. Bruza, D. J. Gladstone, L. A. Jarvis, J. Tian, S. A. Vinogradov, B. W. Pogue, "Tissue pO₂ Distribution Changes Monitored During Fractionated Radiation Therapy by Cherenkov-Excited Phosphorescence Lifetime Imaging" (*in peer review, Nature Communications, 2019*)

Books or other non-periodical, one-time publications.

Nothing to report

Other publications, conference papers, and presentations.

Presentations – Invited/Plenary

1. Brian W Pogue, "Optical Systems for Image Guided Therapy" Invited Talk, AAPM FOrEM on the scientific challenges of image guided cancer treatment, Arlington VA, Nov 2017.
2. Brian W Pogue, "Optical Imaging in Surgery, Radiology & Radiation Therapy" Plenary Speaker, Photonics in Imaging and Medicine Conference, Suzhou China, Sept 25 2017.
3. Brian W Pogue, "Cherenkov Excited Luminescence Scanned Imaging: The highest resolution whole body molecular imaging" Invited Talk, Advances in Optics for Biotechnology, Surgery and Medicine, Engineering Conferences International, Snowmass CO, July 2017.
4. Brian W Pogue, "Cherenkov Excited Luminescence Scanned Imaging: The highest resolution whole body molecular imaging" Invited Talk, From Light to Sound: Frontiers in Deep Tissue Imaging, Janelia Farms, Ashburn VA, June 2017

5.

Conference papers published

- 1) J. Feng, P. Bruza, H. Dehghani, S. C. Davis, B. W. Pogue, Cherenkov-excited luminescence sheet imaging (CELSI) tomographic reconstruction Proceedings of SPIE BiOS, Volume 10049: Molecular-Guided Surgery: Molecules, Devices, and Applications III April 2017

- b. **Website(s) or other Internet site(s)** - *Nothing to report*
- c. **Technologies or techniques** – *Nothing to report*
- d. **Inventions, patent applications, and/or licenses** - *Nothing to report*
- e. **Other Products**

We have produced mostly control software and analysis tools for CELSI. These are available to any researchers interested, and are distributed via our website (www.nirfast.org).

3. PARTICIPANTS & OTHER COLLABORATING ORGANIZATIONS

- a. **What individuals have worked on the project?**

Name:	<i>Mengyu (Jeremy) Jia</i>
Project Role:	<i>Post Doctoral Researcher</i>
Researcher Identifier (e.g. ORCID ID):	<i>n/a</i>
Nearest person month worked:	<i>2.86</i>
Contribution to Project:	<i>Dr Jia worked on CELSI data collection methods and beam geometry optimization.</i>

	<i>He is the lead on data and image acquisition as well as quantitative analysis.</i>
Funding Support:	<i>This award</i>

b.

Name:	<i>Jason Gunn</i>
Project Role:	<i>Lifescience Laboratory Technician</i>
Researcher Identifier (e.g. ORCID ID):	<i>n/a</i>
Nearest person month worked:	<i>1.55</i>
Contribution to Project:	<i>Jason Gunn works on preparation of all animals, cell culture work and tissue collection and analysis.</i>
Funding Support:	<i>This award</i>

c.

Name:	<i>Jennifer Shell</i>
Project Role:	<i>Research Scientist</i>
Researcher Identifier (e.g. ORCID ID):	<i>n/a</i>
Nearest person month worked:	<i>3</i>
Contribution to Project:	<i>Dr Shell is a chemist who focuses on testing of different oxygen sensing probes, and conjugation chemistry and testing of our new immune targeting probes.</i>
Funding Support:	<i>This award</i>

d.

Name:	<i>Brian Pogue</i>
Project Role:	<i>Co-PI</i>
Researcher Identifier (e.g. ORCID ID):	<i>n/a</i>
Nearest person month worked:	<i>2.05</i>
Contribution to Project:	<i>Dr Pogue supervises all laboratory work on data collection, experimental design and analysis of results.</i>
Funding Support:	<i>This award</i>

e.

Name:	<i>Lesley Jarvis, MD PhD</i>
Project Role:	<i>Co-PI</i>
Researcher Identifier (e.g. ORCID ID):	<i>n/a</i>
Nearest person month worked:	<i>2</i>
Contribution to Project:	<i>Dr Jarvis supervises all biological laboratory work on tumor choices and preparation for animal work and analysis of results.</i>
Funding Support:	<i>This award</i>

f.

Name:	<i>David Gladstone</i>
Project Role:	<i>Co-Investigator</i>

Researcher Identifier (e.g. ORCID ID):	<i>n/a</i>
Nearest person month worked:	<i>1</i>
Contribution to Project:	<i>Dr Gladstone supervises all radiotherapy access and work related to beam choices, scanning, machine use and scheduling, and interpretation of results.</i>
Funding Support:	<i>This award</i>

Has there been a change in the active other support of the PD/PI(s) or senior/key personnel since the last reporting period?-

Nothing to report

What other organizations were involved as partners? – nothing to report

4. SPECIAL REPORTING REQUIREMENTS

COLLABORATIVE AWARDS: *For collaborative awards, independent reports are required from **BOTH** the Initiating PI and the Collaborating/Partnering PI. A duplicative report is acceptable; however, tasks shall be clearly marked with the responsible PI and research site. A report shall be submitted to <https://ers.amedd.army.mil> for each unique award.*

The two reports will be uploaded with the same text, as the results are intimately related to one another, but the tasks for Jarvis and Pogue are clearly delineated in section 3 above.

5. **APPENDICES:**

- A. Statement of non-overlap with funded R01 grant.
- B. NIH R01 Specific Aims
- C. Dsouza A, Lin H, Gunn JR, Gladstone DJ, Jarvis LA, Pogue BW. Cherenkov-excited Multi-Fluorophore Sensing in Tissue-Simulating Phantoms and In Vivo from External Beam Radiotherapy. **Radiation Research** 189(2):197-204 (2018). (9 pgs)
- D. S. R. Ahmed, J. M. Jia, P. Bruza, S. Vinogradov, S. Jiang, D. J. Gladstone, L. A. Jarvis, B. W. Pogue, "Radiotherapy-induced Cherenkov Luminescence Imaging in a Human Body Phantom" *Journal of Biomedical Optics* 23(3) 1-4 (2018) (4 pages)
- E. J. R. Shell, E. P. LaRochelle, P. Bruza, J. R. Gunn, S. A. Vinogradov, L. A. Jarvis, D. J. Gladstone, B. W. Pogue "Comparison of Phosphorescent Agents for Noninvasive Detection Imaging of Tumor Oxygenation via Cherenkov Excited Luminescence Imaging" **J. Biomedical Optics** 24(3) 1-8 (2018) (8 pages)
- F. M. Jia, P. Bruza, D. J. Gladstone, B. W. Pogue, "Multi-point and linescan excitation from a linac for improved lateral resolution in Cherenkov-excited molecular luminescence imaging", **Medical Physics** 46(7) 3067-77 (2019) (7 pages)
- G. B. W. Pogue, J. Feng, E. P. LaRochelle, P. Bruza, H. Lin, R. Zhang, J. R. Shell, H. Dehghani, S. C. Davis, S. A. Vinogradov, D. J. Gladstone, L. A. Jarvis "Maps of in vivo oxygen pressure with submillimetre resolution and nanomolar sensitivity enabled by Cherenkov-excited luminescence scanned imaging" **Nature Biomedical Engineering** 2(4) 254-264 (2019) (14 pages)
- H. Jia MJ, Cao X, Gunn JR, Bruza P, Jiang S, Pogue BW. "Tomographic Cherenkov-excited luminescence scanned imaging with multiple pinhole beams recovered via back-projection reconstruction." **Optics Letters** 44(7):1552-1555.(2019).
- I. Jia MJ, Bruza P, Jarvis LA, Gladstone DJ, Pogue BW. "Multi-beam scan analysis with a clinical LINAC for high resolution Cherenkov-excited molecular luminescence imaging in tissue." **Biomedical Optics Express**. 9(9):4217-4234 (2018)
- J. X. Cao, S. R. Allu, S. Jiang, M. Jia, J. R. Gunn, C. Yao, E. P. LaRochelle, J. R. Shell, P. Bruza, D. J. Gladstone, L. A. Jarvis, J. Tian, S. A. Vinogradov, B. W. Pogue, "Tissue pO₂ Distribution Changes Monitored During Fractionated Radiation Therapy by Cherenkov-Excited Phosphorescence Lifetime Imaging" (***accepted into peer-review, Nature Communications, 2019***)

APPENDIX - A

Addressing overlap between this project and recently funded (August 1, 2017) NIH grant R01EB024498-01 (Specific Aims on next page)

In terms of the concerns related to the new NIH grant, R01EB024498-01, there is no scientific overlap. I am enclosing a copy of the specific aims and you can see that they are quite different. The work in Aims 1 and 2 are focused around development of a deep tissue imaging system for whole body imaging of rodents, rather than just lymph node imaging which is fairly superficial. The detectors needed for the deeper tissue imaging are much more sensitive than that used for the CDMRP grant proposal. Additionally, the Aim 2 of the R01 is focused on development of a stand alone system, such that it is not tethered to a clinical linac, but rather is used with a lone short pulse linac, not found in the clinic. This work is supporting Research Scientist Petr Bruza.

The R01 Funding supports the system development for the R01 grant, which has just completed 8 months of funding, as of August 1, 2017. The individuals funded to work on that R01 grant are PhD students Ramish Ashraf (who focuses on the new detection circuitry for triggering) and Ethan LaRochelle (who is focuses on general modeling of CELSI and optimization, without a focus on lymph node imaging).

This CDMRP aims are focused around system optimization and development for breast lymph node imaging, and we have completed a substantial amount of work on this. The system development for this CDMRP grant has been completed now, testing in both rodents as well as human body phantoms for lymph node detection capability, as described in our second annual report.

The CDMRP funding supports the individuals: (Jeremy) Mengyu Jia PhD (who is the lead on linac use and data collection), Jason Gunn (who is lifescience laboratory technician and focuses on preparation of animals and tissue cultures) and Research Scientist Jennifer Shell PhD (who is the lead chemist on probe identification and production). These three individuals are not supported on the R01 grant.

Specific Aims -- R01EB024498-01

There is no molecular imaging tool today which can routinely sense at the μM to nM range with sub-millimeter spatial resolution throughout the rat/mouse body, and most systems other than optical have very low animal throughput. Here we propose a fundamentally new hybrid modality with high resolution capability through several centimeters of tissue, which utilizes molecular specificity of optical tracers. The hypothesized sensitivity is level and spatial resolution near 200 microns. The rationale for this work is that all pre-clinical molecular imaging systems are limited by technical factors that reduce spatial resolution, molecular sensitivity or throughput, which are fundamental to the nature of the imaging. The new approach presented here uses thin sheets of high energy x-rays for **Cerenkov Excited Luminescence for Scanned Imaging (CELSI)**, which excite most traditional organic molecules that are used as biologically compatible molecular probes (**Fig 1**). The system detects the emission in a time-gated manner for superior SNR, and will be tested imaging the molecular microenvironment of deeply seated orthotopic cancer tumors in vivo, which cannot be easily imaged with commercially available fluorescence animal scanners (i.e. Caliper IVIS nor LI-COR Pearl). We propose a technological study of development & performance analysis in a two pronged approach. First, a basic low cost system coupled to existing LINAC sources, and secondly, we will partner with a company to create an optimal standalone system.

Hypothesis 1. A CELSI system can image through an entire rat with linear sensitivity and 200 micron spatial resolution, using molecular probes in the range of nM to μM .

Specific Aim 1. We will **optimize the hardware configuration for CELSI to sense signals for phosphorescence & fluorescence in tissue**, determining the limits to detection, using a scanned *clinical* LINAC beam, testing detector options, phantom studies, & Monte Carlo simulations. Image recover optimization will be completed with deconvolution-attenuation correction as well as NIRFAST-based diffuse tomography recovery. The system as designed will be readily implemented in any radiation oncology department with a clinical LINAC. **Deliverables:** quantify tradeoffs on i) depth, ii) radiation dose, and iii) probe concentration.

Hypothesis 2. A standalone CELSI system will provide superior performance, just as uPET, uCT, uOptical systems provide superior imaging performance relative to human-size correlate systems.

Specific Aim 2. We will **implement a commercial prototype customized system for CELSI imaging in small animals with the best features using a dedicated short pulse LINAC**, allowing superior time-gating for maximal signal to noise. The imaging with maximal spatial, temporal and contrast resolution are compared to a clinical LINAC. **Deliverables:** completed system, quantitative demo of performance specs relative to Aim 1.

Hypothesis 3. Immunologic and metabolic features of orthotopic tumors can be imaged with CELSI whereas they cannot be resolved with standard optical imaging systems.

Aim 3. We will **evaluate the quantitative limits on structural, metabolic and immunologic probes for molecular imaging with CELSI** and establish the ability to measure Standard Uptake Value (SUV) [5, 6], comparing to the best images taken with the IVIS (PerkinElmer) and Pearl (LI-COR) optical systems.

Deliverables: quantitative limits to detection for metabolic & immunologic probes, orthotopic tumors, quantitatively compared to the commercial leading optical systems.

Note, we have designed the aims so that Aims 1 & 2 are complementary and competitive, and the results of Aim 3 will finalize the performance specifications of either system. The strength is that we develop both an inexpensive and readily utilized system on a clinical LINAC (Aim 1), as well as a prototype high-performance small animal system (Aim 2). Note that CELSI has been demonstrated in vivo as well as with quantitative phantoms. We anticipate the as the ability to sense molecular concentrations at low radiation dose gets established, that human use may also be discovered, however, the invention of a high resolution, high molecular sensitivity imaging tool such as this would be extremely important in the field of clinical oncology R&D, and this is the immediate focus of this 4 year application.

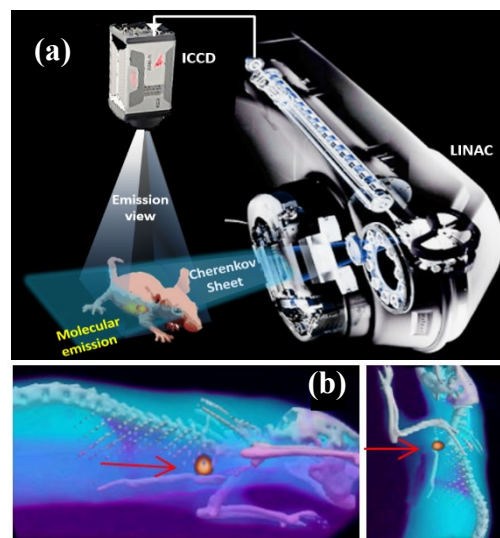


Figure 1. CELSI imaging, set up in (a), allows high resolution images (b) from a whole body rat scan, showing localization of a lymph node. The molecular sensitivity is μM -nM in nature, and spatial resolution $\sim 200 \mu\text{m}$. **This approach is analogous to light sheet microscopy, but with ability to image entire**

- (1) Five (\$5) per word or punctuation alteration.
- (2) Forty-two (\$42) dollars per figure replacement.
- (3) One hundred (\$100) for conversion of each figure to gray scale.

RADIATION RESEARCH **189**, 000–000 (2017)
0033-7587/17 \$15.00
©2017 by Radiation Research Society.
All rights of reproduction in any form reserved.
DOI: 10.1667/RR14943.1

Page proofs and all forms must be returned within 48 hours of receipt.

Cherenkov-excited Multi-Fluorophore Sensing in Tissue-Simulating Phantoms and *In Vivo*

Alisha Dsouza,^{a,1} Huiyun Lin,^{a,d,1} Jason R. Gunn,^a David J. Gladstone,^{a,b,c} Lesley A. Jarvis^{b,c} and Brian W. Pogue^{a,c,2}

^a Thayer School of Engineering and ^b Department of Medicine, Geisel School of Medicine, Dartmouth College, Hanover, New Hampshire 03755;

^c Norris Cotton Cancer Center, Dartmouth-Hitchcock Medical Center, Lebanon, New Hampshire 03756; and ^d Key Laboratory of OptoElectronic Science and Technology for Medicine of Ministry of Education, Fujian Provincial Key Laboratory of Photonics Technology, Fujian Normal University, Fuzhou, 350007, P.R. China

Dsouza, A., Lin, H., Gunn, J. R., Gladstone, D. J., Jarvis, L. A. and Pogue, B. W. Cherenkov-excited Multi-Fluorophore Sensing in Tissue-Simulating Phantoms and *In Vivo*. *Radiat. Res.* **189**, 000–000 (2017).

In this work, Cherenkov-excited molecular sensing was used to assess the potential for simultaneous quantitative sensing of two NIR fluorophores within tissue-simulating phantoms through spectral separation of signals. Cherenkov emissions induced by external beam gamma photon radiation treatment to tissues/tissue-simulating phantoms were detectable over the 500–900-nm wavelength range. The presence of blood was demonstrated to reduce the integrated intensity of detected Cherenkov emissions by nearly 50%, predominantly at wavelengths below 620 nm. The molecular dyes, IRDye 680RD and IRDye 800CW, have excitation and emission spectra at longer wavelengths than the strongest blood absorption peaks, and also where the intensity of Cherenkov light is at its lowest, so that the emission signal relative to background signal is maximized. Tissue phantoms composed of 1% intralipid and 1% blood were used to simulate human breast tissue, and vials containing fluorophore were embedded in the media, and irradiated with gamma photons for Cherenkov excitation. We observed that fluorescence emissions excited by the Cherenkov signal produced within the phantom could be detected at 5-mm depth into the media within a 0.1–25 μM fluorophore concentration range. The detected fluorescence signals from these dyes showed linear relationships with radiation doses down to the cGy level. *In vivo* tests were successful only within the range near a μM , suggesting that these could be used for metabolic probes *in vivo* where the local concentrations are near this range. © 2017 by Radiation Research Society

INTRODUCTION

Molecular imaging *in vivo* requires both high resolution and multi-component information, ideally. Recent work in Cherenkov-excited luminescence scanned imaging (CELSI) has shown potential for sensing and imaging molecular targets with very low volumetric sensitivity in tissue. The demonstration of the concepts of CELSI has been done with *in vivo* and tissue phantom work with oxygen luminescence probes, however, developments around fluorescence reporters have previously been limited (1–3). This was extended into tissue-equivalent phantoms with two near-infrared (NIR) fluorescent reporters within the same volume. The latter issue is important, because many clinical and preclinical studies have shown the need to excite multiple fluorophores in the same tissue volume, for multi-parameter molecular imaging, either for better delineation of tumor volumes (4–7) or accurate quantification of molecular binding.(8–10) In this study, the Cherenkov-excited molecular sensing was extended to test the potential for quantifying two fluorescent tracers at the same time in tissue-equivalent media. Furthermore, these signals were assessed for linearity with concentration and applied radiotherapy dose.

Cherenkov light is produced when radiation in the MeV energy range travels through tissue, as shown in Fig. 1A, giving off a continuous spectrum of light that decays roughly as the inverse-square of the wavelength (1, 11, 12) (light blue line shown in Fig. 1B). Thus, the apparent color of the Cherenkov emission is highly weighted in the ultraviolet and blue wavelengths when undistorted by the media it is in. However, in mammalian tissue, due to the high absorption of short wavelengths by blood, the signal is heavily attenuated and is largely seen as being comprised of red and NIR wavelengths. Figure 1B shows the absorption spectra of hemoglobin (weighted to 1% blood, oxygenated as HbO₂ and deoxygenated as Hb-R), as well as water and lipids, and how the Cherenkov emission spectrum would be dominant in the wavelength region of 600–900 nm, where there is a reduced absorption from either blood or water. However, at the

²Address for correspondence: Thayer School of Engineering, 14 Engineering Drive, Dartmouth College, Hanover NH 03755; email: Brian.w.pogue@dartmouth.edu.

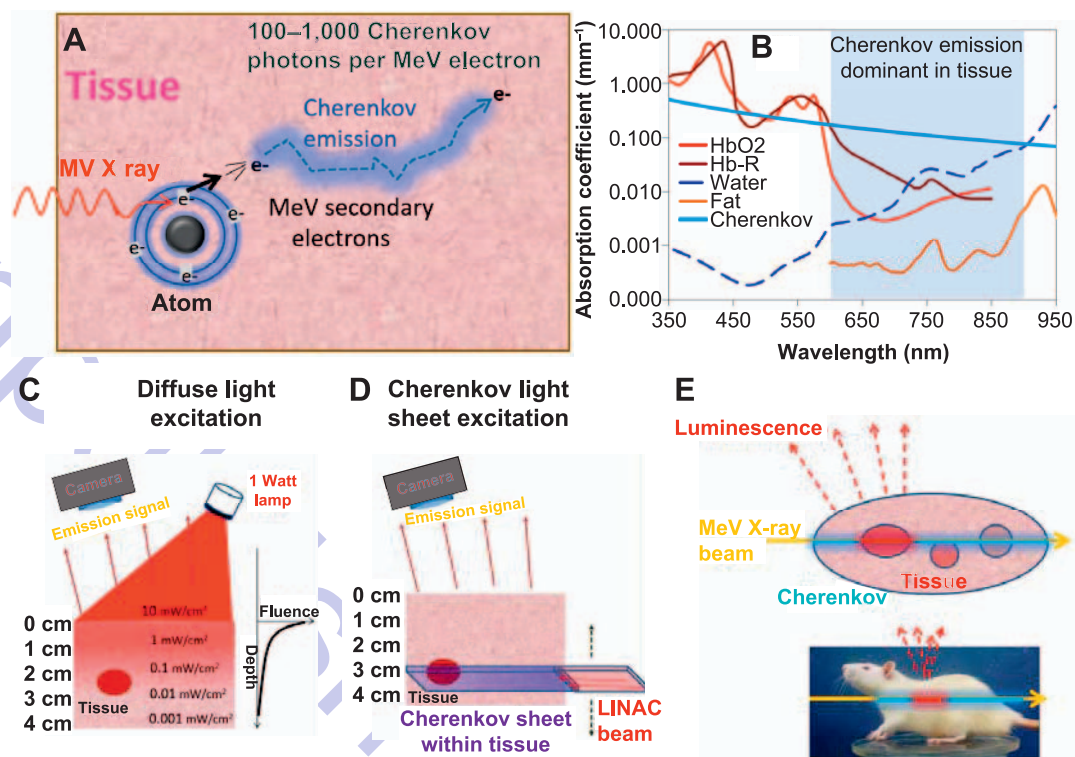


FIG. 1. The generation of Cherenkov light from secondary electrons induced by MV X-ray irradiation of tissue (panel A), with the spectra of Cherenkov light superimposed on the absorbing species present in tissue (panel B), showing the wavelength range where Cherenkov light emission dominates *in vivo*. The benefit of Cherenkov excitation by selective illumination at the point of irradiation (panel D), compared to diffuse light excitation, which decays exponentially with depth into the tissue (panel C). Finally, the entire concept of using selective illumination by MV X-ray beam to induce Cherenkov is shown (panel E), which is subsequently absorbed by local regions of fluorescence, and then the luminescence emission can be captured by a detector.

local level, the Cherenkov light can be used to excite optical absorbing species such as fluorophores, and the resulting fluorescence emissions can exit the tissue as long as the emission peak has sufficient Stokes shift to bring it out to the red-NIR diffusion transport window of tissue (2, 3, 13, 14).

The ability to spatially shape radiation beams delivered by a linear accelerator (LINAC), combined with highly sensitive optical detection instrumentation, allows for the adaptive imaging/measuring of Cherenkov-stimulated light emissions with highly resolved spatial information from the tissue (15, 16). Figure 1C and D shows a comparison of the light excitation in tissue from diffuse light versus LINAC-delivered X rays, emitting Cherenkov light selectively into the media. The diffuse light applied is attenuated exponentially with depth, while the Cherenkov light can be selectively placed anywhere by the LINAC X-ray beam. The MV X-ray radiation travels deep into tissue spinning off secondary electrons (Fig. 1A), and these secondary electrons each give off 100–1,000 optical photons by the Cherenkov effect. Taken together, the selective delivery of Cherenkov combined with localization of molecular probes, as shown in Fig. 1E, can be used to sample signals from a subsurface location, such as a lymph node for metastatic

burden estimation, or to areas for radiation treatment. The benefits of Cherenkov-excited luminescence sensing are summarized below.

1. Cherenkov light is broadband but *in vivo* 600–900-nm light has appreciable penetration.
2. This light is generated at the site of X-ray radiation dose deposition by secondary electrons, which can be throughout tissue for high-MV X-ray LINAC delivery.
3. The selective excitation can then lead to capture of the emission, with knowledge of where the signal came from within the tissue.

Thus, as has been shown in previously reported studies (1, 3), the concept of Cherenkov-excited luminescence detection can work reasonably well, depending on the probe and the tissue geometry. In the current study, spectrometer readout was used to filter the fluorescence emission from the Cherenkov light (excitation signal). This spectral decoupling of the output signals works well, as long as an estimate of contributing spectral bases is available to fit to. Here, the challenge of simultaneously detecting two molecular species from Cherenkov excitation was examined in realistic-tissue-simulating environments.

Please restrict your changes to the correction of typographical errors.

MATERIALS AND METHODS

Experimental Setup and LINAC Beam Delivery

The experimental setup was largely set by the linear accelerator (Varian Clinic 2100C; Varian Medical Systems, Palo Alto, CA), used for MeV energy delivery, in a treatment room of the Norris Cotton Cancer Center (Lebanon, NH). For all experiments, a $10 \times 10 \text{ mm}^2$ beam was used at 6 MV photon energy. The LINAC was set up to deliver radiation in 3.25- μs bursts at 360-Hz repetition rate, with a dose rate of 600 monitor units per minute, roughly equivalent to 600 cGy/min.

A single fiber bundle was used for light collection, and delivery to a spectrometer (Acton InSight™; Princeton Instruments, Trenton, NJ) through a 500-nm longpass filter (Thorlabs Inc., Newton, NJ). A fast-gated intensified CCD camera (ICCD, PI-MAX3; Princeton Instruments) was used at the spectrometer output for multispectral detection. The spectrometer and ICCD camera were placed just outside the radiotherapy room, so that no shielding from the radiation generated by the LINAC was necessary. The single fiber bundle (CeramOptec®, Bonn, Germany) was 15 m in length and housed nineteen 200- μm -diameter silica fibers that conducted emitted light from the treatment region (i.e., tissue-simulating phantom surface or animal skin) to the spectrometer. The LINAC trigger SNYC output was used to trigger acquisitions by the camera at minimum trigger delay equal to the camera insertion delay of 27 ns and radiation pulse gate width of 3.25 μs . The ICCD was cooled to a control point of -25°C and the spectrometer grating used in all experiments was 300 lines/mm, with center wavelength set to 700 nm.

Liquid Phantoms and Fluorescent Inclusions

Liquid tissue simulating “background”-simulating phantoms were prepared to contain 1% v/v intralipid concentration (Fresenius Kabi, Bad Homburg vor der Höhe) as an optical scatterer with scattering properties similar to human tissue, and 1% v/v whole porcine blood (Lampire Biological Laboratories Inc., Pipersville, PA), to match the average blood level of whole tissue (19). These were held in optically clear plastic containers approximately $60 \times 60 \times 120 \text{ mm}$ in size. Containers were positioned in the radiation beam, with the beam edge stopping immediately at the external boundary of the media. Immediately outside the edge of the phantom, a linear fiber array was placed in light contact with the surface, such that light emission could be directly collected from the emission, as shown in Fig. 2A and B. Typical Cherenkov-emission spectra from the two types of homogenous phantoms are shown in Fig. 2C.

Ten 2-ml centrifuge tubes filled with fluorophores, IRDye® 800CW and IRDye 680 RD (both from LI-COR® Biosciences, Lincoln, NE), at concentrations of 0.1–25 μM in 500- μl phosphate buffered saline (PBS), were used to simulate fluorescent inclusions (see Fig. 2C). Both fluorophores were present in all the tubes, and at the same concentrations, i.e., a 1:1 concentration ratio was maintained between dyes for simplicity. Typical spectra of the Cherenkov emission with the absorption and fluorescence emission spectra of the fluorophores used are shown in Fig. 3A. Each tube was then placed in the background liquid phantom, which contained PBS with 1% intralipid or PBS with 1% intralipid and 1% whole blood. Blank control tubes containing only background intralipid and blood were also prepared. The phantom setup was placed on a stirring plate, to prevent red blood cell-stacking and inhomogeneity in scatterer concentrations. The tube was positioned inside the background phantom container such that it was at a distance of 5 mm from the container wall at which the optical fiber tip was fixed. The radiation beam cross-section shape was set to $1 \times 1 \text{ cm}^2$, and was set up to irradiate the inclusion tube from the top, with the LINAC beam isocenter set to be inside the inclusion. This provided a sufficient buildup region for the radiation beam passing through the phantom. Cherenkov emissions and fluorescence emission triggered by radiation delivery were acquired. Five frames of

continuous wavelength spectra were generated with 100–3,000 accumulations on the ICCD chip (AOC) or pulses. Since the dose rate was 10 cGy/s, and there were 360 pulses/s, this range of AOC values corresponds to roughly 2.8–83 cGy.

Spectral Fitting and Data Processing

The collected spectra were temporally median-filtered and wavelength-averaged with a moving window filter, as shown in Fig. 3B. To process the spectra for signals related to dye concentration, the acquired normalized background spectra, from Fig. 3A, were used for spectral fitting, because the signals included all distortions to the Cherenkov emission and fluorescence spectra, which could be caused by fiber and system autofluorescence and attenuation. These were thought to be minimal, but still direct measurement of these spectra on the same system was completed. Then the detected spectra were used as the input to an algorithm for spectral decoupling, based on a linear least-squares solver, fitting in the regions where each component was dominant, as shown in Fig. 3D.

In Vivo Proof-of-Concept Work: Subcutaneous Matrigel-Based Fluorescent Inclusions in Murine Model

Before the above approach could be applied and tested to quantify fluorescent-tracer ratios in animal lymph nodes, a simulated *in vivo* experiment utilizing fluorophores injected subcutaneously in a mouse was performed. In this experiment, IRDye 680RD and IRDye 800CW were mixed with clear phenol red-free and growth factor-reduced Matrigel media (Corning® Inc., Corning, NY) such that their concentration was 3 μM each. The Matrigel that was previously stored in 500- μl aliquots at -20°C was thawed in an ice tub to raise its temperature to 4°C . Care was taken during the handling to prevent overheating of the Matrigel, as this causes it to cross-link and solidify. Dyes dissolved in PBS were cooled and mixed with the Matrigel by pipetting. Insulin syringes with 27g needles were chilled on ice prior to loading. Animals were anesthetized using 1.5–2.5% isoflurane in 1.5 l/min oxygen, and placed on a heating pad. A 200- μl injection of Matrigel mixed with fluorescent dyes was administered subcutaneously such that the Matrigel solidified into a spheroid with minimal flattening. Since Matrigel is a highly viscous substance, care was given to ensure bubbles were not present in the gel.

For the spectra acquisition, the mouse was placed on a black sheet over layers of solid water phantoms (added to 1.5 cm thickness), to provide sufficient buildup region. The optical fiber position was fixed and the animal was adjusted to maintain contact between the fiber tip and the Matrigel bump (Fig. 6A). A 6-MV radiation beam was directed from below the animal such that the beam cross-section size was $1 \times 1 \text{ cm}^2$, with the isocenter near the optical fiber tip. A background spectrum was obtained by measuring a Matrigel-free skin region away from the liver and gut, which are known sources of high autofluorescence. Spectra were acquired using the spectrometer and ICCD camera, and processed in a similar fashion as above to estimate the emission ratio of IRDye 800CW to IRDye 680RD. For the sake of simplicity in treatment, and optical fiber-based measurement, the animal was euthanized prior to any measurement by cervical dislocation. All animal work was performed under protocols approved by the Institutional Animal Care and Use Committee (IACUC) at Dartmouth College (Hanover, NH).

RESULTS

Figure 2C shows the detected Cherenkov emissions from the background phantom with 1% intralipid and no blood and 1% intralipid along with 1% whole blood; note the change in spectral shape when blood was present. The decrease in signal at wavelengths $<620 \text{ nm}$ is apparent and

Please restrict your changes to the correction of typographical errors.

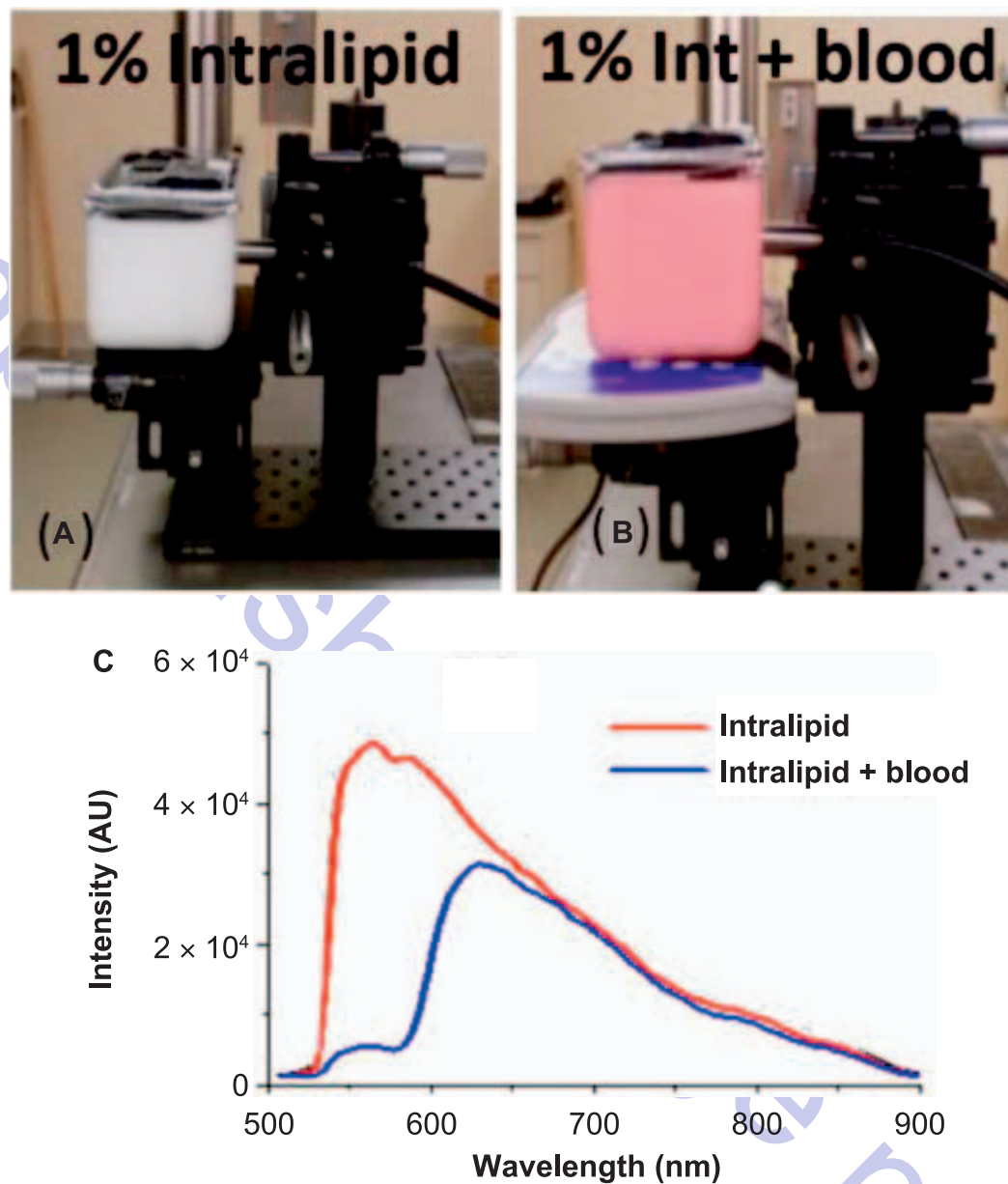


FIG. 2. The tissue phantoms used with 1% intralipid (panel A) and 1% intralipid with 1% porcine blood (panel B) are shown, set up on the radiation treatment table, with the optical fiber setup in contact with the plastic container. Representative Cherenkov spectra measured from LINAC irradiation of these phantoms is shown in panel C. The measurements were taken with a single fiber bundle coupled to the spectrometer.

matches the known attenuation of blood well. Notably, the signal loss is not strong in wavelengths above 620 nm, because the Cherenkov emission is being produced throughout the entire volume of the sample, and so the transport distance of light getting into the detection fiber was moderate. This is the rationale behind using IRDye 800CW and IRDye 680RD in this study.

Figures 4 and 5 show the processed spectra for various fluorophore concentrations (IRDye680:IRDye800 concentration was 1:1) in 1% intralipid in the background (Fig. 4) and the 1% intralipid plus 1% blood background media (Fig. 4). The IRDye 680RD measurement is on the left in both figures,

while that of IRDye 800CW is on the right in all panels in Figs. 4 and 5. The resulting integrated intensity values over the fitted fluorophore peaks for every measurement are plotted as a single point on each graph for each concentration and each radiation dose. Because of high Cherenkov background signals, there is always a lower limit on the concentration of dyes, which could be detected with any accuracy. Also, at the highest dye concentrations, there could be self-quenching of the dye, limiting the linearity of response. Concentrations above and below these extremes were eliminated from the data, to focus on reporting those data that are monotonically related to the reporter signal.

Please restrict your changes to the correction of typographical errors.

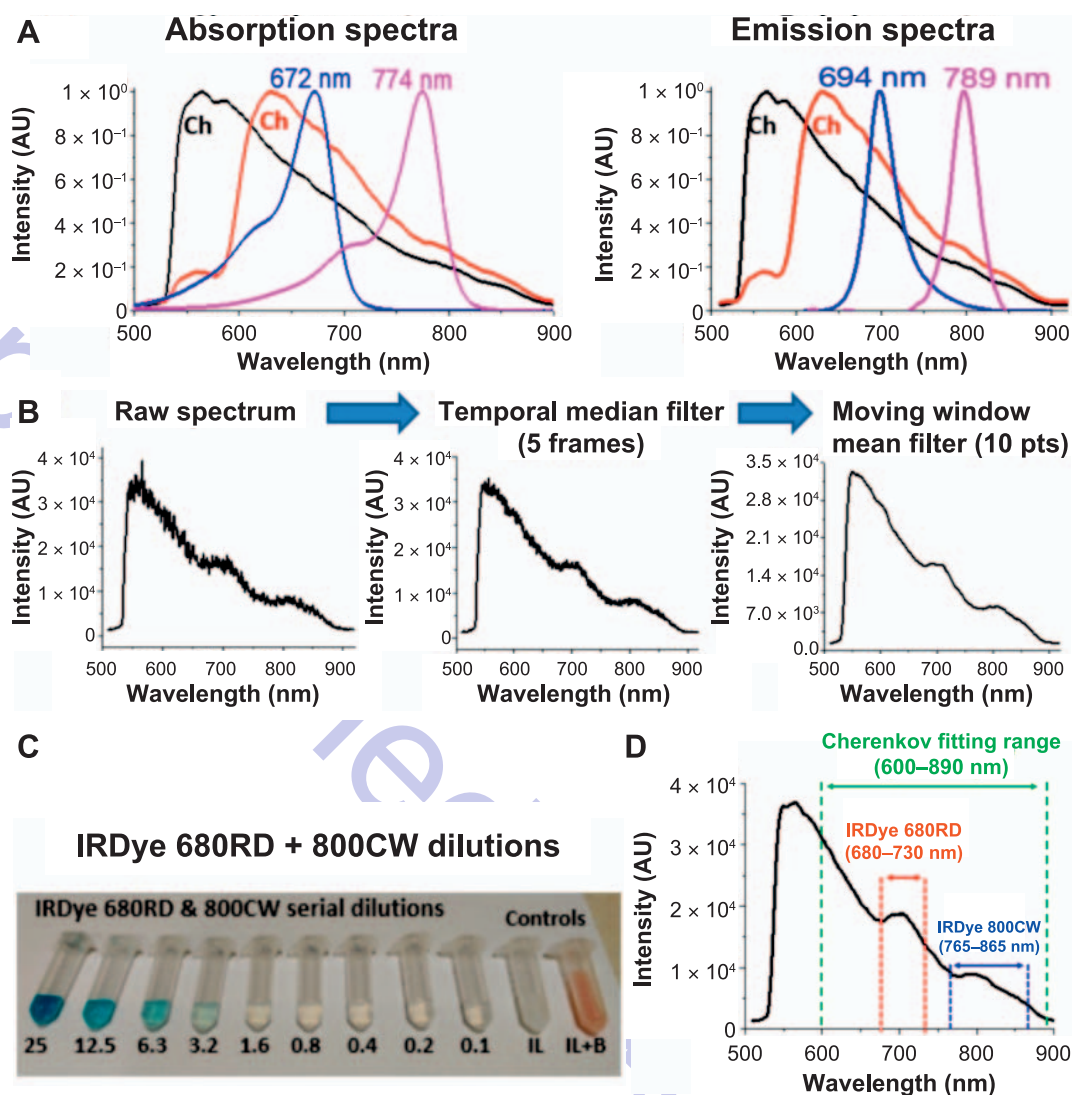


FIG. 3. Dyes in phantoms and intralipid with blood. Panel A: Absorption (left) and emission (right) spectra are shown for Cherenkov emission in intralipid (black), Cherenkov emission in intralipid and blood (red), IRDye 680RD (blue) and IRDye 800CW (pink). Panel B: Example of a raw emission spectrum from a combined phantom, with Cherenkov and the two emission peaks convolved, with temporal filtering, then moving window wavelength filtering to reduce the noise. Panel C: The tubes with serial dilutions are shown for both dyes, systematically decreased together with concentrations listed in micromolar. Panel D: Example spectrum, with the wavelength fitting regions shown, for all three components.

Figures 4A and 5A show the dependence of each fluorophore signal with respect to radiation dose used, at varied concentration of 0.1–25 μM . The signals in the blood-bearing phantoms (Fig. 5) had considerably more noise in Fig. 4, largely because the background Cherenkov of course varies with dose as well, and so the entire signal to noise of the fit degraded more significantly with less dose delivered. To better interpret the data, fits of signal versus dose were plotted in green dotted lines for these figures. In both figures, simultaneous fitting of IRDye 680RD and 800CW was possible over some range of concentrations (Fig. 4B and Fig. 5B). In comparing Fig. 4A to Fig. 5A, it is apparent that the contribution of blood merely limits the output signal by a factor of approximately 2, while the full

range of concentrations could be detected with the radiation dose used here.

Processed and fitted spectra for the murine Matrigel inclusion loaded with 3 μM IRDye 680RD and IRDye 800CW are shown in Fig. 6B. The results indicated that it was possible to resolve signals for the ratio of 800:680 down to 1, as expected.

DISCUSSION

This study focused on the particular question of utilizing fluorescent molecular probes in Cherenkov-excited molecular sensing. The results have large implications as to the utility of spectrally resolved CELSI sensing *in vivo*, and the

Please restrict your changes to the correction of typographical errors.

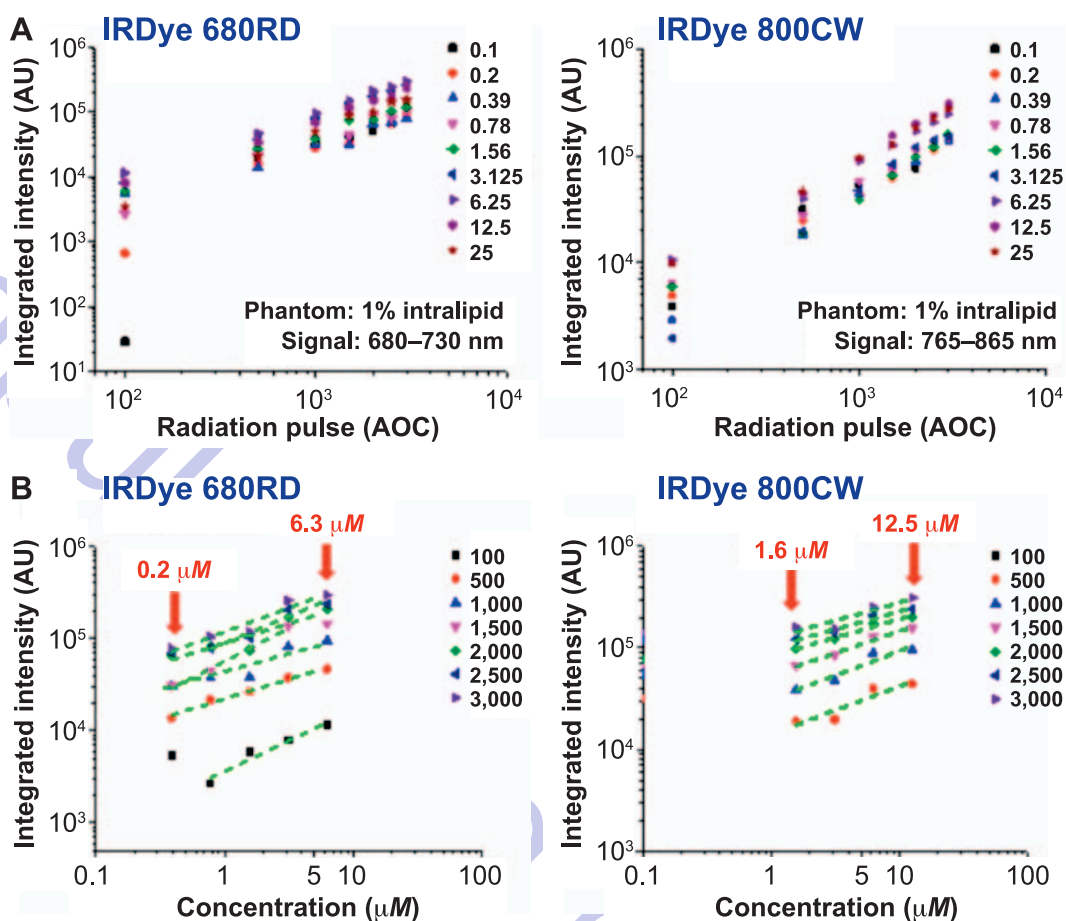


FIG. 4. The measured integrated fluorescence signal intensity from intralipid solutions are shown for IRDye 680RD (left) and IRDye 800CW (right) for varying amounts of radiation dose (panel A) at varied concentrations of 0.1–25 μM . Variation in signal with varying concentration was then examined (panel B) for varied radiation dose of 2.8–83 cGy (AOC 100–3,000). Green dashed lines represent linear fits.

uniqueness of the geometry shown in Fig. 1E, where selective areas of tissue can be probed with careful geometric and spectral choices. The concept of injecting X rays as a way to excite molecular probes *in vivo* with Cherenkov light has not been widely explored, but with the right molecular sensor, the signals can be detected from deeper than most areas that could otherwise be sampled with light. However, the range of concentration and radiation dose required for sensing will directly determine what this imaging tool can be used for, and so these two factors in particular were studied here.

Several previously reported studies have focused on phosphorescent agents, which have emission lifetimes in the tens of microseconds range, allowing for temporal gating of the signal, effectively eliminating Cherenkov completely from the signal. In such a case, luminescence can be sampled well down into the sub-nanomolar concentrations (3), because the background signal has been eliminated. In the case of time-independent spectra detection, the fluorescent signal is embedded on top of the Cherenkov background, and so the deconvolution of the two signals is dependent on the system noise and variability, and

inherently is bound to be orders of magnitude less sensitive. The data shown in Figs. 3 and 4 support this, indicating that the sensitivity range of IRDyes detected in this manner is approximately 1–10 μM in tissue-equivalent media. The upper end of the detection is likely higher than this, but just dependent on the microchemical quenching effect of the dye and the microenvironment that it is in. However, the lower end of this detection range is realistic for *in vivo* imaging, since it has more to do with the detection methodology than the tissue and dye.

Some interesting observations can be taken from the results beyond these simple limits however. For example, the effect of blood, compared to no blood, is quite subtle in the signal, e.g., the signals in Fig. 5A are not that much lower than Fig. 4A. This is perhaps obviously given by the different amounts of Cherenkov light seen in emission from the two solutions, as shown in Fig. 2C. The fact that these are not all that different is likely because the fiber collecting the light picks up through the whole volume, but the Cherenkov is launched through the whole volume as well, and because of the scattering the fiber will preferentially pick up light from near the surface. So, while the Cherenkov

Please restrict your changes to the correction of typographical errors.

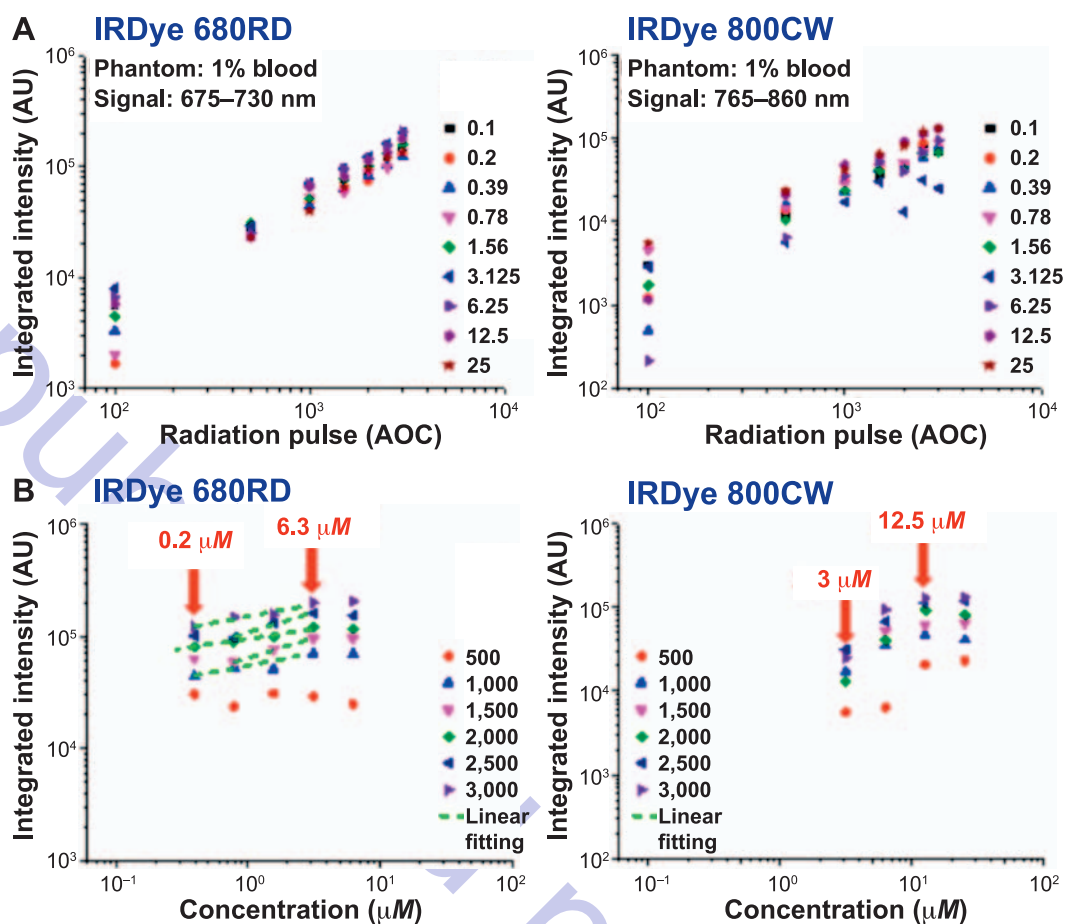


FIG. 5. The effects of integrated signal from intralipid plus blood solutions are shown for IRDye 680RD (left) and IRDye 800CW (right) for varying radiation doses (panel A) at varied concentrations of 0.1–25 μM . Variation in signal with varying concentration was then examined (panel B) for a varied radiation dose of 13.9–83 cGy (AOC 100–3,000).

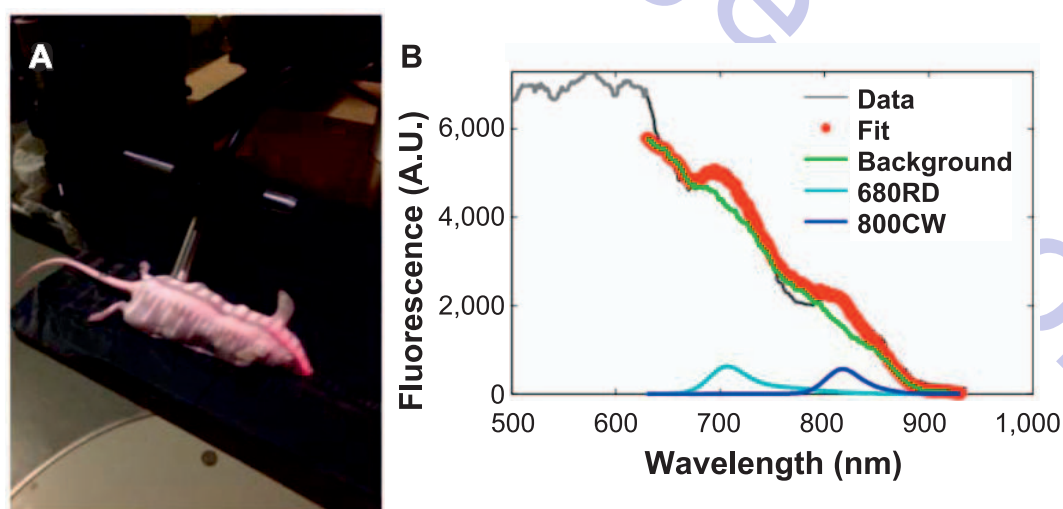


FIG. 6. Preliminary *in vivo* imaging of a nude mouse injected subcutaneously with 200 μl phenol red-free Matrigel basement membrane matrix with 3 μM IRDye 800CW and 3 μM IRDye 680RD. The mouse was positioned on the radiation treatment table and the optical fiber was placed in contact with the Matrigel injection (panel A). Panel B: Processed and fitted spectra. The measured spectrum was spectrally decoupled to estimate the contributions of each fluorophore.

Please restrict your changes to the correction of typographical errors.

light transmission through longer distances of tissue will undoubtedly be more attenuated in the NIR by blood, in the short pathlength, it does not appear to be so. Given that fluorophores are excited locally by the Cherenkov light originating right within the phantom (tissue), the distance effect of attenuation is less of an issue than just the amount of Cherenkov generated. In addition to the tissue-simulating phantom studies, the preliminary *in vivo* testing showed that a ~1:1 ratio of fluorophore concentrations was measurable when 3 μM of each dye was injected simultaneously and subcutaneously in the mouse body, suggesting that the presented approach may be promising in ratiometric fluorescent tracer quantification (8, 17).

The fact that the detectable concentration range is limited to the micromolar regime, will mean that this style of sensing will not be sufficient for immune-tagged fluorophores, where typical cell surface receptors or cell receptor concentrations are routinely in the range of 1–100 nM (18). However, most metabolic events such as enzymatic proteins, minerals and respiratory cell components are present in tissue at the micromolar range and these are primary targets to delineate cancer tumors. Thus, fluorescent sensing of these reporters should be inherently possible for CELSI sensing. Additionally, at least two fluorophores should be detectable. The two dyes used here were chosen based on the results of our previously reported study, and so were thought to be optimally separated in wavelength to allow maximal accuracy in spectral fitting (3).

CONCLUSIONS

The observations from this tissue phantom and preliminary *in vivo* study indicate that Cherenkov is attenuated by blood, but predominantly in wavelengths <620 nm, and so choosing fluorophores with emissions above these wavelengths is optimal. Demonstration of simultaneous detection of two NIR-emitting fluorophores in the Cherenkov spectrum illustrates what is achievable in future tissue studies. The concentration range feasible to detect signals is the 1–10 μM , indicating that metabolic tracer imaging with multiple reporters would be feasible with IRDyes and Cherenkov excitation. Further work to optimize the signal to background might lower this detectable range, either by better time-gating or other means, but in this current state of spectrometer-based detection, it would appear that this range is approximately the working region of use *in vivo*. The doses required are in the range of 3–80 cGy, which is at the upper end of a diagnostically useful dose.

ACKNOWLEDGMENT

This work was funded by the Congressionally Directed Medical Research Program for Breast Cancer Research Program, U.S. Army USAMRAA contract no. W81XWH-16-1-0004.

Received: September 18, 2017; accepted: October 25, 2017; published online: Month 00, 2017

REFERENCES

1. Axelsson J, Davis S, Gladstone D, Pogue B. Cherenkov emission induced by external beam radiation stimulates molecular fluorescence. *Med Phys* 2011; 38:4127–32.
2. Demers JL, Davis SC, Zhang R, Gladstone DJ, Pogue BW. Cherenkov excited fluorescence tomography using external beam radiation. *Opt Lett* 2013; 38:1364–6.
3. Lin H, Zhang R, Gunn JR, Esipova TV, Vinogradov S, Gladstone DJ, et al. Comparison of Cherenkov excited fluorescence and phosphorescence molecular sensing from tissue with external beam irradiation. *Phys Med Biol* 2016; 61:3955–68.
4. Gross S, Piwnica-Worms D. Spying on cancer: molecular imaging in vivo with genetically encoded reporters. *Cancer Cell* 2005; 7:5–15.
5. Shah K, Weissleder R. Molecular optical imaging: applications leading to the development of present day therapeutics. *NeuroRx* 2005; 2:215–25.
6. Yoshida M, Furukawa T, Morikawa Y, Kitagawa Y, Kitajima M. The developments and achievements of endoscopic surgery, robotic surgery and function-preserving surgery. *Jpn J Clin Oncol* 2010; 40:863–9.
7. Elliott JT, Marra K, Evans LT, Davis SC, Samkoe KS, Feldwisch J, et al. Simultaneous in vivo fluorescent markers for perfusion, protoporphyrin metabolism, and egfr expression for optically guided identification of orthotopic glioma. *Clin Cancer Res* 2017; 23:2203–12.
8. Tichauer KM, Samkoe KS, Gunn JR, Kanick SC, Hoopes PJ, Barth RJ, et al. Microscopic lymph node tumor burden quantified by macroscopic dual-tracer molecular imaging. *Nat Med* 2014; 20:1348–53.
9. Samkoe KS, Tichauer KM, Gunn JR, Wells WA, Hasan T, Pogue BW. Quantitative in vivo immunohistochemistry of epidermal growth factor receptor using a receptor concentration imaging approach. *Cancer Res* 2014; 15:7465–74.
10. Sinha L, Wang Y, Yang C, Khan A, Brankov JG, Liu JT, et al. Quantification of the binding potential of cell-surface receptors in fresh excised specimens via dual-probe modeling of SERS nanoparticles. *Sci Rep* 2015; 5:8582.
11. Li C, Mitchell GS, Cherry SR. Cherenkov luminescence tomography for small-animal imaging. *Opt Lett* 2010; 35:1109–11.
12. Axelsson J, Glaser AK, Gladstone DJ, Pogue BW. Quantitative Cherenkov emission spectroscopy for tissue oxygenation assessment. *Opt Express* 2012; 20:5133–42.
13. Dothager RS, Goiffon RJ, Jackson E, Harpstrite S, Piwnica-Worms D. Cherenkov radiation energy transfer (CRET) imaging: a novel method for optical imaging of PET isotopes in biological systems. *PLoS One* 2010; 5:e13300.
14. Thorek DL, Das S, Grimm J. Molecular imaging using nanoparticle quenchers of Cherenkov luminescence. *Small* 2014; 10:3729–34.
15. Zhang R, D'Souza A V, Gunn JR, Esipova TV, Vinogradov SA, Glaser AK, et al. Cherenkov-excited luminescence scanned imaging. *Opt Lett* 2015; 40:827–30.
16. Bruza P, Lin H, Vinogradov SA, Jarvis LA, Gladstone DJ, Pogue BW. Light sheet luminescence imaging with Cherenkov excitation in thick scattering media. *Opt Lett* 2016; 41:2986–9.
17. Samkoe KS, Tichauer KM, Gunn JR, Wells WA, Hasan T, Pogue BW. Quantitative in vivo immunohistochemistry using a dual-tracer receptor concentration imaging approach. *Cancer Res* 2014; 74:7465–74.
18. Pogue BW, Paulsen KD, Hull SM, Samkoe KS, Gunn J, Hoopes J, et al. Advancing molecular-guided surgery through probe development and testing in a moderate cost evaluation pipeline. *Proc SPIE Int Soc Opt Eng* 2015; 9311.
19. Pogue BW, Patterson MS. Review of tissue simulating phantoms for optical spectroscopy, imaging and dosimetry. *J Biomed Opt* 2006; 11:041102.

Please restrict your changes to the correction of typographical errors.

Queries for rare-189-02-09

This manuscript/text has been typeset from the submitted material. Please check this proof carefully to make sure there have been no font conversion errors or inadvertent formatting errors. Allen Press.

Radiotherapy-induced Cherenkov luminescence imaging in a human body phantom

Syed Rakin Ahmed,^{a,†} Jeremy Mengyu Jia,^{a,†} Petr Bruza,^a Sergei Vinogradov,^b Shudong Jiang,^a David J. Gladstone,^{a,c,d} Lesley A. Jarvis,^{c,d} and Brian W. Pogue^{a,d,*}

^aThayer School of Engineering at Dartmouth, Hanover, New Hampshire, United States

^bUniversity of Pennsylvania, Departments of Biophysics and Biochemistry and of Chemistry, Philadelphia, Pennsylvania, United States

^cGeisel School of Medicine at Dartmouth, Department of Medicine, Hanover, New Hampshire, United States

^dDartmouth-Hitchcock Medical Center, Norris Cotton Cancer Center, Lebanon, New Hampshire, United States

Abstract. Radiation therapy produces Cherenkov optical emission in tissue, and this light can be utilized to activate molecular probes. The feasibility of sensing luminescence from a tissue molecular oxygen sensor from within a human body phantom was examined using the geometry of the axillary lymph node region. Detection of regions down to 30-mm deep was feasible with submillimeter spatial resolution with the total quantity of the phosphorescent sensor PtG4 near 1 nanomole. Radiation sheet scanning in an epi-illumination geometry provided optimal coverage, and maximum intensity projection images provided illustration of the concept. This work provides the preliminary information needed to attempt this type of imaging *in vivo*. © The Authors. Published by SPIE under a Creative Commons Attribution 3.0 Unported License. Distribution or reproduction of this work in whole or in part requires full attribution of the original publication, including its DOI. [DOI: 10.1117/1.JBO.23.3.030504]

Keywords: Cerenkov; radiation; therapy; linac; phosphorescence.

Paper 180015LR received Jan. 11, 2018; accepted for publication Feb. 26, 2018; published online Mar. 20, 2018.

1 Introduction

All optical imaging techniques suffer from diminished spatial resolution with increasing depth into tissue because of the severe light scattering present.¹ Yet, in recent studies it has been shown that Cherenkov-based excitation of molecular probes is a feasible way to image deep into tissues, over several centimeters, with submillimeter resolution.² One important application of this is luminescence-based sensing of oxygen over macroscopic depths into tissue. The available depth of sampling is appropriate for imaging oxygenation in lymph nodes. In this study, the feasibility of imaging oxygen in lymph node-sized objects in a human body phantom was assessed to estimate applicability

of this luminescence lifetime sensing technology in human imaging.

Cherenkov radiation is produced in all tissues undergoing treatment with Megaelectron Volt photons or electrons,³ generating broadband optical radiation that can be used to excite molecular probes.^{4,5} Clinical linear accelerators (linacs) operate in pulsed mode with $\sim 4\text{-}\mu\text{s}$ bursts,^{6,7} allowing for excitation of phosphorescent probes that have 10- to 100- μs range emission decay times.⁸ Previous experiments demonstrated this luminescence imaging with Cherenkov excitation in basic tissue phantoms and in rodents,^{9,10} to image tissue oxygenation, with time-gated signals that were sensitive to the luminescence quenching by oxygen. The key advantage of the method was to image centimeters into tissue while retaining submillimeter spatial resolution. At the same time, imaging oxygen is relevant in radiotherapy since it is a radiosensitivity factor that correlates with outcome.¹¹

In this work, sheet-shaped radiation beams from a linac were used to produce Cherenkov photons, to excite luminescence of probes in a volume largely confined to the irradiation sheets. Thus, by shaping the x-ray beam into a thin sheet, images of Cherenkov-excited luminescence from a planar slice within the tissue can be observed. Analogous to light sheet microscopy, a series of luminescence images can be taken at different depths, allowing for three-dimensional (3-D) volumetric rendering. This imaging approach has been termed Cherenkov-excited luminescence scanned imaging (CELSI).^{2,10} Knowing the position of the excitation plane allows for depth-variant attenuation correction, and postprocessed 3-D images show the luminescence distribution from within the tissue.

The aim of this study was to study CELSI in a human body geometry, to demonstrate the capability of imaging local oxygenation in regions similar in size to lymph nodes, as shown in Fig. 1. Specifically, the effects of depth, concentration, and minimum radiation dose were examined here.

2 Materials and Methods

2.1 Phantoms and Geometry

Depth and concentration range evaluation experiments were carried out to assess the signal-to-noise ratio (SNR) and signal-to-background ratio for phosphorescent objects at varying depths. The phosphorescent probe used in our experiments was PtG4, which has a well-demonstrated oxygen-dependent luminescence lifetime, characterized in solution¹² as well as in our previous animal study.² Eppendorf tubes containing 0.5-mL solution of PtG4 of varying concentrations (1 to 100 μM) were positioned at different depths (0 to 3.5 cm) to assess imaging capability with concentration and depth. A semi-infinite tissue phantom, of 1% aqueous solution of intralipid and 1% bovine blood was used to mimic the optical properties of the human tissue.

A full torso PBU-50 phantom (Kyoto Kagaku America Inc., Torrance, California) was used with two sets of measurements. First, Eppendorf tubes were used with 50 μL of 25- μM solution of PtG4 (0.5 nanomoles) in phosphate buffered saline (PBS), and comparing with controls of just PBS and an empty tube. In the second set, five 0.2-mL Eppendorf tubes were used, each containing (1) 50 μL of solution of PtG4 at concentrations: 1, 5, 10, 20, and 25 μM , for total quantities of 0.05, 0.25, 0.5, 1.0, and 1.25 nanomoles, respectively. The tubes were placed in the lateral rib region of the phantom at a sufficient distance from one another to prevent spatial overlap of their signals.

*Address all correspondence to: Brian W. Pogue, E-mail: brian.w.pogue@dartmouth.edu

†Equal contribution.

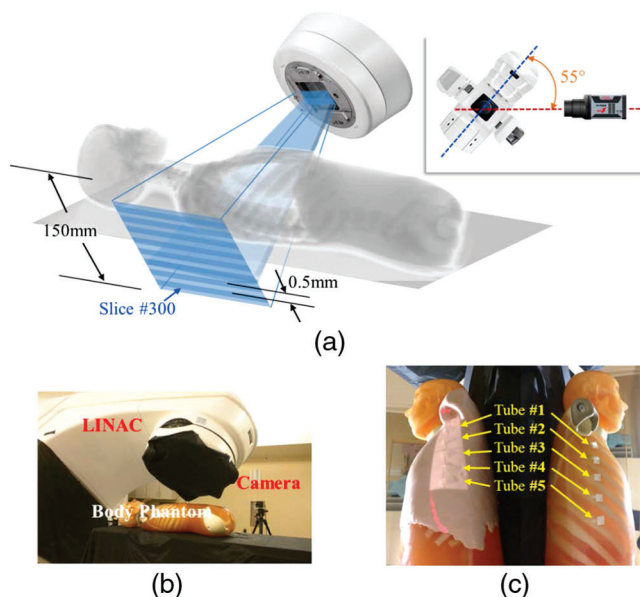


Fig. 1 Measurement geometry for the body phantom is shown with (a) a schematic of the geometry, (b) a photograph of the setup, and (c) the body phantom with skin on (left) and without skin (right) as shown with five tubes fixed onto the lateral rib area.

In both experimental sets, the phantom was imaged both with and without “skin layer” that was mimicked using tissue colored modeling clay (SuperSculpey® Original). Prior to the CELSI experiments, we validated the tissue-like optical properties of the used modeling clay by measuring its absorption and scattering coefficients.¹³ Using a custom tissue spectroscopy device, the DOSI system,¹⁴ we measured values across the spectral range of 650 to 1000 nm. The spectral range of PtG4 phosphorescence emission is peaked at 772 nm, the absorption and scattering coefficients of the clay ($\mu_a = 0.014 \text{ mm}^{-1}$, $\mu_s' = 0.55 \text{ mm}^{-1}$ match reasonable values of skin and/or adipose human tissue. A clinical x-ray CT of the body phantom, with 2.5-mm slice thickness, was obtained to facilitate postprocessing image overlay (LightSpeedCT, GE Healthcare, Chicago, Illinois).

2.2 Linear Accelerator

In each experiment, a Varian linac (2100CD, Varian Medical Systems, Palo Alto, California) was used to deliver six MV x-ray photon beams to the phantoms in the form of thin sheets. Multileaf collimators (MLC) (Millennium 120MLC, Varian Medical Systems) were used to shape and vertically translate the beam profile adaptively. Each sheet was 200-mm wide and 5-mm thick. The MLC leaves translated a total distance of 50 mm with a 0.2-mm step—this resulted in a total of 250 x-ray sheet positions along the length of the treatment area. The maximum dosage of radiation delivered by the linac was 20 MU/position, with up to 25 overlapping positions (5 mm moved in steps of 0.2 mm); this resulted in a maximum of $20 \times 25 = 500$ MU being delivered to the volume as defined by a single beam sheet—roughly equivalent to a maximum absorbed dose of 5 Gy.

2.3 Luminescence Emission Imaging

Images were captured by a gated, intensified charge-coupled device (ICCD, PI-MAX4 1024i, Princeton Instruments) with a 135-mm lens (Nikon), using the associated LightField software. An epi-illumination configuration was used, with the

linac gantry oriented at 145 deg and in the same side as the ICCD. The ICCD gate delays and widths were adjusted with $0.05 \mu\text{s}$ delay and $4 \mu\text{s}$ width for Cherenkov imaging, whereas a $4.2 \mu\text{s}$ delay and $70 \mu\text{s}$ width was used for phosphorescence imaging, and $1500 \mu\text{s}$ delay and $70 \mu\text{s}$ width used for background. Cherenkov, phosphorescence, and background images were acquired with $100\times$ gain on the intensifier. The image intensifier was gated by a predefined number of pulses, whereas the CCD integrated the signal prior to readout. Different values of this approach to accumulations on the chip (AoC) were used for each of the Cherenkov, phosphorescence, and background images for all body phantom CELSI experiments. Room-light images were acquired with $1\times$ gain and 1 AoC. An 8-MHz analog-to-digital conversion rate was used with 2×2 pixel hardware binning upon readout, resulting in 512×512 pixel images.

2.4 Image Processing

Image processing was carried out in MATLAB and Python. The protocol first involved background subtraction, followed by a depth stack (z -stack) median filter, across four frames in sequence, resulting in 250 frames. Next, each image was background corrected relative to its own residual background by subtracting the median from a background region of each image in the z -stack, followed by a 2-D (5×5) and a 3-D ($5 \times 5 \times 5$) spatial median filter. Finally, a 3-D Gaussian Filter with FWHM = 4.7 pixels was applied. Maximum-intensity projection (MIP) images were generated along the z -stack. The processed images were overlaid on the room-light image using both ImageJ and MATLAB Overlay GUI.¹⁵ Subsequently, videos were generated using ImageJ, showing the translation of the sheet beam through the region containing the simulated lymph nodes and static images of these are shown in Fig. 3.

Image display was done for 3-D views in Paraview (Kitware Inc.), using the processed phosphorescence image stack and the MIP images from the final two sets of tube experiments. Specifically, the experiments conducted with simulated skin were used for the 3-D reconstructions. The images were registered using the centroids of the Eppendorf tubes and edge of the phantom as fiducials to coalign the co-ordinate system of the CT to that of the phosphorescence images.

3 Results

In the depth and concentration ranging studies, CELSI experiments were performed for an intralipid-blood phantom embedded with PtG4-containing 0.5-mm Eppendorf tubes. The results are shown in Fig. 2, where sample luminescence and roomlight images are included in (a), and SNR is plotted in (b). The SNR has an exponential shape and the values plateau to their lowest values at deeper depths, as anticipated, because at some extreme depths the presence of the luminescent region cannot be sensed. Consequently, the SNR should be expected to asymptote to 1.0 at deep depths. The relationship between imaging depth and concentration of PtG4 for SNR = 1 is described by the circled plots in Fig. 2(b), indicating that for depths < 1.7 cm there was good SNR, but below this depth, the concentration required for SNR > 1 increased dramatically. However, signal as deep at 3 cm was detectable, at concentrations just above 100 microMolar.

For the first set of geometry studies investigating phosphorescence of tubes containing PtG4 relative to control tubes containing PBS and a blank, a strong phosphorescent signal was detected. This was anticipated because the stock solution

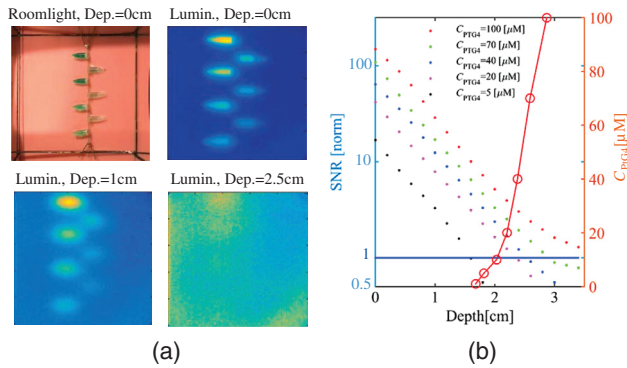


Fig. 2 Experimental results to investigate image quality versus depth for different concentrations of PtG4 (C_{PtG4}) as shown in the legend, showing (a) the room light image and luminescence images of the phantom used at three different depths in the phantom, and (b) the corresponding SNR values extracted from these images are shown as a function of depth by colored dots. In the same graph, the red line shows the C_{PtG4} at which SNR = 1 (values on left y-axis).

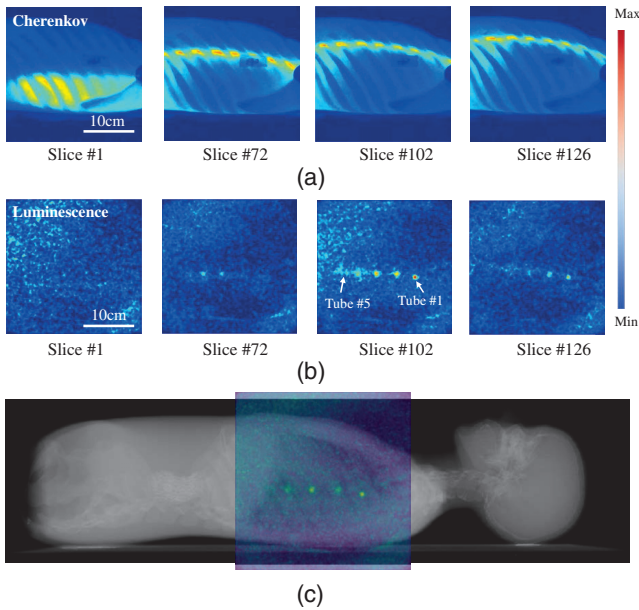


Fig. 3 Raw measurement sequences are shown for (a) Cherenkov emission and (b) luminescence photons, for the sheet at four different slice locations. In (c) a composition image is shown of the phantom CT with color overlay of the CELSI MIP image. A temporal sweep of the signals in (a) and (b) can be seen in the associated video files as the sheet moved across the phantom body.

of 25 µM was a high concentration and was placed at a depth of only 3 mm. At 144 AoC, the SNR was computed to be 59, whereas at 60 AoC the SNR was 66. Overall, the 144 and 60 AoC cases produced similar results, with very similar SNRs, for the experiments with “skin.”

For the second set of experiments investigating different concentrations of PtG4, visible phosphorescent signals were detected from the 5- to 25-µM tubes, whereas the 1-µM tube did not produce a signal with sufficient SNR to be detected. The trend in signal strength, with respect to concentrations on the MIP images was as anticipated, with greater concentrations of PtG4 yielding stronger, brighter signals, with slight variation

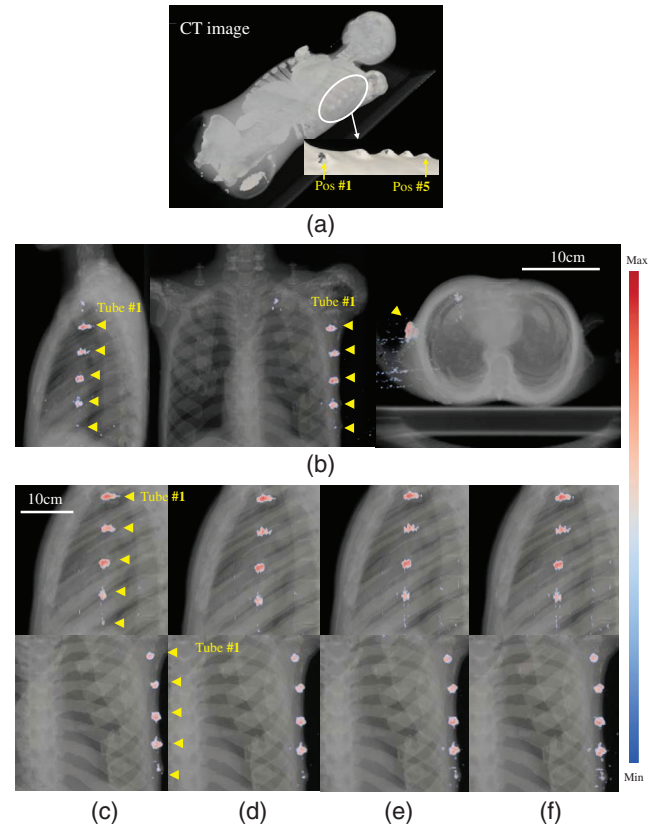


Fig. 4 3-D images of (a) CT and (b) overlaid with CELSI for three orthogonal views: coronal, sagittal, and transverse. Compositions of CT and CELSI images for varying numbers of light sheets, which correspond to less dose delivery. In these images, the number of sheets were: (c) 25, (d) 50, (e) 100, and (f) 250, respectively.

largely due to the thickness of skin overlying the tubes. Videos of the two sets of geometry studies are illustrated.

The angular sheet-beam scanning methodology that is more suitable for imaging a chest region was used, as shown in Fig. 1. Raw measurements of Cherenkov light and luminescence for four specific slice positions are shown in Figs. 3(a) and 3(b), respectively. Figure 3(c) shows a combined image of CT and luminescence maximum intensity projection (MIP). Scanned image data were reprocessed and overlaid on the 3-D volume of the CT scan, to allow visualization of the recovered positions of the tubes. The recovered images are shown in Fig. 4, with a perspective view in (a), and the three orthogonal views of the CT in (b).

To pursue a minimum radiation dose, sparse illumination was investigated, i.e., the number of light sheets was desired to be as few as possible. Here, a total of 25, 50, 100, and 250 light sheets were used with equal spacing, i.e., with spaces 2, 1, 0.5, and 0.2 mm, respectively. Figures 4(c)–4(f) show the compositions of CT and CELSI images for different numbers of light sheet. It can be seen that the image quality was reasonable, even for 25 light sheets.

4 Discussion

Initial studies of depth sensitivity have indicated that CELSI imaging would be viable for a depth of perhaps 2 to 3 cm, likely dependent upon the tissue type involved. Adipose tissues tend to have lower blood volume and consequently reduced absorption

attenuation of the light—this may allow imaging down to 3 cm. In contrast, denser tissues would have higher absorption and therefore be more limited to >2 cm.

The set of experiments conducted here were initially focused on determining the optimum positioning of the body phantom, couch, gantry, and camera for maximal sensitivity. Three orientations were investigated such as (i) vertical with the gantry directly above the body phantom on the couch at 180-deg reference angle and the camera placed directly facing the left side of the body phantom, (ii) horizontal with the gantry directly facing the left side of the body phantom at 90-deg reference angle and a 45-deg front-surface mirror placed above the top surface of the body phantom, allowing horizontal mounting of the ICCD directly facing the mirror, and (iii) angled with the gantry at 145-deg reference angle with ICCD on the same side. The angular orientation in an epi-illumination configuration was determined to be optimum and used for all subsequent experiments. In this orientation, a Cherenkov sheet was clearly visible translating through the body phantom. This orientation was also hypothesized to result in a strong phosphorescence signal from the simulated lymph nodes, and better approximated tangential breast tumor treatment protocol. The recovery of intensity was highly modulated by the depth of tissue overlying the tubes, and it was apparent that the signal was not linear with concentration because of this effect. However with skin thickness measured by the CT scan and geometry, it is feasible to quantify these values based on depth-dependent attenuation correction.¹⁰

These studies illustrate how imaging of lymph node sized objects may have potential with CELSI imaging in radiotherapy. Sensing their oxygenation is feasible, and further exploration of agents and signal analysis could lead to the next clinical trials in molecular sensing in radiotherapy.

Disclosures

The authors have no relevant financial interests in this article and no potential conflicts of interest to disclose, other than Brian Pogue, who is president and founder of DoseOptics LLC.

Acknowledgments

This work has been funded by the Congressionally Directed Medical Research Program for Breast Cancer Research Program, U.S. Army USAMRAA Contract No. W81XWH-

16-1-0004 and National Institutes of Health research Grant Nos. R01 EB024498 and EB018464.

References

1. D. Razansky et al., "Deep tissue optical and optoacoustic molecular imaging technologies for pre-clinical research and drug discovery," *Curr. Pharm. Biotechnol.* **13**(4), 504–522 (2012).
2. R. Zhang et al., "Cherenkov-excited luminescence scanned imaging," *Opt. Lett.* **40**(5), 827–830 (2015).
3. L. A. Jarvis et al., "Cherenkov video imaging allows for the first visualization of radiation therapy in real time," *Int. J. Radiat. Oncol. Biol. Phys.* **89**(3), 615–622 (2014).
4. R. Robertson et al., "Optical imaging of Cherenkov light generation from positron-emitting radiotracers," *Phys. Med. Biol.* **54**(16), N355–N365 (2009).
5. J. Axelsson et al., "Quantitative Cherenkov emission spectroscopy for tissue oxygenation assessment," *Opt. Express* **20**(5), 5133–5142 (2012).
6. M. Constantin et al., "Modeling the truebeam Linac using a CAD to Geant4 geometry implementation: dose and IAEA-compliant phase space calculations," *Med. Phys.* **38**(7), 4018–4024 (2011).
7. L. Grevillot et al., "Simulation of a 6 MV Elekta Precise Linac photon beam using GATE/GEANT4," *Phys. Med. Biol.* **56**(4), 903–918 (2011).
8. H. Lin et al., "Comparison of Cherenkov excited fluorescence and phosphorescence molecular sensing from tissue with external beam irradiation," *Phys. Med. Biol.* **61**(10), 3955–3968 (2016).
9. R. Zhang et al., "Cherenkov radiation emission and excited luminescence (CREL) sensitivity during external beam radiation therapy: Monte Carlo and tissue oxygenation phantom studies," *Biomed. Opt. Express* **3**(10), 2381–2394 (2012).
10. P. Bruza et al., "Light sheet luminescence imaging with Cherenkov excitation in thick scattering media," *Opt. Lett.* **41**(13), 2986–2989 (2016).
11. M. Nordsmark et al., "Prognostic value of tumor oxygenation in 397 head and neck tumors after primary radiation therapy. An international multi-center study," *Radiother. Oncol.* **77**(1), 18–24 (2005).
12. A. Y. Lebedev et al., "Dendritic phosphorescent probes for oxygen imaging in biological systems," *ACS Appl. Mater. Interfaces* **1**(6), 1292–1304 (2009).
13. S. L. Jacques, "Optical properties of biological tissues: a review," *Phys. Med. Biol.* **58**(11), R37–R61 (2013).
14. A. E. Cerussi et al., "Frequent optical imaging during breast cancer neoadjuvant chemotherapy reveals dynamic tumor physiology in an individual patient," *Acad. Radiol.* **17**(8), 1031–1039 (2010).
15. J. T. Elliott et al., "Review of fluorescence guided surgery visualization and overlay techniques," *Biomed. Opt. Express* **6**(10), 3765–3782 (2015).

Comparison of phosphorescent agents for noninvasive sensing of tumor oxygenation via Cherenkov-excited luminescence imaging

Jennifer R. Shell,^{a,*†} Ethan P. LaRochelle,^{a,†} Petr Bruza,^a Jason R. Gunn,^a Lesley A. Jarvis,^b David J. Gladstone,^{a,b} and Brian W. Pogue^a

^aDartmouth College, Thayer School of Engineering, Hanover, New Hampshire, United States

^bDartmouth College, Geisel School of Medicine, Hanover, New Hampshire, United States

Abstract. Cherenkov emission generated in tissue during radiotherapy can be harnessed for the imaging biochemistry of tissue microenvironments. Cherenkov-excited luminescence scanned imaging (CELSI) provides a way to optically and noninvasively map oxygen-related signals, which is known to correlate to outcomes in radiotherapy. Four candidate phosphorescent reagents PtG4, MM2, Ir(btbt)₂(acac), and MitoID were studied for oxygen sensing, testing in a progressive series of (a) in solution, (b) *in vitro*, and (c) in subcutaneous tumors. In each test, the signal strength and response to oxygen were assessed by phosphorescence intensity and decay lifetime measurement. MM2 showed the most robust response to oxygen changes in solution, followed by PtG4, Ir(btbt)₂(acac), and MitoID. However, in PANC-1 cells, their oxygen responses differed with Ir(btbt)₂(acac) exhibiting the largest phosphorescent intensity change in response to changes in oxygenation, followed by PtG4, MM2, and MitoID. *In vivo*, it was only possible to utilize Ir(btbt)₂(acac) and PtG4, with each being used at nanomole levels, to determine signal strength, lifetime, and pO₂. Oxygen sensing with CELSI during radiotherapy is feasible and can estimate values from 1 mm regions of tissue when used in the configuration of this study. PtG4 was the most amenable to *in vivo* sensing on the timescale of external beam LINAC x-rays. © The Authors. Published by SPIE under a Creative Commons Attribution 4.0 Unported License. Distribution or reproduction of this work in whole or in part requires full attribution of the original publication, including its DOI. [DOI: 10.1117/1.JBO.24.3.036001]

Keywords: tumor hypoxia; Cherenkov radiation; phosphorescence; optical imaging.

Paper 180604R received Oct. 31, 2018; accepted for publication Feb. 1, 2019; published online Mar. 4, 2019.

1 Introduction

Extent of oxygenation in tumors is a known indicator of the success of radiation therapy, partly due to the oxygen enhancement ratio,¹ as well as due to oxygen being a surrogate marker for other features of tumor aggressiveness.² Therefore, monitoring of tumor oxygenation during fractionated radiation therapy would be advantageous to gauge the likelihood of response or even to estimate if treatment plan alternations such as a boost to hypoxic areas might be beneficial. Oxygen electrodes have been utilized to measure hypoxia.^{3–5} While this method allows direct measurement of oxygen levels in tumors, it is invasive and is limited to tumors that are easily accessible. Tumor biopsies with indirect measurements for hypoxia, including pimonidazole staining and immunostaining for HIF-1 α , provide valuable information of individual tumor microenvironments,^{6–10} but these methods are also invasive and do not provide real-time measurement of tumor oxygenation levels. Blood oxygen level-dependent magnetic resonance imaging (BOLD-MRI),^{11,12} electron paramagnetic resonance oximetry,^{13,14} and near-infrared spectroscopic tomography¹⁵ provide real-time information based on hemoglobin saturation. Positron emission tomography also measures real-time levels of hypoxia, utilizing ¹⁸F-labeled nitroimidazole derivatives, whose luminescence are dependent on oxygen levels.^{16,17} Despite the potential value, there has not been any clinical convergence on a method for

imaging tumor oxygenation that is noninvasive, precise, and quantitative. In this study, oxygen-related mapping in tumors is demonstrated with Cherenkov-excited luminescence scanned imaging (CELSI), which uses the inherent delivery of radiation to get maps of oxygen-dependent luminescence signals from injected chemical sensors. Current reagents utilized for phosphorescent sensing of oxygen that can be utilized for noninvasive determination of oxygen content [PtG4, MM2, Ir(btbt)₂(acac), and MitoID] are evaluated.

Radiation treatment with MV photons or MeV electrons causes the production of Cherenkov light in tissue. This optical emission occurs when charged primary or secondary electrons pass through the dielectric medium, such as tissue, at a velocity greater than the speed of light. This optical signal has been imaged to visualize surface dose in radiation therapy.^{18–20} In addition, early pilot studies in tissue phantoms and individual animals have shown utilization of Cherenkov emission as the excitation source in imaging applications, including the detection of fluorophores and phosphors in conjunction with radiation therapy.²¹ The potential to sense tumor oxygenation through CELSI with the phosphorescent reagent PtG4 has been shown by us, because the PtG4 phosphorescence is quenched in the presence of oxygen, reducing the observed lifetime of emission. In the presence of ambient oxygen pressure (pO₂), the PtG4 phosphorescence lifetime is 16.9 μ s, and in low pO₂ it is 47 μ s.^{22,23}

In this study, this agent was compared to other oxygen-quenched chemical agents, and each was examined for its potential to sense tumor hypoxia by directly measuring pO₂ levels *in vivo* with mice bearing subcutaneous tumors.²⁴ At the end of the

*Address all correspondence to Jennifer R. Shell, E-mail: jennifer.r.shell@dartmouth.edu

[†]Jennifer R. Shell and Ethan P. LaRochelle contributed equally to this work.

study, the spatial confidence in mapping pO_2 was estimated, using doses typical of fractionated radiotherapy.

2 Methods and Materials

2.1 Chemicals

PtG4 (platinum II G4) was provided by Sergei Vinogradov and colleagues.²³ MM2 was purchased from Luxcel Bioscience, Cork, Ireland,²⁵ bis(2-phenylbenzothiazolato)-(acetylacetonate)iridium(III) $[Ir(bt)_2(acac)]$ ²⁶ was purchased from Sigma Aldrich, Saint Louis, Missouri, and Mito-ID intracellular oxygen sensor was purchased from Enzo Life Sciences, Farmingdale, New York. MDA-MB-231 luc-D3H2LN cells were obtained from Perkin Elmer (Waltham, Massachusetts) and PANC-1 cells were obtained from ATCC (CRL-1469, Manassas, Virginia). Dulbecco Modified Eagle Medium (DMEM), fetal bovine serum (FBS), phosphate buffered saline (PBS), and 0.05% trypsin were purchased from Thermo Fisher Scientific (Waltham, Massachusetts). Molecular Devices Gemini XS (Sunnyvale, California) was utilized for fluorescence plate reader measurements, Agilent Cary 50 UV-Vis (Santa Clara, California) was utilized for absorbance spectra, and Horiba Fluorolog-3 (Edison, New Jersey) was utilized for emission spectra. Fluorescence microscopy was performed on a Zeiss LSM 800 (Jena, Germany) confocal microscope.

2.2 Assessment of Absorbance and Fluorescence Emission Spectra

The absorbance and fluorescence emission spectra of PtG4 (1 μ M, $\lambda_{ex} = 435$ nm, and $\lambda_{em} = 772$ nm), $Ir(bt)_2(acac)$ (1 μ M, $\lambda_{ex} = 337, 480$ nm, and $\lambda_{em} = 620$ nm), MM2 (1 μ M, $\lambda_{ex} = 400$ nm, and $\lambda_{em} = 650$ nm), and MitoID (1 μ M, $\lambda_{ex} = 380$ nm, and $\lambda_{em} = 650$ nm) were measured as validation prior to employing these reagents in cell and *in vivo* studies.

2.3 Cell Culture

PANC-1 cells and MDA-MB-231 luc-D3H2LN cells were grown in DMEM with 10% FBS in an incubator at 37°C with 5% CO_2 , and 100% humidity and divided utilizing 0.05% trypsin when desired confluency was reached.

2.4 Fluorescence Assay In Vitro

PANC-1 cells were seeded in black 96-well plates with a clear bottom at 5000 cells/well. MM2, $Ir(bt)_2(acac)$, and MitoID (10, 20, 30 μ g/mL in PBS) were added to the cells and allowed to incubate for 24 h at 37°C. Media containing the reagents were removed and cells were rinsed with PBS. 10% FBS in PBS with or without glucose oxidase catalase oxygen scavenger (100 nM glucose oxidase, 1.5 μ M catalase, and 56 mM glucose) was added after rinsing and the fluorescence intensity was analyzed with an excitation of 380 nm and emission of 660 nm. For limits of detection studies, 20, 2, 0.2, and 0.02 μ g/mL of MM2 and $Ir(bt)_2(acac)$ were utilized in the same fashion as described above. A student's *t*-test was utilized to assess differences in fluorescence between oxygenated versus oxygen scavenged conditions.

2.5 Cherenkov Imaging

Cherenkov emission was induced by a linear accelerator (Varian LINAC 2100CD, Palo Alto, California). The imaging system consisted of a time-gated intensified CCD camera (ICCD, PI-MAX4 1024i, Princeton Instruments) and a commercial lens (Canon EF 135 mm f/2L USM). The camera was focused on a mirror that reflected the imaging field ~ 1 m away. The time-gated ICCD camera was synchronized to the radiation pulses (~ 3.25 μ s duration and 360 Hz repetition rate) with the intensifier set as $\times 100$ and turned on at a 4.26- or 1000- μ s gate delay following each radiation pulse for phosphorescence or background measurement, and luminescence generated during 85.60- μ s gate width (PtG4 and MM2), or 7.77 μ s $[Ir(bt)_2(acac)]$ was integrated via this ICCD. Images of the luminescence at different delay times between LINAC pulse and phosphorescence emission were acquired to construct emission lifetime. To maximize signal and minimize background interference, the room lights were shut off throughout these studies, and all lights in the room were masked off with black cloth and black tape.

2.6 CEL Studies In Vitro

Concentrations of 20, 2, 0.2, and 0.02 μ g/mL of MM2, $Ir(bt)_2(acac)$, MitoID, and PtG4 were utilized 96-well plate as above. For solution studies, 300 μ L of each solution with and without oxygen scavenger were utilized. For cellular studies, PANC-1 cells were seeded in black 96-well plates with a clear bottom at 5000 cells/well. The reagents were added to the cells and allowed to incubate for 24 h at 37°C. Media containing the reagents were removed and cells were rinsed with PBS. 10% FBS in PBS was added after rinsing.

2.7 General Animal Imaging

All animal procedures were approved by the Institutional Animal Care and Use Committee, and the studies here were carried out in compliance with these approved procedures.

2.8 In Vivo Imaging

Briefly, 10^5 MDA-MB-231 luc-D3H2LN cells were injected under the skin on the flank of a nude mouse (two tumors per mouse, eight tumors per reagent studied). After ~ 3 weeks of growth, animals were chosen for use when their tumor was $\sim 6 \times 6 \times 3$ mm³ in size. The CELSI scan was completed vertically. Images of the luminescence at different delay times between LINAC pulse and phosphorescence emission were acquired to construct emission lifetime. Under general anesthesia of inhaled isoflurane, 50 μ L of 50 μ M of each reagent was directly injected into the tumors and the animal was imaged alive and then again at 30 min after euthanize, which allows determination of emission lifetime at ambient pO_2 (alive) low pO_2 environments (dead), respectively.

2.9 Statistical Analysis

The tissue pO_2 was determined utilizing the Stern-Volmer relationship. The differences between the live and dead conditions, as shown in Fig. 5 with $n = 8$ paired samples each, were assessed using a two-tailed Student's *t*-test, with $\alpha = 0.05$ and resulting $P < 0.001$. This shows that there are significant differences between the values of both emission lifetime and

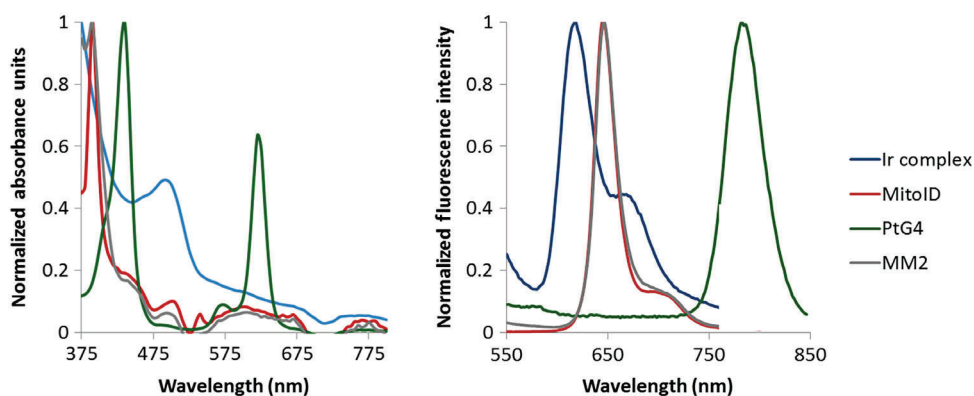


Fig. 1 Absorbance and emission spectra for oxygen sensors. The absorbance and fluorescence emission spectra for Ir(bt_b)₂(acac) (blue), MitoID (red), PtG4 (green), and MM2 (gray).

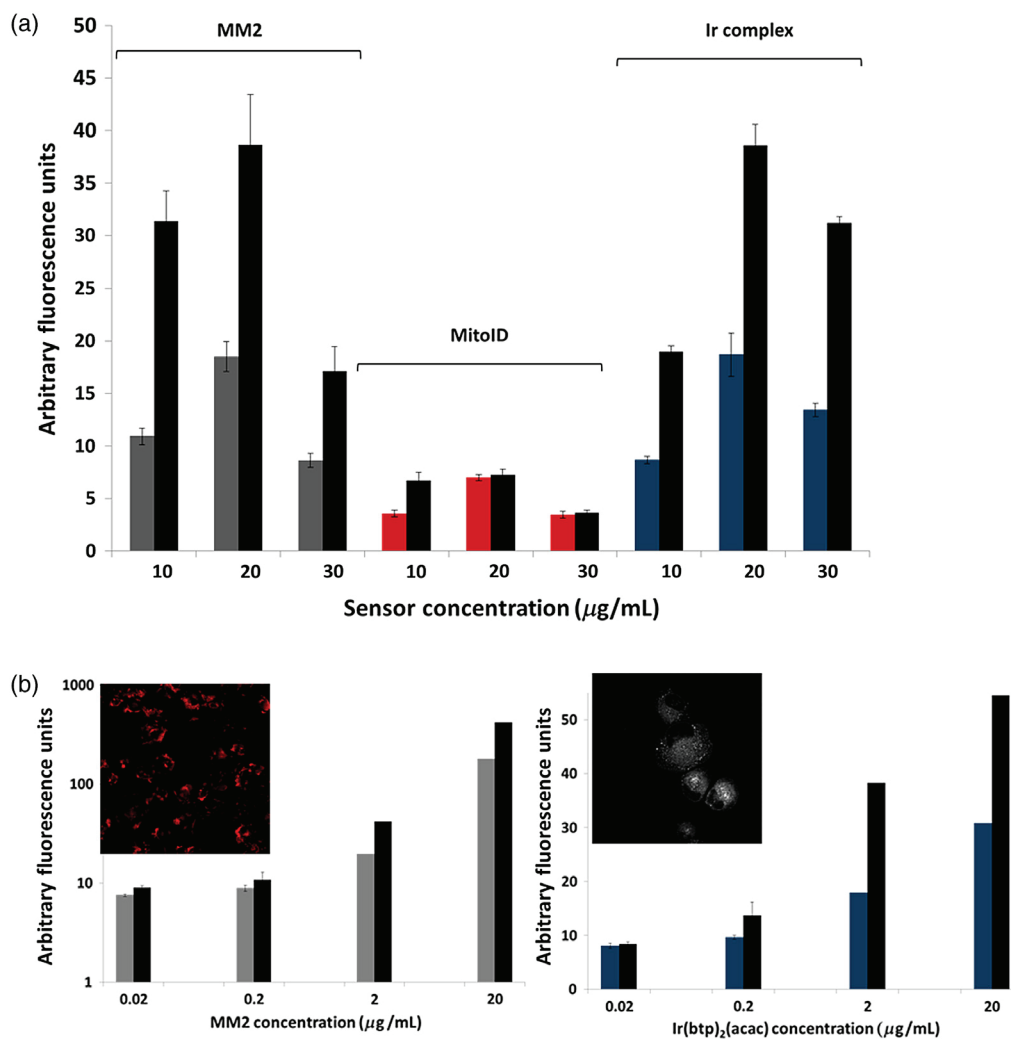


Fig. 2 Comparison of commercially available oxygen sensors in PANC-1 cells. (a) MM2 (gray), MitoID (red), and Ir(bt_b)₂(acac) (blue) were incubated with PANC-1 cells overnight. Fluorescence was measured in the presence of ambient oxygen [light gray, MM2, medium gray, MitoID, and dark gray, Ir(bt_b)₂(acac)] and with glucose oxidase catalase enzymatic oxygen scavenging (black). (b) The brightest commercial oxygen sensors were explored at decreasing concentrations (20, 2, 0.2, and 0.02 µg/mL) to determine the lowest concentration that can be detected. Inset shows fluorescence microscopy of each sensor (20 µg/mL) loaded into PANC-1 cells. Excitation and emission were measured at 380 and 660 nm, respectively. The fluorescence intensity represents the average of six experiments ± SEM.

pO_2 of the animals alive versus dead. Figure 5 was generated using Python 3.4.3 with the library matplotlib 2.0.0.

3 Results

The set of four phosphorescent oxygen sensors were directly compared to determine which of these reagents would be ideal for use in CELSI in tumors. These agents were chosen based upon published data, and they represented the most promising mix of agents for use *in vivo* with longer lifetime emission from phosphorescence. The absorbance and emission spectra of PtG4 (green), MM2 (gray), Ir(bt_b)₂(acac) (blue), and MitoID (red) are shown in Fig. 1.^{25,26} Relative brightness of the commercially available MM2, Ir(bt_b)₂(acac), and MitoID was assessed at increasing concentrations (10, 20, and 30 $\mu\text{g}/\text{mL}$) in PANC-1 cells in the presence and absence of ambient oxygen, through the addition of the enzymatic oxygen-scavenging system of glucose oxidase and catalase (GODCAT). Measurements of emission were taken via fluorescence plate reader. MM2 and Ir(bt_b)₂(acac) exhibited the maximum signal under deoxygenated conditions at 20 $\mu\text{g}/\text{mL}$, and the MitoID intensity in the presence and absence of oxygen scavengers was lower in comparison [Fig. 2(a)]. Statistically significant changes in oxygenation can be detected at concentrations as low as 0.2 $\mu\text{g}/\text{mL}$ for Ir(bt_b)₂(acac) and 0.02 $\mu\text{g}/\text{mL}$ for MM2 [Fig. 2(b)], as assessed by a student's t-test.

We sought to evaluate the effectiveness of these reagents to be imaged with Cherenkov excited luminescence (CEL). Solutions of PtG4, MM2, Ir(bt_b)₂(acac), and MitoID at decreasing concentrations (20, 2, 0.2, and 0.02 $\mu\text{g}/\text{mL}$) were placed in a 96-well plate with and without GODCAT and evaluated via epiluminescence. The background corrected phosphorescence intensities from this experiment at the maximum concentration of 20 $\mu\text{g}/\text{mL}$ are as follows (first number for each compound represents ambient oxygen, second number represents GODCAT): MM2 (565, 1349); PtG4 (230, 1269); Ir(bt_b)₂(acac) (45.7, 168); MitoID (119, 150) [Fig. 3(a)]. This experiment was repeated by loading all of these reagents into PANC-1 cells with and without GODCAT and imaging via CEL. The phosphorescence intensities from this experiment at the maximum concentration of 20 $\mu\text{g}/\text{mL}$ are as follows (first number for each compound represents the signal under ambient

oxygen, and the second number is the signal deoxygenated with GODCAT): MM2 (153, 376); PtG4 (181, 406); Ir(bt_b)₂(acac) (235, 633); MitoID (223, 288) [Fig. 3(b)].

A murine experiment to sense tissue oxygenation was completed in mice with subcutaneous MDA-MB-231Luc-D3H2LN tumors. The setup for CELSI is shown in Figs. 4(a) and 4(b). Briefly, gantry head of the linear accelerator that delivers the radiation is positioned below the mouse, which is located on the treatment couch. A mirror is placed that redirects the photons to the ICCD camera for imaging. A total of four tumors per compound were imaged, with local injection of 50 μL of each reagent [50 μM PtG4, 2.5 nmol, 1.75 mg per tumor and 50 μM Ir(bt_b)₂(acac), 2.5 nmol, 35 μg per tumor]. Each mouse was imaged while alive and then repeated 30 min after euthanasia to capture both normoxic and hypoxic conditions, respectively. In the euthanized animal, the drop in blood circulation and respiration causes a dramatic decrease in pO_2 values. Temperature was controlled using a heating pad under each animal, throughout the study, and the CELSI scan was completed vertically for these cases. Images of the luminescence were captured at different delay times after the LINAC pulse to determine emission lifetimes for each reagent. The maximum intensity projection images of CELSI from both PtG4 and Ir(bt_b)₂(acac) at a delay time of 4.26 μs are shown in Fig. 4(c). A comparison of the intensity differences between PtG4 phosphorescence at various delay times in an alive and dead mouse are shown in Fig. 5(a). The emission lifetimes were mapped for the alive and euthanized mouse for PtG4 and are quantified and displayed via a box and whiskers plot [Fig. 5(b)]. Using the Stern–Volmer equation, we estimated the average tissue pO_2 with the reported quenching constant for PtG4²⁷ [Fig. 5(c)]. The phosphorescence at different delay times for a euthanized mouse is shown for Ir(bt_b)₂(acac) [Fig. 5(d)]. In addition, we created a map of emission lifetimes and estimated the average pO_2 using the reported quenching constant for Ir(bt_b)₂(acac) using the Stern–Volmer relationship.¹⁴

4 Discussion

Due to the redshifted emission of PtG4 (772 nm) in comparison to the other reagents, it was originally hypothesized that this reagent would be the most effective for imaging in tumors

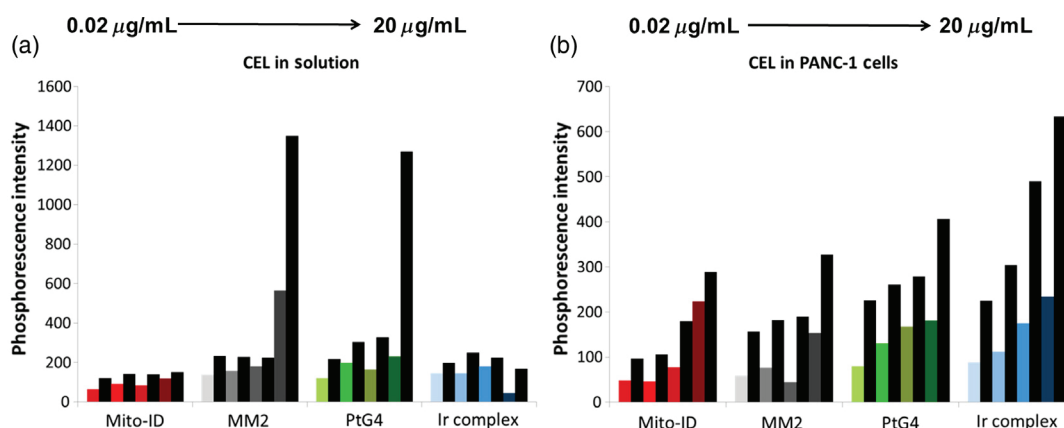


Fig. 3 Comparison of CEL with phosphorescent oxygen sensors. Increasing concentrations of each sensor indicated by darker shades of each color [0.02, 0.2, 2, and 20 $\mu\text{g}/\text{mL}$, MitoID (red), MM2 (gray), PtG4 (green), and Ir(bt_b)₂(acac) (blue)] were analyzed in ambient oxygen or with enzymatic oxygen scavenger glucose oxidase/catalase (black). A 96-well plate with these reagents in (a) solution or (b) loaded into PANC-1 cells was exposed to 6-MV radiation from a LINAC, and the phosphorescence intensity was measured via ICCD.

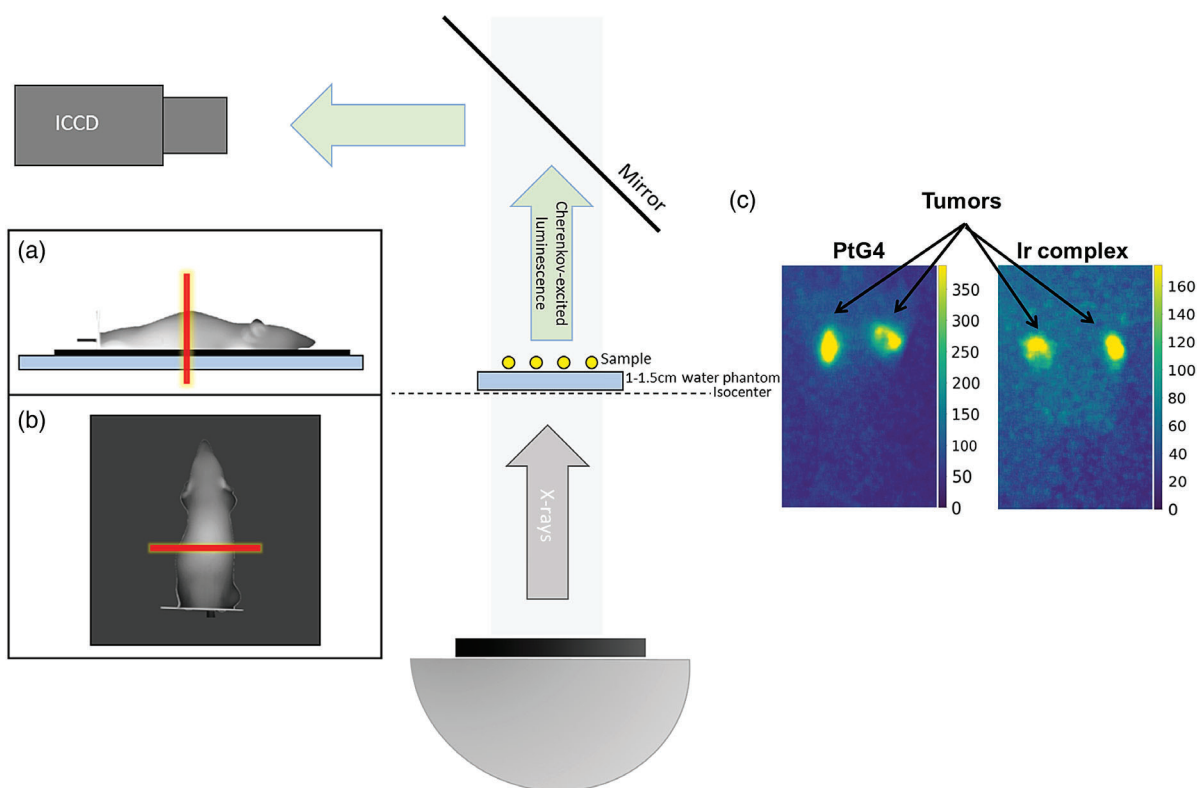


Fig. 4 CELSI setup and *in vivo* imaging with PtG4 and Ir(btbt)₂(acac). The LINAC gantry head that delivers radiation is placed below the mouse that is positioned on the treatment couch. A mirror above redirects the photons to the ICCD. (a) Lateral view of the mouse depicting passage of radiation sheet in red (b) aerial view as imaged from the ICCD camera. (c) Under anesthesia of isoflurane, 2.5 nmol of each reagent was injected into subcutaneous MDA-MB-231 luc-D3H2LN tumors. Maximum intensity projection of PtG4 and of Ir(btbt)₂(acac) at 4.26 μ s delay time, respectively. Tumors are indicated with line arrows.

since this wavelength would achieve the most effective tissue penetration. However, we wanted to compare PtG4 with other commercially available phosphorescent oxygen sensors to identify the reagents with the best qualities for utilization in CELSI. Several factors are involved in the selection of ideal compounds. As with fluorescence imaging, the quantum yield of the compound is a significant factor that determines the efficiency of imaging. In CEL imaging, time gating is used to separate Cherenkov emissions from luminescence, so luminescence lifetime is also important to consider. Medical LINACs have a 4- μ s radiation pulse, and so this moderate pulse time limits the time gating to the microsecond regime, and without significant change to the LINAC or acquisition, nanosecond lifetimes would not be possible to measure. The luminescent agents that are available with microsecond lifetimes are typically phosphorescent. It has not been feasible to detect fluorescent agents that have nanosecond lifetimes, other than through wavelength filtering and continuous wave detection.²¹ The typical timing used for image acquisition that is coupled to the LINAC is shown in Fig. 6(a). Experimentally, the gate width is generally set between 5 and 10 times the deoxygenated lifetime of the reagent of interest (τ_0). The CEL is then detected at multiple delay times in order to determine the emission lifetime of each phosphorescent agent. The time between radiation pulses is one factor that will limit the maximum lifetime when choosing a phosphorescent compound. The LINAC generates radiation pulses at a repetition rate between 2.7 and 17 ms (600 to 100 MU/min). Shorter lifetimes can be difficult

to discriminate from the radiation-induced Cherenkov light. The LINAC radiation pulse does not immediately turn off, and both stray charge and Cherenkov emissions may be detected during the transition phase. Phosphorescent compounds with lifetimes in this range (<4.5 μ s) will be difficult to detect. A plot of the decay curves depicting lifetime measurements as a function of quantum yield for each compound used in the study is shown in Fig. 6(b). Ir(btbt)₂(acac) has been utilized in LED applications and has a high quantum yield of 0.33,²⁶ which should also impart ideal imaging properties; however, its shorter emission lifetime of 5.8 μ s²⁶ may limit its application in CELSI. While PtG4, MM2, and MitoID have lower quantum yields, their longer emission lifetimes should be advantageous for signal detection. In addition, MM2 and MitoID are nanoparticles with multiple copies of oxygen-sensitive porphyrins,²⁵ which should provide enhanced signal-to-noise ratio.

With optimization in mind, a comparison of commercially available oxygen sensors was completed *in vitro*, comparing signals in ambient oxygen to that in the presence of oxygen-scavenging GODCAT. These conditions were employed since phosphorescent oxygen sensors exhibit maximum luminescence in the absence of oxygen. PtG4 was not employed in this study since the maximum cutoff for the fluorescence emission of the plate reader is shorter than the PtG4 fluorescence emission. As expected, these reagents show a signal enhancement in the presence of GODCAT conditions, indicating a response to change in oxygenation levels. MM2 and Ir(btbt)₂(acac) gave the most robust responses in sensing oxygen changes via steady state

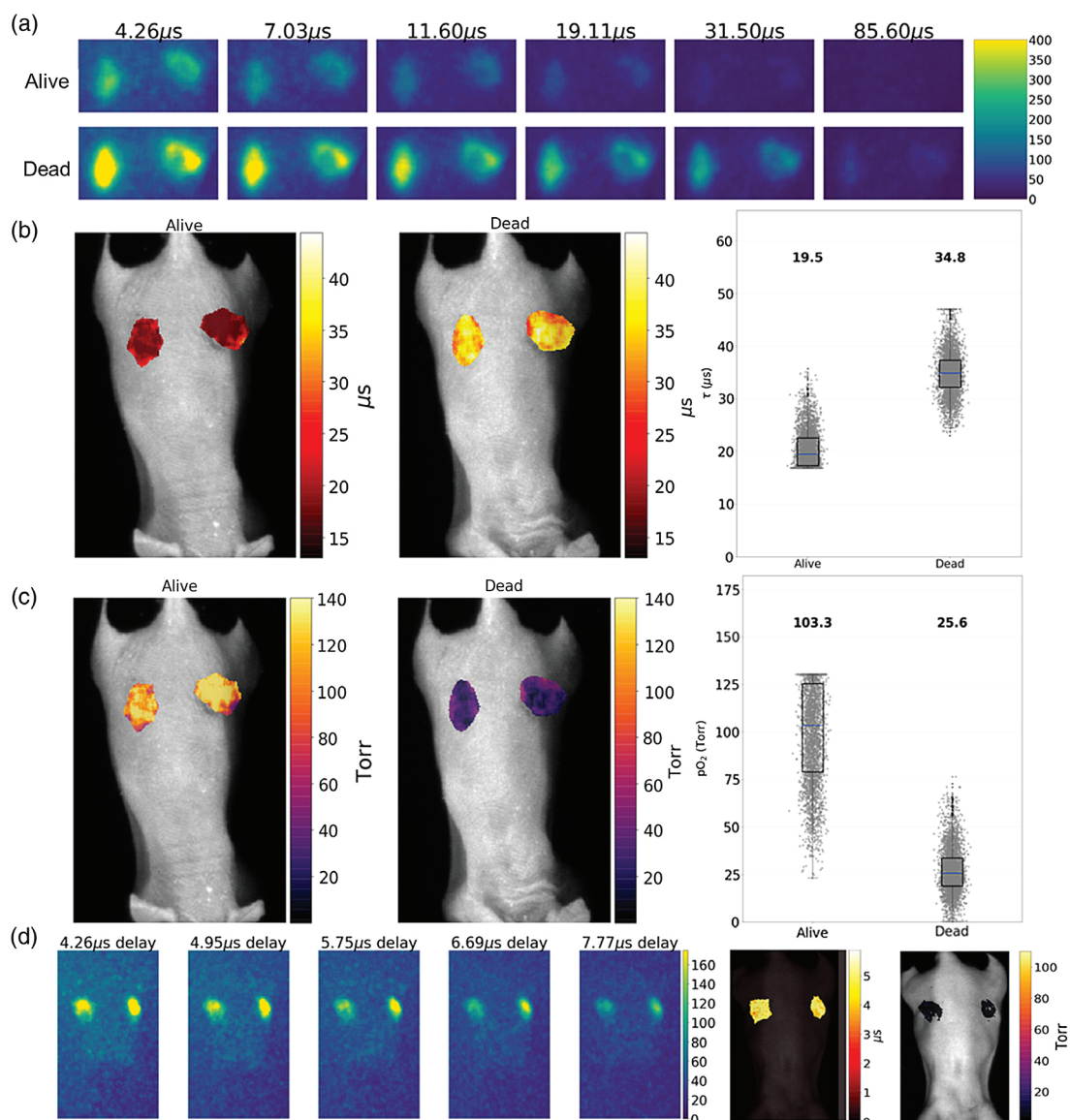


Fig. 5 *In vivo* lifetime imaging with PtG4 and Ir(btbt)₂(acac). Under anesthesia of isoflurane, the animal was imaged at various delay times based on reported lifetimes of each reagent to gain emission lifetime information alive and 30 min after euthanize, when the drop in blood circulation and respiration causes a marked decrease in pO₂ values. (a) Comparison of PtG4 phosphorescence intensity at various delay times based on known PtG4 emission lifetime in subcutaneous tumors alive (top) and 30 min after euthanize(bottom). (b) PtG4 emission lifetime maps and box and whiskers plot of emission lifetimes of alive and euthanized mouse for PtG4. (c) pO₂ maps and box and whiskers plot of oxygen levels in alive and euthanized mouse for PtG4. (d) Phosphorescence intensity of tumors injected with Ir(btbt)₂(acac) at different delay times informed from the reported Ir(btbt)₂(acac) emission lifetime, map of emission lifetime, and pO₂ map in euthanized mouse. All lifetime maps and subsequent pO₂ maps for both reagents were constructed utilizing data from the 4.26- μ s delay time.

fluorescence [Fig. 2(a)]. At the highest concentration utilized (30 μ g/mL), the signal was attenuated in comparison to the 20 μ g/mL samples, which could be attributed to self-quenching, although further investigation of this was not done. Due to these observations, since MM2 and Ir(btbt)₂(acac) gave the best signal, the next focus was to determine the lowest concentration of each sensor that could be utilized to detect oxygen levels *in vitro*. We found that Ir(btbt)₂(acac) still elicited a luminescence signal in response to oxygen changes in PANC-1 cells at 0.2 μ g/mL. While MM2 exhibited a statistically significant response to oxygen scavenging conditions at a lower

concentration (0.02 μ g/mL), the responses to oxygenation changes were not robust at concentrations lower than 2 μ g/mL [Fig. 2(b)].

We investigated CEL both in solution and loaded into PANC-1 cells of the previously studied PtG4 as well as MM2, Ir(btbt)₂(acac), and MitoID. Both PtG4 and MM2 exhibited strong phosphorescence at 20 μ g/mL in solution, particularly with oxygen scavenging, when excited by Cherenkov emission, with phosphorescence intensities of 1349 and 1269, respectively, whereas Ir(btbt)₂(acac) and MitoID did not display significant phosphorescence in solution, with intensities of 250 and

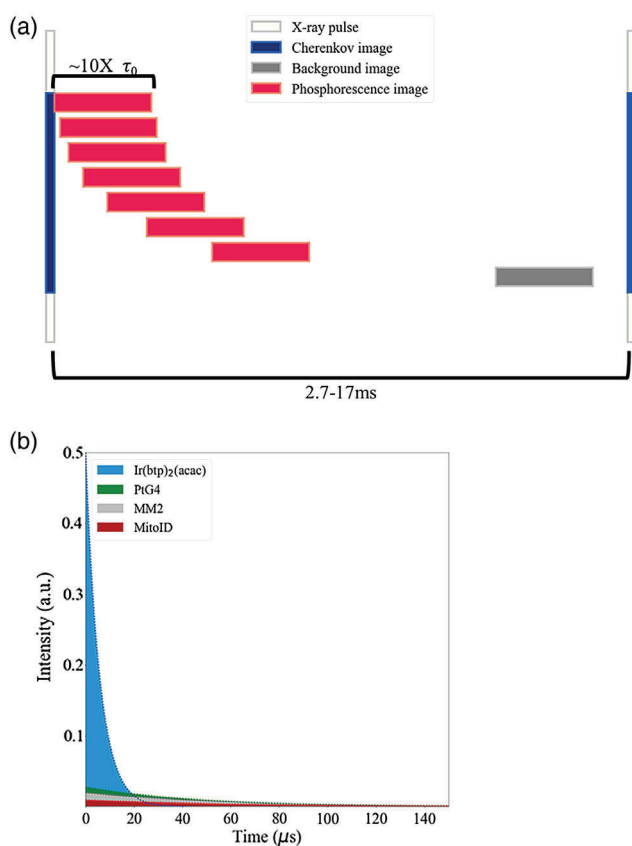


Fig. 6 Considerations for CELSI. (a) Cherenkov imaging timing. Experimentally, the gate width is generally set between 5 and 10 times the deoxygenated lifetime (τ_0) of the reagent of interest. Luminescence is detected at a series of delay times (red blocks) after the Cherenkov emission (blue column) to assess the emission lifetime of phosphorescent agents. The LINAC generates radiation pulses at a repetition rate between 2.7 and 17 ms (600 to 100 MU/min). (b) Plot of emission decay curves as a function of quantum yield.

150, respectively [Fig. 3(a)]. We have previously seen excellent results with CELSI with PtG4,^{19,21,22} and since MM2 contains multiple copies of a porphyrin grafted to a nanoparticle, enhanced signal in response to oxygen was anticipated for both of these reagents. As expected, we found that the intracellular phosphorescence intensity was markedly decreased in comparison to the phosphorescence measured in solution. Interestingly, Ir(btbt)₂(acac) exhibits a much better phosphorescence signal in cells versus solution, giving the largest detectable signal in comparison to the other reagents [Fig. 3(b)]. This is likely due to the fact that this complex binds to albumin or another cellular protein, thereby enhancing permeability. However, previous reports indicate that it is no longer sensitive to oxygen when bound to albumin *in vitro*. Our results and other cell studies with Ir(btbt)₂(acac) that show oxygen sensitivity indicate that binding to albumin is not the mechanism that imparts enhanced signal in cells versus solution.²⁶ The performance of MM2 was diminished intracellularly, possibly due to lower cell permeability than Ir(btbt)₂(acac). In fact, Ir(btbt)₂(acac) was found to penetrate cells far more rapidly than MM2 (30 min versus 24 h). PtG4 gave a robust response to oxygenation changes in cells; however, the intensity was somewhat attenuated in comparison to Ir(btbt)₂(acac). One critical advantage of PtG4 is that the dendrimer shell prevents its

Table 1 Side-by-side comparison of phosphorescent oxygen sensors utilized for CEL.

Compound	CEL solution	CEL cells	CELSI <i>in vivo</i>	Biomolecule interaction	Stability	Self-quenching
PtG4	+	+	+	-	+	-
Ir(btbt) ₂ (acac)	+	+	+	+	+	+
MM2	+	+	-	-	-	+
MitoID	-	+	-	+	-	+

interaction with other biomolecules that could potentially perturb its emission lifetime and thus pO₂ estimations. This is considered to be a key factor in making this agent a linear reporter of tissue pO₂, and in fact PtG4 and similar reagents have been calibrated appropriately in extensive studies.^{19-24,27} While MitoID displays an enhanced signal in cells versus solution, it still elicits the weakest phosphorescent response to changes in oxygen concentration.

PtG4, Ir(btbt)₂(acac), and MM2 seemed to have promise for use in CELSI. Therefore, we investigated these reagents for sensing oxygenation levels in subcutaneous tumors. We were unable to detect significant phosphorescence with MM2 *in vivo*. However, we were able to sense emission lifetime and as such calculate tissue oxygenation utilizing CELSI for both PtG4 and Ir(btbt)₂(acac) at the nmol level [Figs. 5(b)-5(d)]. Unfortunately, we were not able to measure fluorescence lifetime or tissue pO₂ in live mice with Ir(btbt)₂(acac). This is likely because the luminescence lifetime in a fully oxygenated sample of Ir(btbt)₂(acac) is shorter than we can detect since the shortest delay time feasible for imaging after the radiation pulse is 4.26 μ s. We also observed quenching with Ir(btbt)₂(acac) at concentrations higher than 50 μ M in subcutaneous tumors, as we did in the fluorescence plate reader experiments.

A summary of the results as well as a comparison of the pros and cons of the oxygen sensors we utilized for this study are provided in Table 1. Briefly, both PtG4 and Ir(btbt)₂(acac) are stable indefinitely, whereas MM2 and MitoID nanoparticles have a short shelf life of only 1 to 2 weeks once resuspended. PtG4 has a dendrimer shell that prevents its interaction with biomolecules, allowing accurate determinations of fluorescence lifetime and pO₂ calculations. Ir(btbt)₂(acac) and MitoID appear to interact with biomolecules in some way, given the difference in phosphorescent intensities discovered in solution versus cells. Finally, we have observed that MM2, MitoID, and Ir(btbt)₂(acac) exhibit self-quenching at higher concentrations, where we have not seen this effect with increasing concentrations of PtG4.

5 Conclusion

When used *in vitro* in PANC-1 cells at the same concentrations, the signal strengths suggest that the optimal agents would be Ir(btbt)₂(acac), followed by PtG4, and then MM2 and MitoID. However, *in vivo*, only PtG4 and Ir(btbt)₂(acac) were found to be measurable at nmol doses in the tumors, and assessment of tissue oxygenation accomplished. On the timescale of LINAC produced x-ray imaging, PtG4 is the more ideal agent because of the lifetime on the scale of tens of microseconds versus Ir(btbt)₂(acac), which has a lifetime

of a few microseconds, which hinders detection at higher tissue pO_2 values. This work represents: (1) a unique way to harness Cherenkov emission for imaging purposes in conjunction with radiotherapy, (2) a noninvasive determination of tumor pO_2 , and (3) a direct comparison of phosphorescent sensors available to probe tissue oxygenation.

Disclosures

The authors report no conflicts of interest.

Acknowledgments

This work was financially supported by the Department of Defense, Congressionally Directed Medical Research Program (CDMRP) Breast Cancer Innovator Award (BC150584P1), as well as the National Institutes of Health NIBIB R01 EB024498, and the NCI Cancer Center Support Grant 5P30CA023108-37. This material was also based on work supported by the National Science Foundation Graduate Research Fellowship.

References

1. P. Vaupel, A. Mayer, and M. Hockel, "Impact of hemoglobin levels on tumor oxygenation: the higher, the better?" *Strahlenther. Onkol.* **182**(2), 63–71 (2006).
2. S. M. Evans and C. J. Koch, "Prognostic significance of tumor oxygenation in humans," *Cancer Lett.* **195**(1), 1–16 (2003).
3. J. Bussink et al., "Effects of nicotinamide and carbogen on oxygenation in human tumor xenografts measured with luminescence based fiberoptic probes," *Radiother. Oncol.* **57**(1), 21–30 (2000).
4. A. Turaka et al., "Hypoxic prostate/muscle ratio predicts for outcome in patients with localized prostate cancer: long-term results," *Int. J. Radiat. Oncol. Biol. Phys.* **82**(3), e433–e439 (2012).
5. P. Vaupel and D. K. Kelleher, "Blood flow and oxygenation status of prostate cancers," *Adv. Exp. Med. Biol.* **765**, 299–305 (2013).
6. O. Genbacev et al., "Human cytotrophoblast expression of the von Hippel-Lindau protein is downregulated during uterine invasion in situ and upregulated by hypoxia in vitro," *Dev. Biol.* **233**(2), 526–536 (2001).
7. C. J. Koch, "A two-component assay for hypoxia incorporating long-term nitroreduction and short-term DNA-damage allows differentiation of the three hypoxia sub-types," *Radiat. Res.* **190**(1), 72–87 (2018).
8. S. K. Loftus et al., "Hypoxia-induced HIF1 α targets in melanocytes reveal a molecular profile associated with poor melanoma prognosis," *Pigm. Cell Melanoma Res.* **30**(3), 339–352 (2017).
9. H. B. Stone and H. R. Withers, "Tumor and normal tissue response to metronidazole and irradiation in mice," *Radiology* **113**(2), 441–444 (1974).
10. K. Y. Aguilera and R. A. Brekken, "Hypoxia studies with pimonidazole in vivo," *Bio-Protocol* **4**(19), e1254 (2014).
11. M. R. Gonçalves et al., "Decomposition of spontaneous fluctuations in tumour oxygenation using BOLD MRI and independent component analysis," *Br. J. Cancer* **113**(8), 1168–1177 (2015).
12. D. Li et al., "Correlation between BOLD-MRI and HIF expression level in renal carcinoma," *Int. J. Clin. Exp. Pathol.* **8**(10), 13759–13763 (2015).
13. H. Gustafsson et al., "EPR oximetry of cetuximab-treated head-and-neck tumours in a mouse model," *Cell Biochem. Biophys.* **75**(3–4), 299–309 (2017).
14. H. M. Swartz, The measurement of oxygen in vivo using EPR techniques, in *In Vivo EPR (ESR): Theory and Application*, L. J. Berliner, Ed., pp. 403–440, Springer US, Boston, Massachusetts (2003).
15. S. Srinivasan et al., "In vivo hemoglobin and water concentrations, oxygen saturation, and scattering estimates from near-infrared breast tomography using spectral reconstruction," *Acad. Radiol.* **13**(2), 195–202 (2006).
16. O. J. Kelada et al., "Quantification of tumor hypoxic fractions using positron emission tomography with [(18)F]fluoromisonidazole ([18)F]FMISO) kinetic analysis and invasive oxygen measurements," *Mol. Imaging Biol.* **19**(6), 893–902 (2017).
17. S. Stieb et al., "Longitudinal PET imaging of tumor hypoxia during the course of radiotherapy," *Eur. J. Nucl. Med. Mol. Imaging* **45**(12), 2201–2217 (2018).
18. A. K. Glaser et al., "Projection imaging of photon beams by the Cerenkov effect," *Med. Phys.* **40**(1), 12101 (2013).
19. R. Zhang et al., "Cerenkov radiation emission and excited luminescence (CREL) sensitivity during external beam radiation therapy: Monte Carlo and tissue oxygenation phantom studies," *Biomed. Opt. Express* **3**(10), 2381–2394 (2012).
20. R. Zhang et al., "Superficial dosimetry imaging based on Cerenkov emission for external beam radiotherapy with megavoltage x-ray beam," *Med. Phys.* **40**(10), 101914 (2013).
21. H. Lin et al., "Comparison of Cerenkov excited fluorescence and phosphorescence molecular sensing from tissue with external beam irradiation," *Phys. Med. Biol.* **61**(10), 3955–3968 (2016).
22. R. Zhang et al., "Oxygen tomography by Cerenkov-excited phosphorescence during external beam irradiation," *J. Biomed. Opt.* **18**(5), 50503 (2013).
23. T. V. Esipova et al., "Two new 'protected' oxyphors for biological oximetry: properties and application in tumor imaging," *Anal. Chem.* **83**(22), 8756–8765 (2011).
24. R. I. Dmitriev and D. B. Papkovsky, "Intracellular probes for imaging oxygen concentration: how good are they?" *Methods Appl. Fluoresc.* **3**(3), 34001 (2015).
25. R. I. Dmitriev and D. B. Papkovsky, "Optical probes and techniques for O_2 measurement in live cells and tissue," *Cell Mol. Life Sci.* **69**(12), 2025–2039 (2012).
26. S. Zhang et al., "Phosphorescent light-emitting iridium complexes serve as a hypoxia-sensing probe for tumor imaging in living animals," *Cancer Res.* **70**(11), 4490–4498 (2010).
27. C. T. Sullender et al., "Imaging of cortical oxygen tension and blood flow following targeted photothrombotic stroke," *Neurophotonics* **5**(3), 035003 (2018).

Biographies of the authors are not available.

Cherenkov-excited luminescence scanned imaging using scanned beam differencing and iterative deconvolution in dynamic plan radiation delivery in a human breast phantom geometry

Mengyu Jeremy Jia*, Petr Bruza, and Jacqueline M. Andreozzi
Thayer School of Engineering, Dartmouth College, Hanover, NH 03755, USA

Lesley A. Jarvis
Department of Medicine, Geisel School of Medicine Dartmouth College, Hanover, NH 03755, USA

David J. Gladstone
Thayer School of Engineering, Dartmouth College, Hanover, NH 03755, USA
Norris Cotton Center Dartmouth-Hitchcock Medical Center, Lebanon, NH 03756, USA
Department of Medicine, Geisel School of Medicine Dartmouth College, Hanover, NH 03755, USA

Brian W. Pogue^{a)}
Thayer School of Engineering, Dartmouth College, Hanover, NH 03755, USA
Norris Cotton Center Dartmouth-Hitchcock Medical Center, Lebanon, NH 03756, USA

(Received 13 August 2018; revised 2 April 2019; accepted for publication 3 April 2019; published 18 May 2019)

Purpose: The purpose of this study was to demonstrate high resolution optical luminescence sensing, referred to as Cherenkov excited luminescence scanning imaging (CELSI), could be achieved during a standard dynamic treatment plan for a whole breast radiotherapy geometry.

Methods: The treatment plan beams induce Cherenkov light within tissue, and this excitation projects through the beam trajectory across the medium, inducing luminescence where there can be molecular reporter. Broad beams generally produce higher signal but low spatial resolution, yet for dynamic plans the scanning of the multileaf collimator allows for a beam-narrowing strategy by recursively temporal differencing each of the Cherenkov images and associated luminescence images. Then reconstruction from each of these size-reduced beamlets defined by the differenced Cherenkov images provides a well-conditioned matrix inversion, where the spatial frequencies are limited by the higher signal-to-noise ratio beamlets. A built-in stepwise convergence relies on stepwise beam size reduction, which is associated with a widening of the bandwidth of Cherenkov spatial frequency and resultant increase in spatial resolution. For the phantom experiments, europium nanoparticles were used as luminescent probes and embedded at depths ranging from 3 to 8 mm. An intensity modulated radiotherapy (IMRT) plan was used to test this.

Results: The Cherenkov images spatially guided where the luminescence was measured from, providing high lateral resolution, and iterative reconstruction convergence showed that optimization of the initial and stopping beamlet widths could be achieved with 15 and 4.5 mm, respectively, using a luminescence imaging frame rate of 5/s. With the IMRT breast plan, the original lateral resolution was improved 2X, that is, 0.08–0.24 mm for target depths of 3–8 mm. In comparison, a dynamic wedge (DW) plan showed an inferior image fidelity, with relative contrast recovery decreasing from 0.86 to 0.79. The methodology was applied to a three-dimensional dataset to reconstruct Cherenkov excited luminescence intensity distributions showing volumetric recovery of a 0.5 mm diameter object composed of 0.5 μM luminescent microbeads.

Conclusions: High resolution CELSI was achieved with a clinical breast external beam radiotherapy (EBRT) plan. It is anticipated that this method can allow visualization and localization for luminescence/fluorescence tagged vasculature, lymph nodes, or superficial tagged regions with most dynamic treatment plans. © 2019 American Association of Physicists in Medicine [<https://doi.org/10.1002/mp.13545>]

Key words: Cherenkov, Deconvolution, EBRT, external beam radiotherapy, IMRT, intensity modulated radiotherapy, molecular imaging, tomography

1. INTRODUCTION

The Cherenkov emission spectrum from MV radiation is composed of optical photons with a limited penetration in human tissue, and so irradiated tissue can be selectively

excited with this light signal, which comes from the secondary electrons in the irradiated volume. Imaging the emitted light from the surface of tissue shows the entrance beam as projected on the patient's skin, which has motivated the concept of real-time visualization of surface dose on patients

during delivery of their external beam radiation therapy (EBRT).^{1–3} However, there is also potential to use Cherenkov light for molecular sensing of the tissue to assist in adaptive radiotherapy based upon the tumor microenvironment, using diagnostically useful molecular sensors (e.g., tissue oxygen pO₂, acidity pH, or protein labels and reporters) within critical planning target volume (PTV) structures. The Cherenkov excited luminescence scanned imaging (CELSI) technique has been examined to sense luminescent molecular probes deep within tissue, using x-rays generated by a therapeutic MV linear accelerator (LINAC), as shown in Fig. 1(a).^{4,5} The outgoing Cherenkov and luminescence signals can be captured sequentially by a time-resolved camera with different pulse delays relative to the LINAC radiation pulse. Typically LINAC pulses are 3–5 μs during which Cherenkov emissions can be detected, and time-gating beyond this can be achieved for detection of luminescence with emission lifetimes near tens of μs. These signals can come from up to a few centimeters deep within the tissue if emitted in the near infrared wavelength range.

The major limiting factor in CELSI is the signal attenuation from optical light blur going from the point of luminescence emission to the tissue surface, but this can be compensated for by knowledge of where the excitation x-ray scan beam is incident within the tissue. There is also a smaller contribution from the Cherenkov light blur as well. The optical signal is attenuated and blurred out by elastic scattering and small absorption effects as the photons pass through the tissue, which is largely modeled as a diffusive process in thick tissue. The degradation model can be expressed as a convolution equation:

$$\mathbf{Y} = \mathbf{X} \otimes \mathbf{P}_{\text{Chk}} \otimes \mathbf{P}_{\text{lum}} + \mathbf{N} \quad (1)$$

where \mathbf{Y} is raw luminescence; \mathbf{P}_{Chk} and \mathbf{P}_{lum} denote the position-dependent point spread functions (PSF) of Cherenkov and luminescence, respectively; \mathbf{X} is the undistorted latent luminescence image; \otimes is the convolution operator; and \mathbf{N} is acquisition noise, which can be significant. It is assumed here that the system is time invariant, and linear.

For general applications of CELSI, the contribution to Cherenkov blur from the x-ray and electron scattering is important to include for completeness, complicating the estimation of \mathbf{P}_{Chk} , as it requires full Monte Carlo radiation modeling for this to be accurate. In comparison, \mathbf{P}_{lum} could often be reasonably accurately estimated with elastic photon transport models such as diffusion theory or optical elastic scattering Monte Carlo which are less computationally intensive.⁶ With the analysis above, the deconvolution operation in Eq. (1) is ill-conditioned, and so is mitigated through the use of regularization techniques, that is, replacing the ill-conditioned problem with a well-conditioned one.⁷

In this paper, a novel iterative deconvolution method is proposed for CELSI with an edge-scanned excitation beam. Since smaller beam sizes have been demonstrated to produce higher spatial resolution for CELSI,⁸ in this method, raw Cherenkov measurements were iteratively differenced to form width-reduced effective excitations (termed as beamlets), improving the sensitivity to high spatial frequency data. The resultant stepwise widened frequency band renders a potential way for a converged iteration process towards a realistic result with broadband frequency. In the first iteration, difference Cherenkov measurement with a largest scanning position gap (b) was used to deconvolve corresponding difference luminescence one. This relationship between the cropped excitation and its resultant emission is based on the superposition principle of linear system. Then the calculated result was in turn utilized as a “noise-reduced measurement” to be deconvolved for next iteration. The reconstruction methodology was tested out with a beam geometry and radiation dose used in a typical fraction of intensity modulated radiation therapy (IMRT)⁹ to assess the type of information that could be derived in standard fractionated breast radiotherapy. Experiments were performed with a progressive series of test phantoms, which illustrated the capabilities for depth recovery and high spatial resolution, and luminescent agent, which has the potential for protein reporter imaging.

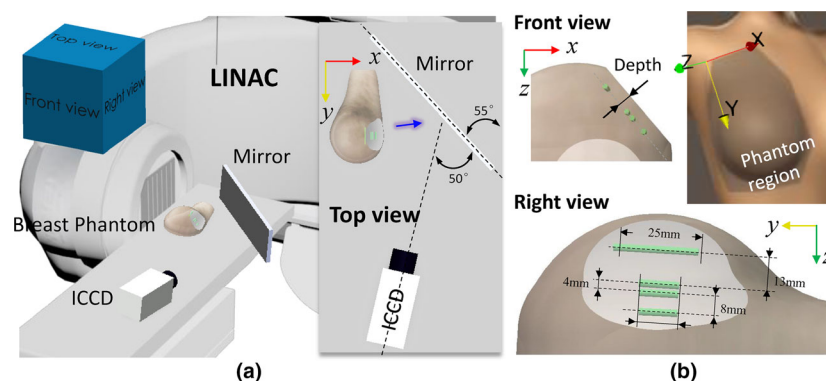


FIG. 1. The experimental setup: (a) measurement geometry with a schematic inserted to specify the relative positions of the phantom, plane mirror, and camera, and (b) configuration of a full-size breast phantom with four capillaries inside filled with europium (green cylinder). The blue arrow indicates the direction of detected luminescence light. [Color figure can be viewed at wileyonlinelibrary.com]

2. MATERILAS AND METHODS

2.A. System and setup

Most EBRT treatment plans in patients dynamically shape the beam with the multi-leaf collimators (MLCs) and jaws within the LINAC, targeting the tumor region and minimizing dose to nearby critical structures. As a result, it was hypothesized that the natural spatial modulation done in clinical radiotherapy could be used to achieve an enhanced CELSI, based upon how the beamlets were formed. To investigate this, we herein examined a widely used IMRT treatment plan. A clinical radiotherapy accelerator (Varian Clinac 2100 CD, Varian Medical Systems, Palo Alto, CA, USA) was used to perform the breast IMRT with the following parameters: photon energy of 6 MV, radiation dose of 210 MU, dose rate of 600 monitor units per minute (MU/min), a fixed repetition rate of 360 Hz with a pulse width of 3.25 μs , and gantry angles of 270° and 90° used for medial and lateral tangent beamlets, respectively. For proof-of-concept, measurements were collected only for the geometry with 270° gantry position in this paper. The luminescence was imaged by a gated, intensified charge-coupled device (ICCD, PI-MAX4 1024i, Princeton Instruments, Acton, MA, USA). The camera worked with a focal length of 85 mm and f/1.2 lens. The luminescence signal was detected with time-gated acquisition of the ICCD (100 μs integration time and 4.26 μs delay after each x-ray pulse). The luminescence images were acquired with 100 \times gain on the ICCD intensifier, 30 pulses integrated on-chip as accumulations prior to each frame readout, and 2 \times 2 hardware pixel binning at readout, from chip size of 1024 pixels \times 1024 pixels.⁵ Cherenkov images were acquired in the same way, but with 0 μs pulse delay and a 3.5 μs integration time.⁵

The transmittance measurement geometry is shown in Fig. 1(a), where a plane mirror was used to reflect the outgoing Cherenkov and luminescence into a horizontally positioned camera as indicated in the insert. Note that only the reflected luminescence portion was captured by the camera. A tilt camera was intent to keep it within the bench area. A full-size right breast phantom was made of soft clay (B00LH2DWDW, Sculpey Inc., Stockbridge, GA) to facilitate targets embedding, and demonstrated with a spatial frequency domain imaging (SFDI) system (Reflect RS, Modulated Imaging Inc., Irvine, CA) to have tissue optical properties of $\mu_a = 0.008$ and $\mu'_s = 2 \text{ mm}^{-1}$ at 625 nm.¹⁰ The phantom was computed tomography (CT)-scanned and the shape transferred to the Eclipse treatment planning system (Varian Medical Systems, Palo Alto, CA) for radiotherapy treatment planning. The luminescent probe used europium nanoparticles, which, characterized by long lifetime, sharp spectral profiles, nontoxic to cells, etc., have been widely used to tag proteins with antibody labeling.^{11,12} As indicated in Fig. 1 (b), four europium capillaries (0.5 μM) with a diameter of 0.5 mm were placed at a depth of 5 mm to mimic blood vessels. There was no specific reason for tilting the capillaries with respect to the Y-Z coordinate system, that was just the configuration of the breast phantom. To keep the

same depths for the capillaries, a part of the phantom lateral surface was cropped to be flat as shown in the right view and the IMRT treatment plan was made before cropping.

2.B. Theory

A fast and simple method to solve this task posed in Eq. (1) is Wiener filtering¹³ which is essentially a regularized inversion of the convolution via the Fourier domain. However, this direct or linear method is prone to noise amplification at high frequencies and ringing artifacts especially when \mathbf{P}_{lum} is noninvertible.¹⁴ Many algorithms have been proposed to solve this problem: a regularized constraint based upon total-variation minimization was introduced to stabilize the solution^{15,16}; in a wavelet basis approach, the true image can be efficiently represented by a few large coefficients while noise distributes over a large number of smaller ones, so that either thresholding or filtering strategy could be leveraged to denoise the deconvolved result.^{17,18} Although direct deconvolution is computationally expensive, most solutions are based on iterative or nonlinear strategies. The advantages of iterative deconvolution include¹⁹: (a) *a priori* knowledge of the data's statistics are usually not required (sometimes called blind deconvolution); (b) prior information can easily be incorporated into the algorithm as a constraint term; and (c) iterations can cease when errors exceed a given bound. Most of these are based on Van Cittert's method, where a correction item times a real relaxation factor was added to adjust the iteratively obtained result at a given rate of convergence.²⁰ Others are mostly based on a Bayesian theorem with maximum likelihood (ML) solution, for example, Landweber⁷ and Lucy-Richardson deconvolutions^{21,22} have been developed for Gaussian and Poisson noise types, respectively. Since the inverse process is ill-conditioned, negative effects will emerge as the iteration number increases or the regularization decreases. This is especially obvious when the iteration number becomes infinitely large, and there is only noise left. For iterative deconvolution, extra attention should be paid to defining a stopping criterion and acceptable rate of convergence. Most convergence criteria in iterative deconvolution are based on mathematical approaches with limited *a priori* information involved in measurement, e.g., inherent non-negativity and continuity.^{23–25} The conclusion derived from the above analysis was that an effective deconvolution depends on the factors of PSF estimation, noise control, and convergence criterion for iterative approaches.

To get a decreased “beam size” for higher spatial resolution and acquisition-noise suppression, we utilized difference Cherenkov images between two scanning positions with an overlapped scanning area, which resulted in corresponding difference luminescence images according to the superposition principle. An absolute form of the difference images in between the scanning positions of i and $i + b$ can be expressed as

$$\Delta\Psi_{i,b} = |\Psi_i - \Psi_{i+b}|, \Psi \in \{\mathbf{C}, \mathbf{Y}\}, \quad (2)$$

where \mathbf{C} and \mathbf{Y} are the raw measurement of Cherenkov and luminescence, respectively. It is noteworthy in the above equation that $i \leq I - b$ with I being the maximum scan number. As an example, the resultant Cherenkov merged with roomlight images at scanning positions $i = 20, 40$ and 60 , are shown in the first column of Fig. 2(a), and the associated difference images are shown in the second and third columns for $b = 20$ and 1 , respectively. It can be seen from Fig. 2(b) that spatial resolutions improve in the progression from edge-scanning to line-scanning, as expected. However, much more noise can be found for the case of $b = 1$, because of the strong positive dependency of signal-to-noise ratio (SNR) on the x-ray beam size in CELSI.⁸ Consequently, we started the iterative deconvolution procedure from a large beamlet size. Considering $\Delta\mathbf{C}_{i,b(-20)}$ covers only a small range of effective spatial frequency (those with a magnitude below 10% could be noise), as shown in the leftmost image of Fig. 3, deconvolution of Eq. (1) is cutoff at a limited spatial frequency $\omega = R$, termed the cutoff frequency. The small cutoff frequency R and difference operation in Eq. (2) make acquisition noise \mathbf{N} small enough, which made the deconvolution of Eq. (1) well-conditioned. The deconvolution approach used here is as follows

$$\Delta\mathbf{X}'_{i,b} = \begin{cases} F^{-1} \left\langle \frac{F(\Delta\mathbf{Y}_{i,b})(\omega)}{F(\Delta\mathbf{C}_{i,b})(\omega) + \varepsilon} \right\rangle, & \text{if } |\omega| < R \\ 0, & \text{if } |\omega| \geq R \end{cases}, \quad (3)$$

where $\mathbf{X}' = \mathbf{X} \otimes \mathbf{P}_{\text{lum}}$; ε is an infinitesimal integer to circumvent division by zero; and F and F^{-1} represent Fourier and inverse Fourier transforms, respectively.

As a potential way to improve lateral resolution, we could further reduce the beamlet size by continuing recursive difference operations on the baseline result $\Delta\mathbf{C}_{i,b^{(0)}}$, and the k th expression is

$$\mathbf{C}_i^{(k)} = \Delta\mathbf{C}_{i,b^{(k-1)}}, \quad k > 0. \quad (4)$$

As seen from Fig. 3, a widening of the spatial frequency bandwidth can be found for recursive difference Cherenkov images, enriching the resultant luminescence images with broadband frequency, and implying a potential convergence of the iterative procedure.²⁶ A crucial step in this method is to use the deconvolved result from last iteration as the “measured” image for present deconvolution:

$$\mathbf{Y}_i^{(k)} = \Delta\mathbf{X}'_{i,b^{(k-1)}}, \quad (5)$$

due to the much lower SNR of the raw difference “measured” luminescence images as discussed for Fig. 2(b). For the k th iteration, an iterative deconvolution can be formed as:

$$\Delta\mathbf{X}'_{i,b^{(k)}} = \begin{cases} F^{-1} \left\langle \frac{F \left\langle \frac{\Delta\mathbf{Y}_{i,b^{(k)}}(\omega)}{F \left\langle \Delta\mathbf{C}_{i,b^{(k)}}(\omega) + \varepsilon \right\rangle} \right\rangle}{F \left\langle \Delta\mathbf{C}_{i,b^{(k)}}(\omega) + \varepsilon \right\rangle} \right\rangle, & \text{if } |\omega| < R^{(k)} \\ 0, & \text{if } |\omega| \geq R^{(k)} \end{cases}, \quad (6)$$

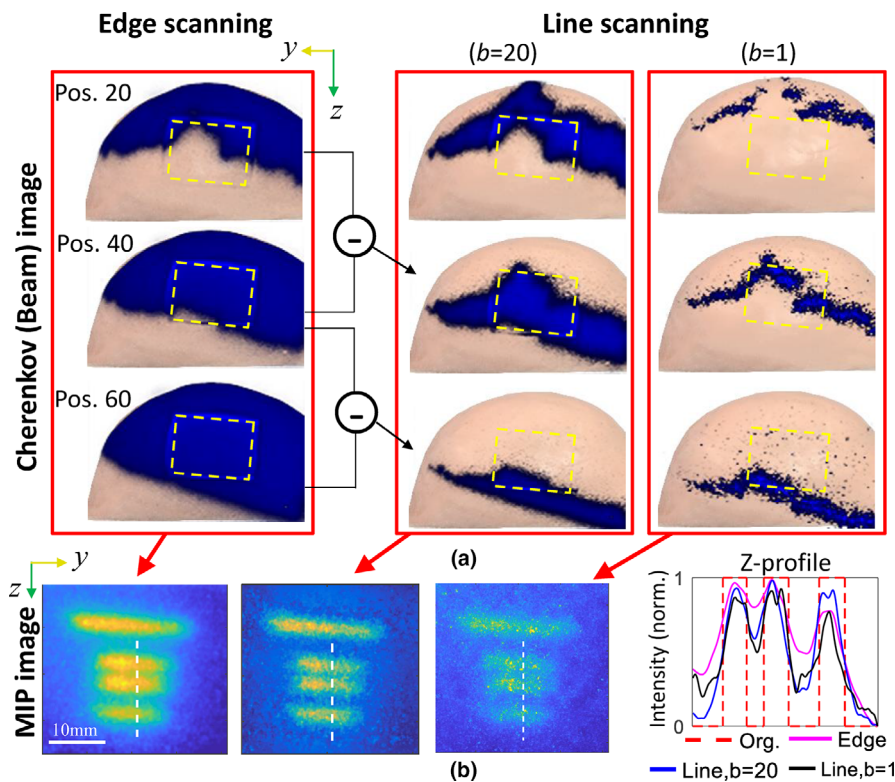


FIG. 2. Comparisons among the results recovered from different beamlet size: (a) Cherenkov images of the original and difference beamlets projected on the breast phantom, and (b) the maximum intensity projection images and corresponding Z-profiles along the white dashed lines. The yellow frames in (a) indicate the regions of interest. Each of the Z-profiles in (b) was normalized to the maximum intensity. [Color figure can be viewed at wileyonlinelibrary.com]

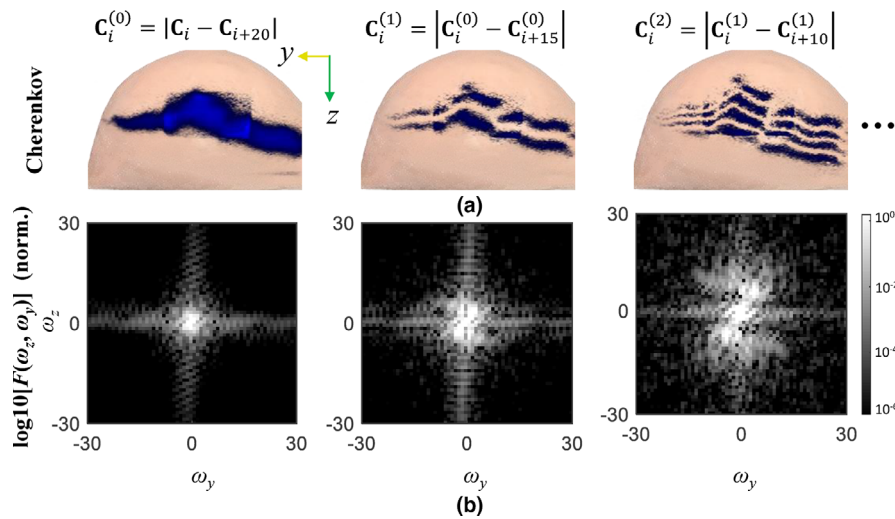


FIG. 3. The spatial frequency images for recursive difference irradiation beamlets from the intensity modulated radiotherapy scan, with position gaps being 20, 15, and 10 from left to right columns: (a) the corresponding difference Cherenkov images in the top row, and (b) two-dimensional spectrogram images in the bottom row. (a) denotes the Cherenkov intensity map captured at the i th scanning. [Color figure can be viewed at wileyonlinelibrary.com]

where $R^{(k)}$ was inversely proportional to the beamlet size as discussed, and its specific value could be chosen according to effective frequency coverage as exemplified in Fig. 3. The recovered image $\mathbf{X}_i^{(k)}$ at each iteration is a maximum intensity projection (MIP) of $\Delta \mathbf{X}_{i,b}^{(k)} (= \Delta \mathbf{X}_{i,b}^{(k)} \otimes \mathbf{P}_{lum})$ for all scanning positions. As mentioned earlier, the SNR can reach a noise floor level as the beamlet size decreases. Further investigation of stopping criterion of the iteration process is presented in Section 3.A. After the iterative deconvolutions, the latent image, \mathbf{X} , can be obtained by continuing to complete a direct deconvolution with \mathbf{P}_{lum} , which was calculated from the diffusion equation combined with a Robin-type boundary condition.²⁷

3. RESULTS

3.A. Investigations of iteration criterion

In Fig. 4(b), we show results obtained via three different iterative-deconvolution strategies (denoted in the Figure as #1, #2 and #3), each of which is defined by initial choice of b and an associated sequence of iterations of Eq. 6 (as shown in labels above the images). The corresponding z -profiles are summarized in Fig. 4(b), with each plot displaying curves for different iteration strategy. To quantify the spatial resolution performance, a metric of success was introduced, defined as $r = (I_{max} - I_{z=69mm}) / (I_{max} - I_{min})$, with I_{max} and I_{min} being the maximum and the minimum in the z -profile, essentially providing a relative measure of contrast recovery. Note that the r value was only calculated for the two most closely spaced capillaries, the distance of which along the white dashed lines is centered at $z = 69$ mm as indicated in Fig. 4(b). With this definition, $r = 1$ represents that the two targets can be completely separated, with full contrast recovery. In the characteristics of the human vision system, it is normally assumed that two targets are distinguishable for $r > 0.1$ (when a 10% dip in intensity is observed between them).²⁸

We investigated the effect on r of varying initial beamlet size b and number of iterations, choosing initial values 20, 10, and 6 for b . As shown in Fig. 4(a), for any choice of initial b , r increases significantly with number of iterations until $b = 3$. Consequently, $b = 3$ was taken as a beamlet size for the final iteration in this context, corresponding to an actual beamlet width of 3 mm. A convergence condition could be based on the change of r , that is, the iteration process stops in case of a small change of r . Considering that each iteration is associated with a decreased beamlet size, we would expect that convergence is reached with fewer iterations by beginning with a narrower line beam (i.e., smaller b). As shown in the different rows of Fig. 4(a), those with initial beamlet sizes of $b = 20$ and $b = 10$ show similar performance for the final iteration. In comparison, the one starting from $b = 6$ led to a final image with more noise, although a slightly higher r value was found for the first iteration. This implies that, the amplitude of measurement noise ranged within this frequency passband was considerable, leading to an unstable deconvolution. In conclusion, an optimized iteration scheme could start from $b = 10$ and end at $b = 3$, which was used for all the deconvolutions below in case of no specific statement. With a readout frame rate of 5 fps from the camera and a dose rate of 600 MU/min used in the IMRT plan, b values of 10 and 3 correspond to physical metrics of 15 and 4.5 mm, respectively. These values might be different for other treatment plans with distinct dose rate and scanning area, depending on the movement speed of the leaves or jaws.

3.B. Imaging for varying target depths

In this section, the effect of increasing target depth was analyzed. The raw MIP images and processed results are shown in the top and middle rows of Fig. 5, respectively, and the corresponding Z -profiles are shown in the bottom row. We can see that the iteratively deconvolved results show great

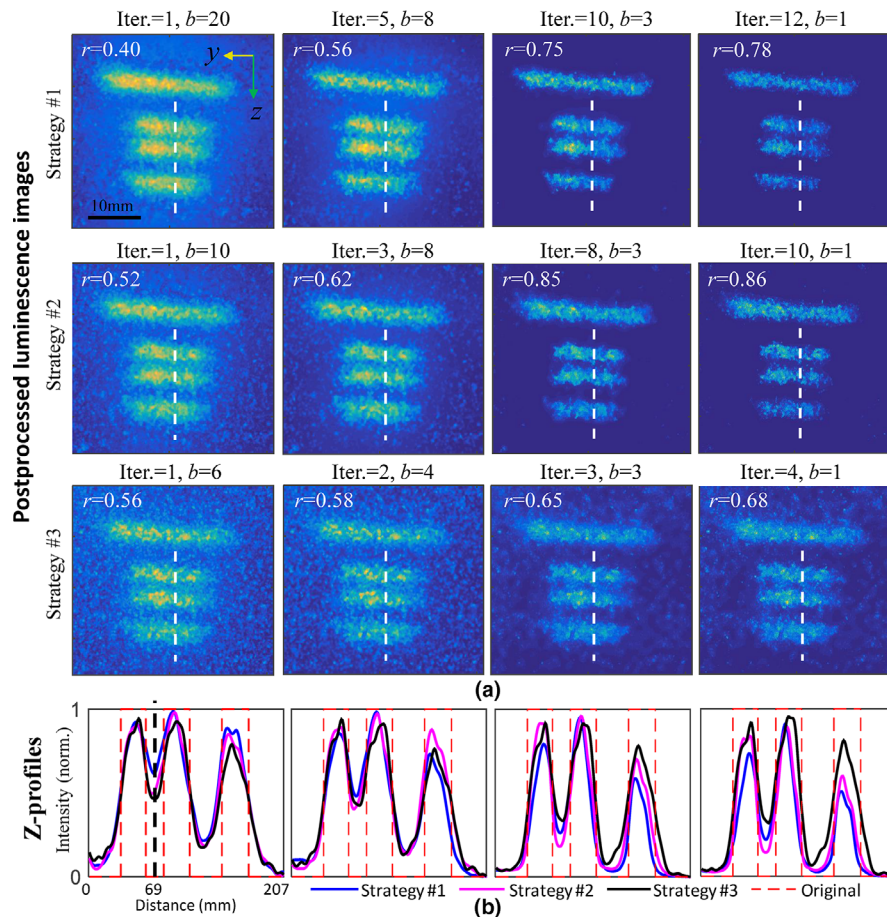


FIG. 4. Comparisons among the proposed method with different iteration strategies indicated with #1(top), #2(middle), and #3(bottom), respectively: (a) the resultant luminescence images, and (b) corresponding z-profiles along white dashed lines in (a). r values are inset in each image to qualify contrast recovery. Each of the z-profiles in (b) was normalized to the maximum intensity. (A full scanning video of iteratively tailored Cherenkov image sequences and the resultant luminescence sequences for iteration strategy #2 is available in Video S1.) [Color figure can be viewed at wileyonlinelibrary.com]

improvement compared to the original images. With increasing target depth, separate capillaries become less readily distinguishable. In particular, for the deepest targets embedded at 8 mm, the middle two capillaries with a gap of 4 mm are characterized with an r of 0.27. After iterative deconvolution, the background becomes clear and contrast recovery is enhanced to $r = 0.74$. Note that the excitation PSF estimated by Cherenkov images were fixed for different target depths. For deeper targets, diffusive scattering of emission photons is more responsible for image blurring than is diffusive scattering of excitation photons.

3.C. Modulation transfer function analyses

To quantify spatial frequencies that can be resolved vs depth, raw images, as shown in the upper row of Fig. 6, were analyzed to obtain modulation transfer functions (MTFs). Results as measured for target depths of 3, 5, and 8 mm are plotted in Figs. 6(a)–6(c), respectively, where deconvolved results truncated at iteration number of 1, 3, 6, and 8 are shown for reference. The line spread functions (LSFs) are inset correspondingly and fitted to Gaussian curves in the subplots, and demonstrate the available spatial frequencies

from which information can be obtained. Spatial resolutions achievable are related to the inverse of the MTF function where there is measurable amplitude, and here it was taken as 10% of the maximum. These are defined at different target depths, as recorded in Table I, where the effective lower limit on resolution was estimated. It can be seen from Table I that: (a) the spatial resolution increases greatly with iteration number for all target depths — the value as estimated for 8th iteration is almost double the value estimated for the first iteration; (b) resolution also improves with reduced depth for fixed iteration number, and the rate of improvement increases with number of iterations. For example, the rate of improvement between 5 and 8 mm increased from 9.7% in the 1st iteration to 26% in the 8th iteration. This can be attributed to the enhanced higher spatial frequency response with the increasing iterations due to the narrowed Cherenkov excitation source as analyzed in Fig. 3.

3.D. Comparisons between CELSI with IMRT and DW treatment plans

As discussed before, an original edge-scanning x-ray or electron irradiation is requisite to accommodate difference

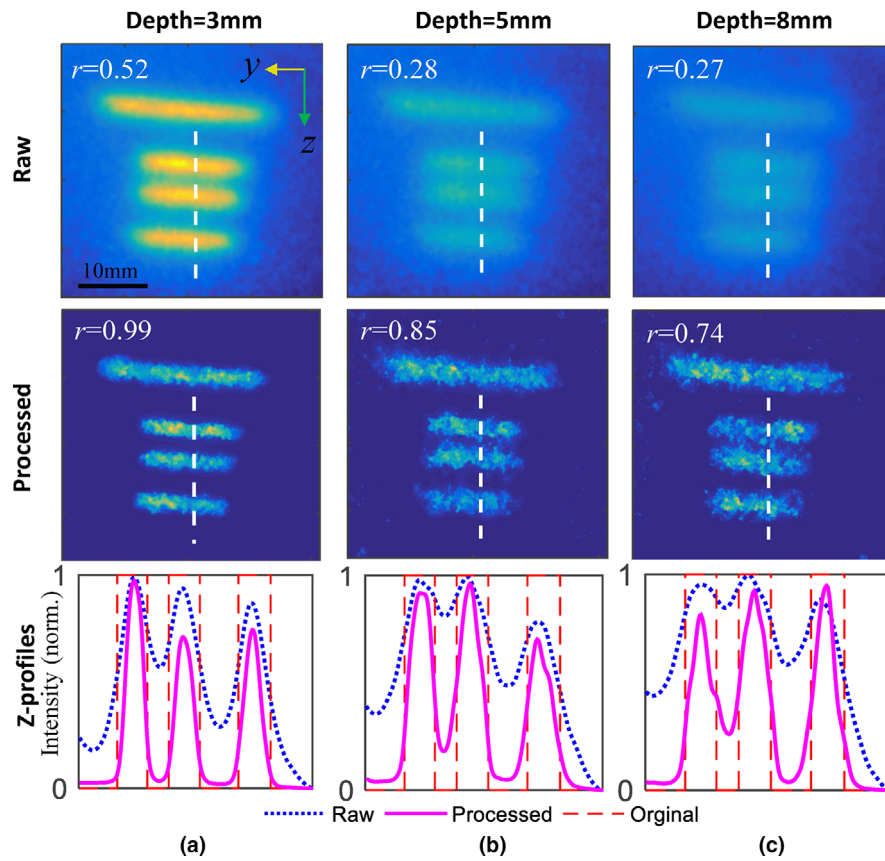


FIG. 5. Raw (top) and postprocessed (middle) luminescence images for target depths of (a) 3 mm, (b) 5 mm, and (c) 8 mm, respectively. The corresponding Z-profiles were plotted in the bottom row along the dashed white lines in above images. Each Z-profiles was normalized to the maximum intensity. [Color figure can be viewed at wileyonlinelibrary.com]

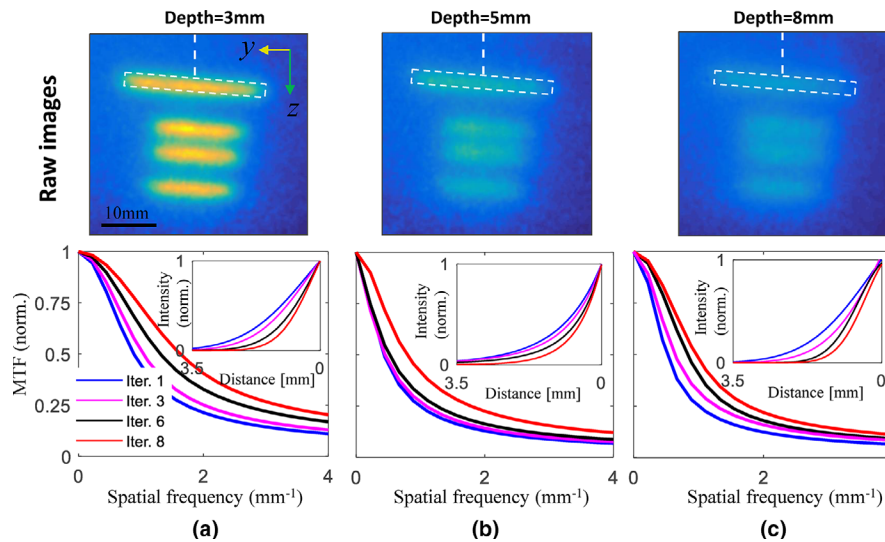


FIG. 6. Normalized modulation transfer function curves estimated for target depths of (a) 3 mm, (b) 5 mm, and (c) 8 mm, respectively, and different number of iterations. The insert curves correspond to Gaussian-fitted line spread functions along the white dashed lines indicated in the top row images. [Color figure can be viewed at wileyonlinelibrary.com]

operations to create downsized beamlets. Fortunately, most modern radiation treatment plans were designed in this way to minimize radiation exposure in normal tissue. Here, another plan named a dynamic wedge (DW) was investigated, which instead uses the jaws in the LINAC to slowly close to

the desired shape. In this experiment, three europium capillaries ($0.5 \mu\text{M}$) with a diameter of 0.7 mm were placed at a depth near 5 mm in the breast phantom, as shown in Fig. 7(a), while the measurement geometry is the same as that used in Fig. 1. Cherenkov images in the third iteration

TABLE I. Inverse of limiting spatial frequency (10% of the modulation transfer function amplitude) defined at varying depths for different number of iterations.

Depth (mm)	Iter.			
	1 (mm)	3 (mm)	6 (mm)	8 (mm)
3	0.23	0.16	0.10	0.08
5	0.41	0.35	0.25	0.19
8	0.45	0.35	0.28	0.24

with $b = 8$ are shown in Fig. 7(b) for both IMRT and DW plans. The radiation dose used was 204 MU, and other settings for the LINAC including beam energy, dose rate, geometry settings, and impulse duration were kept the same for the DW plan as those for the IMRT plan. The recovered images

with this proposed method are shown in Fig. 7(c). It can be seen that the DW result presented degraded image fidelity with lower signal-to-background contrast recovery. This can be explained by the fact that, in comparison with the IMRT plan, much more radiation dose of the DW plan was delivered with a fixed beam shape, which means the difference operations would result in zero Cherenkov and luminescence for this part of dose.⁸ To investigate lateral spatial resolution, Z-profiles along the white dashed lines in Fig. 7(c) are shown in Fig. 7(d), and we can see that imaging with IMRT obviously outperforms that with the DW plan. This is due to the expanded spatial frequency along multiple directions as shown in the two-dimensional (2D) spectra of Fig. 7(b), which improved spatial resolution correspondingly.²⁵ In order to determine the difference in spatial frequency distribution, the beam mappings in Fig. 7(b) can be examined, where the

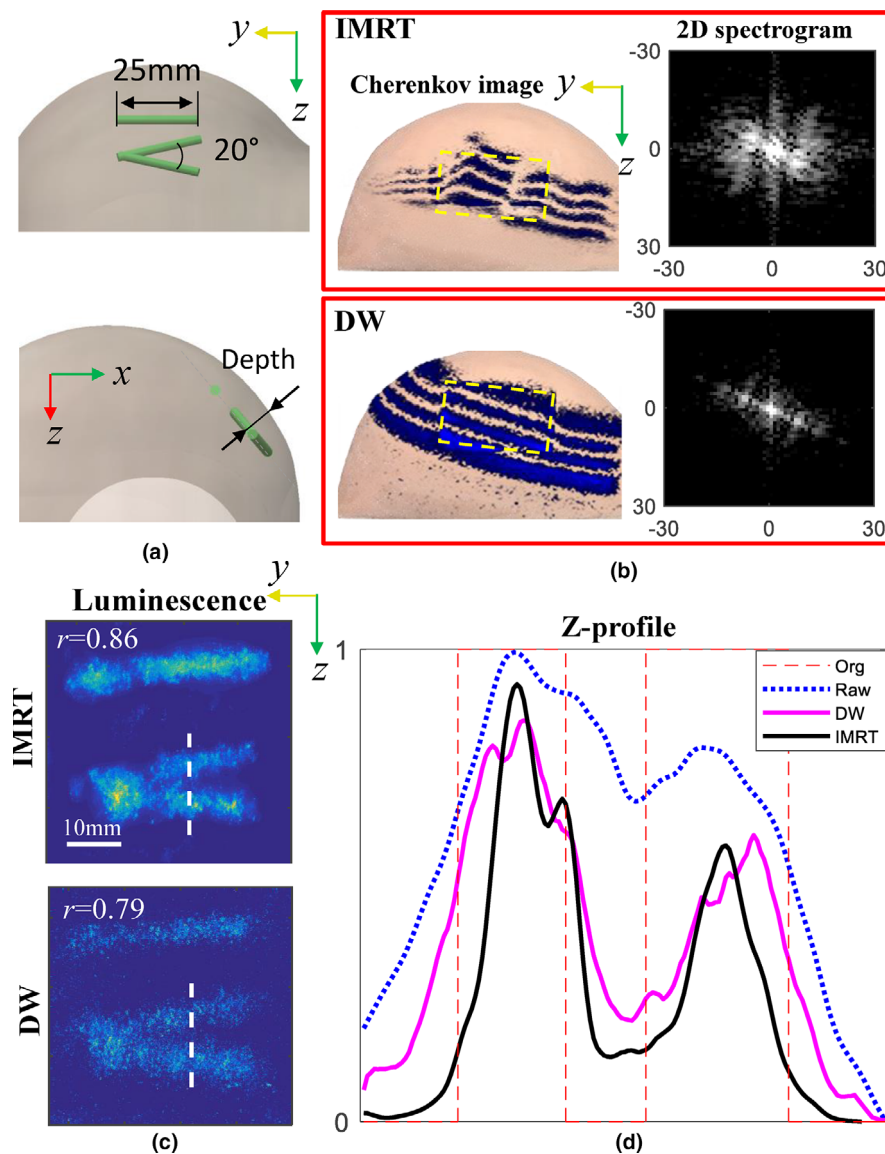


FIG. 7. Comparisons of imaging results by using intensity modulated radiotherapy and dynamic wedge (DW) plans: (a) the phantom configuration, (b) Cherenkov and two-dimensional spectrogram images, (c) luminescence images, and (d) the corresponding Z-profiles across the dashed white lines in (c). The raw data in (d) were measured for the DW plan. [Color figure can be viewed at wileyonlinelibrary.com]

edges of the IMRT beam are not as smooth as that in DW result. This was caused by the MLC mechanics in the former, where the leaf movement is not well synchronized.

3.E. 3D CELSI Scan and Reconstruction

Three-dimensional (3D) restoration has been realized for CELSI using a light sheet imaging approach.⁴ The measurement geometry is shown in Fig. 8(a), while the difference is that the camera was placed at the top of the phantom and light sheet was created by differencing the original edge-scanned beam [Fig. 8(b)]. By shaping the x-ray beam into a thin sheet and observing the Cherenkov-excited luminescence orthogonally to the sheet beam, we were able to capture a luminescence image emanating from only a single plane within the phantom. In this section, we achieved 3D distributions for both Cherenkov and luminescence light. To demonstrate this, a 3 mm diameter and 8 mm length europium-microsphere-containing tube at a concentration of 0.5 μM was embedded in the breast phantom at a depth of 10 mm, as indicated in Fig. 8(a), to mimic a lymph node.

Processing of the raw measurements is similar to that for the 2D imaging, including three steps: (a) iterative deconvolution for luminescence images frame-by-frame, (b) restorations for 3D Cherenkov and luminescence distributions, and

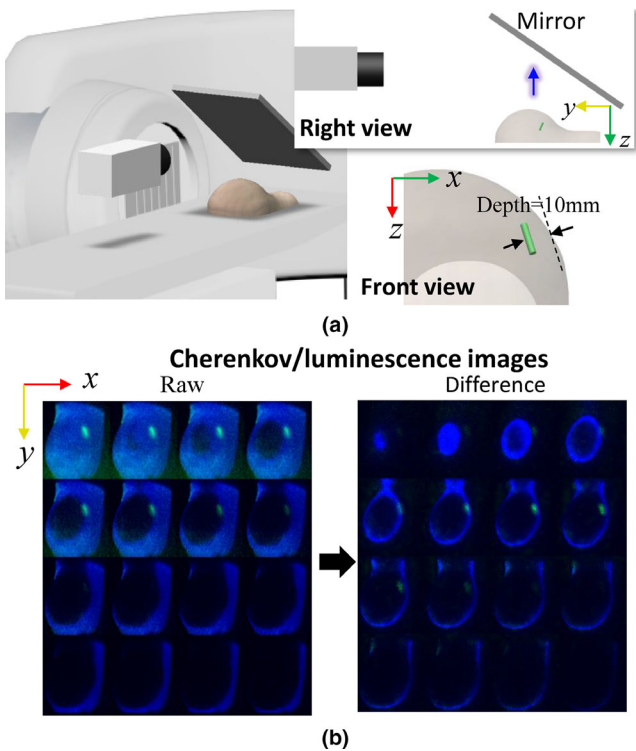


FIG. 8. A three-dimensional realization for Cherenkov and luminescence distributions with a dynamic wedge treatment plan: (a) the experimental setup with the linear accelerator lateral, phantom, and intensified charge-coupled device camera on the patient bed, and (b) raw and differenced Cherenkov images. A right view to specify the relative positions of the phantom, mirror, and camera is inserted in (a), and below that is the front view to show the target location. The blue arrow indicates the direction of detected luminescence light. [Color figure can be viewed at wileyonlinelibrary.com]

(c) diffusion corrections for luminescence light. Operations in step 1 are similar as those for 2D imaging by using Eqs. (4)–(6). The luminescence MIP images before and after deconvolution are shown in Fig. 9(a), as well as x-profiles along the white dashed lines. In step 2, to realize 3D restoration, we have to know z-positions of all layer-scanned beamlets. As a result, single-line shaped beamlets as shown in the difference Cherenkov image of Fig. 8(b) were utilized to replace the above multiple-line ones in Fig. 7(a). For this, only the positive pixels of the difference images were stored, and so Eq. (2) can be rewritten as

$$\Delta\Psi_{i,b} = (\Psi_i - \Psi_{i+b})^{0+}, \quad i + b \leq I, \quad (7)$$

where the superscript 0+ means only the positive elements were preserved. In addition, for advanced radiation treatment, gantry rotation generally forces a back-and-forth movement of the leaves in the MLC to adjust the beamlet area dynamically. Consequently, a one-way scanning episode was sufficient to sample and reconstruct a 3D image stack of the volume.

A three-dimensional view of the recovered Cherenkov light distribution is shown in Fig. 9(b), whose surface profile was extracted to acquire depth information. Then diffusion corrections can be made for luminescence target based on photon transport models, e.g., diffuse approximation for simplicity.⁴ To some extent, step 1 (iterative deconvolution) and step3 compensated for the diffusion effects along X-Y plane and Z-direction, respectively. In step 2, depth resolution basically depended on the frame-rate of the camera. The final 3D combinations of Cherenkov and luminescence, before and after the corrections, are displayed in the left and right columns of Fig. 9 (b), respectively. As expected, after correction (a) the “skin effect” was mitigated, i.e., the centroid of the target moved from z = 22.9 mm to z = 24.2 mm, closer to its real position as indicated in the front-view of Fig. 9(b); (b) the target volume shrunk toward its true size as indicated with black boxes in the front- and right- views of Fig. 9(b).

4. DISCUSSION

CELSI has been previously demonstrated to have an imaging depth of 3–4 cm,^{4,5,29} which is ideal for imaging breast lymph nodes and superficial tumors. In supplement to this, this study focused on a method for high resolution CELSI recovery to image mesoscopic biological structures (e.g., subcutaneous blood capillaries and lymphatics) testing for Ø = 0.5 mm as used in the phantom experiments. Based upon our previous conclusion from studying patterned illumination, that is, that the SNR for induced luminescence is proportional to the target area covered within the irradiation beam,⁸ the advantage of IMRT or DW scanning come in with large areas providing large signals for detection. As discussed before, downsized beam could be achieved by an original edge-scanned irradiation, and thus the edges should sweep over the target. This could be satisfied for most

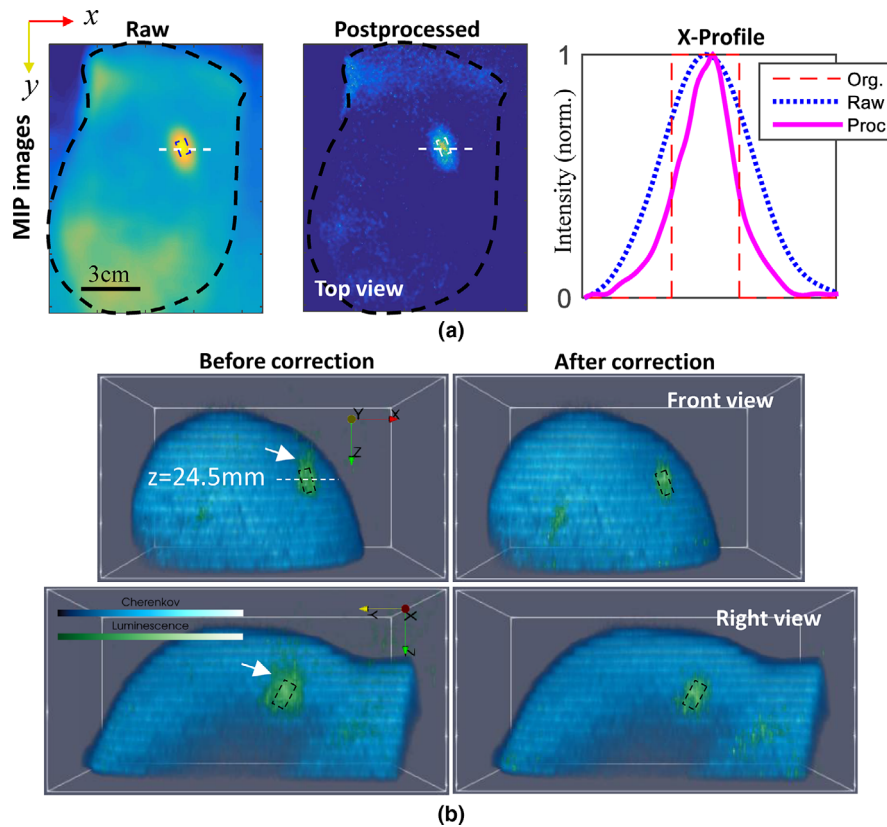


FIG. 9. Postprocessed results: (a) Iteratively deconvolved luminescence maximum intensity projection image and corresponding X-profiles along the dashed white lines, and (b) three-dimensional (3D) recovery of Cherenkov and luminescence distributions. 3D luminescence distributions are shown without and with diffusion correction in the left and right rows of (b). Dashed frames indicate real positions, and white arrows in (b) point to the part outside of the frames before corrections. [Color figure can be viewed at wileyonlinelibrary.com]

inverse-planning based dynamic treatment plans, for example, IMRT, volumetric modulated arc therapy (VMAT),²⁹ and DW. However, this is not the case for the simple and older forward-planning based ones, for example, 3D conformal radiation therapy (3DCRT), where the profile of each radiation beam for each gantry angle is shaped to fit the profile of the target from a beam eye view.³⁰ To uniformly cover the target, radiation is usually delivered from multiple LINAC gantry positions, and the trend is to be more conformal which means more beamlets from more angles, providing high spatial frequency scan information. In this way, 3D imaging combines very nicely with the trends in therapy, and provides a dataset quite analogous to x-ray CT.

5. CONCLUSION

This paper described a resolution enhancement strategy to postprocess CELSI measurements obtained from standard breast radiation treatment plans. Instead of making a tradeoff between spatial resolution and signal SNR, the proposed method benefits from a well-conditioned deconvolution and high spatial frequency resolved luminescence that results from wide and narrow beams, respectively. In order to address the ill-conditioned deconvolution of narrow beams, a successive approximation approach was developed to recursively generate difference Cherenkov images and instead take

the pre-deconvolved result as a distorted luminescence measurement. A built-in stepwise convergence relies on stepwise decreasing of the beam size, which is associated with a widening of the bandwidth of Cherenkov spatial frequency and resultant increasing spatial resolution.²⁵ In comparison to luminescence, the Cherenkov signal is much stronger and its fundamental spatial frequency is limited below a certain value (as shown in Fig. 3), which is set as a cutoff frequency for deconvolution to reduce its ill-posed nature. The stopping criterion was made based upon how small of a beam size would be acceptable for measurement with reasonable SNR. Investigation of the iteration criterion in Section 3.A showed that an effective and conservative iteration could start from a beamlet width $b = 10$ and end by $b = 3$, corresponding to physical sizes of 15 and 4.5 mm, respectively. These values were tested for a medium with tissue-like optical properties and a moderate target depth of 5 mm. An added benefit of this method is that the excitation PSF could be estimated based on the Cherenkov image locations, instead of relying upon the luminescence for localization. Although the measured \mathbf{P}_{Chk} is not the exact width as Cherenkov deeper in the tissue, the deconvolution with \mathbf{P}_{Chk} shapes is a reasonable approach for superficial applications through a few cm where the beamlet width does not change all that much.³

In basic applications of luminescence/fluorescence imaging, oxygen sensitivity lifetime probes have been used to

directly sample partial pressure of oxygen (pO_2) *in vivo* for mammalian tissue with CELSI.^{4,5,31} We could readily apply the proposed method into these CELSI procedures and might improve the mapping of oxygen concentration in tissues.

ACKNOWLEDGMENTS

This work was funded by the Congressionally Directed Medical Research Program (CDMRP) for Breast Cancer Research Program (BCRP) under U.S. Army USAMRAA contract W81XWH-16-1-0004 as well as the National Institutes of Health research grant R01 EB024498.

CONFLICT OF INTEREST

The authors have no conflicts to disclose.

*Department of Radiation Oncology, Stanford University, Palo Alto, CA 94304, USA

^{a)}Author to whom correspondence should be addressed. Electronic mail: brian.w.pogue@dartmouth.edu

REFERENCES

1. Andreozzi JM, Zhang R, Gladstone DJ, et al. Cherenkov imaging method for rapid optimization of clinical treatment geometry in total skin electron beam therapy. *Med Phys*. 2016;43:993–1002.
2. Andreozzi JM, Brůža P, Tendler II, et al. Improving treatment geometries in total skin electron therapy: experimental investigation of linac angles and floor scatter dose contributions using Cherenkov imaging. *Med Phys*. 2018;45:2639–2646.
3. Andreozzi JM, Mooney KE, Brůža P, et al. Remote Cherenkov imaging-based quality assurance of a magnetic resonance image-guided radiotherapy system. *Med Phys*. 45: 2647–2659.
4. Brůža P, Lin H, Vinogradov SA, Jarvis LA, Gladstone DJ, Pogue BW. Light sheet luminescence imaging with Cherenkov excitation in thick scattering media. *Opt Lett*. 2016;41:2986–2989.
5. Pogue BW, Feng J, LaRochelle EP, et al. Maps of *in vivo* oxygen pressure with submillimetre resolution and nanomolar sensitivity enabled by Cherenkov-excited luminescence scanned imaging. *Nat Biomed Eng*. 2018;2:254–264.
6. Kienle A, Patterson MS. Improved solutions of the steady-state and the time-resolved diffusion equations for reflectance from a semi-infinite turbid medium. *JOSA A*. 1997;14:246–254.
7. Vonesch C, Unser M. A fast thresholded landweber algorithm for wavelet-regularized multidimensional deconvolution. *IEEE Trans Image Process*. 2008;17:539–549.
8. Jia M, Bruza P, Jarvis LA, Gladstone DJ, Pogue BW. Multi-beam scan analysis with a clinical LINAC for high resolution Cherenkov-excited molecular luminescence imaging in tissue. *Biomed Opt Express*. 2018;9:4217–4234.
9. Webb S. *Intensity-Modulated Radiation Therapy*. Boca Raton, FL: CRC Press; 2015.
10. Jacques SL. Optical properties of biological tissues: a review. *Phys Med Biol*. 2013;58:R37–R61.
11. Härmä H, Soukka T, Lövgren T. Europium nanoparticles and time-resolved fluorescence for ultrasensitive detection of prostate-specific antigen. *Clin Chem*. 2001;47:561–568.
12. Millward JM, Ariza de Schellenberger A, Berndt D, et al. Application of europium-doped very small iron oxide nanoparticles to visualize neuroinflammation with MRI and fluorescence microscopy. *Neuroscience*. 2017;403:136–144.
13. Pratt WK. Generalized Wiener filtering computation techniques. *IEEE Trans Comp*. 1972;100:636–641.
14. Dong W, Feng H, Xu Z, Li Q. A piecewise local regularized Richardson-Lucy algorithm for remote sensing image deconvolution. *Opt Laser Technol*. 2011;43:926–933.
15. Dey N, Blanc-Feraud L, Zimmer C, et al. Richardson-Lucy algorithm with total variation regularization for 3D confocal microscope deconvolution. *Microsc Res Tech*. 2006;69:260–266.
16. Rodríguez P, Wohlberg B. Efficient minimization method for a generalized total variation functional. *IEEE Trans Image Process*. 2009;18:322–332.
17. Neelamani R, Choi H, Baraniuk R. Wavelet-domain regularized deconvolution for ill-conditioned systems. *IEEE Int Conf Image Process*. 1999;1:204–208.
18. Zhang W, Zhao M, Wang Z. Adaptive wavelet-based deconvolution method for remote sensing imaging. *Appl Opt*. 2009;48:4785–4793.
19. Starck JL, Pantin E, Murtagh F. Deconvolution in astronomy: a review. *Publ Astron Soc Pac*. 2002;114:1051–1069.
20. Frieden BR. *Image Enhancement and Restoration*. Vol. 6. New York, NY: Springer-Verlag Press Ltd; 1975:177–248.
21. Hojjatoleslami SA, Avanaki MR, Podoleanu AG. Image quality improvement in optical coherence tomography using Lucy-Richardson deconvolution algorithm. *Appl Opt*. 2013;52:5663–5670.
22. Ströhl F, Kaminski CF. A joint Richardson—Lucy deconvolution algorithm for the reconstruction of multifocal structured illumination microscopy data. *Methods Appl Fluoresc*. 2015;3:014002.
23. Hill NR, Ioup GE. Convergence of the van Cittert iterative method of deconvolution. *J Opt Soc Am*. 1976;66:487–489.
24. Morris CE, Richards MA, Hayes MH. Iterative deconvolution algorithm with quadratic convergence. *J Opt Soc Am A*. 1987;4:200–207.
25. Teng Y, Zhang Y, Li H, Kang Y. A convergent non-negative deconvolution algorithm with Tikhonov regularization. *Inverse Pro*. 2015;31: 035002.
26. Ströhl F, Kaminski CF. Frontiers in structured illumination microscopy. *Optica*. 2016;3:667–77.
27. Ripoll J, Nieto-Vesperinas M, Weissleder R, Ntziachristos V. Fast analytical approximation for arbitrary geometries in diffuse optical tomography. *Opt Lett*. 2002;27:527–529.
28. Zhou X, Fan Y, Hou Q, et al. Spatial-frequency-compression scheme for diffuse optical tomography with dense sampling dataset. *App Opt*. 2013;52:1779–1792.
29. Teoh M, Clark CH, Wood K, Whitaker S, Nisbet A. Volumetric modulated arc therapy: a review of current literature and clinical use in practice. *Br J Radiol*. 2011 Nov;84:967–996.
30. Schlegel WC, Bortfeld T, Grosu AL. (eds). *New technologies in radiation oncology*. Berlin: Springer; 2006: p. 257.
31. Zhang R, Davis SC, Demers JH, et al. Oxygen tomography by Cherenkov-excited phosphorescence during external beam irradiation. *J Biomed Opt*. 2013;18:0505031–0505033.

SUPPORTING INFORMATION

Additional supporting information may be found online in the Supporting Information section at the end of the article.

Video S1. Fully-scanned Cherenkov and the resultant luminescence sequences.

Maps of in vivo oxygen pressure with submillimetre resolution and nanomolar sensitivity enabled by Cherenkov-excited luminescence scanned imaging

Brian W. Pogue^{1,2*}, Jinchao Feng³, Ethan P. LaRochelle¹, Petr Bruža¹, Huiyun Lin⁴, Rongxiao Zhang¹, Jennifer R. Shell¹, Hamid Dehghani⁵, Scott C. Davis^{1,2}, Sergei A. Vinogradov⁶, David J. Gladstone^{1,2,7} and Lesley A. Jarvis^{2,7}

Low signal-to-noise ratios and limited imaging depths restrict the ability of optical-imaging modalities to detect and accurately quantify molecular emissions from tissue. Here, by using a scanning external X-ray beam from a clinical linear accelerator to induce Cherenkov excitation of luminescence in tissue, we demonstrate in vivo mapping of the oxygenation of tumours at depths of several millimetres, with submillimetre resolution and nanomolar sensitivity. This was achieved by scanning thin sheets of the X-ray beam orthogonally to the emission-detection plane, and by detecting the signal via a time-gated CCD camera synchronized to the radiation pulse. We also show with experiments using phantoms and with simulations that the performance of Cherenkov-excited luminescence scanned imaging (CELSI) is limited by beam size, scan geometry, probe concentration, radiation dose and tissue depth. CELSI might provide the highest sensitivity and resolution in the optical imaging of molecular tracers in vivo.

Optical luminescence is the dominant preclinical imaging modality for the molecular probing of cells and tissue physiology, both in vitro and in vivo^{1–3}. The sensitivity of optical detectors to small concentrations of molecular emitters and the ease of use of the detection technology make optical molecular imaging much more widely used than X-rays, ultrasonography, nuclear medicine or magnetic resonance imaging (MRI). However, because of elastic scattering of light in tissue, the tissue depths accessible by optical imaging in vivo are fundamentally limited^{4–6}. Although fluorescence and bioluminescence have been used extensively to elucidate intracellular signalling in vitro, their use in vivo is largely limited to bulk temporal kinetics, surface tissue imaging^{7–9} or invasive/surgical measurements⁷. The inability to reconstruct the spatial origin of a detected photon generally limits non-invasive in vivo luminescent molecular imaging, where high spatial resolution has never been achieved beyond microscopy. Additionally, the decrease in signal intensity with depth into tissue is exponential, creating highly non-linear excitation during imaging, as illustrated in Fig. 1a.

Here, Cherenkov-excited luminescence scanned imaging (CELSI)^{10,11} was used to sense luminescent molecular probes deep within tissue, using megavoltage (MV) X-ray radiation, and adopting an orthogonal excitation geometry that allows scanning of the region of interest, similarly to the way fluorescent light sheet microscopy works¹², as shown in Fig. 1b. As the illuminated area is consistently at a known distance from the detector, this geometry maximizes the signal-to-noise ratio, which tends to be the dominant factor in quantitative imaging of thick and optically turbid samples. Importantly, Cherenkov light of organic molecules is based on the

electronic energy level of the excitation beam. Thus, with high MV X-ray sheet illumination, the spatial targeting of X-rays can be optimally combined with biological organic probes⁹ already widely used in animals for other imaging modalities, and is translatable to humans. CELSI is intended as an optical imaging tool that can preserve the linearity of the emitted optical signal with depth, and is not overly affected by scatter dominance in tissue. Further illustration of the value of CELSI relative to other imaging modalities can be seen in the Supplementary Fig. 1. The geometry used here is illustrated in Fig. 1c and temporal and spatial parameters in Fig. 1d.

Cherenkov light is generated in tissue from the scatter-induced secondary electrons produced from X-rays, here generated by a therapeutic MV linear accelerator (LINAC), that interact with the dielectric media. The spectrum of Cherenkov light is broadband, peaks in the ultraviolet (UV) and decays in intensity (I) with a wavelength dependence of $I \approx 1/\lambda^2$ (Fig. 1e). Luminescence of the probe is therefore excited only within the volume that is directly in the path of the scanning radiation beam (Fig. 1b), so that all luminescent signals detected by the intensified charge-coupled device (ICCD) are considered as originating exclusively from within the pathway of the LINAC beam. This geometrical arrangement adopts some of the principles of directed excitation imaging tools, such as ultrasound, where depth-dependent attenuation correction can be applied to the data because of knowledge of the excitation or emission beam depth. The limiting factor remains the intensity attenuation with distance by diffusion scatter and absorption as the emitted light passes through the tissue. The luminescent probe used here, Platinum Oxyphor G4 (PtG4),

¹Thayer School of Engineering, Dartmouth College, Hanover, NH, USA. ²Norris Cotton Cancer Center, Dartmouth-Hitchcock Medical Center, Lebanon, NH, USA. ³Faculty of Information Technology, Beijing University of Technology, Beijing, China. ⁴Key Laboratory of OptoElectronic Science and Technology for Medicine of Ministry of Education, Fujian Provincial Key Laboratory of Photonics Technology, Fujian Normal University, Fuzhou, China. ⁵School of Computer Science, University of Birmingham, Birmingham, UK. ⁶Department of Biochemistry and Biophysics, Perelman School of Medicine, University of Pennsylvania, Philadelphia, PA, USA. ⁷Department of Medicine, Geisel School of Medicine, Dartmouth College, Hanover, NH, USA. *e-mail: brian.w.pogue@dartmouth.edu

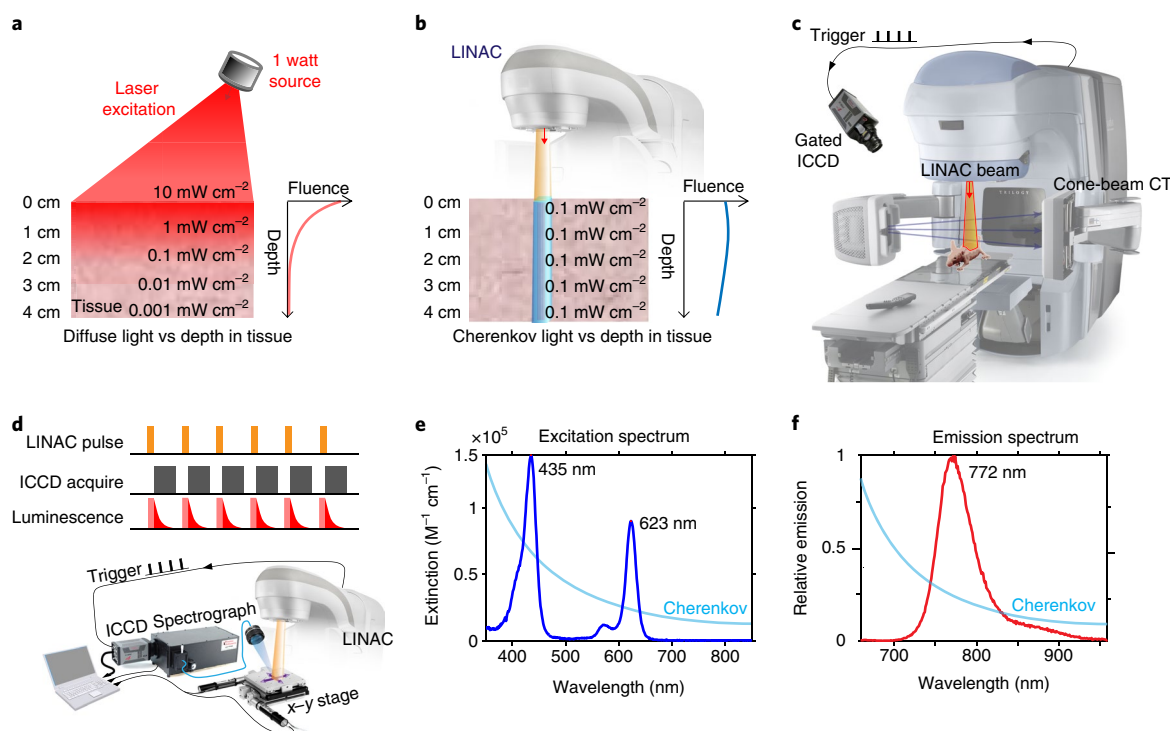


Fig. 1 | Excitation fluence decrease with depth into tissue for normal fluorescence imaging versus CELSI; the temporal sequence and molecular probe characteristics. **a, b**, Comparison of the loss of fluence using a standard laser/LED excitation source (**a**) with the stability of Cherenkov excitation generated from a linear accelerator (LINAC) radiation beam (**b**). **c**, A diagram of the experimental Cherenkov-excited luminescence scanned imaging (CELSI) set-up; the LINAC beam triggers a series of gated acquisitions using an intensified charge-coupled device (ICCD) camera, whereas animal position and anatomy are defined by a computed tomography (CT) scan. **d**, A raster scan approach to image acquisition measured by the ICCD shown with gated emission detected via a spectrograph. **e, f**, The Cherenkov spectrum (blue) from single solution scans is overlaid on the absorption (**e**) and the luminescence emission (**f**) spectra for the fluorophore platinum(II)-G4 (PtG4). The structure of PtG4 is provided in Supplementary Fig. 2.

is optimized for oxygen sensing, with a luminescent lifetime in the range of 22–44 μs and an emission wavelength in the near-infrared^{13,14} (Fig. 1e, f).

Deep-tissue Cherenkov excitation from ionizing radiation of isotopes can also excite molecular luminescence^{15,16}, with the signal increasing proportionally to the emitted γ -ray energy. Similarly, radiation delivered by a medical LINAC generates Cherenkov emission within the treated tissue¹⁷ and can be visualized for patient dosimetry studies¹⁸, as well as excitation of molecular probes^{19,20}. This process can be used to excite fluorescent or phosphorescent probes in tissue to sense diagnostic molecular features, and has been demonstrated at low radiation doses¹⁰, where high-energy MV photons have the highest generation of Cherenkov emission, yet the lowest deposited dose level in tissue. The excitation light from Cherenkov emission is directed by the incident beam, and so the observation of emission need not be highly localized because the signal is backprojected along the line of the Cherenkov beam. This also enables attenuation correction to be readily applied to the signal, based on the depth of the beam. Additionally, altering the orthogonal angle of the excitation beam to the collection plane allows some advantages in contrast-to-background improvement, as used in thick tissue fluorescence microscopy^{12,21}. This geometry makes CELSI's approach to signal measurement much more useful for whole body imaging, as it eliminates the need to estimate the depth of the optical signal origin.

The aim of this work was to evaluate the potential for Cherenkov excited luminescence scanned imaging to directly sample partial pressure of oxygen (p_{O_2}) in vivo for mammalian tissue, estimating the spatial resolution, depth and probe concentration sensitivity bounds, and estimate the contrast-to-background values available for realistic tumour imaging applications.

Results

Beam size. By measuring total luminescence signal and considering prior information about the position of the scanning beam, the distribution of optical signal along the direction of scanning can be recovered. In Fig. 2a–c, the possible beam geometries are illustrated, where the X-ray sheet can be shaped as a broad beam covering the entire tissue volume (as is commonly used in radiotherapy), or a 2D sheet of 5 mm thickness, or a pencil beam of $5 \times 5 \text{ mm}^2$, which can be raster scanned around the tissue. The benefit of a pencil beam would be the highest spatial resolution, in step sizes of 0.1 mm, whereas the benefit of a broad sheet is the fast imaging acquisition. However, the choices here make a large impact on the image quality and signal strength. In Fig. 2d, a broad homogenous phantom was imaged with a large square beam of $100 \times 100 \text{ mm}^2$, and then by a thin sheet beam of $5 \times 100 \text{ mm}^2$, and then a pencil beam of $5 \times 5 \text{ mm}^2$, as described in the Methods. The phantom had an embedded luminescent square of $10 \times 10 \text{ mm}^2$, at depth within it, to test for signal recovery, and the contrast-to-noise ratio (CNR) was plotted in the region of interest (ROI1) relative to the background (ROI2) (Fig. 2e) for each of the three cases at different depths of the object.

Imaging geometry. Radiation beam energies are carefully chosen to reach specific depths in the body, and a set of beams from different gantry angles can be delivered to the patient from these planned entrance positions. In general, arbitrary angles, beam energies and dose values are chosen based on an optimization algorithm to maximize dose to target regions and minimize dose to organs at risk of radiation damage. It is this flexibility of targeting that makes radiation-based excitation flexible for molecular imaging. The simplest angular geometries orthogonal or lateral to the subject are shown in

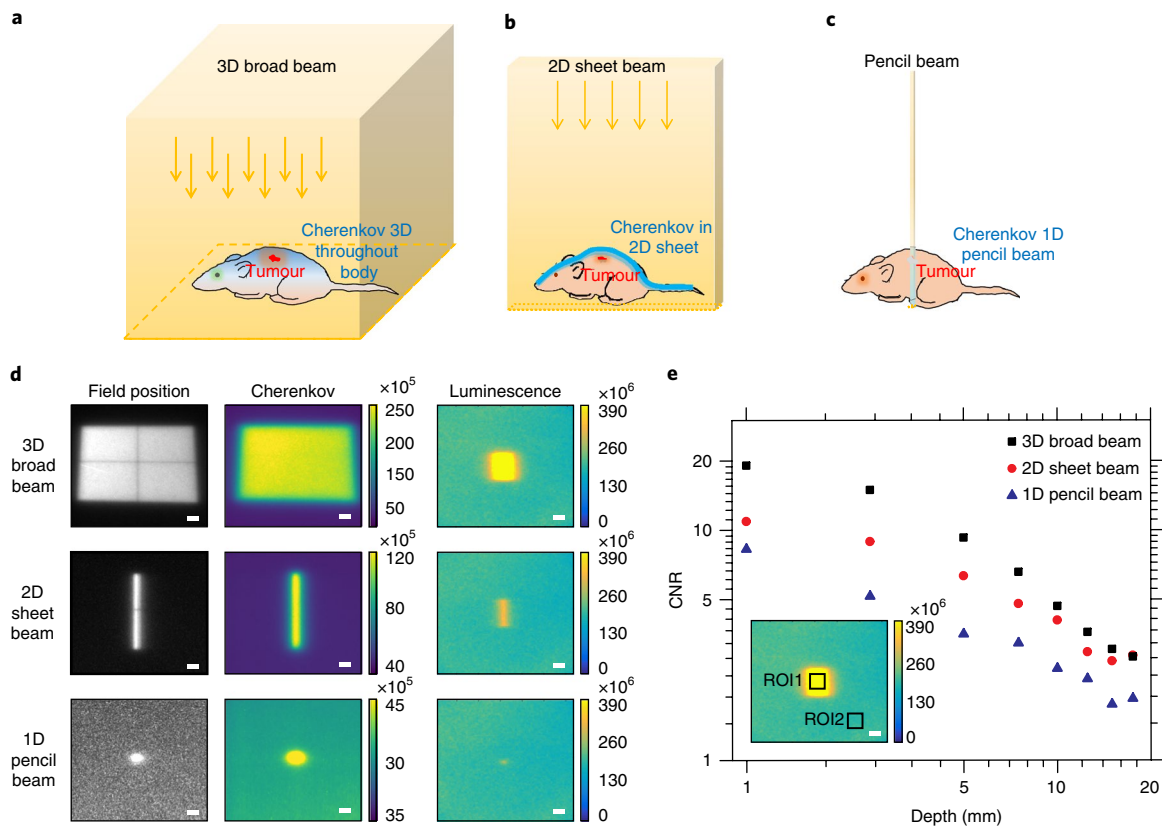


Fig. 2 | Radiation beam shape configuration and region of the tissue where Cherenkov light is generated affects contrast to noise measured. **a**, A single broad beam crossing the 3D volume of the animal generates broad Cherenkov emission. **b,c**, A 2D sheet beam generates an axial plane through the mouse (**b**), whereas a 1D pencil beam generates an axial excitation line (**c**). These geometric choices affect the possible contrast-to-noise ratio (CNR), and hence the sensitivity of other parameters such as minimum concentration and depth of imaging feasible, as well as acquisition time. **d**, Images from a phantom of the field light position, the Cherenkov emission and the luminescence of a single square target embedded in the phantom are shown for the geometries in **a–c** (duplicate images taken during separate imaging sessions show near-identical image quality). **e**, The CNR of the target relative to the background as measured by individual scans, where each data point represents an individual acquisition. Colour bars (**d,e**), detected photons $\text{cm}^{-2} \text{s}^{-1}$. Scale bars, 1 cm.

Fig. 3a,b, where the beam could be placed roughly orthogonal to the camera direction for sheet-like imaging, or aligned along it for epi-illumination. While the range of possible angles is much greater than this, these were chosen as the extremes of contrast-to-background, as will be shown. A complete analysis of the effect of geometry on the singular value index, matrix condition number and matrix rank, for the Jacobian to be inverted, is shown in Supplementary Fig. 3, using coefficient values listed in Supplementary Table 1.

The experimental set-up was photographed and is shown in Fig. 3c,d, and a resulting luminescence image of a single 1 mm diameter capillary filled with $500 \mu\text{M}$ PtG4 at 5 mm depth into a tissue phantom solution is shown for each geometry in Fig. 3e,f, respectively. The phantom was a broad flat liquid media of $200 \times 200 \text{ mm}^2$, with the single luminescent capillary within it. A scanned sheet beam was used for imaging with approximately 30 mGy per position of the beam. The colour bar for each result is the same and so the significantly higher background near 9,600 counts leads to a contrast ratio of 1.14 and CBR value of 14% for the epi-illumination, while the lower background near 2500 counts is seen for lateral illumination, leading to a contrast ratio of 3.5 and CBR of 220%. The higher background comes from the fact that the entire volume being imaged is being excited by Cherenkov, and so the signal comes from a mix of depths below the surface. Because of this observation, the lateral excitation geometry was used throughout most of the next experiments, providing a depth-selective excitation. A detailed analysis of the centroid position error and full width

at half maximum (FWHM) values of recovered regions is shown in Supplementary Fig. 4.

Dose, concentration and depth of imaging. The dominant factors affecting image recovery were explored systematically by varying one parameter at a time (Fig. 4). The contrast-to-background ratio (CBR) was used as a metric of success, assessing how this varied with radiation dose delivered, concentration of PtG4 and depth of the object into the medium. This figure of merit was chosen because CELSI is a background-dominated imaging geometry, as are most luminescent and fluorescent imaging modalities²². CELSI of PtG4 in a 1 mm diameter capillary was assessed with different concentrations, depths (distance from capillary to phantom surface) and radiation doses. First, using a fixed depth of 5 mm, the concentrations range was varied logarithmically from $500 \mu\text{M}$ down to $0.78 \mu\text{M}$ inside a 1 mm capillary, measuring CBR for a 1 s acquisition time for a dose of 0.1 Gy, with the overlapping excitation volume being $3.9 \times 10^{-6} \text{ l}$, making the number of moles used vary from $2.0 \mu\text{mol}$ down to 3 nmol. The results are shown in Fig. 4a, being monotonic in shape and reducing to a CBR of 1 at about 6–8 nmol. Next the CBR was tracked for a fixed concentration of $500 \mu\text{M}$ in the 1 mm capillary, for 200 nmol in the excitation volume, varying the depth down to 20 mm into the phantom, also using a 0.1 Gy dose (Fig. 4b). This was monotonic with depth and appears to decrease near $\text{CBR} = 1$ well beyond the 20 mm depth. Finally, the variation with radiation pulses added together was studied at a target depth of

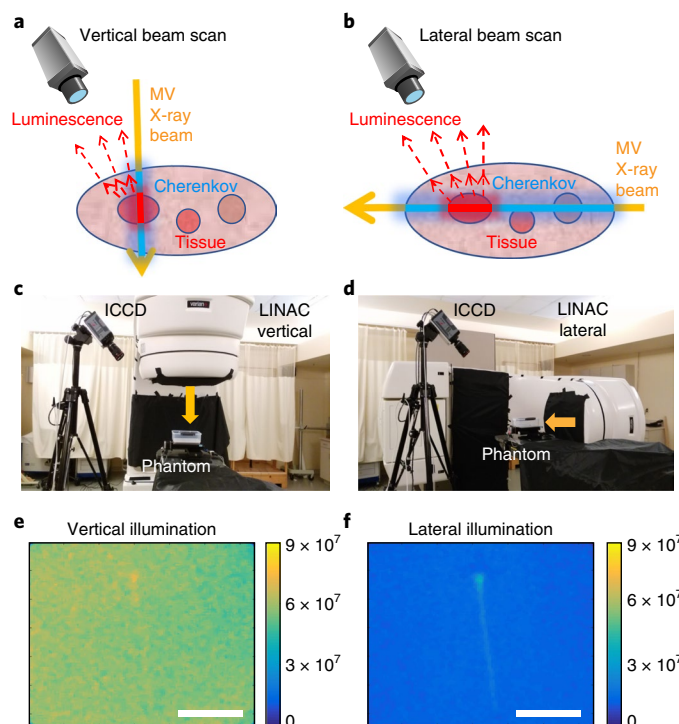


Fig. 3 | The geometry of the imaging camera relative to the X-ray beam entrance position affects image contrast. **a,b**, Cherenkov luminescence emissions provide less depth-related information from a vertical (or epi-illumination) scan (**a**) than a lateral sheet scan (**b**). **c,d**, Photographs of the camera and LINAC positions for vertical and lateral scan geometries (reflecting the schematics in **a,b**). **e,f**, Single-frame images of PtG4 luminescence from one capillary placed in a broad tissue phantom for the vertical (**e**) and lateral (**f**) geometries, with colour bars representing the full range available on the camera. These representative individual snapshot images illustrate the high background and hence poorer contrast obtained from the epi-illumination geometry. The contrast-to-background values are 15% for **e** and 220% for **f** above the background level. Colour bars (**e,f**), detected photons $\text{cm}^{-2}\text{s}^{-1}$. Scale bars, 5 mm.

5 mm and fixed concentration of $100\ \mu\text{M}$, or 2 nmol, showing monotonic dependence on dose in Fig. 4c, and decreasing to CBR of 1 at 2 radiation pulses, roughly equivalent to a 1.67 mGy dose.

Scan directions and tomographic reconstruction. The direction and range of scan parameters in CELSI is quite large, and three particular geometries were examined as analogous to other tomographic systems, and also used to compare CELSI to fluorescence tomography systems. First, a study of fluorescence tomography as acquired in the epi-illumination geometry was completed, as well as transmission geometry. For this, 1% noise was randomly added to the simulated forward data with either a single embedded object or the 3 objects, as shown in Fig. 5. The stopping criteria for the iterative reconstruction was when either a change in projection error of less than 0.01% was reached between iterations or the maximum iteration number of 40 was achieved. A Cartesian pixel basis of 30×30 squares was used in Fig. 5, and shown in Fig. 5a,b respectively with the test object shown; reconstructed images are shown in Fig. 5d,e. The CELSI tomography image with lateral excitation and vertical detection is shown in the schematic (Fig. 5c) and reconstructed object in Fig. 5f. In this case, CELSI signal is shown to improve signal detection compared to epi-illumination fluorescence tomography, and has higher contrast than transmission-based fluorescence tomography, with further numerical analysis of the Jacobian matrix improvement shown in Supplementary Fig. 3.

Next, the range of possible scans available with CELSI was explored to investigate how it would affect image recovery. As shown in Fig. 5g–i, the horizontal, vertical and diagonal aspects of a scan can more fully interrogate the image space, and reconstructed images for these three respective geometries are shown in Fig. 5j–l,

with recovery from the combination of all of them shown in Fig. 5m. From these simulations, it is obvious that the excitation line directions distort the recovered objects in the axial direction of the source–detector lines. As with all tomography applications, the larger the range of angles sampled, the better the image recovery can become (Fig. 5m), better resolving the object in all directions. In this numerical study, three angles were used, as these were sufficient to resolve the three objects, yet in principle an unlimited number of angles could be used, limited only by the added dose given to the subject. So, as in CT imaging, ultimately there is a dose-resolution-contrast tradeoff that dictates the imaging system performance.

Spatial resolution. Both experiments and simulation studies were completed to assess the ultimate limits to spatial resolution with optimized conditions. The reconstruction set-up and convergence criteria were the same as in the previous section, but a larger pixel basis of 100×100 pixels was used to improve the quality of the reconstructed images in Fig. 6 (and Supplementary Fig. 4). Simulation studies were carried out with varying depths and using a standard resolution test, varying the distance between two small objects (Fig. 6a). The reconstructed images are shown with intensity in terms of the reconvened yield, as defined by the PtG4 absorption coefficient multiplied by the quantum yield of emission. The results reveal that when the depth of inclusions was smaller than 5 mm, the CELSI tomography has the ability to discriminate the two inclusions with edge-to-edge distance of 0.1 mm (Fig. 6b). When the depth of inclusions was increased to 2.5 cm, the two inclusions could still be discriminated with edge-to-edge distance but nearer 0.5 mm, and when it was increased to 3 cm, the two inclusions could be discriminated with edge-to-edge distance but nearer 1.8 mm.

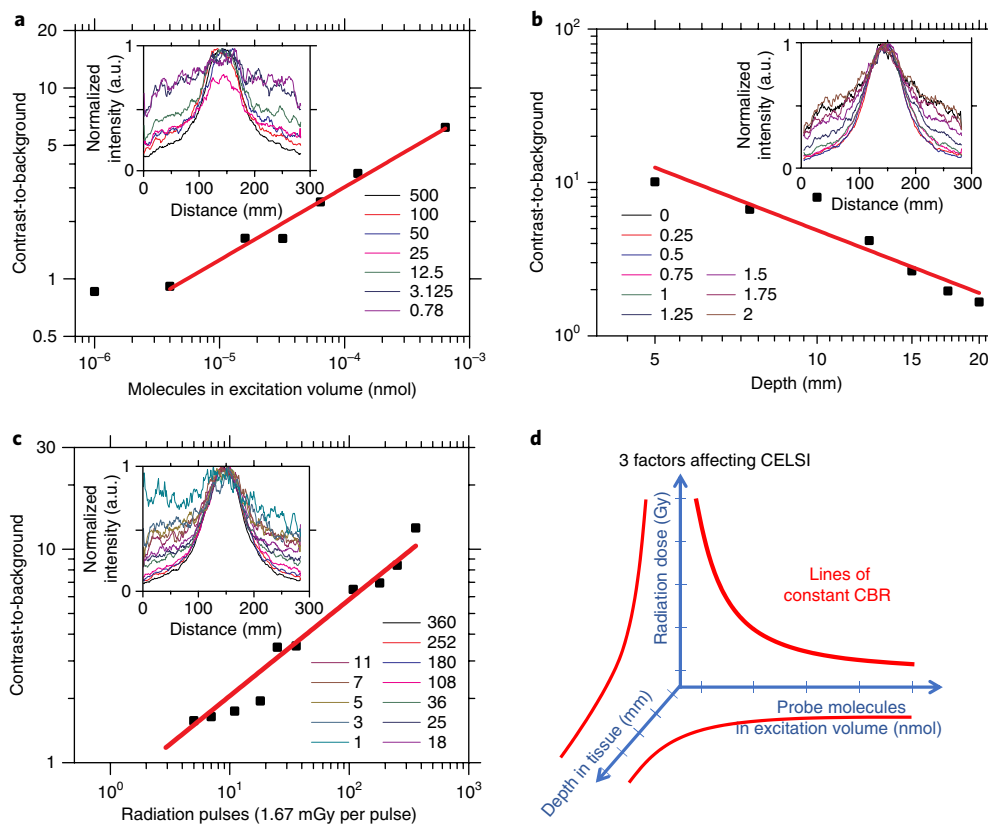


Fig. 4 | Contrast-to-background ratio is affected by the concentration and depth of the object, and the radiation dose used in scanning. a–c, Data points are shown for increasing concentrations of PtG4 in the physiologically relevant range (**a**); increasing depth between the capillary and the surface of the phantom imaged (**b**); and increasing radiation dose between 1 and 500 radiation pulses, using 1.67 mGy per pulse (**c**). For each graph, the inset shows the line scan of the raw data. Each individual data point represents the extracted contrast-to-background ratio for a single scan of a test object. The red lines in each graph illustrate the linear trendline of the data on the log-log plots. **d**, The factors affecting CELSI signal strength are schematically illustrated as reciprocal in their effect on the contrast-to-background ratio, as illustrated by the red lines.

The results show that CELSI tomography can yield high spatial resolution, but that this spatial resolution does degrade with depth into the medium, as expected, due to the loss of light penetration depth at these wavelengths. These CELSI results can be compared to epi-FT and full-FT results, which have significantly lower spatial resolution, ranging from a few millimetres to beyond 10 mm at depths of 15 and 25 mm into the medium. Fig. 6b shows the minimum spatial resolution as a function of depth of inclusions. Epi-FT could not reconstruct the inclusions accurately when the depth of inclusions was deeper than 15 mm, and so the spatial resolution was not calculated.

Experimental studies were carried out to attempt to match the simulations, but using a simpler geometry of a single capillary rod positioned at 5 mm into the tissue, simulating phantom medium. A range of capillaries with diameters varying from 1 mm down to 0.1 mm were used and filled with PtG4 at 50 μM . The FWHM recovered was extracted and the observed FWHM is plotted against the true value in Fig. 6d, showing nearly perfect linearity and matching the expected value of the smallest spatial resolution tested (100 μm).

Rodent and phantom imaging for sensitivity and resolution testing. To verify that imaging in a complex tissue shape would be possible, the XFM-2 phantom was imaged with 1 mM PtG4 within 7 μl at the tip of the cylinder (for 7 nmol total PtG4) inserted into the central part of the body. For these mouse phantom experiments, 35 radiation sheets were used, and the vertical step of each sheet was approximately 0.52 mm. The 3D forward simulation mesh contained 18,496 nodes, 93,818 elements and 1,712 boundary nodes,

and the absorption and reduced scattering coefficients for excitation and emission were both set at $\mu_a = 0.007 \text{ mm}^{-1}$ and $\mu_s' = 1.0 \text{ mm}^{-1}$. The reconstruction pixel basis was $25 \times 25 \times 25$ voxels. The initial guess of regularization parameter was 10, and the convergence criteria to stop the iterative update was when a change in projection error was less than 0.01% between successive iterations or when the maximum number of iterations was reached at $n = 10$. The remitted luminescence image from above is shown in Fig. 7a, with the Cherenkov beam in the plane of the tube, the luminescence from the tube showing a blurry image and FWHM of $10.4 \times 11.9 \text{ mm}$ in the two orthogonal directions. This signal is superimposed on the white light image of the mouse phantom. Reconstructed images are shown in the 3 orthogonal directions superimposed on CT scan images of the phantom (in grey scale). This recovery showed good localization and recovery of the shape as might be expected (Fig. 7b), with FWHM values of the reconstructed inclusion of $5.1 \times 5.1 \times 4.7 \text{ mm}$ in total. Note that these dimensions are less than half of the FWHM values of planar projection imaging.

To further advance and test the performance of CELSI reconstruction, an in vivo experiment with breast cancer MDA-MB-231 xenograft tumours in a mouse was performed, with two separate injection sites on each of the mouse hind limbs. The mouse was injected with 50 nmol of PtG4 into the right-side tumour and 10 nmol into the left-side tumour, using a 50 μM stock solution. These doses were specifically chosen to be just above and just below the detection threshold, respectively. Given the sizes of the tumours ($9 \times 9 \times 6 \text{ mm}^3 \approx 500 \text{ mm}^3$), these corresponded to approximately 0.4 nM and 0.10 nM, when averaged over the tumour volume.

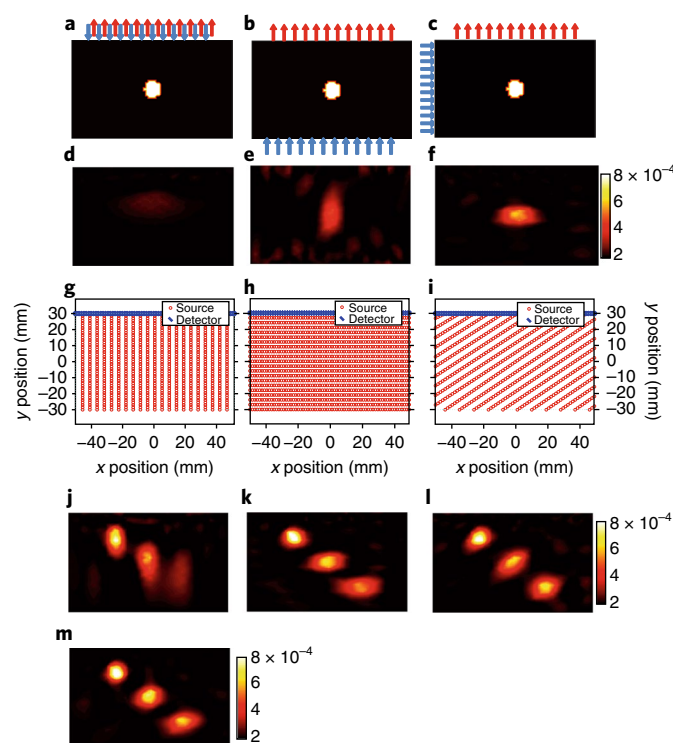


Fig. 5 | Source and detector placement affects the reconstructed CELSI images. **a–c**, In silico source and detector pairing for epi-fluorescence tomography (epi-FT) (**a**); the full-FT (or transmission) geometry (**b**); and the lateral CELSI excitation pattern with tomographic orthogonal reconstruction (**c**). The blue arrows represent the source locations, and the red arrows denote the detector locations. **d–f**, Reconstructed luminescence distributions corresponding to the epi-FT (**d**), the full-FT (**e**) and the CELSI (**f**). **g–i**, Three angles of scanning for CELSI were examined for horizontal (**g**), vertical (**h**) and diagonal (**i**) positions, and three test objects at different depths were used to test reconstruction accuracy as shown in **j–l**, respectively. **m**, The combined set of all three scan geometries was used to create a reconstructed image, showing the best preservation of the three objects' spatial locations and intensities, using 30 iterations in each reconstruction. These simulations were carried out once for each in the individual graph shown and are shown in units of luminescent yield, $\eta\mu_{at}$ (colour bar).

The mouse was imaged within 30 min of injection. The other experimental settings were identical to the phantom experiment. Fig. 7c shows the CT scan of the animal, and Fig. 7d shows the acquired luminescent maximum intensity projection image overlaid on the colorized CT scan, with this luminescence image showing very blurry localization, and with FWHM of 18.9×14.8 mm in the two orthogonal directions. The CT images were used to generate a finite element mesh, and the optical properties of tissues in the mouse were estimated by average homogeneous values for a mouse, based on published values¹⁷.

For these in vivo experiments, the mouse was scanned with a sheet illumination procedure. A total of 19 irradiation sheets were used with a step between them of 0.8 mm. The forward simulation mesh contained 13,185 nodes, 63,852 elements and 3,716 boundary nodes, and the absorption and scattering coefficients for excitation and emission were both set to $\mu_a = 0.01 \text{ mm}^{-1}$ and $\mu_s' = 1.0 \text{ mm}^{-1}$. The voxel basis for reconstruction was $25 \times 25 \times 25$ pixels, and the initial guess of regularization parameter is 1. The convergence criteria was when the projection error changed by less than 0.01% between successive iterations or the maximum iteration number of $n = 10$ was reached. Fig. 7e–g show the CELSI tomography

reconstructed results from the 3 orthogonal views of the body interior, with reconstructed CELSI data in red. The FWHM value of the reconstructed CELSI image was $2.2 \times 2.2 \times 1.9 \text{ mm}^3$. Note that these dimensions were 7–8 times smaller than with planar imaging. Thus, the tumour could be located accurately for the larger injected concentration, and the recovered size was substantially smaller than that achieved with planar diffuse imaging, as is conventional for either epi-fluorescence or Cherenkov-excited luminescence imaging without a scanned source. For the lower-concentration tumour, the recovered regions were not visible above the noise level of the reconstructed image, illustrating that the detection threshold was between 0.4 and 0.1 nM of total contrast agent in the scan volume at these tumour depths. The individual mouse shown is representative of the image quality and recovery possible within this concentration range, with a rotating view of the 3D volume in Supplementary Video 1.

Rodent imaging for P_{O_2} sensing. A final murine experiment to map out P_{O_2} was carried out in mice with subcutaneous MDA-MB-231 tumours. A total of 4 animals and 8 tumours were imaged (2 tumours per animal), with local injections of $50 \mu\text{l}$ of $25 \mu\text{M}$ PtG4 (a total of 1.25 nmol per tumour). Each mouse was imaged while alive and then images were repeated 30 min after euthanasia, when the drop in blood circulation and respiration causes a marked decrease in P_{O_2} values. Temperature was controlled using a heating pad: $35.1 \pm 1.5^\circ\text{C}$ for live mice and $31.9 \pm 1.2^\circ\text{C}$ for dead mice. The CELSI scan was completed vertically (see Supplementary Video 2 for the experimental data capture). Images of the luminescence at different delay times between LINAC pulse and emission captured are shown in Fig. 8a. These were used for each mouse to create images of lifetime (Fig. 8b) and with the Stern-Volmer equation, the tissue P_{O_2} (Fig. 8c). The summary of total lifetimes and P_{O_2} values are shown in Fig. 8d,e, respectively, as box and whisker plots. The entire range of values in live or dead animals do not overlap, indicating a significant difference in both lifetime and P_{O_2} ($P < 0.001$ for each). But, more importantly, the range of values is $\pm 30\%$ in lifetime, and $\pm 40\%$ in P_{O_2} value, as would be expected in heterogeneous tumours.

Discussion

Optical imaging of tissue has the potential for retrieving large amounts of molecular information, but image recovery has been plagued by the scattering of light in tissue, which makes the signal nonlinear and affected by the shape of tissue, its optical properties and its layers and regions. In practice, the signal-to-noise ratio is often unacceptably low, and doesn't provide appreciable depth into the tissue. CELSI can use high-energy radiotherapy beams to launch light directly into the tissue, and by the knowledge of where the light was placed, it can allow high-resolution recovery of luminescent sources. Although this approach to imaging has been introduced in the past few years^{10,11}, the factors that dictate the performance have not been exhaustively analysed, and nonlinear tomography has not been applied to fully vet the imaging-contrast recovery and spatial resolution. In this study, these issues have been fully examined, and the capabilities of this type of imaging can now be established for P_{O_2} imaging of tumours. A steered beam that provides localization of the excitation has inherent value, as it allows avoiding organs at risk and multiplexing the beam to multiple animals or multiple tissue volumes. The geometrical demonstrations of scanning explored in this study form the basis of what can be done with a LINAC that is designed for highly conformal radiotherapy delivery.

The beam shape and angle of orientation have perhaps the largest effects on the signal, with larger beam shapes having substantially larger signals and resulting contrast-to-background ratio, as shown in Fig. 3d, presumably based on the fact that the light scatters and builds up within the tissue. Additionally, there is an output

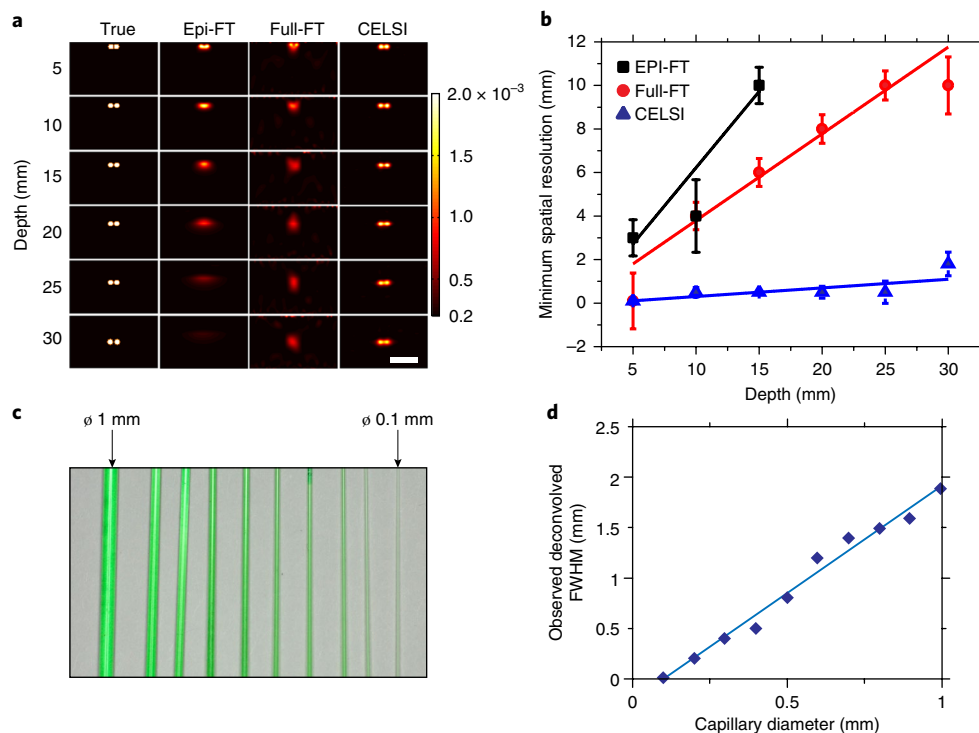


Fig. 6 | The spatial resolution of CELSI is below 1 mm down to depths in tissue of 25 mm. Simulated data for a pair of 5 mm diameter inclusions containing 50 μ M PtG4 with a fixed edge-to-edge distance, placed at increasing depths in a phantom. **a**, For each depth, data was reconstructed for epi-illumination fluorescence tomography, diffuse fluorescence tomography and CELSI tomography. Data of representative simulations are shown in units of luminescent yield, $\eta\mu_{si}$ (colour bar). Scale bar, 30 mm. **b**, The minimum resolvable distance between the two inclusions was estimated for each geometry and illustrate CELSI's near-linear resolution at depths of up to 30 mm. **c**, Capillaries, varying from 0.1 mm diameter up to 1.0 mm diameter, filled with 50 μ M of PtG4 were embedded into a tissue mimicking phantom. The phantoms were scanned using CELSI. **d**, The reconstructed data was used to extract the full-width-at-half-maximum (FWHM) value for each tube size. Each data point reports a single measurement, and fitting was completed with $r^2 > 0.9$.

factor for the beam that reduces with smaller beam sizes, and so while smaller or thinner beams provide the best spatial resolution (as shown in Fig. 3), they inherently provide the lower signal intensities as well. The direction of the beam relative to the camera is perhaps the second most important factor, as a separation of the source from the surface being imaged inherently improves the observed contrast by suppressing background signals from surface tissues (as illustrated in the images of Fig. 4). For these reasons, much of the work following these two initial studies focused on using the lateral beam geometry predominantly, and with a wide sheet of radiation, to maximize build-up and light irradiance in the tissue. It is this localization of the excitation beam that provides the inherent value of CELSI relative to isotope-based Cherenkov excitation studies^{16,23,24}. In isotope-based molecular sensing, the sensitivity can be as high, or even higher, right down to the sub-nanomole range, but the ability to reconstruct and localize the emission is not dictated by anything other than the detected emission. In CELSI imaging, the high-precision knowledge of the beam allows both deconvolution and depth-dependent attenuation correction, leaving a reconstructed signal that is highly localized in space to better than 1 mm accuracy throughout the imaged volume of tissue.

Testing the key performance factors beyond these initial choices leads to a complex array of possible parameters. The radiotherapy dose, the probe concentration and the depth into the tissue each contribute to the detected signal in ways that would have reciprocity, as illustrated in Fig. 4d. The imaging of luminescent targets is possible within the range of concentrations, doses and depths that are suitable for small-animal imaging. The molecule number ranges near μ M are typical for metabolites and higher concentration receptors, and the ability to resolve uptake within many millimetres of

tissue is an important application in preclinical imaging. Within the volume of excitation, this corresponds to sensitivity needed near μ mol to nmol levels. Radiation doses used here have been in the range of X-ray exams, so although the concept of using a linear accelerator for imaging appears dangerous from a radiation safety perspective, it is critical to appreciate that this is done with very a very low dose delivered. Additionally, the radiation dose is selectively deposited only where the scanned beam passes, so radiosensitive organs or dose-limiting volumes could be strategically avoided in an optimized scan.

A goal of this work has been to establish the feasibility of high spatial resolution several millimetres into animal tissue. The spatial resolution is largely dictated by the precision with which the X-ray beam can be controlled, because the signal origin can be localized to where the beam excited the luminescent agent. The imaging tests, both experimentally and computationally, support the belief that the spatial resolution is in the range of 100–300 μ m for objects as deep as 5 mm into the tissue. Computationally, this spatial resolution appears to be resolvable down to 20 mm depth, and this fundamental limit is a fascinating goal for deep-tissue imaging, as it essentially implies achieving near-microscopic resolution deep into tissue with optical imaging. This realization is fundamental in molecular sensing in deep tissue.

Finally, the tests used with mouse phantoms and mouse tumours demonstrate both the localization concepts and how the accuracy of reconstruction is superior to diffuse tomography and to superficial MIP images of luminescence. This latter comparison to superficial imaging is important, because the vast majority of preclinical luminescence imaging is done with epi-illumination box systems, where a single superficial surface image of the animal is obtained.

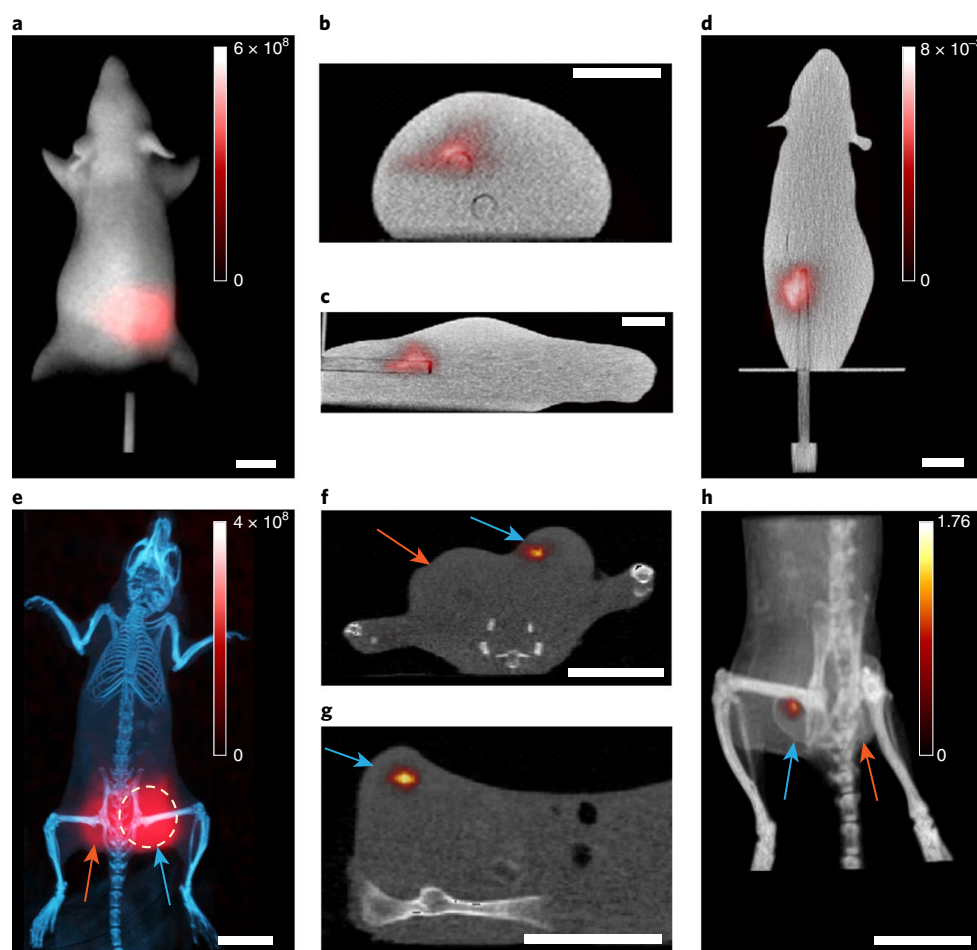


Fig. 7 | Animal phantom tomography and in vivo validation of the luminescence yield. **a**, Image for the luminescent yield of a $7\ \mu\text{l}$ inclusion placed within an animal phantom and overlaid on the surface extracted from the microCT image. Colour bar, photons $\text{cm}^{-2}\ \text{s}^{-1}$. **b-d**, CELSI reconstructed images are shown with three orthogonal views: axial (**b**), sagittal (**c**) and transverse (**d**). Colour bar, $\eta\mu_{\text{eff}}$. In vivo CELSI is shown from a single representative animal carrying two subcutaneous MDA-MB-231 tumours on the hindlimb flanks (arrows); $50\ \text{nmol}$ PtG4 was injected into the tumour indicated with a blue arrow, and $10\ \text{nmol}$ PtG4 was injected into the tumour with the orange arrow. The entire body of the animal was scanned and reconstructed with CELSI. **e**, An X-ray CT scan is overlaid to the summed intensity projection image of the luminescence. Colour bar, photons $\text{cm}^{-2}\ \text{s}^{-1}$. **f-h**, The reconstructions from the CELSI tomographic data are overlaid on the high resolution microCT images in axial (**f**), sagittal (**g**) and 3D perspective views (**h**). The reconstructed image shows recovery of the $50\ \text{nmol}$ injection while the $10\ \text{nmol}$ injection is not recovered; the data illustrate the detectable limit is in the range of tens of nanomoles. A full rotating 3D video of this mouse is available in Supplementary Video 7. Scale bars, 1 cm.

Being able to bring optical imaging to a significantly higher spatial resolution throughout the animal's whole body would have a profound impact in molecular imaging. The mouse phantom tested the potential of CELSI imaging in conditions matching the geometry, size and average tissue optical properties of a mouse, where the reconstruction of the embedded $7\ \mu\text{l}$ of PtG4 was found to be spatially accurate. CELSI imaging was then tested in the heterogeneous tissue conditions of a mouse in vivo, addressing the lack of realistic internal heterogeneities in the phantom. The more detailed CELSI images of tumour oxygenation shown in Fig. 8 illustrate how this method can be used to sense tumour P_{O_2} , and potentially with high spatial resolution. The features mapped out in this figure have sub-millimetre lateral spatial resolution, showing the heterogeneity of the P_{O_2} ranging from 40–90 mmHg, and confirms existing reported values for these tumours. The heterogeneity seen within intratumoural regions and between the tumours on the left and right flanks presumably illustrates areas of high and low P_{O_2} variation. Areas that are high P_{O_2} are thought to be closer to blood vessels whereas those with lower P_{O_2} are consistent with areas distal from blood supply. The ability to map P_{O_2} , pH and other features such as enzyme concentrations, protein expression, cell-receptor density or

metabolites would be valuable to understand responses to therapy. This methodology will be most important for molecular features at higher spatial resolution, where tumour heterogeneity plays an important factor in therapeutic response.

In molecular imaging, there can be a separation between the physical capabilities of the imaging system and the pharmacokinetics and localization of the biochemical targeting moiety. Yet, the value of a system is defined by the intersection of these two properties, where the physical resolution and contrast of the biochemical agent gets localized in biological features of the tissue. In the current realization of CELSI, the agents were delivered directly into solid tumours, avoiding the issue of plasma pharmacokinetics and tumour retention. As such, the chosen focus here has been largely technological development, combined with localized delivery of the agent to tumours. While there are clear limitations to this, the approach does still match with radiotherapy delivery as well, where the location of delivery is well planned as targeted to the treatment volume. As such, while the compound has its limitation at the site of injection, the knowledge of the oxygenation of these radiotherapy target sites is still of considerable value to radiation sensitization. Thus, we present the application

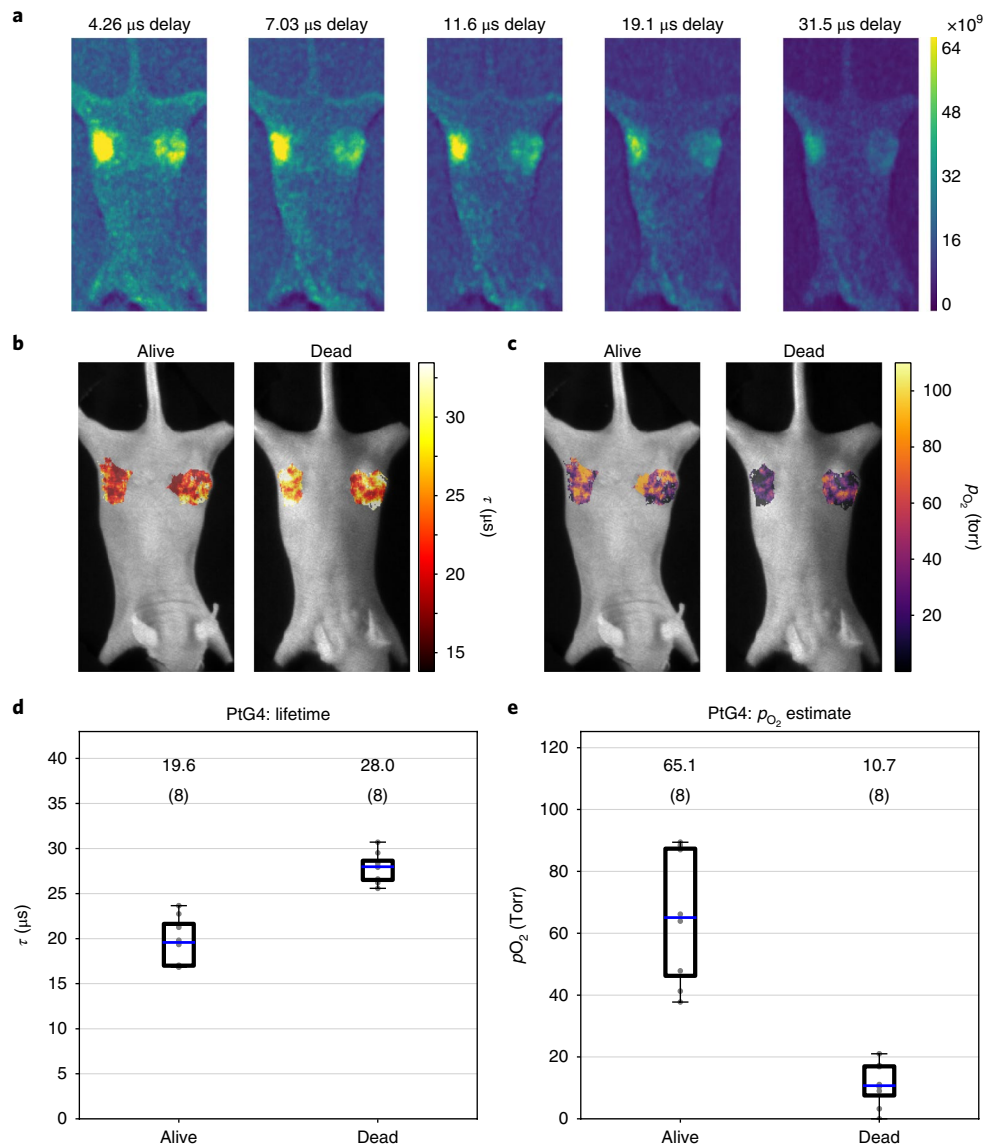


Fig. 8 | In vivo imaging of p_{O_2} in subcutaneous breast adenocarcinomas. **a**, Maximum intensity projection (MIP) images from CELSI acquisitions are shown with increasing time delays for nude mice with two MDA-MB-231 tumours growing on the hindlimb flank injected with 50 ml of 25 μ M PtG4 in each tumour. Colour bars, photons $\text{cm}^{-2} \text{s}^{-1}$. **b**, The pixel-wise lifetimes (τ) estimated alive and after euthanasia as a low- p_{O_2} control. **c**, Calculated p_{O_2} maps via the Stern-Volmer relationship. **d, e**, Box-plots show lifetime estimates (**d**) and the calculated p_{O_2} estimates for all tumours ($n=8$) (**e**). Measurement scans were acquired once for each animal, and the mean value is provided at the top of each box. A video of a single scan sequence is available in Supplementary Video 7.

of localized oxygen sensing with high-resolution CELSI in this format with clear potential to be further advanced by improvements in the biotargeting of luminescent reporters. Recent studies have examined multiple agents for Cherenkov-excited sensitivity with fluorescence^{14,20,25} and for the capability of detecting multiple emitters at the same time²⁶—yet in all of these studies, PtG4 has been shown to be the most sensitive probe in terms of lower limit on concentration. Also, with its design for oxygen sensitivity from quenching, which is accessed by measurement of emission lifetime, it also provides one of the most practical tools for radiation therapy, where tissue oxygenation is known to be an important factor in therapy efficacy. However, there is also potential for other lifetime phosphor sensing agents such as pH^{27,28}.

Outlook. Cherenkov-excited luminescence scanned imaging (CELSI) allows p_{O_2} imaging at a spatial resolution close to 0.1 mm, detected at

tissue depths of several millimetres through an intact living mouse, by using nanomolar levels of an oxygen-sensitive biological probe. X-ray beams from a linear accelerator are shaped into thin sheets to scan a field of view in arbitrary directions, and collect the Cherenkov emissions via time-gating of the captured luminescence, enabling molecular sampling of a number of agents relevant to the tissue microenvironment. The depths and signal recovery possible are suitable for applications using small-animal biomedical imaging models. Results from computer simulations and experimental studies suggest that, when fully automated, CELSI may have the highest sensitivity and spatial resolution of any preclinical whole-body molecular-imaging system.

Methods

LINAC and Cherenkov imaging. Cherenkov was induced by a linear accelerator (Varian Linac 2100CD, Varian Medical System) based at the Norris Cotton Cancer Center, at Dartmouth-Hitchcock Medical Center. The LINAC multi-leaf collimator

(MLC) provided high flexibility in shaping the output beam to make arbitrary-shaped treatment fields. Leaves are 5 mm wide in this LINAC and oriented in many long thin sheets that are controlled to move in and out of the output beam, and can be controlled to a level of 0.1 mm precision. The effect of beam shape on the contrast-to-background recovered acquisition was studied with radiation beam sizes using a larger square beam of $100 \times 100 \text{ mm}^2$, a thin sheet beam of $5 \times 100 \text{ mm}^2$ and a thin square pencil beam $5 \times 5 \text{ mm}^2$ with a vial of PtG4 of 5 μM in the phantom. CELSI of a capillary containing PtG4 500 μM was studied with radiation beam sizes of $40 \times 40 \text{ mm}^2$ (epi-illumination) and $5 \times 40 \text{ mm}^2$ (lateral illumination). Background was acquired with acquisition 500 μs trigger delay. Each of these were studied for epi-illumination imaging; the thin sheet beam was then also used for lateral sheet excitation for optimal contrast. To maximize signal and minimize background contribution, the room lights were switched off throughout these studies, and all lights in the room were masked off with black cloth and black tape, as shown in the photographs.

Luminescent reporter and tissue phantoms. NIR fluorescent phosphorescent probe PtG4 Oxyphor²⁷ was prepared in standard $1 \times \text{PBS}$ at 500 μM concentration. This reporter has a strong oxygen sensitivity as described in previous work^{13,14}, as well as emission of near-infrared wavelengths and excitation across the visible spectrum, matching Cherenkov excitation. Previous studies have examined the comparison of luminescence from phosphors and fluorophores form Cherenkov excitation, and in all studies, time-gated luminescence provides superior signal to noise, because of the superior background suppression provided by time-gating technology^{25,29,30}.

The tissue-simulating phantoms were prepared using 1% Intralipid (Fresenius Kabi). A capillary with 1 mm diameter of the probe at concentrations from 0.75 to 500 μM were placed inside the phantom at a depth that was varied between 2.5 to 20 mm from the phantom surface being imaged. To study the dose efficacy for CELSI, the capillary containing the solution of the probe was irradiated with doses which varied from 360 pulses (approximately 5 Gy) down to 1 pulse (approximately 1.4 cGy) at 500 μM concentration and 5 mm depth^{31–35}.

Luminescence imaging. The imaging system consisted of a time-gated intensified CCD camera (ICCD, PI-MAX4 1024i, Princeton Instruments), a commercial lens (Canon EF 135 mm f/2L USM) and a tripod for mounting the camera. The camera was focused on the imaging field approximately 1 m away. This distance was optimized through earlier studies where the signal-to-noise ratio was found optimal, by moving back from the field, to avoid too much backscatter-generated noise. The time-gated ICCD camera was synchronized to the radiation pulses (approximately of 3.25 μs duration, 360 Hz repetition rate) with the intensifier set as $\times 100$ and turned on at a 3.5 μs or 500 μs gate delay following each radiation pulse for phosphorescence or background measurement, and luminescence generated during 50 μs gate width was integrated via this ICCD. The luminescence emission images were originally captured in counts per pixel, as read from the camera. The background-subtracted images were then calibrated to photons $\text{mm}^{-2} \text{s}^{-1}$ by calibration of the number of photons detected per count, which was previously studied and found to be 95 counts read out at the CCD per one photon incident on the ICCD photocathode. Similarly, the camera has $13 \times 13 \text{ mm}^2$ pixels, and so this was converted from pixels to mm^2 .

Initial experiments focused on examining the contrast-to-background issue, using a single 1 mm inner diameter glass capillary tube (Hampton Research Corp, glass number 50 capillaries), filled with 500 μmol PtG4, and imaging with the LINAC vs camera in two different geometries, as shown in Fig. 3. In the vertical scan direction (also sometimes called epi-illumination geometry), where the LINAC and camera have the same perspective, higher background would be expected due to the high Cherenkov at the surface of the phantom, shown in Fig. 3c. When the LINAC beam was orthogonal to the camera direction, Cherenkov is not produced at the surface, and background would be expected to be lower as viewed by the camera, shown in Fig. 3d. These studies were carried out to experimentally verify this with a single capillary image.

Dose, concentration and depth. These are factors that affect contrast. The signal contrast in all imaging systems is a function of key parameters and so for CELSI it was hypothesized that these key factors would be linearly related to the radiation dose used, the concentration of probe present in the tissue, and the logarithm of the depth in which the target was located. The depth dependence on signal is likely to be more complex because of the light diffusion process, but might be expected to fall off over macroscopic distances with the effective attenuation coefficient of the medium, estimated by diffusion theory to be $\mu_{\text{eff}} = (3\mu_a\mu_s')^{1/2}$, where μ_a is the absorption coefficient and μ_s' is the transport scattering coefficient of the tissue. The dose delivered was varied by simple linear summation of the signal over more LINAC pulses, to effectively build up signal with delivered dose. The concentration of PtG4 was varied in solution within the embedded object, from 500 μM down to 0.78 μM using a 1 mm capillary present at 5 mm depth into the medium. The excitation volume of this was given by the overlap of the 5 mm beam with the 1 mm capillary, which was $V = \pi r^2 h = 3.9 \times 10^{-6} \text{ l}$.

The contrast-to-background ratio (CBR) was used as a metric of recovery success in this study, with the simple calculation defined by the ratio of the average intensity values: $\text{CBR} = (I_{\text{ROI}} - I_{\text{B}}) / I_{\text{B}}$, where I_{ROI} is the mean pixel intensity in the region of interest (ROI) and I_{B} is the mean pixel intensity in the background,

outside the ROI. In some studies, the contrast-to-noise ratio was used as a metric, which was defined as: $\text{CNR} = (I_{\text{ROI}} - I_{\text{B}}) / \sigma_{\text{B}}$, where σ_{B} was defined as the standard deviation of intensities in the background region.

Spatial resolution assessment. The spatial resolution of imaging was assessed with a range of glass capillary tubes of varying inner diameter, from 0.1 mm up to 1.0 mm (Hampton Research Corp, glass number 50 capillaries). These tubes were placed into tissue simulating phantom at 5 mm depth one by one, and all were filled with 50 μM PtG4 to provide a high contrast target for resolution assessment. The sheet radiation beam was scanned laterally across the tube, to vary the signal with position, and the linescan full width at half maximum (FWHM) was recovered for each capillary experiment.

Computed tomography recovery. CELSI data can be scanned for different beam angles and the performance expected varies considerably based on these choices. The range of options is so large that experimental study of these is prohibitive, and so a series of computer simulations were carried out, in particular to compare CELSI images to diffuse fluorescence tomography images where traditional light excitation is used as compared to Cherenkov excitation. Additionally, different combinations of scanning angles and different depths and sizes of objects could be simulated much more quickly than carrying out all the experiments. The computer simulations were carried out using the NIRFAST software package (available at www.nirfast.org), used to model light transport in tissue and carry out regularized iterative reconstruction of the luminescent reporter in the medium. The recovery of the reporter was in terms of units of luminescent yield, $\eta\mu_{\text{ab}}$, where η is the reporter quantum yield for phosphorescence emission and μ_{ab} is the absorption coefficient of the reporter (see the Supplementary Information for further explanation of the theory). This quantity is a direct report of the amount of light produced per unit volume. To assess spatial resolution of CELSI tomography, a classic resolution test was performed with two small inclusions and varying the spatial distance between them and assessing when they could not be resolved as separate objects. The edge-to-edge distance was varied from 0.1 mm to 5 mm, in the plausible range of limiting spatial resolutions given the physical constraints of the LINAC MLCs used. The yield contrast of inclusion was set as 10:1. A finer mesh with 6161 nodes and 12,000 linear triangular elements was used in reconstruction. Inspired by the results of combining of scan modes, the following reconstructions were performed by summing up scan modes.

Animal phantom imaging. In order to assess performance in a more complex tissue geometry, a commercially available mouse phantom was used (Xfm-2, PerkinElmer Health Sciences), using rod of material inserted which was filled with 1 mM PtG4, in 7 μl (7 nmol). This phantom has tissue optical properties within the NIR wavelengths 650–800 nm, approximated by $\mu_a = 0.003\text{--}0.008 \text{ mm}^{-1}$ and $\mu_s' = 1.5\text{--}0.9 \text{ mm}^{-1}$ (manufacturer-supplied data sheet). This phantom was created for phantom studies which would allow imaging in a realistic tissue volume and geometry that directly mimics the shape and absorption and reduced scattering coefficient values representative of murine tissue. The CELSI imaging was carried out with lateral beam excitation and vertically oriented emission capture, using a long lifetime gate on the camera, to sync out the Cherenkov light and noise, and maximize luminescence emission detection. X-ray tomography was completed on the IVIS Spectrum CT (PerkinElmer Inc) with the full field of view $120 \times 120 \times 30 \text{ mm}^3$, with a 150 μm voxel scan acquired in 90 s.

Tumour cell lines. MDA-MB-231 cells were purchased directly from ATCC as a confirmed cell type and mycoplasma free, no further testing was performed, and the cells lines are not listed in the ICLAC database of cross-contaminated or misidentified cell lines. Cells were grown in culture media in an incubator at 37°C in DMEM with 10% (v/v) fetal bovine serum (FBS) and 1% penicillin-streptomycin. When ready for use, cells were trypsonized, counted, spun down into a slurry, and used for inoculation into animals.

Animal studies. All animal procedures were approved by the Dartmouth Institutional Animal Care and Use Committee, and the studies here were carried out in compliance with these approved procedures. Nude female mice were purchased at 6 weeks of age from Charles River Labs. After a week of acclimatization, animals were used for injections of 10^5 cells under the skin on each flank of the mouse in individual 0.050 ml injections. After approximately 3 weeks of growth, when a tumour with an average of 6 mm diameter was observed on both flanks, the animals were then used for imaging studies. All mice were under general anaesthesia of inhaled isoflurane at 1.5% in flowing air through a nose cone throughout imaging. For the tomography study, to demonstrate the detection level, a total of 0.5 ml PtG4 was directly injected into the tumours of a mouse: 50 nmol concentration into one tumour and 10 nmol into the other. This animal was imaged by 3D CELSI tomography 30 min after injection, and then again imaged in the IVIS Spectrum CT system for X-ray tomography. The X-ray scan used 50 kVp standard 150 μm resolution imaging of the mouse in a $12 \times 12 \times 3 \text{ cm}^3$ field size. In further P_{O_2} imaging studies, 4 mice with a tumour in each flank (2 tumours per mouse, for $n = 8$ tumours) were used for imaging when the average dimension diameter was 6 mm as measured over the two orthogonal axes.

Statistical analysis. The differences between the live and dead conditions, as displayed in Fig. 8, with $n=8$ paired samples each, was established by a two-tailed Students t -test, with $\alpha=0.05$ and resulting $P<0.001$. These indicate that both in lifetime as well as P_{O_2} , there are significant differences between the values of the animals in the two conditions. However, more pertinent to the value of the study is the observation of the total range of values, presented as a percentage of the median value. Figure 8d,e was generated using Python 3.4.3 with the library matplotlib 2.0.0. The function used to make the box plot is called `boxplot`, available online (https://matplotlib.org/api/_as_gen/matplotlib.pyplot.boxplot.html). The box extends from the lower to the upper quartile values of the data, with a line at the median. The whiskers extend from the box to show the range of the data. Flier points are those past the end of the whiskers.

Reporting summary. Further information on experimental design is available in the Nature Research Reporting Summary linked to this article.

Code availability. Image-reconstruction code was custom developed for this study, and is available for download in bulk at www.nirfast.org. Individual MATLAB routines are available from the corresponding author upon request.

Data availability. The data that support the findings of this study are available within the paper and its Supplementary Information. Source datasets generated and analysed during the study are available from the corresponding author upon request.

Received: 15 July 2017; Accepted: 12 March 2018;

Published online: 13 April 2018

References

- Hoebe, R. A. et al. Controlled light-exposure microscopy reduces photobleaching and phototoxicity in fluorescence live-cell imaging. *Nat. Biotechnol.* **25**, 249–253 (2007).
- Brismar, H. & Ulfhake, B. Fluorescence lifetime measurements in confocal microscopy of neurons labeled with multiple fluorophores. *Nat. Biotechnol.* **15**, 373–377 (1997).
- Nie, S., Chiu, D. T. & Zare, R. N. Probing individual molecules with confocal fluorescence microscopy. *Science* **266**, 1018–1021 (1994).
- Zipfel, W. R. et al. Live tissue intrinsic emission microscopy using multiphoton-excited native fluorescence and second harmonic generation. *Proc. Natl Acad. Sci. USA* **100**, 7075–7080 (2003).
- Bjorn, S., Ntziachristos, V. & Schulz, R. Mesoscopic epifluorescence tomography: reconstruction of superficial and deep fluorescence in highly-scattering media. *Opt. Express* **18**, 8422–8429 (2010).
- Georgakoudi, I. et al. Fluorescence, reflectance, and light-scattering spectroscopy for evaluating dysplasia in patients with Barrett's esophagus. *Gastroenterology* **120**, 1620–1629 (2001).
- Mittapalli, R. K., Manda, V. K., Bohn, K. A., Adkins, C. E. & Lockman, P. R. Quantitative fluorescence microscopy provides high resolution imaging of passive diffusion and P-gp mediated efflux at the in vivo blood-brain barrier. *J. Neurosci. Methods* **219**, 188–195 (2013).
- Leblond, F., Davis, S. C., Valdes, P. A. & Pogue, B. W. Pre-clinical whole-body fluorescence imaging: review of instruments, methods and applications. *J. Photochem. Photobiol. B* **98**, 77–94 (2010).
- Pogue, B. W. Optics in the molecular imaging race. *Opt. Photon. News* **9**, 25–31 (2015).
- Zhang, R. et al. Cherenkov-excited luminescence scanned imaging. *Opt. Lett.* **40**, 827–830 (2015).
- Bruza, P. et al. Light sheet luminescence imaging with Cherenkov excitation in thick scattering media. *Opt. Lett.* **41**, 2986–2989 (2016).
- Chen, B. C. et al. Lattice light-sheet microscopy: imaging molecules to embryos at high spatiotemporal resolution. *Science* **346**, 1257998 (2014).
- Spencer, J. A. et al. Direct measurement of local oxygen concentration in the bone marrow of live animals. *Nature* **508**, 269–273 (2014).
- Zhang, R. et al. Oxygen tomography by Cherenkov-excited phosphorescence during external beam irradiation. *J. Biomed. Opt.* **18**, 50503 (2013).
- Dothager, R. S., Goiffon, R. J., Jackson, E., Harpstrite, S. & Piwnicki-Worms, D. Cherenkov radiation energy transfer (CRET) imaging: a novel method for optical imaging of PET isotopes in biological systems. *PLoS ONE* **5**, e13300 (2010).
- Thorek, D. L., Ogirala, A., Beattie, B. J. & Grimm, J. Quantitative imaging of disease signatures through radioactive decay signal conversion. *Nat. Med.* **19**, 1345–1350 (2013).
- Axelsson, J., Glaser, A. K., Gladstone, D. J. & Pogue, B. W. Quantitative Cherenkov emission spectroscopy for tissue oxygenation assessment. *Opt. Express* **20**, 5133–5142 (2012).
- Jarvis, L. A. et al. Cherenkov video imaging allows for the first visualization of radiation therapy in real time. *Int J. Radiat. Oncol. Biol. Phys.* **89**, 615–622 (2014).
- Axelsson, J., Davis, S., Gladstone, D. & Pogue, B. Cherenkov emission induced by external beam radiation stimulates molecular fluorescence. *Med. Phys.* **38**, 4127–4132 (2011).
- Demers, J. L., Davis, S. C., Zhang, R., Gladstone, D. J. & Pogue, B. W. Cherenkov excited fluorescence tomography using external beam radiation. *Opt. Lett.* **38**, 1364–1366 (2013).
- Keller, P. J., Schmidt, A. D., Wittbrodt, J. & Stelzer, E. H. Reconstruction of zebrafish early embryonic development by scanned light sheet microscopy. *Science* **322**, 1065–1069 (2008).
- Keereweer, S. et al. Image-guided surgery in head and neck cancer: current practice and future directions of optical imaging. *Head Neck* **34**, 120–126 (2012).
- Mitchell, G. S., Gill, R. K., Boucher, D. L., Li, C. & Cherry, S. R. In vivo Cherenkov luminescence imaging: a new tool for molecular imaging. *Phil. Trans. A Math. Phys. Eng. Sci.* **369**, 4605–4619 (2011).
- Das, S., Thorek, D. L. & Grimm, J. Cherenkov imaging. *Adv. Cancer Res* **124**, 213–234 (2014).
- Lin, H. et al. Comparison of Cherenkov excited fluorescence and phosphorescence molecular sensing from tissue with external beam irradiation. *Phys. Med Biol.* **61**, 3955–3968 (2016).
- Dsouza, A. et al. Cherenkov-excited multi-fluorophore sensing in tissue-simulating phantoms and in vivo. *Radiat. Res.* (in the press).
- Esipova, T. V. et al. Two new “protected” oxyphors for biological oximetry: properties and application in tumor imaging. *Anal. Chem.* **83**, 8756–8765 (2011).
- Czupryna, J. et al. Cherenkov-specific contrast agents for detection of pH in vivo. *J. Nucl. Med.* **56**, 483–488 (2015).
- Holt, R. W. et al. Cherenkov excited phosphorescence-based pO₂ estimation during multi-beam radiation therapy: phantom and simulation studies. *Phys. Med Biol.* **59**, 5317–5328 (2014).
- Zhang, R. et al. Cherenkov radiation emission and excited luminescence (CREL) sensitivity during external beam radiation therapy: Monte Carlo and tissue oxygenation phantom studies. *Biomed. Opt. Express* **3**, 2381–2394 (2012).
- Lehmann, S. et al. In vivo fluorescence imaging of the activity of CEA TCB, a novel T-cell bispecific antibody, reveals highly specific tumor targeting and fast induction of T-cell-mediated tumor killing. *Clin. Cancer Res.* **22**, 4417–4427 (2016).
- Tang, Q. et al. Depth-resolved imaging of colon tumor using optical coherence tomography and fluorescence laminar optical tomography. *Biomed. Opt. Express* **7**, 5218–5232 (2016).
- Kepshire, D. S. et al. Imaging of glioma tumor with endogenous fluorescence tomography. *J. Biomed. Opt.* **14**, 030501 (2009).
- Dehghani, H. et al. Near infrared optical tomography using NIRFAST: Algorithm for numerical model and image reconstruction. *Commun. Numer. Methods Eng.* **25**, 711–732 (2008).
- Jermyn, M. et al. Fast segmentation and high-quality three-dimensional volume mesh creation from medical images for diffuse optical tomography. *J. Biomed. Opt.* **18**, 86007 (2013).

Acknowledgements

This work has been funded by the Congressionally Directed Medical Research Program for Breast Cancer Research Program, US Army USAMRAA contract W81XWH-16-1-0004 and National Institutes of Health research grants R01 EB024498 and R01 EB018464.

Author contributions

B.W.P. conceived the study, supervised all aspects of the work and drafted the manuscript; J.F., H.L., P.B., E.P.L., R.Z. and J.R.S. each completed measurements and data analysis as well as designed the experiments, wrote initial parts of the manuscript, and edited the entire manuscript. H.D. and S.C.D. helped design and analyse the tomography work with J.F., and each edited the manuscript. S.A.V. provided the molecular probe, provided advice on experimental design and data analysis and edited the manuscript. D.J.G. and L.A.J. each contributed advice on radiotherapy design and data interpretation, as well as edited the manuscript.

Competing interests

The authors declare no competing interests.

Additional information

Supplementary information is available for this paper at <https://doi.org/10.1038/s41551-018-0220-3>.

Reprints and permissions information is available at www.nature.com/reprints.

Correspondence and requests for materials should be addressed to B.W.P.

Publisher's note: Springer Nature remains neutral with regard to jurisdictional claims in published maps and institutional affiliations.

Reporting Summary

Nature Research wishes to improve the reproducibility of the work that we publish. This form provides structure for consistency and transparency in reporting. For further information on Nature Research policies, see [Authors & Referees](#) and the [Editorial Policy Checklist](#).

Statistical parameters

When statistical analyses are reported, confirm that the following items are present in the relevant location (e.g. figure legend, table legend, main text, or Methods section).

n/a Confirmed

- The exact sample size (n) for each experimental group/condition, given as a discrete number and unit of measurement
- An indication of whether measurements were taken from distinct samples or whether the same sample was measured repeatedly
- The statistical test(s) used AND whether they are one- or two-sided
Only common tests should be described solely by name; describe more complex techniques in the Methods section.
- A description of all covariates tested
- A description of any assumptions or corrections, such as tests of normality and adjustment for multiple comparisons
- A full description of the statistics including central tendency (e.g. means) or other basic estimates (e.g. regression coefficient) AND variation (e.g. standard deviation) or associated estimates of uncertainty (e.g. confidence intervals)
- For null hypothesis testing, the test statistic (e.g. F , t , r) with confidence intervals, effect sizes, degrees of freedom and P value noted
Give P values as exact values whenever suitable.
- For Bayesian analysis, information on the choice of priors and Markov chain Monte Carlo settings
- For hierarchical and complex designs, identification of the appropriate level for tests and full reporting of outcomes
- Estimates of effect sizes (e.g. Cohen's d , Pearson's r), indicating how they were calculated
- Clearly defined error bars
State explicitly what error bars represent (e.g. SD, SE, CI)

Our web collection on [statistics for biologists](#) may be useful.

Software and code

Policy information about [availability of computer code](#)

Data collection

n/a

Data analysis

Image reconstruction code was custom developed for this study, and is available for download in bulk through our website www.nirfast.org, and individual MATLAB routines are available from the corresponding author. Public shareware Python code was used for plotting of the box plots, as well as for the students t-test, as described in the methods section.

For manuscripts utilizing custom algorithms or software that are central to the research but not yet described in published literature, software must be made available to editors/reviewers upon request. We strongly encourage code deposition in a community repository (e.g. GitHub). See the Nature Research [guidelines for submitting code & software](#) for further information.

Data

Policy information about [availability of data](#)

All manuscripts must include a [data availability statement](#). This statement should provide the following information, where applicable:

- Accession codes, unique identifiers, or web links for publicly available datasets
- A list of figures that have associated raw data
- A description of any restrictions on data availability

Datasets generated and analyzed during the current study are available from the corresponding author upon email request. All data generated or analyzed during this study are included in this published article (and its supplementary information files).

Field-specific reporting

Please select the best fit for your research. If you are not sure, read the appropriate sections before making your selection.

Life sciences Behavioural & social sciences

For a reference copy of the document with all sections, see [nature.com/authors/policies/ReportingSummary-flat.pdf](https://www.nature.com/authors/policies/ReportingSummary-flat.pdf)

Life sciences

Study design

All studies must disclose on these points even when the disclosure is negative.

Sample size	The sample sizes were determined based upon the preliminary variance in the measurements of pO ₂ and secondarily lifetime, and the goal of detecting a difference in the tumors when the animals were awake oxygenated versus after death. The change in pO ₂ was expected to be about 40 mmHg and the variance expected to be about 20 mmHg, which for student's t-test predicts a sample size near 6 for an alpha of 0.05 and a power of 0.9. In this study, a sample of 4 mice were used with 2 tumors each, for a total sample of 8. This was thought to be sufficient to test the hypothesis that the sample of pO ₂ in living vs dead mice was significantly measured.
Data exclusions	No data were excluded in this study.
Replication	Replication number of all studies is explicitly described in each figure caption. In basic studies where the variance was very low compared to the signal, repeated measures were not used (such as in phantom data with high concentrations). However in selected experiments where variation was significant compared to the mean value, up to 3 repeated measures were taken. Each experiment has a description of the number of measurements in the figure legend.
Randomization	Randomization was not used, since there was not more than one arm of animals used.
Blinding	Blinding was not used, since this was a pilot study of a new technology, and there was not more than one arm of animals used.

Materials & experimental systems

Policy information about [availability of materials](#)

n/a	Involved in the study
<input checked="" type="checkbox"/>	<input type="checkbox"/> Unique materials
<input checked="" type="checkbox"/>	<input type="checkbox"/> Antibodies
<input type="checkbox"/>	<input checked="" type="checkbox"/> Eukaryotic cell lines
<input type="checkbox"/>	<input type="checkbox"/> Research animals
<input type="checkbox"/>	<input type="checkbox"/> Human research participants

Eukaryotic cell lines

Policy information about [cell lines](#)

Cell line source(s)	ATCC
Authentication	the cells came authenticated from ATCC and grown from sterile culture directly for these experiments.
Mycoplasma contamination	the cells lines were confirmed mycoplasma free from ATCC, and no further testing was done from the cell culture samples.
Commonly misidentified lines (See ICLAC register)	the cells lines are not listed in the ICLAC database of cross-contaminated or misidentified cell lines, and so we did no further testing or analysis of this.

Research animals

Policy information about [studies involving animals](#); [ARRIVE guidelines](#) recommended for reporting animal research

Animals/animal-derived materials

Female, nude mice were used, purchased from Charles River Labs, at 6 weeks of age. Mice were acclimatized for 1 week prior to use, and the inoculated with MDA-MB-231 tumor cells at 10^5 cells in a 50 μ L injection in both flanks. When the tumors were an average diameter of 6mm, they were used for imaging experiments. Animals were sacrificed immediately after imaging, and no further tissue analysis was done.

Human research participants

Policy information about [studies involving human research participants](#)

Population characteristics

n/a

Method-specific reporting

- | n/a | Involvement in the study |
|-------------------------------------|---|
| <input checked="" type="checkbox"/> | <input type="checkbox"/> ChIP-seq |
| <input checked="" type="checkbox"/> | <input type="checkbox"/> Flow cytometry |
| <input checked="" type="checkbox"/> | <input type="checkbox"/> Magnetic resonance imaging |



Optics Letters

Tomographic Cherenkov-excited luminescence scanned imaging with multiple pinhole beams recovered via back-projection reconstruction

MENGYU J. JIA,^{1,3}  XU CAO,¹  JASON R. GUNN,¹ PETR BRUZA,¹ SHUDONG JIANG,¹ AND BRIAN W. POGUE^{1,2} 

¹Thayer School of Engineering, Dartmouth College, Hanover, New Hampshire 03755, USA

²e-mail: brian.w.pogue@dartmouth.edu

³e-mail: jeremy18@stanford.edu

Received 13 December 2018; revised 15 February 2019; accepted 16 February 2019; posted 21 February 2019 (Doc. ID 355312); published 19 March 2019

Cherenkov-excited luminescence scanned imaging (CELSI) is achieved with a clinical linear accelerator during external beam radiotherapy to map out molecular luminescence intensity or lifetime in tissue. In order to realize a deeper imaging depth with a reasonable spatial resolution in CELSI, we optimized the original scanning procedure to complete this in a way similar to x-ray computed tomography and with image reconstruction from maximum-likelihood expectation maximization and multi-pinhole irradiation for parallelization. Resolution phantom studies showed that a 0.3 mm diameter capillary tube containing 0.01 nM luminescent nanospheres could be recognized at a depth of 21 mm into tissue-like media. Small animal imaging with a 1 mm diameter cylindrical target demonstrated that fast 3D data acquisition can be achieved by this multi-pinhole collimator approach to image high-resolution luminescence through a whole animal. © 2019 Optical Society of America

<https://doi.org/10.1364/OL.44.001552>

Cherenkov-excited luminescence scanned imaging (CELSI) uses the collimating system of a radiotherapy linear accelerator (LINAC) to send a sheet of radiation traveling across the imaged subject in a manner equivalent to the excitation-beam shaping used in light-sheet microscopy [1,2]. In CELSI, luminescence and Cherenkov images can be acquired in the same view for molecular and anatomical imaging, respectively, but with different pulse delay and integration time. By restricting the x-ray excitation to a single, narrow sheet, the origin of the optical photons can be inferred regardless of where these photons were detected, or how many times they scattered in tissue. Depth information for estimating intensity attenuation and emission diffuseness can be obtained according to the distance from the medium surface, which can be calculated from the recovered Cherenkov images. Previous demonstrations of CELSI showed that superb spatial resolution on the order of 100 micrometers can be achieved within a depth of 5 mm. In this

Letter, a novel image modality named tomographic CELSI (T-CELSI) was proposed to take advantage of the CELSI as combined with computed tomography (CT) algorithms.

X-ray luminescence CT (XLCT) has been demonstrated with tomographic x-rays stimulating luminescence emissions with linear reconstruction [3], using continuous diagnostic kV energy x-ray photons, below the Cherenkov threshold, allowing for direct excitation of nanoparticulate contrast agents via the photoelectric effect and optical emission from radioluminescence. In XLCT, tomographic data are generated by irradiating the object in a CT scanning method, where a sequence of programmed x-ray beams is systematically projected at each position and beam angle. Since measured photons are created somewhere on the narrow path of the x-ray beam along different beam directions, the optical sensor is not required to spatially resolve photons. Instead, all the pixels can be summed up to obtain a higher signal-to-noise ratio (SNR), as has been demonstrated in CELSI. By arranging an x-ray detector at a position orthogonal to the optical detector, anatomical imaging is performed simultaneously with molecular imaging via standard x-ray CT. Then the co-registered anatomical images with extra auxiliary-like fiducial points can be used to extract depth information for the tomographic algorithm.

In the proposed T-CELSI method demonstrated here, the design to optimize this was as follows: (1) a single-pixel camera concept was introduced to increase imaging depth via better integrated signal strength; (2) boundary information for estimating target depth was obtained from Cherenkov images at each incident beam location, which could perfectly match the time-delayed luminescence data without any need for co-registration; and (3) based on a standard LINAC, the x-ray beam sequence and multiple projections were realized with multi-leaf collimator (MLC) and gantry movement, respectively.

In T-CELSI imaging, selective pulsed x-ray beams were emitted from a LINAC (Varian Clinac 2100 CD, Varian Medical Systems, USA), with parameter settings as follows: photon energy of 6 MV, dose rate of 600 monitor units per minute, and a fixed repetition rate of 360 Hz. As shown in

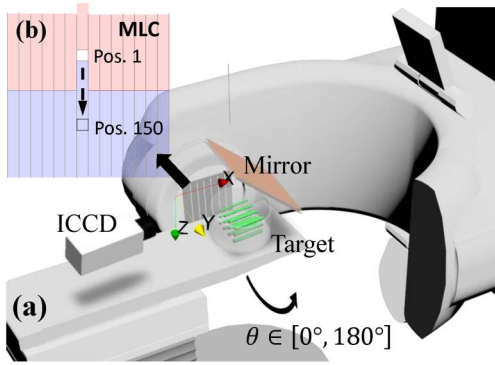


Fig. 1. (a) Measurement geometry for tomographic CELSI. At each gantry position, scanning beams are generated by the programmable MLC (b).

Fig. 1, a $1 \times 1 \text{ mm}^2$ square beam was raster scanned with the MLC, and the emitted optical photons on the top surface were imaged by an intensified time-gated camera (C-Dose, Dose Optics, Lebanon, New Hampshire) worked with a focal length of 50 mm and $f/1.2$ lens. The ICCD was time-gated for Cherenkov acquisition with no pulse delay and a $3.5 \mu\text{s}$ integration time to capture just during the LINAC pulse, and then for luminescence detection with a $4.26 \mu\text{s}$ delay from the LINAC pulse and $100 \mu\text{s}$ integration time. Of note, the camera worked in a single-pixel mode. Europium chelate microspheres (Bangs Laboratories, Inc.) were used as nanophosphors, which had $0.3 \mu\text{m}$ diameter, broadband UV excitation and peaked 605–625 nm emission, and approximately 2000 μs lifetime. These particles can be made biocompatible with coating and ultimately functionalized with binding proteins for molecular imaging applications. Half-angle projection images were obtained with $\theta \in [0^\circ, 180^\circ]$ and a step of 5° , i.e., 37 angular positions. The acquisition time for each projection was 20 s for a total approximate dose of 2 Gy. Squared beams were continuously scanned without stops to save time, and 135 ms was assumed as an exposure time leading total scanning/radial positions of 150. All the phantoms or the mouse were placed at the LINAC isocenter.

In the T-CELSI system, x-rays travel through the tissues with the expected secondary electron buildup over the first 1.5 cm typically for a beam energy of 6 MV [4], followed by decay for deeper depths, and this electron dose induces Cherenkov light that secondly excites the nanophosphors. Image reconstructions were twofold involving: (1) a standard maximum-likelihood expectation-maximization (ML-EM) method in x-ray CT was used to recover Cherenkov light distribution, as it is seldom scattered [5]; and (2) a modified ML-EM (mML-EM) was designed to solve luminescent concentration $\rho(\mathbf{r})$ at position \mathbf{r} . Here, the k -th ($k \geq 0$) updated $\rho^{(k)}(\mathbf{r})$ on y - z slice [i.e., $\mathbf{r} = (y, z)$] is given as follows:

$$\rho^{(k+1)}(\mathbf{r}) = \frac{\rho^{(k)}(\mathbf{r})}{\mathcal{R}^*[\bar{\Gamma}]} \mathcal{R}^* \left[\frac{\Gamma_{\text{meas.}}(y, \theta)}{\Gamma^{(k)}(y, \theta)} \right], \quad (1)$$

where $\mathcal{R}^*[\cdot]$ represents the inverse radon transform (IRT); $\Gamma_{\text{meas.}}$ or Γ is the emission light intensity measured or predicted at the top surface; and $\bar{\Gamma}$ is an all-ones vector with the same as Γ or $\Gamma_{\text{meas.}}$, which is used to normalize $\rho^{(k)}(\mathbf{r})$. Here, $\rho^{(0)}(\mathbf{r})$ is assumed to be an all-ones matrix. Note that the $\Gamma(y, \theta)$ image

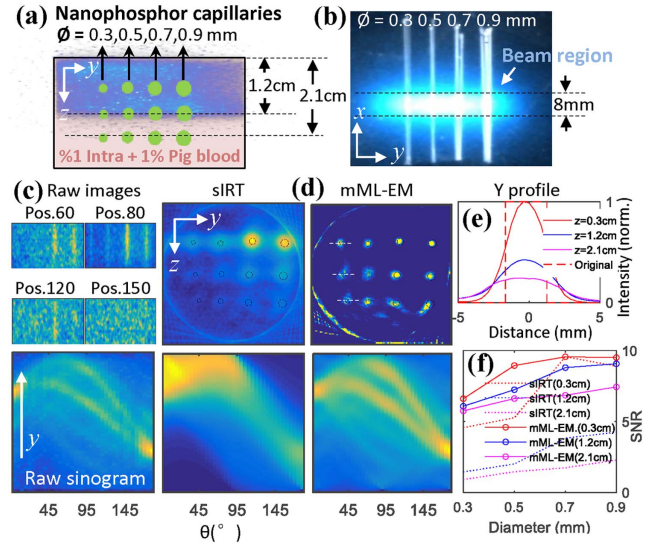


Fig. 2. Resolution phantom imaging. (a) y - z view of a cylindrical tank as shown in Fig. 1(a) incorporated with capillaries of different diameters and overlaid with a recovered Cherenkov image. (b) x - y view of the capillaries photograph, merged with a Cherenkov image to indicate the x-ray beam region. (c) Exemplary raw images at several radial positions with 0° projection, and the raw sinogram. (d) Recovered targets and associated sinograms via sIRT and mML-EM algorithms. (e) y profiles plotted along the dashed white lines in (d), and (f) contrast-to-background ratios for different capillary sizes and target depths.

is actually a sinogram as exemplified in Fig. 2(c), where the number of y positions is the same as that of the MLC scanned squares. Equation (1) can be interpreted with the ML-EM principle as [5]: the back-projection of the ratio between $\Gamma_{\text{meas.}}$ and Γ is used as a multiplicative coefficient to update $\rho(\mathbf{r})$. Here, the forward solution of emission light intensity Γ measured at the top surface under a specified gantry angle is calculated by

$$\begin{cases} P(z, \theta) = e^{-\mu_{\text{eff}}(z-z_{\text{max}})} / (f(\theta) + z)^2, \\ Q^{(k)}(\mathbf{r}, \theta) = \eta P(z, \theta) \rho^{(k)}(\mathbf{r}), \\ \Gamma^{(k)}(y, \theta) = Q^{(k)}(\mathbf{r}, \theta) \otimes G(\mathbf{r}, y), \end{cases} \quad (2)$$

where f is the source-to-surface distance (SSD); z_{max} represents the depth of the maximum value of relative absorbed dose P [6]; μ_{eff} is the effective x-ray linear attenuation coefficient for the primary beam inside the medium; $Q(\mathbf{r})$ is the source term; η is the emission quantum yield ratio between x ray and luminescence light; \otimes is the convolution operator; and $G(\mathbf{r}, \varepsilon)$ are the system Green functions for luminescence light transport, which was calculated for a diffusion equation combined with a Robin-type boundary condition [7]. Any other modeling for photon transport in tissue could be used to solve $Q(\mathbf{r}) \otimes G(\mathbf{r}, \varepsilon)$, e.g., the Monte Carlo method. Since the Cherenkov and luminescence images were detected by the same camera but with different time delays, these two images can be co-registered well and the Cherenkov-extracted surface was used to estimate the z distance from the reconstructed target.

A resolution phantom was designed to investigate the influence of lesion size on detectability. As shown in Fig. 2(a), four cylindrical capillaries, with diameter 0.3 mm, 0.5 mm, 0.7 mm, and 0.9 mm, were filled with phosphor concentrations of

0.01 nM and embedded at depths of 0.3 cm, 1.2 cm, and 2.1 cm inside the tissue-mimicking phantom, which was %1 porcine blood mixed (Lamphire Inc., Pipersville, PA) with 1% Intralipid (dilute from 10% Intralipid, Sigma-Aldrich). As a validation of using Cherenkov signal to locate the medium boundary, the reconstructed Cherenkov y - z slice is overlaid in Fig. 2(a). An x - y view of a Cherenkov maximal intensity projection (MIP) image at 90° beam projection (i.e., when the collimator is opposite to the detector) is shown in Fig. 2(b), merged with unfilled phantom under roomlight. Caused by diffusion and divergent x-ray irradiation from the LINAC collimator, the beam band covering 90% intensity maximum has a width of 8 mm, much larger than the original 1 mm. The raw image captured for four radial positions at 0° projection is shown in Fig. 2(c), as well as the raw sinusoidal trajectories of the 12 cylinders. Based on the raw sinogram, reconstructions via a standard IRT (sIRT) method and the mML-EM with 50 iterations are compared, and the recovered $\rho(\mathbf{r})$ and $\Gamma(y, \theta)$ are shown in the upper and bottom lines in Fig. 2(d), respectively. For those 0.3 mm diameter capillaries, y profiles along the dashed white lines in (d) are shown in Fig. 2(e). SNRs for all recovered 12 targets via sIRT and mML-EM methods are plotted in Fig. 3(f).

A sensitivity phantom was imaged to assess the minimum detectable nanophosphor distribution for different target depths. Three 0.7 mm diameter cylinders were filled with nanophosphor concentrations of 0.005 nM, 0.01 nM, and 0.05 nM and embedded at depths of 1 cm, 2 cm, and 3 cm, as shown in Fig. 3(a). To further improve data acquisition efficiency, half of the original projections (i.e., 19 angles and $\theta \in [0^\circ, 90^\circ]$) were adopted to generate the raw sinogram as a proof of concept. Reconstructed results are present in Fig. 3(b), and the calculated SNRs against target depths are depicted in Fig. 3(c). Then SNRs were averaged (SNR) over different depths, and their relation to concentration is plotted in Fig. 3(d).

For *in vivo* imaging, all animal procedures were approved by the Dartmouth Institutional Animal Care and Use Committee, and the studies were carried out in compliance with these approved procedures. Nude female mice were purchased at 6 weeks of age from Charles River Labs. To evaluate the performance of the proposed method, we implanted a transparent

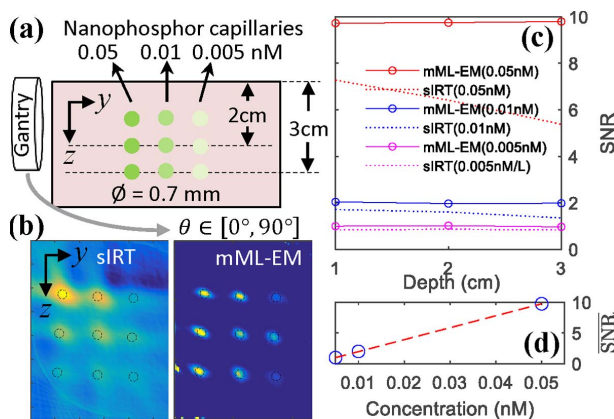


Fig. 3. Sensitivity phantom imaging: (a) geometry sketch of the phantoms, (b) reconstructed results via sIRT and mML-EM methods, (c) resultant contrast-to-background ratio curves, and (d) averaged SNR versus concentrations of europium.

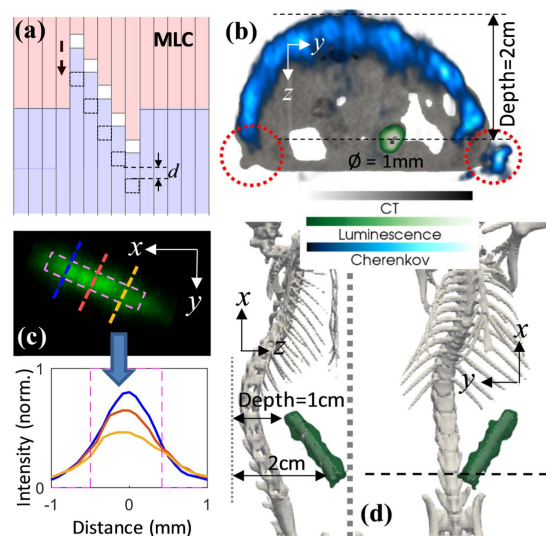


Fig. 4. 3D *in vivo* T-CELSI imaging demonstration of a 1 mm diameter tube loaded with nanophosphors: (a) detailed multi-hole irradiation design from the linac MLC, (b) Cherenkov, luminescence, and CT overlay axial images sliced along the dashed black line in (d), (c) luminescence MIP image on the x - y plane, and (d) merged luminescence and CT images for sagittal and coronal planes.

tube (inner diameter 1.0 mm) at a depth ranging from 1 cm to 2 cm, which was filled with the nanophosphors at a concentration of 1.1 nM, into the body of the mouse near the liver inside the peritoneal cavity.

In order to 3D render the luminescent target, a multi-pinhole collimator was designed to provide the complete data necessary, as exemplified in Fig. 4(a). Different from the multi-pinhole XLCT [8–10], no extra beam shaping appliance is requisite. The measurement geometry is shown in Fig. 1 with 37 angular positions. By making use of the MLC control, an array of multiple pinholes could be moved vertically in parallel. For this 3D scenario, there was a cluster of raw sinograms depending on the number of pinholes used, and each pixel was the sum of several lined values (depending on the size of the squared beam) of the raw image. A 3D image was achieved by stacking all the 2D reconstructed results along x direction. Figure 4(b) shows the recovered cross section of merged luminescence, Cherenkov, and a CT image, which was obtained from a commercial imager (IVIS SpectrumCT, PerkinElmer, USA) with source voltage 50 kVp and current of 1 mA. We can see that the glass-made tube recovered with T-CELSI shows good agreement with that from CT. The tube can be found with an ellipse shape due to the off-axis placement, and some white areas inside the body are thought to be air in the digestive tract. The luminescence MIP on the x - y plane is shown at the top in Fig. 4(c), where the dashed box indicates the original position, and profiles along the colored dashed lines in (c) are plotted at the bottom with full width half maxima (FWHMs) of 1.0 mm (blue), 1.1 cm (red), and 1.3 cm (yellow). Differences among these profiles are caused by different imaging depths: 1 cm (blue), 1.5 cm (red), and 2 cm (yellow), as indicated in Fig. 4(d).

Similar to CELSI, the whole measurement geometry in T-CELSI relies on a radiotherapy LINAC, which can provide a pathway for specified molecular sensing during external beam

radiation therapy, since sophisticated dynamic trajectories involving gantry and MLC motions can always be found in most modern radiation treatment plans, e.g., intensity modulated radiation therapy (IMRT), and stereotactic body radiation therapy (SBRT). However, T-CELSI maintains higher resolution and molecular sensitivity at significant depths inside tissue. As exemplified in Fig. 2(c), only the superficial targets can be clearly recognized, as numbered with position 80. As a result, stacking these noisy images for a 3D rendering as in CELSI can be challenging. In comparison, each pixel in the sinogram in Fig. 2(c) is a sum of the corresponding raw image, which greatly enhances the measurement SNR in T-CELSI. Other specific denoising strategies on low-dose CT can also be employed [11,12].

In T-CELSI, Cherenkov images were used to provide anatomy information for image reconstruction. We can see in Figs. 2(a) and 4(b) that the outline of Cherenkov distribution matches well with the target surface toward the camera. Compared to the CT-based prior information in XLCT, Cherenkov images can be better matched with luminescence ones without delicate co-registration. Limited by a fixed view ranging to 180° with one mirror, some surface places might not be visible in extreme cases, e.g., the portions much closer to the bench, as circled in Fig. 4(b). For those cases, a smooth interpolated connection for a complete boundary is reasonable for most tissue applications. An alternative is to use sufficient mirrors or cameras.

Because the Cherenkov and luminescence beams are both attenuated and diffused while traversing the sample, the sinogram is not perfectly symmetrical, which is why it is preferable to perform a full 360° scan. For practical purposes, acquisition time or radiation dose should be optimized. As a preliminary trial, reconstruction based on half (180°) and quarter (90°) projection ranges were discussed. The reconstruction performance clearly depended upon the angular positions used, and thus only the most promising choices of angles are shown here. In addition, a full 3D visualization was demonstrated with a multi-pinhole illumination to achieve the same detection efficiency as a 2D process, as shown in Fig. 4(a). To save x resolution, the gap distance d was set to 1 cm to circumvent a crosstalk effect between beams. However, limited by the MLC mechanical size, the x resolution was inherently lower than the y or z resolution, depending on the squared scanning interval. By taking advantage of flexible patterning with MLC, further accelerated acquisition can be achieved by irradiating multiple point lines for 3D imaging in a way similar to the coded CELSI [13]. Other algorithms fairly developed for sparse view XLCT or CT can be borrowed in T-CELSI [14–16].

In comparison to traditional fluorescence molecular tomography (FMT) [17], fluorophore positions can always be accurately recovered in T-CELSI. As exemplified in Fig. 2(d), the geometric centers of the targets agree well with the real ones, regardless of reconstruction methods. This is attributed to the narrow x-ray beam, and thus the target can be localized accurately with a back-projection algorithm. By bringing an optical tomography technique to the ML-EM framework, reconstructions of target intensity can basically get rid of depth dependence (reconstructed signal via mML-EM varied by $<3\%$ when the depth changed from 1 cm to 3 cm), which was quantized with SNR as plotted in Figs. 2(f) and 3(c). After correction, an approximated linear relationship was found between SNR and nanophosphor concentration, as shown in Fig. 3(d).

Funding. National Institutes of Health (NIH) (R01 EB024498); Congressionally Directed Medical Research Programs (CDMRP) (W81XWH-16-1-0004).

REFERENCES

1. P. Brůža, H. Lin, S. A. Vinogradov, L. A. Jarvis, D. J. Gladstone, and B. W. Pogue, *Opt. Lett.* **41**, 2986 (2016).
2. B. W. Pogue, J. Feng, E. P. LaRochelle, P. Bruža, H. Lin, R. Zhang, J. R. Shell, H. Dehghani, S. C. Davis, S. A. Vinogradov, and D. J. Gladstone, *Nat. Biomed. Eng.* **2**, 254 (2018).
3. G. Prax, C. M. Carpenter, C. Sun, and L. Xing, *IEEE Trans. Med. Imag.* **29**, 1992 (2010).
4. G. Kragl, S. Wetterstedt, B. Knausl, M. Lind, P. McCavana, T. Knoos, B. McClean, and D. Georg, *Radiother. Oncol.* **93**, 141 (2009).
5. G. J. Hine and G. L. Brownell, *Radiation Dosimetry* (Elsevier, 2013).
6. J. Ripoll, M. Nieto-Vesperinas, R. Weissleder, and V. Ntziachristos, *Opt. Lett.* **27**, 527 (2002).
7. L. A. Shepp and Y. Vardi, *IEEE Trans. Med. Imag.* **1**, 113 (1982).
8. W. Zhang, D. Zhu, M. Lun, and C. Li, *Biomed. Opt. Express* **7**, 2506 (2016).
9. S. Tzoumas, D. Vernekohl, and X. Lei, *IEEE Trans. Biomed. Eng.* **65**, 1892 (2018).
10. T. Sasaya, N. Sunaguchi, S. J. Seo, K. Hyodo, T. Zeniya, J. K. Kim, and T. Yuasa, *Nucl. Instrum. Methods Phys. Res. A* **886**, 71 (2018).
11. J. Wang, T. Li, H. Lu, and Z. Liang, *IEEE Trans. Med. Imag.* **25**, 1272 (2006).
12. Y. Chen, D. Gao, C. Nie, L. Luo, W. Chen, X. Yin, and Y. Lin, *Comput. Med. Imag. Graph* **33**, 495 (2009).
13. M. J. Jia, P. Bruža, L. A. Jarvis, D. J. Gladstone, and B. W. Pogue, *Biomed. Opt. Express* **9**, 4217 (2018).
14. X. Han, J. Bian, E. L. Ritman, E. Y. Sidky, and X. Pan, *Phys. Med. Biol.* **57**, 5245 (2012).
15. X. Liu, Q. Liao, and H. Wang, *Opt. Lett.* **38**, 4530 (2013).
16. S. Niu, Y. Gao, Z. Bian, J. Huang, W. Chen, G. Yu, Z. Liang, and J. Ma, *Phys. Med. Biol.* **59**, 2997 (2014).
17. V. Ntziachristos, *Annu. Rev. Biomed. Eng.* **8**, 1 (2006).



Multi-beam scan analysis with a clinical LINAC for high resolution Cherenkov-excited molecular luminescence imaging in tissue

MENGYU JEREMY JIA,^{1,*} PETR BRUZA,¹ LESLEY A. JARVIS,³ DAVID J. GLADSTONE,^{1,2,3} AND BRIAN W. POGUE^{1,2}

¹*Thayer School of Engineering, Dartmouth College, Hanover, NH 03755, USA*

²*Norris Cotton Center, Dartmouth-Hitchcock Medical Center, Lebanon, NH 03756, USA*

³*Department of Medicine, Geisel School of Medicine, Dartmouth College, Hanover, NH 03755, USA*

*Mengyu.jia@dartmouth.edu

Abstract: Cherenkov-excited luminescence scanned imaging (CELSI) is achieved with external beam radiotherapy to map out molecular luminescence intensity or lifetime in tissue. Just as in fluorescence microscopy, the choice of excitation geometry can affect the imaging time, spatial resolution and contrast recovered. In this study, the use of spatially patterned illumination was systematically studied comparing scan shapes, starting with line scan and block patterns and increasing from single beams to multiple parallel beams and then to clinically used treatment plans for radiation therapy. The image recovery was improved by a spatial-temporal modulation-demodulation method, which used the ability to capture simultaneous images of the excitation Cherenkov beam shape to deconvolve the CELSI images. Experimental studies used the multi-leaf collimator on a clinical linear accelerator (LINAC) to create the scanning patterns, and image resolution and contrast recovery were tested at different depths of tissue phantom material. As hypothesized, the smallest illumination squares achieved optimal resolution, but at the cost of lower signal and slower imaging time. Having larger excitation blocks provided superior signal but at the cost of increased radiation dose and lower resolution. Increasing the scan beams to multiple block patterns improved the performance in terms of image fidelity, lower radiation dose and faster acquisition. The spatial resolution was mostly dependent upon pixel area with an optimized side length near 38mm and a beam scan pitch of $P = 0.33$, and the achievable imaging depth was increased from 14mm to 18mm with sufficient resolving power for 1mm sized test objects. As a proof-of-concept, *in-vivo* tumor mouse imaging was performed to show 3D rendering and quantification of tissue pO_2 with values of 5.6mmHg in a tumor and 77mmHg in normal tissue.

© 2018 Optical Society of America under the terms of the [OSA Open Access Publishing Agreement](#)

OCIS codes: (170.3010) Image reconstruction techniques; (170.3880) Medical and biological imaging; (170.7440) X-ray imaging; (170.6920) Time-resolved imaging; (260.3800) Luminescence.

References and links

1. R. W. Holt, R. Zhang, T. V. Esipova, S. A. Vinogradov, A. K. Glaser, D. J. Gladstone, and B. W. Pogue, "Cherenkov excited phosphorescence-based pO_2 estimation during multi-beam radiation therapy: phantom and simulation studies," *Phys. Med. Biol.* **59**(18), 5317–5328 (2014).
2. R. Zhang, A. Glaser, T. V. Esipova, S. C. Kanick, S. C. Davis, S. Vinogradov, D. Gladstone, and B. W. Pogue, "Cherenkov radiation emission and excited luminescence (CREL) sensitivity during external beam radiation therapy: Monte Carlo and tissue oxygenation phantom studies," *Biomed. Opt. Express* **3**(10), 2381–2394 (2012).
3. P. Vaupel, "Tumor microenvironmental physiology and its implications for radiation oncology," *Semin. Radiat. Oncol.* **14**(3), 198–206 (2004).
4. S. V. Apreleva, D. F. Wilson, and S. A. Vinogradov, "Tomographic imaging of oxygen by phosphorescence lifetime," *Appl. Opt.* **45**(33), 8547–8559 (2006).
5. R. Zhang, A. V. D'souza, J. R. Gunn, T. V. Esipova, S. A. Vinogradov, A. K. Glaser, L. A. Jarvis, D. J. Gladstone, and B. W. Pogue, "Cherenkov-excited luminescence scanned imaging," *Opt. Lett.* **40**(5), 827–830 (2015).

6. P. Brůža, H. Lin, S. A. Vinogradov, L. A. Jarvis, D. J. Gladstone, and B. W. Pogue, "Light sheet luminescence imaging with Cherenkov excitation in thick scattering media," *Opt. Lett.* **41**(13), 2986–2989 (2016).
7. P. Brůža, "MLC Planner," <https://github.com/petrbruza/MLCplanner>.
8. P. Vaupel, A. Mayer, and M. Höckel, "Impact of hemoglobin levels on tumor oxygenation: the higher, the better?" *Strahlenther. Onkol.* **182**(2), 63–71 (2006).
9. M. Nordmark, J. Loncaster, C. Aquino-Parsons, S. C. Chou, M. Ladekar, H. Havsteen, J. C. Lindegaard, S. E. Davidson, M. Varia, C. West, R. Hunter, J. Overgaard, and J. A. Raleigh, "Measurements of hypoxia using pimonidazole and polarographic oxygen-sensitive electrodes in human cervix carcinomas," *Radiother. Oncol.* **67**(1), 35–44 (2003).
10. J. L. Demers, S. C. Davis, R. Zhang, D. J. Gladstone, and B. W. Pogue, "Čerenkov excited fluorescence tomography using external beam radiation," *Opt. Lett.* **38**(8), 1364–1366 (2013).
11. T. V. Esipova, A. Karagodov, J. Miller, D. F. Wilson, T. M. Busch, and S. A. Vinogradov, "Two new "protected" oxyphors for biological oximetry: properties and application in tumor imaging," *Anal. Chem.* **83**(22), 8756–8765 (2011).
12. A. Y. Lebedev, A. V. Cheprakov, S. Sakadzic, D. A. Boas, D. F. Wilson, and S. A. Vinogradov, "Dendritic phosphorescent probes for oxygen imaging in biological systems," *ACS Appl. Mater. Interfaces* **1**(6), 1292–1304 (2009).
13. P. J. Shaw and J. R. David, "The point spread function of a confocal microscope: its measurement and use in deconvolution of 3-D data," *J. Microsc.* **163**(2), 151–165 (1991).
14. P. Sarder and A. Nehorai, "Deconvolution methods for 3-D fluorescence microscopy images," *IEEE Signal Process. Mag.* **23**(3), 32–45 (2006).
15. D. J. Brady, A. Mrozack, K. MacCabe, and P. Llull, "Compressive tomography," *Adv. Opt. Photonics* **7**(4), 756–813 (2015).
16. D. J. Cuccia, F. Bevilacqua, A. J. Durkin, F. R. Ayers, and B. J. Tromberg, "Quantitation and mapping of tissue optical properties using modulated imaging," *J. Biomed. Opt.* **14**(2), 024012 (2009).
17. M. Sibai, I. Veilleux, J. T. Elliott, F. Leblond, and B. C. Wilson, "Quantitative spatial frequency fluorescence imaging in the sub-diffusive domain for image-guided glioma resection," *Biomed. Opt. Express* **6**(12), 4923–4933 (2015).
18. X. Chen, W. Lin, C. Wang, S. Chen, J. Sheng, B. Zeng, and M. Xu, "In vivo real-time imaging of cutaneous hemoglobin concentration, oxygen saturation, scattering properties, melanin content, and epidermal thickness with visible spatially modulated light," *Biomed. Opt. Express* **8**(12), 5468–5482 (2017).
19. A. P. Cuadros and G. R. Arce, "Coded aperture optimization in compressive X-ray tomography: a gradient descent approach," *Opt. Express* **25**(20), 23833–23849 (2017).
20. I. Odina, J. A. O'Sullivan, D. G. Polite, K. P. MacCabe, Y. Kaganovsky, J. A. Greenberg, M. Lakshmanan, K. Krishnamurthy, A. J. Kapadia, L. Carin, and D. J. Brady, "Joint system and algorithm design for computationally efficient fan beam coded aperture X-ray coherent scatter imaging," *IEEE Trans. Comput. Imag.* **3**(4), 506–521 (2017).
21. S. Tzoumas, D. Vernekohl, and X. Lei, "Coded-aperture compressed sensing X-ray luminescence Tomography," *IEEE Trans. Biomed. Eng.* **65**(8), 1892–1895 (2018).
22. C. M. Watts, D. Shrekenhamer, J. Montoya, G. Lipworth, J. Hunt, T. Sleasman, S. Krishna, D. R. Smith, and W. J. Padilla, "Terahertz compressive imaging with metamaterial spatial light modulators," *Nat. Photonics* **8**(8), 605–609 (2014).
23. S. W. Paddock and K. W. Eliceiri, "Laser scanning confocal microscopy: history, applications, and related optical sectioning techniques," in *Confocal Microscopy: Methods in Molecular Biology* (Methods and Protocols), S. W. Paddock, ed. (Humana, 2014).
24. M. Wojtkowski, T. Bajraszewski, P. Targowski, and A. Kowalczyk, "Real-time in vivo imaging by high-speed spectral optical coherence tomography," *Opt. Lett.* **28**(19), 1745–1747 (2003).
25. S. Yuan, Q. Li, J. Jiang, A. Cable, and Y. Chen, "Three-dimensional coregistered optical coherence tomography and line-scanning fluorescence laminar optical tomography," *Opt. Lett.* **34**(11), 1615–1617 (2009).
26. B. W. Pogue and M. S. Patterson, "Review of tissue simulating phantoms for optical spectroscopy, imaging and dosimetry," *J. Biomed. Opt.* **11**(4), 041102 (2006).
27. S. L. Jacques, "Optical properties of biological tissues: a review," *Phys. Med. Biol.* **58**(11), R37–R61 (2013).
28. M. Subbarao, T. C. Wei, and G. Surya, "Focused image recovery from two defocused images recorded with different camera settings," *IEEE Trans. Image Process.* **4**(12), 1613–1628 (1995).
29. F. Diaz, F. Goudail, B. Loiseaux, and J.-P. Huignard, "Increase in depth of field taking into account deconvolution by optimization of pupil mask," *Opt. Lett.* **34**(19), 2970–2972 (2009).
30. S. Webb, *Intensity-Modulated Radiation Therapy* (CRC Press, 2015).
31. G. Helmlinger, F. Yuan, M. Dellian, and R. K. Jain, "Interstitial pH and pO₂ gradients in solid tumors in vivo: high-resolution measurements reveal a lack of correlation," *Nat. Med.* **3**(2), 177–182 (1997).
32. B. W. Pogue, J. Feng, E. P. LaRochelle, H. Bruža, H. Lin, R. Zhang, J. R. Shell, H. Dehghani, S. C. Davis, S. A. Vinogradov, D. J. Gladstone, and L. A. Jarvis, "Maps of in vivo oxygen pressure with submillimetre resolution and nanomolar sensitivity enabled by Cherenkov-excited luminescence scanned imaging," *Nat. Biomed. Eng.* **2**(4), 254–264 (2018).

33. R. Zhang, S. C. Davis, J. L. Demers, A. K. Glaser, D. J. Gladstone, T. V. Esipova, S. A. Vinogradov, and B. W. Pogue, "Oxygen tomography by Čerenkov-excited phosphorescence during external beam irradiation," *J. Biomed. Opt.* **18**(5), 050503 (2013).

1. Introduction

Radiation therapy induces Cherenkov light emission within tissue, and this signal provides potential for direct molecular sampling of the tissue microenvironment [1–4]. The approach to using Cherenkov Excited Luminescence Scanned Imaging (CELSI) was examined here, specifically varying the spatial patterns used to excite Cherenkov light from megavoltage (MV) X-rays in external beam radiation therapy (EBRT) [5,6]. CELSI can provide three-dimensional luminescence images through layer-scanned Cherenkov light sheet, which is carried out by movements of the multi leaf collimator (MLC) on the linear accelerator (LINAC), which is commonly used to provide conformal shaping of radiotherapy treatment beams [7]. This application has been experimentally demonstrated *in-vivo* and is hopeful for clinical trial use, taking advantage of the dynamics already inherent in radiotherapy treatments [5,6]. In this study, progressive approaches to scan beam size and shape were explored to understand how incorporation with dynamic treatment plans might occur.

Since tissue partial pressure of oxygen (pO_2) is well known to affect the efficacy of radiotherapy [1,8,9], imaging this signal has been a primary focus of previous CELSI studies. In order to image pO_2 in tissue for EBRT, megavoltage (MV) photon beams have been utilized to induce Cherenkov emission in thin sheets within the tissue which in turn excites an oxygen-sensitive phosphorescent probe. An example is excitation of Platinum (II)-G4 (PtG4) [10–12] via Cherenkov light emission, which efficiently absorbs blue light ($\lambda_{\max} = 435\text{nm}$) and emits phosphorescence in the NIR region ($\lambda_{\max} = 772\text{nm}$). Epi-illumination based CELSI in tissue allows for imaging to a depth of one centimeter or more, depending on the fluorophore concentration and radiation dose used. The scattering-induced blurring can be compensated by deconvolution processing based on the point spread function (PSF), evaluated by radiative transport models [6,13,14]. The hypothesis examined in this study was that when designing this irradiation scheme, the beam shape could be chosen to optimize the spatial-resolution of recovered CELSI images. Further, it might be possible that existing clinical treatment plans allow for high resolution imaging.

Patterned illumination schemes have been investigated more recently with the emergence of compressed sensing, where computed image recovery is utilized to improve the image quality without extra radiation exposure and/or acquisition time [15]. While the ultimate extent of compressed sensing methods uses complex patterns, the methodology for this could include a simpler spatial-frequency-domain imaging (SFDI) approach or more complex techniques such as used in coded aperture imaging (CAI). Current SFDI instruments typically use projected spatially modulated light, projected onto the sample, and then knowledge of the illumination patterns are used to demodulate the images [16–18]. CAI requires a coded mask placed either, in front of the radiation beam source to shape the incident beam, and at the detector to block the transmitted beam and disambiguate scatter angles [19–21]. For both of these structured imaging modalities, the excitation beam is modulated by a projector or a coded aperture, and the measured reflectance or transmittance is demodulated in post-processing. This modulation-demodulation method (MDM) has the capacity to mathematically filter the low frequency out-of-focus scattered photons beyond the depth of field of the imaging objective. For the MDM process using a point raster scanned beam, the narrow beam acts as a virtual pinhole, analogous to the emission light captured through a pinhole in confocal microscopy. Diversification of the illumination pattern based on an MLC is clinically convenient in CELSI and could be time-saving, and in principle the type of spatially modulated patterns could be extremely beneficial to provide high resolution imaging. In particular, using coded apertures in conjunction with multiplexed illumination can reduce the acquisition time, given that projections from more than one source may be acquired in a single step [19].

Motivated by the idea of using patterned illumination schemes, the study here examined if the spatial resolution and contrast recovery of CELSI could be improved on using different spatial illumination patterns and post processing with MDM. The input radiation beam was modulated and raster-scanned by programming the MLC, and post-processing demodulation was performed by deconvolving the measured luminescence image with the kernel function of the Cherenkov image. This approach, referred to as MDM-CELSI, examined several EBRT-compatible MLC plans, and specifically how the measurement geometry affected the acquisition time, and radiation dose. Modulation of the radiation (X-ray) beam was investigated using basic illumination patterns including squares and lines, and multiple combinations of these.

2. Methodology

2.1 Incidence modulation

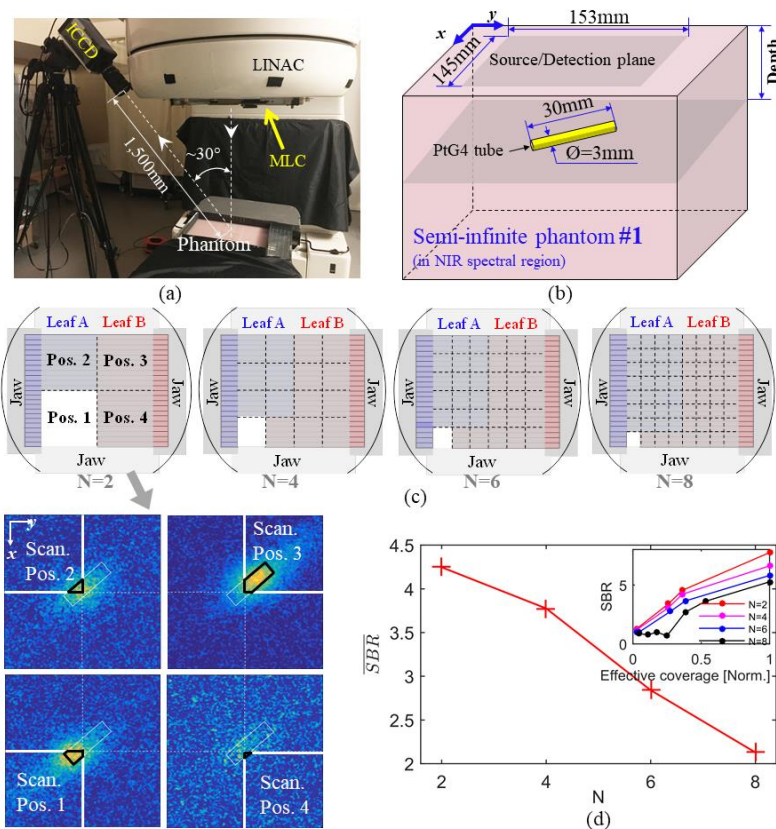


Fig. 1. The experimental setup used to investigate the effect of radiation beam size is shown in (a) with a photo of the experimental setup with LINAC, phantom and ICCD camera; (b) the internal phantom geometry; (c) the basic $N \times N$ square-raster scanning patterns tested initially with different pixel areas and the luminescence images measured for $N = 2$ (below this), and (d) the calculated Signal to Background ratio (SBR) versus target area for $N = 2, 4, 6,$ and $8,$ respectively.

A clinical radiotherapy accelerator (Varian Clinac 2100 CD, Varian Medical Systems, USA) was used to generate a pulsed beam with the following parameters: photon beam energy of 6 MV, dose rate of 600 monitor units per minute (MU/min), at a fixed repetition rate of 360 Hz, and a $\sim 3.25 \mu\text{s}$ pulse duration. The X-ray beam impinged on the tissue-equivalent phantom, embedded with a 70 μM PtG4 target (inner diameter $\text{\O} \approx 3\text{mm}$, and length of 30mm) at a depth of $\sim 1.2\text{cm}$, which is detailed in Fig. 1(a) and (b). The camera with a focal length of

85mm and $f/1.2$ lens was mounted close to LINAC as shown in Fig. 1(a), resulting into an inclined angle of $\sim 30^\circ$ and a distance of $\sim 1,500$ mm from the sample. The luminescence signal was detected with time-gated acquisition of the ICCD ($100 \mu\text{s}$ integration time and $4.26 \mu\text{s}$ delay after each x-ray pulse). The luminescence images were acquired with $100 \times$ gain on the ICCD intensifier, 30 pulses integrated on-chip as accumulations prior to each frame readout, and 2×2 hardware pixel binning at readout, from chip size of $1024 \text{ pixels} \times 1024 \text{ pixels}$. Cherenkov images were acquired in the same way, but with $0 \mu\text{s}$ pulse delay and a $3.5 \mu\text{s}$ integration time. Measurement at an increased pulse delay of $\sim 500 \mu\text{s}$ was also acquired as ‘background images’ from the same field of view (FOV), which was used to subtract out stray signals in the camera and room.

In order to utilize LINAC-based EBRT for the CELSI illumination plan, a patterned beam design must be created with consideration of the geometry and orientation the MLC, which does put some limit onto what is possible. For the MLCs used here, the lateral length (along the direction orthogonal to movement) of a single MLC leaf was 5mm with step sizes of 0.1mm; the smallest point excitation available realistically was on that spatial scale. The geometry of these MLCs are optimal for targeting single-connected regions or distributions along the central axis, but it can be impossible to form more complicated shapes that might be optimal, like the Hadamard matrices for example [22]. X-ray beams were raster-scanned with different sized squares as shown in Fig. 1(c), which was performed by delivering a custom dynamic dose plan, created in MLC code [13]. The measured luminescence images for an $N \times N$ ($N = 2$) raster-scanned illumination are shown below Fig. 1(c), where the regions encircled with black lines are the pixel areas included within the radiation beam, named as the effective coverage. The relationship of Signal to Background ratio (SBR) with the effective coverage, and N , are shown in Fig. 1(d), where the SBR can be found strongly dependent upon both. A reasonable square/beam area could be more than 1 mm^2 .

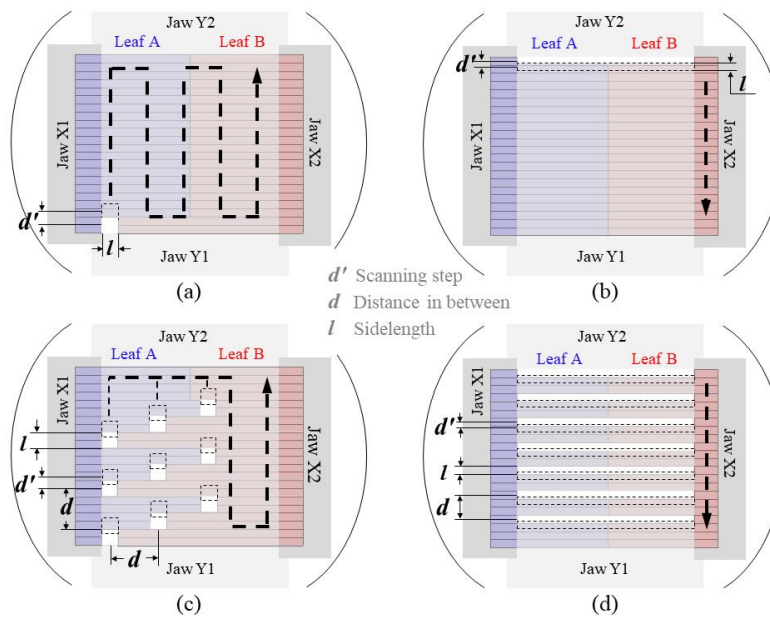


Fig. 2. Two basic illumination patterns studied are displayed from the top-view of the MLC, including: (a) a single square, raster scanned in 2 dimensions across the entire field of view, (b) a thin line, scanned in one dimension vertically down through the field, (c) a multiple-square pattern which is scanned; and (d) a multiple-line pattern scanned downwards. The blue and red rectangles represent leaves of Groups A and B, respectively, while the black dashed frames indicate movement to the next scanning positions, and the thicker dotted arrow lines indicate the total movement plan.

To accelerate the acquisition process, several square-illuminations are simultaneously enabled, which allowed for reduction of total scan time. As a proof-of-concept, one type of multi-square illumination with equal spaces is shown in Fig. 2 (c), where the dashed squares represent the next scanning positions. The multi-square distribution depends on following two parameters: (1) the square side-length l , which is found by a compromise between spatial resolution and measurement SNR; and (2) the beam pitch $P = d' / l$, where d' is the step size. $P < 1.0$ denotes there is an overlap in between the continuous squares and vice versa. For full-field illumination, we assume $P = 1$, which indicates a contiguous scanning for adjacent positions. For multiple scanning, $d' = (Nl - d) / (N - 1)$, where d is distance in between each square, and the total scan positions should be N^2 times the number of squares in a multi-square shape. To be comparable with the point-raster strategy, d should be large enough to avoid cross-talk effect. The minimum of d (d_{\min}) depends on the system SNR, which is the critical source-detector separation estimated by fluorescence Monte-Carlo simulation. For typical optical properties of normal human tissue under the wavelength $\lambda = 772\text{nm}$ (PtG4 phosphorescence peak), *i.e.*, the absorption coefficient μ_a , scattering coefficient μ_s , and anisotropic factor g values common in soft tissue, at $\mu_a = 0.01\text{mm}^{-1}$, $\mu_s = 10\text{mm}^{-1}$, and $g = 0.9$, d_{\min} is near 2mm.

As an alternative way to accelerate acquisition, line-scan field illumination has been demonstrated in confocal microscopy [23], optical coherence tomography (microscopy) [24,25], and laminar optical tomography [25]. Further accelerations can be similarly reached by multiple enablement strategy, named as multi-lines illumination, as shown in Fig. 2(d). Also, the distance in between each line should be greater than d_{SNR} . Comparisons between point- and line- shaped patterns with different combinations of l and P was examined.

2.2 Image demodulation

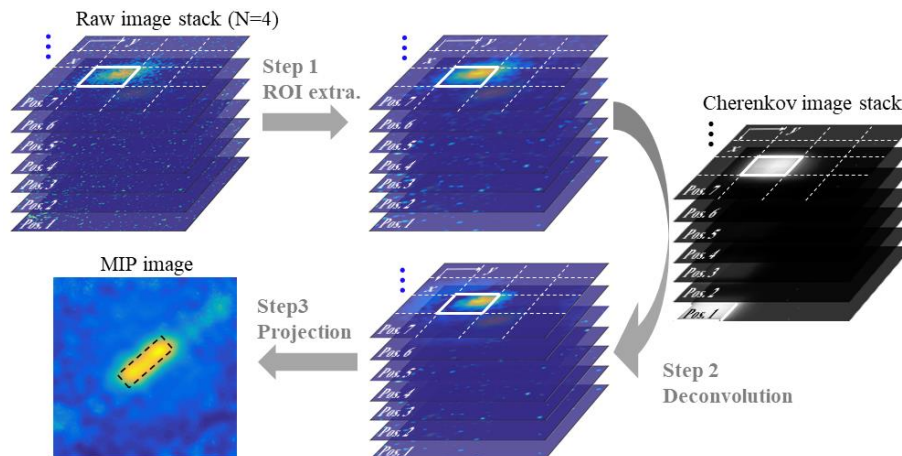


Fig. 3. Diagram of the patterned-CELSI ($N = 4$) postprocessing sequence involving acquisition of both luminescence and Cherenkov at each of the raster scanned positions and region of interest (ROI) extraction (step 1) followed by deconvolution of the luminescence by the Cherenkov shape (step 2) and combining together for a MIP image (step 3). The dashed black square in the MIP images indicates the true position of the target.

The procedure of image demodulation is illustrated by the flow chart in Fig. 3. For simplicity, a 2D square-raster scan is illustrated here with 4×4 uniformly distributed scanning positions. The resulting input raw image is composed of 16 pixels corresponding to the 16 positions. The steps are: (1) the raw images were processed frame-by-frame to mainly extract the region of interest through subtracting ‘background’ ones; (2) the Cherenkov image was used as the

kernel function to deconvolve the corresponding luminescence images; and (3) demodulation is done by combing all the frames into a Maximum Intensity Projection (MIP) image. Considering the multiple deconvolutions in step 2, an economical one-step deconvolution algorithm was used for i th scanning position, which can be formulated as

$$\mathbf{X}_i = \begin{cases} F^{-1} \left\langle \frac{F \langle \mathbf{Y}_i \rangle (w)}{F \langle \mathbf{C}_i \rangle (w) + \varepsilon} \right\rangle, & \text{if } |w| < R \\ 0, & \text{if } |w| > R \end{cases}, \quad (1)$$

where \mathbf{Y} and \mathbf{X} is the raw and undistorted luminescence image, respectively; \mathbf{C} is the Cherenkov image; ε is an infinitesimal integer; and $F \langle \cdot \rangle$ and $F^{-1} \langle \cdot \rangle$ represent Fourier and inverse Fourier transforms, respectively. Note that the range of spatial frequencies w can be physically limited in a radius of R ($\in [1.5, 2.5]$ in this paper), which is regulated by a specified beam pattern, and can be estimated instead through the high signal-to-background ratio Cherenkov image.

3. Result

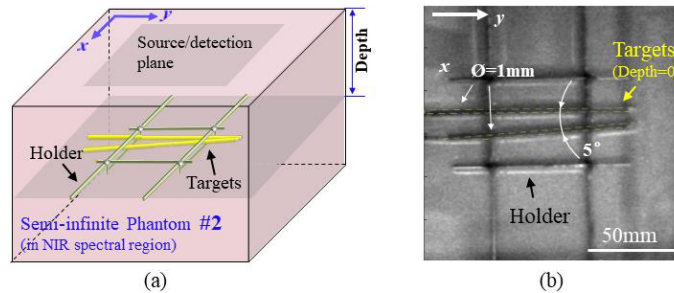


Fig. 4. Phantom experiments for image fidelity demonstration, with (a) an 3D schematic of the Intralipid-blood tissue phantom with two capillaries inside filled with PtG4 (yellow cylinder); and (b) a photograph of this geometry with target depth being zero, for illustration.

A series of phantom studies were carried out using a tissue-equivalent phantom, which consisted of 1% Intralipid and 1% porcine blood per unit volume of solids, with absorption and reduced scattering coefficients estimated to be $\mu_a = 0.01 \text{mm}^{-1}$ and $\mu'_s = 1 \text{mm}^{-1}$ in the NIR spectral region at 800nm [26,27]. The measurement geometry is shown in Fig. 1, and the phantom adopted (#2) is illustrated in Fig. 4, where two plastic capillaries (inner diameter $\text{Ø} \approx 1 \text{mm}$) containing 70 μM PtG4 solution were placed with an angle of 5° in between as shown in Fig. 4. The angled capillaries were designed to pick up a reasonable Y-period between unresolvable and completely resolved status for X-profile analysis. A holder, which is fixed to the wall of phantom container, was used to clamp the capillaries. Without specific notification, the depth of target is 8mm.

3.1 Comparisons between line- and square scanning pattern

In the first study, line- and square- raster scanning were compared for $P = 0.50, 0.33,$ and $0.25,$ respectively, and a fixed square size of $l = 77 \text{ mm}$, as shown in Fig. 5. To quantify the spatial resolution performance, a metric of success was introduced, defined as $R = (I_{\max} - I_{x=69\text{mm}}) / (I_{\max} - I_{\min})$, with I_{\max} and I_{\min} being the maximum and the minimum in the x-profile of the image, essentially providing a relative measure of contrast recovery. Considering the possible artifacts & distortion for the plastic capillaries walls themselves and uneven PtG4 distribution inside, X-profiles for the period included by the two white dashed lines were averaged to obtain a more robust estimate of R . Since there was a 5° angle in

between the two rods, X-profile was not accurately specified for a fixed Y-value in this case. With this definition, $R = 1$ represents that the two targets can be completely separated, with full contrast recovery. In the characteristics of the human vision system, it is normally assumed that two targets are distinguishable for $R > 0.1$ (when a 10% dip in intensity is observed between them). In addition to spatial resolution, radiation dose and acquisition time were also estimated and all are listed in Table 1. Acquisition time was calculated as: “Dose(MU)” / “Dose rate(MU/min)”, which just estimated total scanning time, excluding mechanical switching issues which vary from machine to machine. We assume that Cherenkov emission, luminescence and background signals can be read out in one pulse cycle, which is the time period between two LINAC pulses. This can be realized with a time-resolved camera by specifying the corresponding pulse delays.

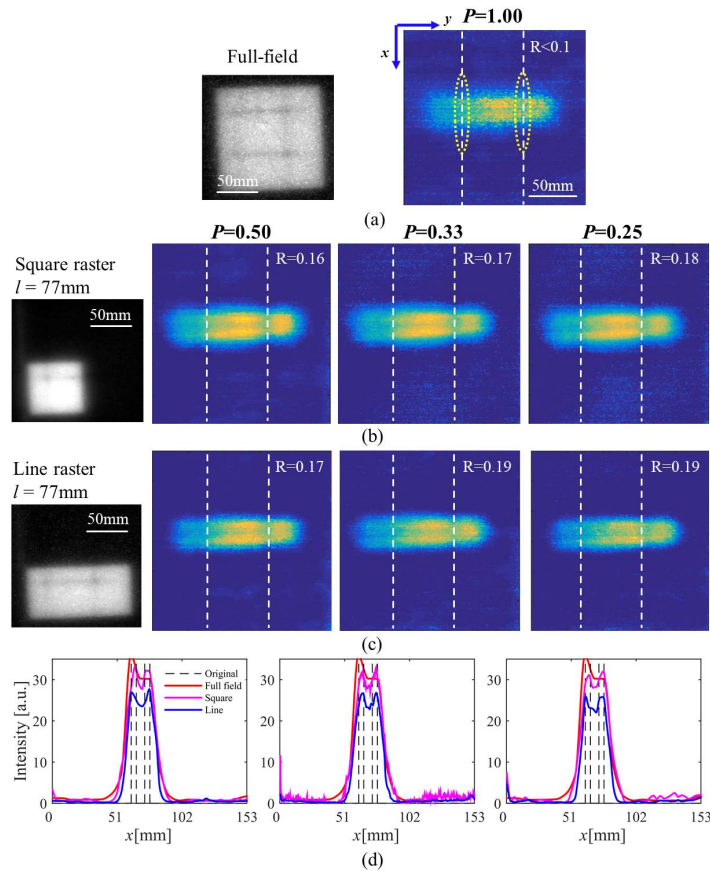


Fig. 5. Luminescence (color) and Cherenkov (greyscale left) images are shown, as measured under (a) full-field covering the entire frame, (b) a larger square 2D-raster scanned field, and (c) a thick line 1D-raster scanned. The corresponding X-profiles below (d) were averaged along the Y-axis direction for a distance in between the two white dashed lines indicated in (a)-(c). The value of R is inset in each image to qualify contrast recovery.

Table 1. Comparisons between line and point raster for $P = 0.50, 0.33,$ and $0.25,$ respectively, and a fixed $l = 77\text{mm}.$

P	Dose (MU)			Time (s)			R		
	0.50	0.33	0.25	0.50	0.33	0.25	0.50	0.33	0.25
Full field		138			14			<0.1	
Point raster	311	466	615	124	221	345	0.16	0.17	0.18
Line raster	184	276	345	42	55	69	0.17	0.19	0.19

In general, beam projections shaped by the MLCs are clinically defined by the targeting for the tumor region. The most unresolved shape used is a squared ‘full-field’ shape, with its Cherenkov image shown in Fig. 5(a). It is worth noting that, the full-field region was slightly smaller than FOV to conserve the diffused edges for both Cherenkov and luminescence images, to allow for complete measurements of the kernel function by the raw Cherenkov image for the deconvolution. For the luminescence imaging, one artifact noted was that the metal-made holder could attenuate some fluorescence emission, which led to ‘slightly-dimmer regions’ on the PtG4 target as indicated with yellow dashed circles, but these was avoided in the analysis, and not present in the line scans analyzed, Fig. 5(d).

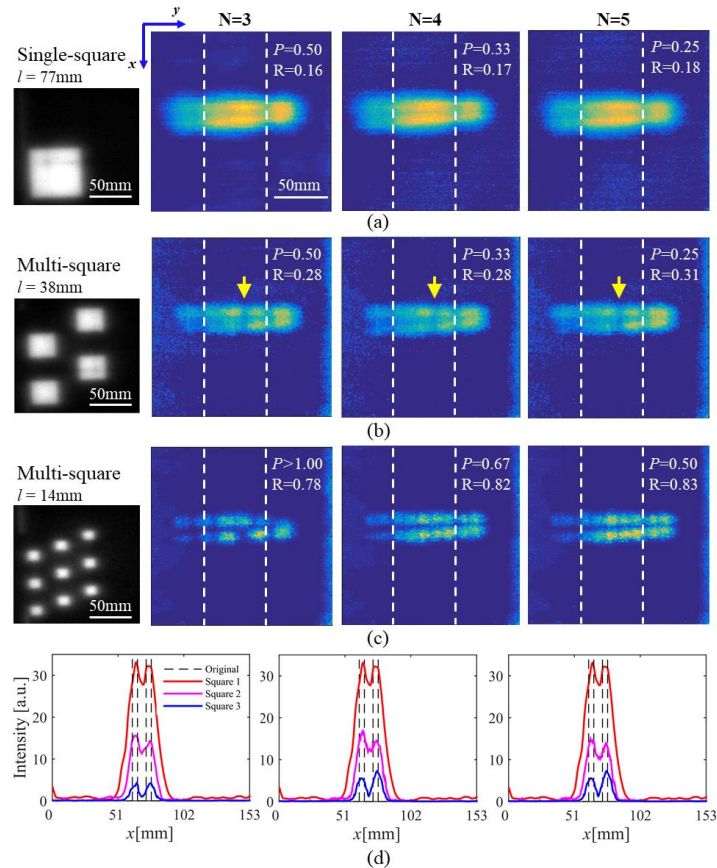


Fig. 6. Luminescence (color) and Cherenkov (greyscale left) images as measured under (a) large 77mm block beam raster scanned, (b) a series of 4 parallel 38mm square raster scanned beams, and (c) a series of 9 parallel 14mm square raster scanned beams. The corresponding X-profiles (d) were averaged along the Y-axis in between the two white dashed lines indicated in (a)-(c). N values decide the scanning step d' . R values recovered are overlaid on each luminescence image, showing the large improvement in R with smaller beam sizes. (A full scanning video of merged Cherenkov and deconvolved Luminescence image sequence for N = 4 is available in [Visualization 1](#)).

Several conclusions can be drawn from Fig. 5. (1) Both square- and line- raster results show higher contrast recovery ($R > 0.15$) than that of the full-field ones ($R < 0.1$). Basically, the two capillary rods cannot be discriminated in the ‘full-field’ image. (2) Image resolution seldom varies with scanning step since no space exists in between two adjacent squares, *i.e.*, $P < 1$. However, the recovered image would degrade a lot if $P > 1$, *e.g.*, the capillary rods were found to be discontinuous in Fig. 6(c) when $P > 1$. (3) In this case, the line-scan results slightly outperformed the square point-scan ones. This could be explained by the nearly parallel

direction between the capillaries placed and the illumination orientation. In other words, resolution would be reduced if the two directions were orthogonal. For example, as pointed out by the yellow arrows in Fig. 6(c), some dimmed regions could be more clearly discerned in square point-scan images, which, however, are not visible in line-scan results as shown in Fig. 6(b). These regions were highly resolved in Fig. 7, and also visible in Fig. 8. An improvement to the line-scan methods would be multi-direction scanning, which could render a full-direction resolution enhancement, however, this would come at the cost of doubling the radiation dose and acquisition time.

Multi-point scanning of squares is therefore demonstrated above to be ideal compromise between optimal resolution, minimal scan time and minimal dose. Further investigations were aimed at optimization of the pattern parameters as discussed in Section 2.A, *i.e.*, l and P . Three kinds of square patterns were deliberately designed for this test, with their Cherenkov images displayed in greyscale as shown in Fig. 6, progressing from larger to smaller block sizes with separation of them sufficiently large to avoid any crosstalk. From the luminescence images in Fig. 5, R -value was not strongly dependent upon the value of d' . In comparison, the square size characterized by side-length l imposed a significant influence on spatial resolution, *e.g.*, from the images (bottom line of Fig. 5) with $R < 0.2$ when $l = 77\text{mm}$ to those (middle line of Fig. 5) with $R > 0.77$ when $l = 14\text{mm}$. However, the measurement intensity of the former cases was 5 times higher than the latter ones, which is in agreement with the conclusions of intensity versus illumination area in Section 2.1. Consequently, we applied a trade-off, where a side length of 38.3mm and $P = 0.33$ were tested here.

3.2 Imaging for varying target depths

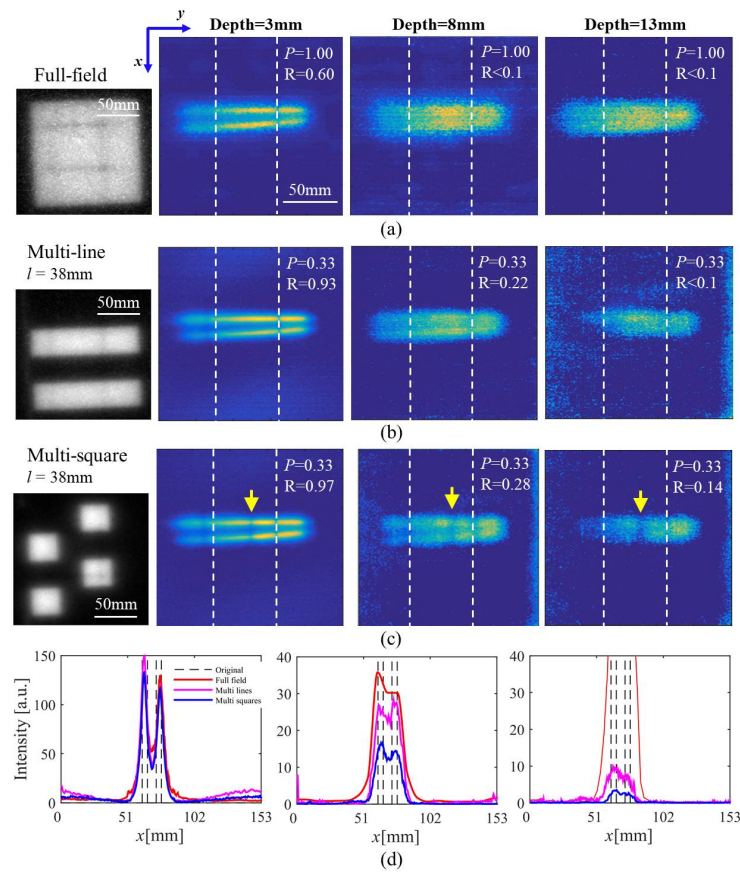


Fig. 7. Luminescence (color) and Cherenkov (greyscale left) images as measured under (a) full-field, (b) square raster scanned, and (c) line raster scanned beams, for target depths of 3, 8, and 13mm, respectively, from left to right columns. The corresponding X-profiles (e) were averaged along the X-axis in between the two white dashed lines indicated in (a)-(c). The R values of each scan are overlaid on each luminescence image, showing the large decrease with depth into the medium, but that the raster scanned square beams (c) allow sufficient R resolution down to the lowest depth of 13mm.

In this section, the effect of increasing target depth was analyzed. It can be seen from Fig. 7 that, all the methods could provide clearly discerned images for the smallest target depth. In comparison, the full-field image presents a result of lower spatial resolution as well as SNR, and an available imaging depth of less than 8mm. For the deepest target at 13mm, only the imaging result with the square beams could provide a spatial resolution of $R > 0.1$. Since the deblurring strategy herein only considered Cherenkov photon scattering, the recovered images for large-depth targets embedded in a scattering medium should have diffused edges. Depth-corrections for fluorescence photon scattering have been widely developed in (fluorescence) diffuse optical tomography. Besides, depth-related image deconvolution has been customized for CELSI in previous work [6].

3.3 Modulation transfer function analysis

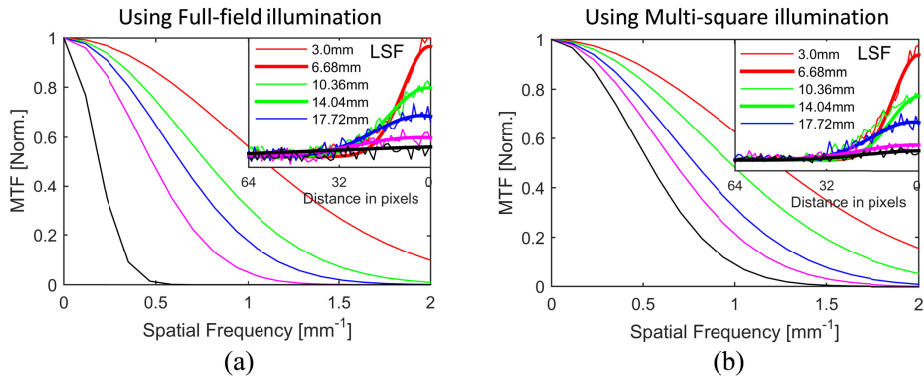


Fig. 8. Normalized Modulation Transfer Function curves estimated for (a) full-field, and (b) multi-square illuminations. The insert curves are corresponding line spread functions and their Gaussian fitting results.

To quantify spatial frequencies that can be resolved versus depth, a phantom embedded with a single target (capillary of $\varnothing \approx 1\text{mm}$, filled with $70\ \mu\text{M}$ PtG4) was imaged to obtain the Modulation Transfer Function (MTF) from line scan data. Results as measured under both full-field and multi-square illumination are plotted in Figs. 8 (a) and (b), respectively, where the squared beam shape was scanned with an optimized parameter set at $l = 38\text{mm}$ and $P = 0.25$. The line spread functions (LSF) are inset correspondingly and fitted to Gaussian curves in the subplots, and demonstrate the available spatial frequencies from which information can be obtained.

Table 2. Inverse of limiting spatial frequency (50% of the MTF amplitude) defined at varying depths for full-field and multi-square illumination.

Target depth	3.0mm	6.7mm	10mm	14mm	18mm
Full field	0.9mm	1.3mm	1.6mm	2.1mm	5.2mm
Multi square	0.8mm	1.0mm	1.2mm	1.5mm	1.8mm

Spatial resolutions achievable are related to the inverse of the MTF function where there is measurable amplitude, and here it was taken as 50% of the maximum. These are defined at different target depths, as recorded in Table 2, where the effective lower limit on resolution was estimated. It can be seen from Table 2 that, the difference in spatial resolution between these two methods increases significantly from roughly 0.1mm at a target depth of 3mm to a difference of 3.4mm at 18mm. For a target depth of 14mm, both full-field illumination and the scanned multi-square method retain reasonable resolution near 1mm, but just slightly beyond this depth (18mm depth) the true capillary diameter could not be resolved with full field illumination but likely could be with the scanned multi-square approach.

3.4 Correction for defocused blurring

To acquire high signal intensity or measurement SNR, a large-NA lens is generally applied for fluorescence imaging, which however renders a limited depth of field (DOF). The adopted lens used in this study was $FL = 85\text{mm}$ and $f/1.2$, for instance, which provides only a $DOF = 9.4\text{cm}$ for coupling to the PI-MAX4 camera. Since defocus blur can be seen simply as the convolution between a sharp image and a blur kernel, one can solve for the sharp image again by deconvolving the blurred image with the same point spread function (PSF) used to blur the original sharp image [6,28]. However, the PSF has to be either estimated by scaling a depth-dependent PSF, or experimentally obtained through capturing the out-of-focused target with different camera-target distance [29].

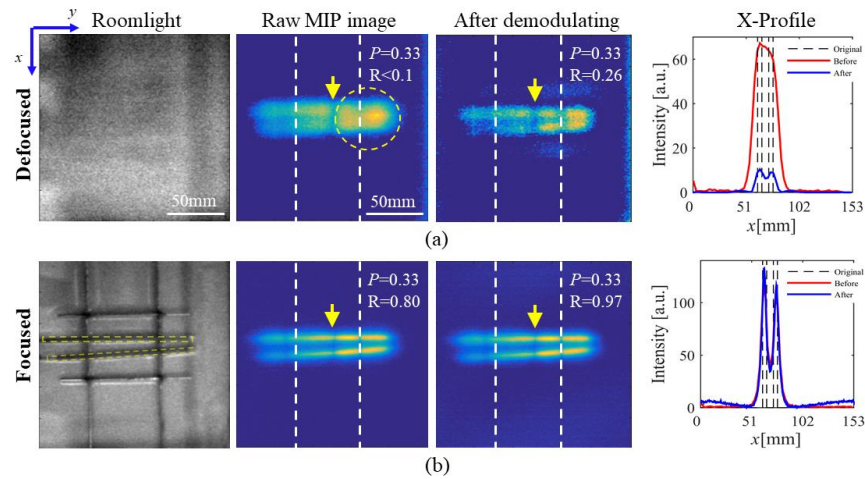


Fig. 9. (a) Defocused and (b) focused imaging results are shown. From left to right the columns are photograph, then luminescence images before and after demodulation, and the corresponding X-profiles, respectively. The X-profiles are averaged for Y-distance in between the two white dashed lines indicated.

A small target depth of 3mm was investigated to highlight the value of this deblurring by inducing a defocusing acquisition instead of photon scattering. The experimental results are shown in the Fig. 9(a), where luminescence images before and after demodulating and correction are displayed correspondingly. As references, all-in-focus images are shown in the lower line of Fig. 9. It can be seen from the defocused image before correction, the two capillaries are hard to separate ($R < 0.1$) and even overlapped with each other at the place indicated by the yellow dashed circle. After correction, the capillaries can be discerned with R increasing to 0.26.

4. Clinical geometry studies in breast scanning

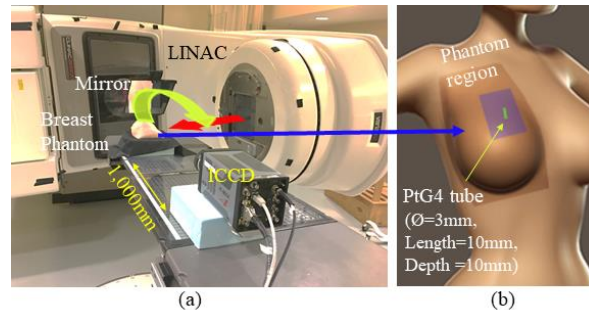


Fig. 10. CELSI applied in breast EBRT: (a) measurement geometry, and (b) schematic of a full-size right-sided breast phantom. A tube filled with $70 \mu\text{M}$ PtG4 was embedded at a depth of 10mm to simulate a lymph node. The red and green arrows track X-ray and luminescence signals, respectively. The blue rectangle region in (b) is the field of view.

Most EBRT treatment plans in patients dynamically shape the beam with the MLCs and Jaws within the LINAC, targeting the tumor region and minimizing dose to nearby critical structures. As a result, it was hypothesized that the natural spatial modulation done in clinical radiotherapy could be used to achieve an enhanced CELSI, based upon how the beams were formed. To investigate this, we used three typical breast treatment plans, *e.g.*, a conformal radiation therapy (3D-CRT), an over modulated 3D-CRT (3D-CRT^{OM}), and an Intensity Modulated Radiation Therapy (IMRT) [30]. In addition, a dynamic wedge (DW) plan was investigated, which instead uses the Jaws slowly closing to the desirable shape. A full-size

breast phantom with tissue equivalent optical properties was created, CT-scanned and the shape transferred to the Eclipse treatment planning system (Varian Medical Systems, Palo Alto, CA) for radiotherapy treatment planning. In these treatment plans, gantry angle of 270° or 280° was used for medial tangent beam, and angles of 90° or 100° was used for lateral tangent for right breast cases. Radiation doses used for 3D-CRT, 3D-CRT^{OM}, DW and IMRT were 194MU, 246MU, 204MU, and 210MU, respectively, with fixed beam energy of 6MV (note, 100MU corresponds to a dose of 1 Gy at the isocenter of the beam at D_{\max} depth). The measurement geometry is shown in Fig. 10(a), where a mirror was used to reflect the outgoing luminescence light into a horizontally positioned camera. The breast phantom was positioned in a whole-body model in Fig. 10(b). The camera worked at a frame-rate of 10fps to make a tradeoff between measurement SNR and time resolvable snapshot.

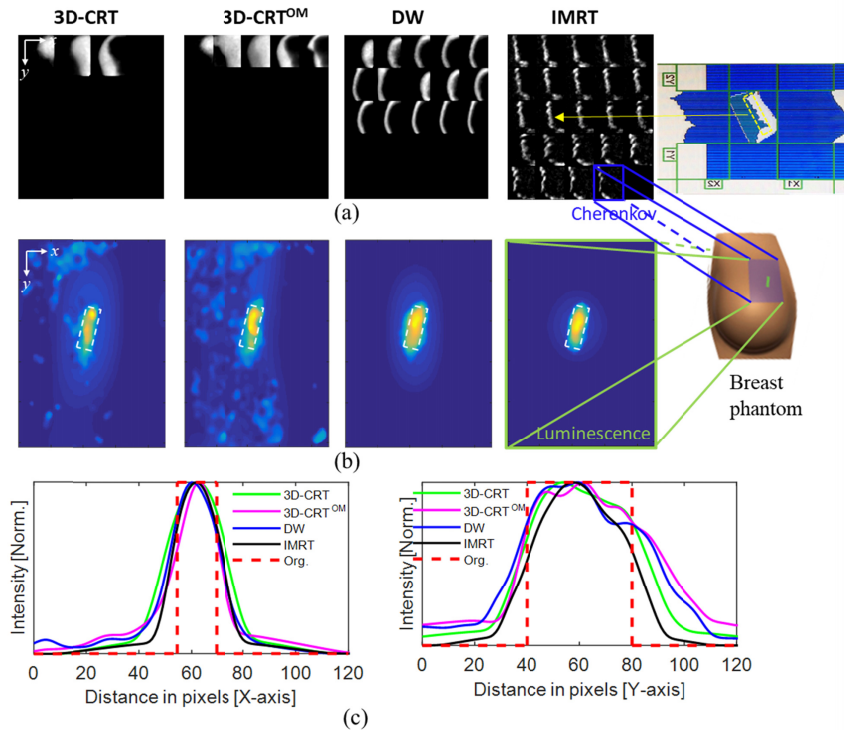


Fig. 11. CELSI results with beam scanning with clinical breast treatment plans. (a) Difference Cherenkov images merged with deconvolved luminescence ones showing the beam shape differences; (b) luminescence images reconstructed of the 10mm deep target; and (c) corresponding profiles along the two orthogonal axes through the target centroid point. (A scanning video of merged Cherenkov and deconvolved Luminescence image sequence is available in [Visualization 2](#) for both the original and difference results).

Investigations on these beam shapes show that most of them were confirmed with widely opening MLCs or Jaws. As discussed before, proper beam size is crucial to obtain a high fidelity images. To maximize the spatial value of the kernel in the modulation-demodulation method, a finite differencing process was used in between original frames to get difference images and the resultant luminescence images were then differenced correspondingly, as illustrated in Fig. 11(a). Note that irradiation in the DW plan was performed in an edge scanning way, which then was converted to a linescan one after the difference operation. Edge scanning was also tested with the IMRT plan, while the difference is that the IMRT instead used the MLCs to shape the beam. Since it was hard to make all the leaves move at a same speed, an original line-shaped beam was distorted as shown in Fig. 11(a). However, because of this distortion, the resultant beam was actually shaped somewhat between a full

linescan or square beam scan. A screen shot from the MLC console recorded the transient status of all the leaves corresponding to one scanning position, as shown in Fig. 11(a).

The recovered images with the proposed method are shown in Fig. 11(b), with their X- and Y- profiles plotted in the left and right positions of Fig. 11(c), respectively. Significant background noise was found in the first two results, the 3D-CRT and 3D-CRT^{OM} plans respectively, because the beamlets were less effective at excitation as shown in Fig. 11(a), leading to a reduced frame rate in the image sequence acquired. For the latter two plans, the IMRT result performed better, which was due to the combined beam shapes between a line and a square, leading to an additional improvement along Y-axis as shown in Fig. 11(c). At present, the IMRT plans are used to treat the more complex cancers, *e.g.*, head and neck, and central nervous system [30]. For the images recovered with 3D-CRT and 3D-CRT^{OM} plans, due to the insufficient effective inputs, targets are erroneously positioned and a bit oddly formed because of the limited beam shapes.

5. In-vivo mouse studies

In this section, the MDM-CELSI technique was used for 3D imaging of a tumor in a living mouse, and the pO₂ concentration was estimated for both tumor and non-tumor regions. All animal procedures were approved by the Dartmouth Institutional Animal Care and Use Committee, and the studies here were carried out in compliance with these approved procedures. Nude female mice were purchased at 6 weeks of age from Charles River Labs. After a week of acclimatization, animals were used for injections of 10⁵ MDA-MB-231 cells under the skin on one upper limb flank of the mouse in individual 0.050 ml injections. After approximately 3 weeks of growth, when a tumor with an average of 6 mm diameter was observed on the flank, the animals were then used for imaging studies. All mice were under general anesthesia of inhaled isoflurane at 1.5% in flowing air through a nose cone throughout imaging. A total of 50ml of 25μM PtG4 was directly injected into the tumor and normal regions on both blanks. For LINAC settings, a 6MV beam with a dose rate of 600MU/min was used. Dynamic MLC plans were used to generate the specified beam shapes for 3D CELSI acquisition and subsequent pO₂ estimation, respectively. In order to recover the pO₂, a range of delays were created between the linac pulse and the emission collection, so that the emission intensity lifetime at each position could be recovered. Finally, this animal was imaged in the IVIS Spectrum CT system for X-ray tomography for spatial reference.

5.1 3D rendering

To render a 3D view, the beam was introduced in the lateral direction as a sheet, which was scanned bottom to top, typical of previous CELSI results, and then images captured by a vertically placed camera could be 3D stacked along depth direction [6]. A room light image under the same FOV was captured and is displayed in Fig. 12 (a). The resultant Cherenkov combined with demodulated luminescence images at each scanning positions are shown in Fig. 12(b). Similar to the scanning process in Section 4, Cherenkov beamlets swept over the target areas, which gives access to the MDM method. As a comparison, we show the raw and processed MIP images in Fig. 12(d), where the corresponding X- and Y- profiles across the tumor region is also present.

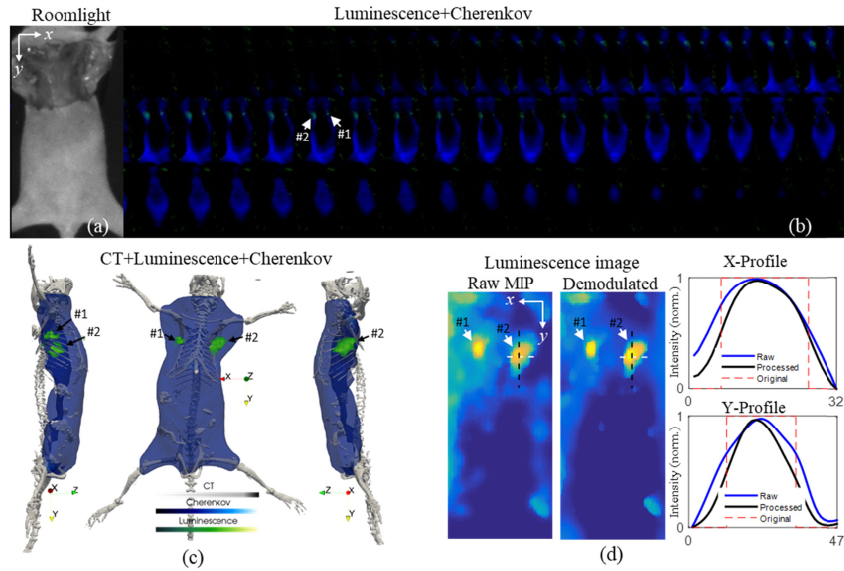


Fig. 12. In-vivo mouse experiment for 3D MDM-CELSI: (a) photograph of nude mouse with one MDA-MB-231 tumor growing on the upper limb flank injected with 50 μ l of 25 μ M PtG4, (b) merged Cherenkov and demodulated luminescence images, (c) 3D perspective views of combined CT, Cherenkov and luminescence images, and (d) comparisons of luminescence MIP image before and after demodulation and their X-profiles across tumor center. Arrows labeled with #1 and #2 point to the non-tumor and tumor regions, respectively.

5.2 Oxygen sensing with the MDM-CELSI technique

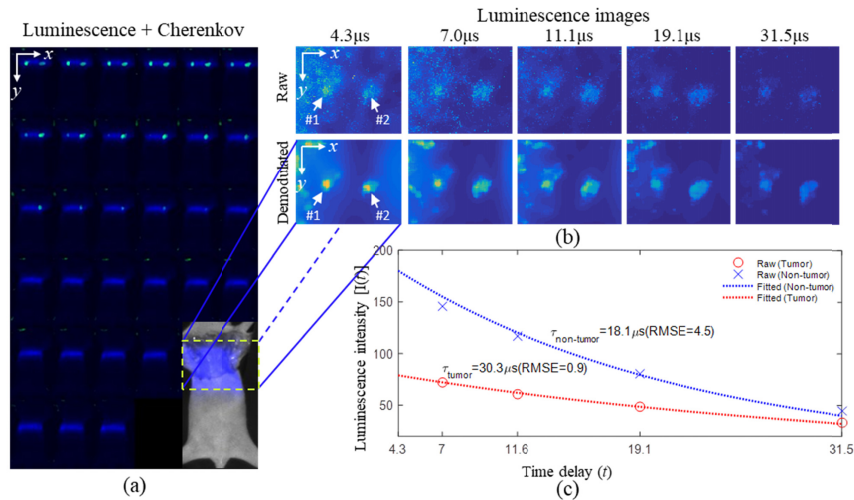


Fig. 13. pO_2 sensing demonstration: (a) merged Cherenkov and demodulated luminescence images, (b) luminescence images of the scanned region before and after demodulation at different post-excitation time points, and (c) raw and fitted luminescence decay curves for the tumor and non-tumor regions. A photograph overlaid with Cherenkov MIP image is shown at the last position of (a). Arrows labeled with #1 and #2 point to the non-tumor and tumor regions, respectively.

To estimate pO_2 concentration reasonably, time-resolved luminescence decay needs to be detected in a limited period. As a result, a localized scanning was performed around the mouse chest region. The transmittance measurements of Cherenkov and demodulated luminescence are shown in Fig. 13(a), where a room light image was overlaid with a

Cherenkov MIP image to indicate the scanning area framed by yellow dashed line. Luminescence images before and after demodulation are shown in upper and lower lines of Fig. 13(b), respectively, for five time delays (t). To pursue high SNR, these measurements were measured as an integration over $100\mu\text{s}$ with a specified t after Cherenkov period. The curves of luminescence intensity against t [$I(t)$] for tumor and non-tumor regions were plotted in Fig. 13(c). Curve fitting procedures were performed to achieve a more substantial lifetime (τ), which was calculated according to the following equation:

$$I(t) = I_0 \tau \left(e^{-\frac{t}{\tau}} - e^{-\frac{t+100}{\tau}} \right), \quad (2)$$

with I_0 being the decay initial intensity. The estimated τ values for tumor and non-tumor regions were $30.3\mu\text{s}$ and $18.1\mu\text{s}$, with root-mean-square errors (RMSE) being 0.9 and 4.5, respectively. Then $p\text{O}_2$ values were calculated via the Stern-Volmer relationship: 5.6 mmHg and 76.8 mmHg for the tumor and non-tumor regions, respectively. As expected, lower $p\text{O}_2$ was detected for tumor region, which accords with general reports on tumor oxygen level: hypoxic or anoxic [31]. More details can be found in our previous studies on $p\text{O}_2$ tomography with CELSI technique [32,33]. In addition, excitation efficiency of PtG4 proportionally depends on oxygen concentration to some extent, which explains why the intensity in non-tumor region is higher than that in tumor one.

6. Discussion and conclusion

Based on beam scan parameters examined here, and the methodology of post processing the images, a reliable enhancement approach for CELSI imaging is proposed, with an available depth of $\sim 17\text{mm}$ into tissue or tissue-like medium with PtG4-dyed target. By making use of spatial control of the LINAC beam through the programmable MLCs, a modulation of the source (*i.e.*, collimated X-ray) beam could be automatically done, as is typical for radiotherapy regimens today. Phantom experiments showed that a square block pattern generally outperformed the linescan approach, by achieving a similar spatial resolution while providing less radiation dose. The linescan has the potential for faster acquisition but the dose increase can be problematic. Further investigations about these pattern parameters with respect to image fidelity gave a recommended side length of 38mm and beam pitch of 0.33 as specified for the measurement geometry adopted in this paper. From the MTF study results, it is possible to conclude that the spatial resolution at a target depth of 18mm improves from 5.2mm to 1.8mm with the optimized beam parameters. In addition to spatial-resolution enhancement, the proposed strategy was experimentally demonstrated to be capable of out-of-focus deblurring, which could be meaningful for non-contacting imaging modalities.

In most fluorescence imaging modalities, the model-based excitation light fluence-rate is hard to be well predicted with experimentally or empirically estimated optical properties. For CELSI, the excitation source is from X-ray induced Cherenkov photons, which can be captured by the same device for luminescence measurement with a different pulse delay. In this sense, the proposed deconvolution method matches very well with CELSI.

For deeper applications, efforts can be made towards using more optimized oxygen-sensitive probes at lower concentrations [11]. At the same time, scattering-caused blurring by luminescence photons could be compensated with the image deconvolution or reconstruction strategies for diffuse optical imaging [6]. Future work will focus on applying the proposed method to improve depth-resolved CELSI with angled incidence/detection configurations.

Funding

Congressionally Directed Medical Research Program for Breast Cancer Research Program; U.S. Army USAMRAA grant (W81XWH-16-1-0004); National Institutes of Health research grant (R01 EB024498).

Disclosures

The authors declare that there are no conflicts of interest related to this article.

Tissue pO₂ Distribution Changes Monitored During Fractionated Radiation Therapy by Cherenkov-Excited Phosphorescence Lifetime Imaging

Xu Cao^{1,2}, Srinivasa Rao Allu^{3,4}, Shudong Jiang^{1,5}, Mengyu Jia¹, Jason R. Gunn¹, Cuiping Yao^{1,6}, Ethan P. LaRochelle¹, Jennifer R. Shell¹, Petr Bruza¹, David J. Gladstone^{1,4,7}, Lesley A. Jarvis^{4,7}, Jie Tian^{2,8}, Sergei A. Vinogradov^{3,4*}, and Brian W. Pogue^{1,5,6*}

¹Dartmouth College, Thayer School of Engineering, Hanover, New Hampshire, USA

²Xidian University, Engineering Research Center of Molecular and Neuro Imaging of the Ministry of Education, School of Life Science and Technology, Xi'an, Shaanxi, China

³Department of Biochemistry and Biophysics, Perelman School of Medicine, University of Pennsylvania, Philadelphia, PA, USA.

⁴Department of Chemistry, School of Arts and Sciences, University of Pennsylvania, Philadelphia, PA, USA.

⁵Norris Cotton Cancer Center, Dartmouth-Hitchcock Medical Center, Lebanon, NH, USA.

⁶Xi'an Jiaotong University, Institute of Biomedical Analytical Technology and Instrumentation, School of Life Science and Technology, Key Laboratory of Biomedical Information Engineering of Ministry of Education, Xi'an, Shaanxi, China

⁷Department of Medicine, Geisel School of Medicine, Dartmouth College, Hanover, New Hampshire, USA.

⁸CAS Key Laboratory of Molecular Imaging, Institute of Automation, Chinese Academy of Sciences, Beijing, China.

* Manuscript correspondence to: Brian W. Pogue brian.w.pogue@dartmouth.edu or Sergei A. Vinogradov vinograd.upenn@gmail.com

ABSTRACT

Hypoxia in solid tumors is thought to be an important factor in resistance to therapy, but the extreme microscopic heterogeneity of the partial pressures of oxygen (pO₂) between the capillaries leads to an inability to effectively characterize the scope of this phenomenon without invasive sampling of the oxygen distributions throughout the tissue. In this study, we developed a non-invasive way to track oxygen spatial distributions in tumors each day during fractionated radiotherapy, using oxygen-dependent quenching of phosphorescence probe Oxyphor PtG4 in combination with the radiotherapy-induced Cherenkov light to excite and image the luminescence lifetimes within tissue. The Oxyphor PtG4 probe remained present in tumor tissue for one week after a single intravenous injection, and the pO₂ images were obtained from millimeters of subsurface tissue. Two tumor lines were studied during each of 5 fractions of 5 Gy, delivered from a clinical linear accelerator with 6MV X-rays. During the treatment course, a radiation responsive tumor line (MDA-MB-231) had a mean pO₂ increase by a factor of 2, with a hypoxic fraction decrease to 25% of the baseline leading to acute tumor volume regression, while a radiation resistant line (FaDu) remained unchanged in either mean pO₂ or hypoxic fraction with a much later tumor volume response. This study is the first demonstration of subsurface *in-vivo* mapping of tumor pO₂ distributions directly from radiotherapy on a spatial resolution scale that matches typical inter-capillary distances, providing a fundamentally new methodology to track tumor pO₂ response in fractionated radiotherapy.

INTRODUCTION

Low levels of partial pressure of oxygen (pO_2) in tissue that define hypoxia, are known to reduce the potential for therapeutic radiation damage, inducing tumor cell resistance and facilitating tumor cells escape from treatment.¹⁻³ Meta-analyses reveal that improvement in regional control is primarily observed in patients with well-oxygenated tumors and not in patients with hypoxic tumors^{4,5}. Clinical trials have tried to reduce hypoxia in radiotherapy by patient administration of carbogen and nicotinamide^{6,7} or to provide radiation boost to these areas with dose intensification⁸ although no methodology has yet gained widespread adoption. Part of the issue is that progress in understanding and clinically addressing consequences of hypoxia has been limited due to the lack of methods for non-invasive, fast and repeatable mapping of pO_2 distributions in tumor tissues in a manner which reflects the microscopic biological distributions and temporal changes in pO_2 . Multiple track oxygen electrode measurements⁹ or *ex-vivo* tissue immunohistochemistry¹⁰ suffer from obvious invasive issues limiting their practical utility. Macroscopic assessment of tumor oxygenation in humans has been performed by Positron Emission Tomography (PET) with fluoromisonidazole (FMISO) hypoxia tracer^{11,12} and Blood Oxygen Level Dependent (BOLD) Magnetic Resonance Imaging^{13,14}. However, these macroscopic imaging tools do not fully sample the heterogeneity of microenvironment on the spatial scale of inter-capillary distances, where both chronic and transient hypoxia are documented to be microregional¹⁵. Additionally, measurements originating from blood oxygenation can report on changes in the vasculature, whereas in tissues with abnormally developed vasculature, such as tumors, blood pO_2 levels are only poorly correlated with extravascular 'tissue' pO_2 , and hence tissue oxygen may be misrepresented. The two issues of i) measuring pO_2 at inter-capillary locations and ii) measuring the heterogeneity of these distributions, were key motivating factors for this study.

Oxygen-dependent quenching of phosphorescence^{16,17} has been used in the past to map oxygen distributions in subcutaneous tumors in animal models¹⁸⁻²¹ showing both macroscopic and microscopic sensitivity depending upon the magnification of the imaging system used. These measures have also shown correlation between tumor pO_2 levels and radiation sensitivity^{22,23}. When applied in conjunction with dendritically-protected, PEGylated oxygen probes^{21,24,25} the phosphorescence quenching method enables unbiased and accurate measurements of absolute tissue oxygen concentrations. However, high-resolution imaging by phosphorescence is possible only at relatively shallow depths, typically not exceeding 0.5-1 mm, by means of two-photon microscopy^{24,27}, while volumetric phosphorescence lifetime tomography²⁸ suffers from low resolution similar to other diffuse tomographic methods.

Recently, a new approach has been developed that combines phosphorescence quenching with excitation by the Cherenkov light generated 1-3 centimeters deep within tissues that are subjected to high-energy radiation for the purpose of fractionated radiotherapy²⁹⁻³¹. This method, termed here Cherenkov-Excited Phosphorescence Lifetime Imaging (CEPLI), has been used in the present study with the goal of realizing direct, real-time high-resolution imaging of tumor pO_2 distributions precisely at the time of radiation delivery. It is well known that hypoxic changes can dynamically cycle on the timescale of even a single radiotherapy fraction, and the ability to image oxygen within the tumor tissue at the actual time of radiation delivery would be an invaluable asset for planning and monitoring outcome of clinical radiation therapy. With CEPLI imaging of a broad beam irradiated tissue, the luminescence captured is known to come from an average of 3-6 mm axial depth within the tumor, and the lateral spatial resolution is defined by the optics of the imaging camera, but can be several hundred microns³¹. The result is that there is high depth sensitivity to measuring pO_2 , with lateral spatial resolution near 100 microns.

In this study, CEPLI with Oxyphor PtG4 (**Supplementary Fig. 1**) was used. Cherenkov light generated within tissue from therapeutic megavolt (MV) X-ray irradiation, providing a light source. This excitation of the luminescence of Oxyphor PtG4 is implicitly pulsed by the linear accelerator (Linac), and the imaging was temporally synchronized by a time-gated intensified charge coupled device (ICCD) camera that captured emission at different microsecond delay times after each radiation pulse (**Supplementary Fig. 2a**). The images of phosphorescence at different delays were used to construct an image of phosphorescence lifetimes by applying pixel-wise exponential fitting (**Supplementary Fig. 2b**). The PtG4 emission lifetime is a direct sensor of micro-environmental pO_2 within the tissue, since the calibration parameters of dendritic probes are stable in biological environments^{21,24}. Notably here, the tissue pO_2 values are obtained through phosphorescence lifetimes, not absolute intensity, thereby being unaffected by optical heterogeneities of the tissue and insensitive to changes in the probe distribution and/or probe quantity, as long as sufficient amounts of the

probe are present for adequate signal acquisition. The value of this approach was studied in a hypofractionated radiation therapy scheme, using a single intravascular injection of Oxyphor PtG4 before the first fraction radiation, to allow tracking of oxygen dynamics in each tumor for every day of treatment.

RESULTS

Bio-distribution of PtG4

To understand the bio-distribution of Oxyphor PtG4 after tail vein intravenous (IV) injection, optical phosphorescence imaging was used to image the harvested organs at different time points. The phosphorescence signal from Oxyphor PtG4 reached a peak within 5 minutes in the heart, lung, liver, spleen, kidneys and brain, while the highest phosphorescence signal in tumor was at 24-hour in the temporal trends (Fig. 1a). The phosphorescence signals at 24-hour are shown *ex-vivo* (Fig. 1b) and quantitative analysis (Fig. 1c). The *in-vivo* images for three mice at the 24-hour time point yielded visibly higher phosphorescence signals in the tumors consistently with the results observed *in-vivo* (Fig. 1d). The bulk signal ratios of tumor to normal tissue reached double at this time point (Fig. 1e).

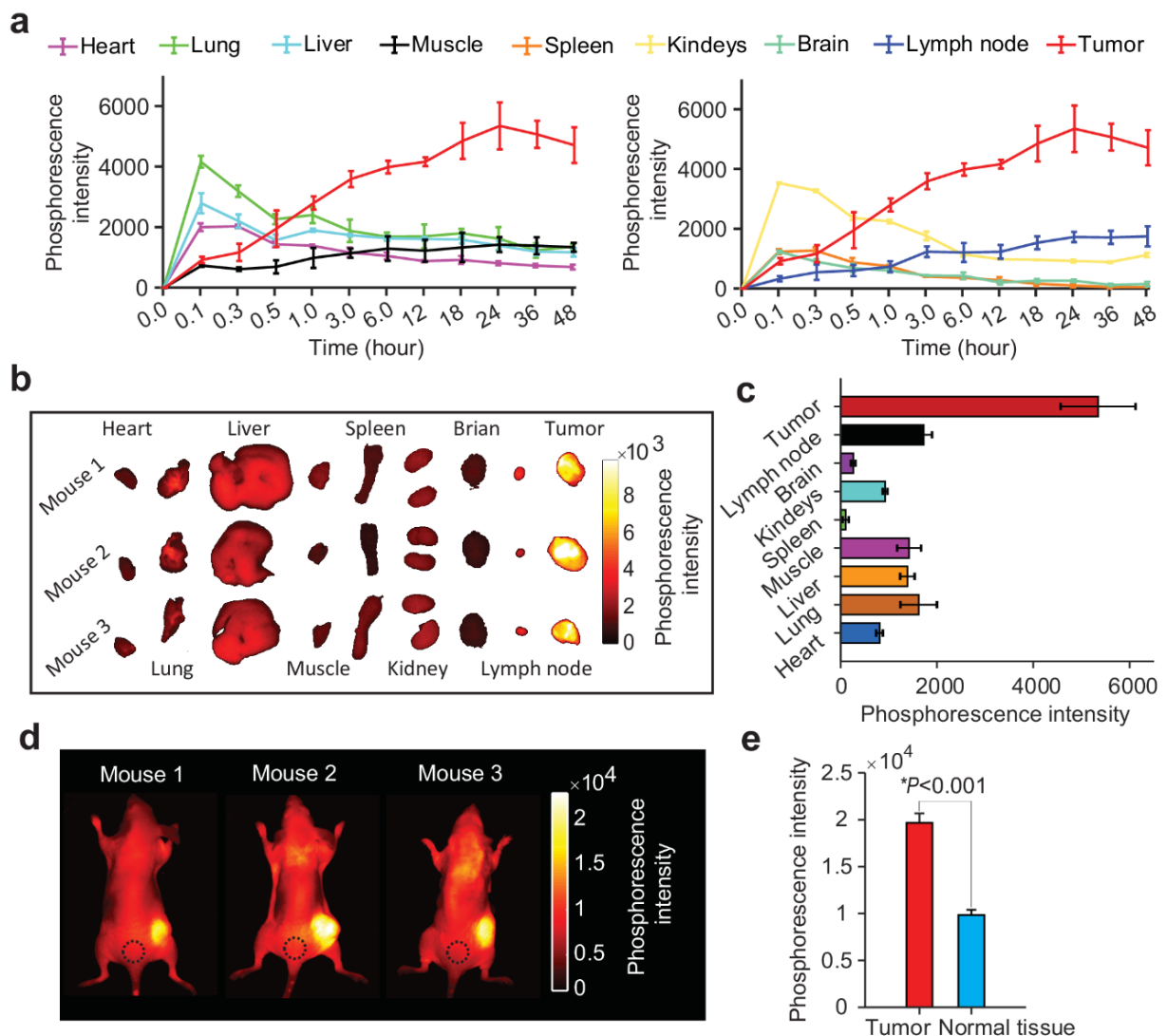
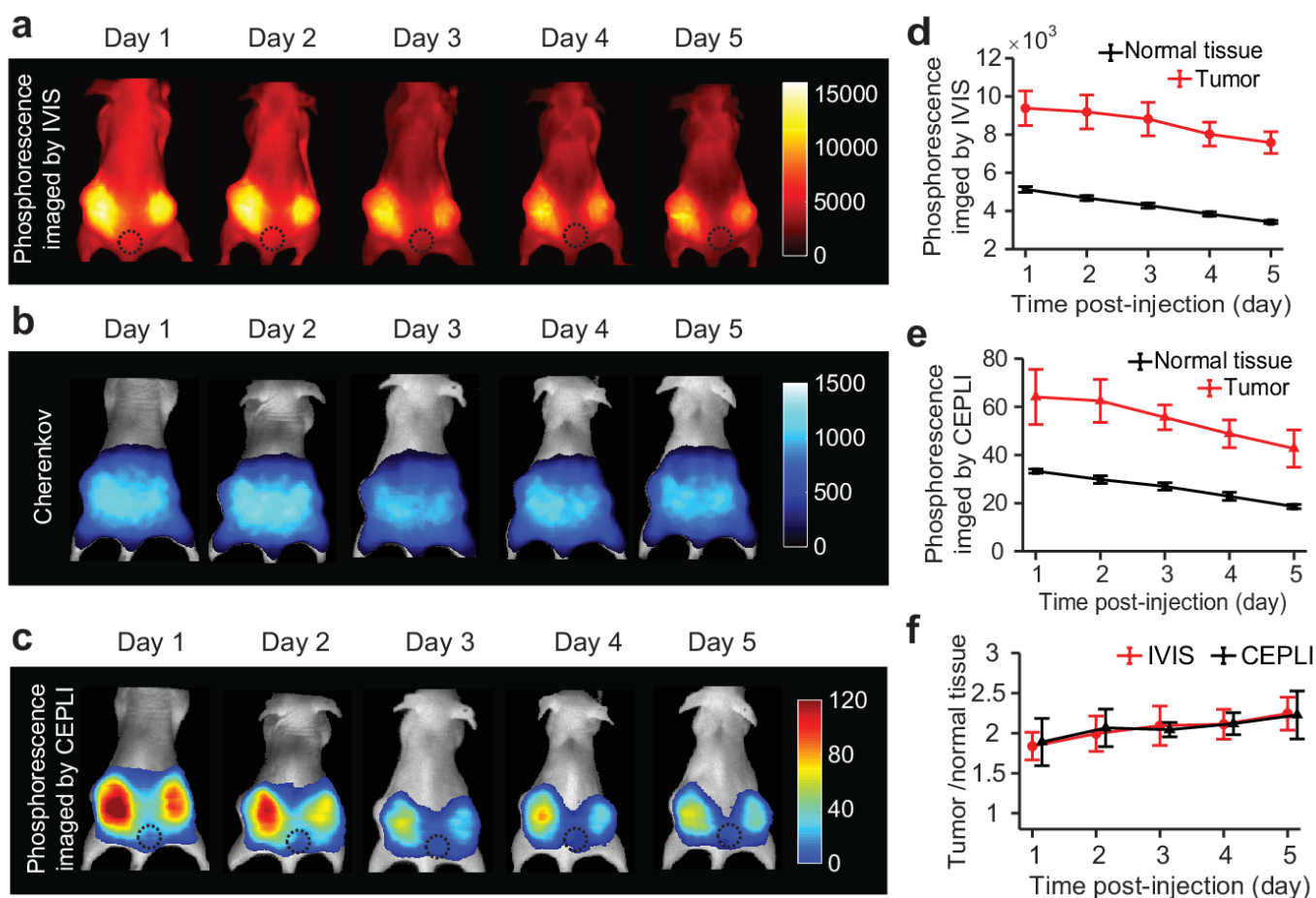


Figure 1 Bio-distribution of PtG4 at different time points in MDA-MB-231 tumors. (a) Longitudinal phosphorescence signals from different organs and tumors (mean \pm SE, n= 3), from a total of 12 time points were captured (n=3 mice per time point, n=36 mice total). After sacrifice and excision, *ex-vivo* images were acquired as shown in (b), with quantitative values at the 24-hour timepoint (c) after IV injection of PtG4 (mean \pm SE, n= 3). The *in-vivo* phosphorescence images (d) and bar graph (e) of 3 mice at 24-hour after PtG4 injection, with normal tissue areas marked by a black dashed circle. The mean signal from tumor ($1.97\pm 0.16\times 10^4$ counts) was twice that relative to normal tissue ($0.98\pm 0.09\times 10^4$ counts) (n=3 mice).

105 Four mice were imaged by IVIS and CEPLI every day for 5 days, after IV injection of PtG4. The radiation used for CEPLI
 106 was a broad beam, as shown in the Cherenkov images, that covered the entire abdomen and both tumor areas (Fig. 2b,
 107 false colored in blue). Phosphorescence images acquired by IVIS and CEPLI indicated that the PtG4 in the tumor lasted
 108 for 5 days, which provided a possibility for imaging hypoxia over the multiple-fraction radiotherapy with a single PtG4
 109 injection (Fig. 2a, c). The phosphorescence intensity of PtG4 in the tumor reached its peak on day 3 and decreased
 110 gradually in the latter 2 days, while the signal intensity in the normal tissue decreased monotonically from day 1 to day
 111 5 (Fig. 2d, e). Since the signal intensity of normal tissue decreased faster than that of tumors, the signal ratio of tumor to
 112 the normal tissue slightly increased from 1.8 ± 0.4 to 2.2 ± 0.2 (mean \pm SE, $n = 3$) from day 1 to day 5 (Fig. 2f).



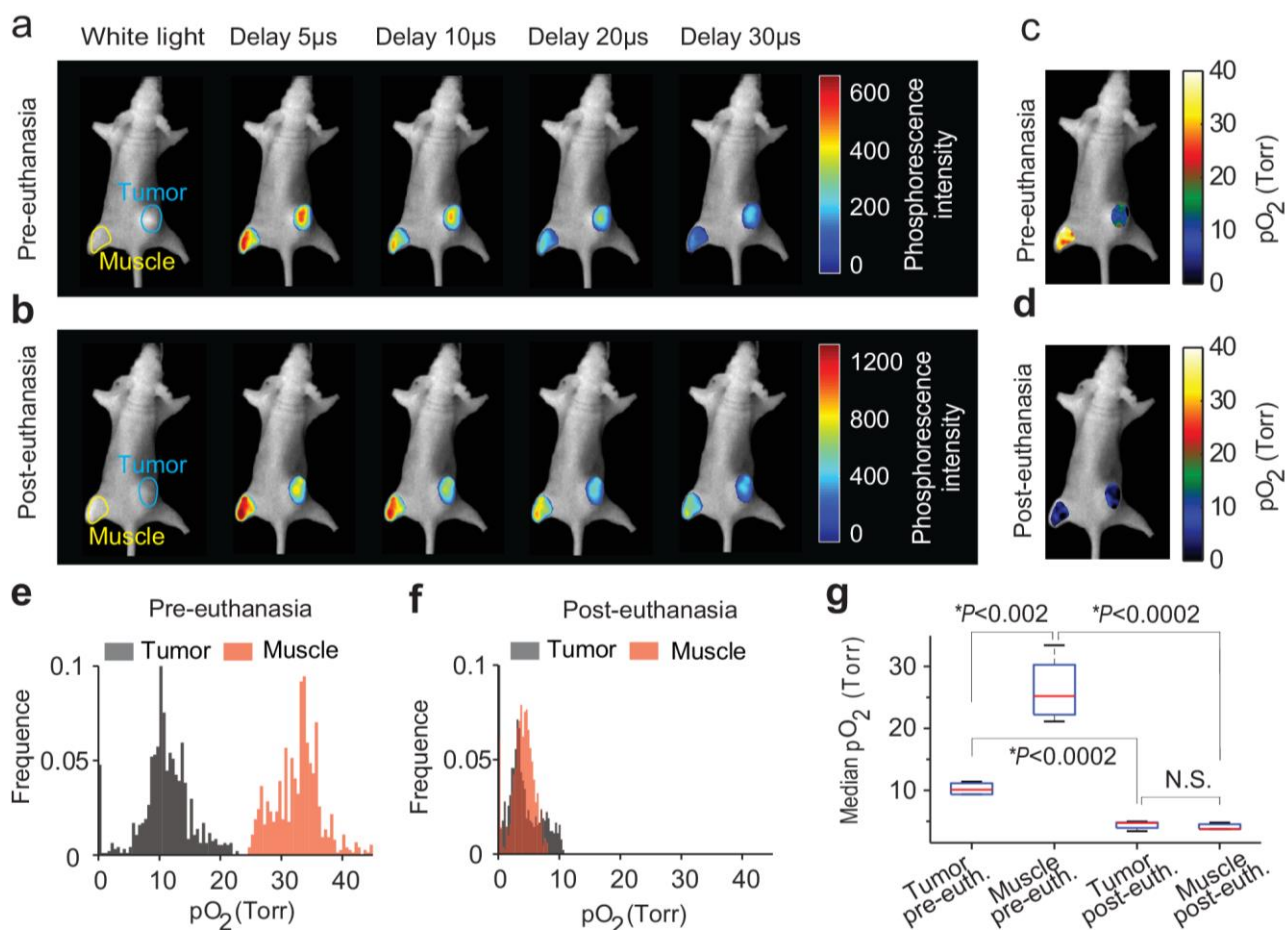
113
 114 **Figure 2** Longitudinal *in-vivo* imaging of PtG4 in MDA-MB-231 tumors up to 5 days after IV injection. (a) Phosphorescence
 115 images acquired by using IVIS optical emission, and in (b) Cherenkov images were taken while the radiation was carried out to
 116 confirm the radiation beam cover the entire tumor areas. In (c) phosphorescence CEPLI images are shown for these 5 day. Average
 117 phosphorescence signals from IVIS (d) and CEPLI (e) are plotted from tumor and normal tissue (mean \pm SE, $n = 4$). The signal ratio
 118 of tumor to normal tissue (f) imaged by IVIS and CEPLI (mean \pm SE, $n = 4$) are shown.

119
 120
 121

122 *In-vivo* pO₂ imaging for tumor and muscle with local PtG4 injection

123 To demonstrate the possibility of *in-vivo* pO₂ imaging of tumor and muscle under pre-euthanasia and post-euthanasia
 124 conditions, PtG4 was locally injected in situ into the tumor and thigh muscle 10 minutes before imaging. CEPLI images
 125 were captured with different delay times, including before (Fig. 3a), and 30 minutes after (Fig. 3b) euthanasia. For both
 126 pre-euthanasia and post-euthanasia, phosphorescence signals in both areas decreased in response to delay time increases
 127 from 5 μ s to 30 μ s. Phosphorescence signals in both pre-euthanasia tumor and muscle areas were higher than those in
 128 post-euthanasia cases (Fig. 3a, b). The *in-vivo* oxygen maps were obtained by first exponential fitting the

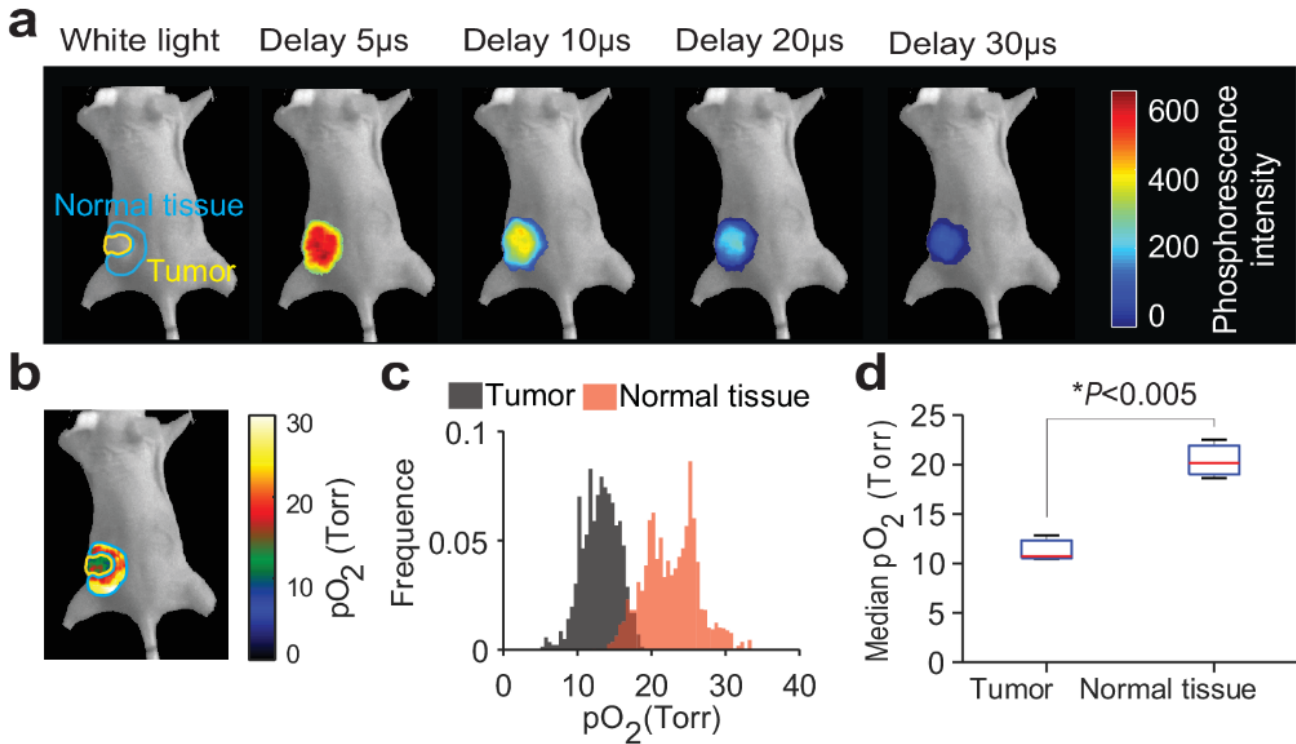
129 phosphorescence signals versus delay time at each point, to create lifetime maps of the tissue, and then calculating the
 130 pO_2 using the Stern-Volmer equation, on a pixel by pixel basis (Fig. 3c, d). The accuracy of lifetime measurement for
 131 PtG4 based on CEPLI was first verified *ex-vivo* by a time-resolved fluorimeter (**Supplementary Fig. 3**). The pO_2 values
 132 in tumor were significantly lower than that in muscle when the mouse was alive (Fig. 3c), while pO_2 values in both tumor
 133 and muscle dropped to near zero when the mouse was euthanatized (Fig. 3d). The distributions of pO_2 values in tumor
 134 and muscle were different before euthanasia, but almost the same after euthanasia as shown in pO_2 histograms (Fig. 3e,
 135 f). Boxplots of the median pO_2 values in tumor and muscle areas showed a significant difference between tumor and
 136 muscle before euthanasia (P-value < 0.002, n=4), but no difference after euthanasia (Fig. 3g). Furthermore, significant
 137 differences of pO_2 values were found between pre-euthanasia and post-euthanasia for both of tumor (P-value < 0.0002,
 138 n=4) and muscle (P-value < 0.0002, n=4) (Fig. 3g).



139
 140 **Figure 3** *In-vivo* pO_2 imaging of tumor and muscle before and 30 minutes after euthanasia. PtG4 was directly injected into
 141 MDA-MB-231 tumor (blue circle) and muscle (yellow circle) before the imaging started. (a, b) CEPLI images were acquired with
 142 different delay times, before (a) and after euthanasia (b). CEPLI images are overlaid on the white light image, which was taken before
 143 CEPLI. Tumor and muscle areas for analysis are circled in (a) in the mouse white light images. The delay time were 5, 10, 20, and 30
 144 μs , respectively. In (c-d) tissue oxygen maps are shown and (e-f) histograms are shown before and after euthanasia, respectively. (g)
 145 Box plots of oxygen in tumor and muscle are shown for (n=3 mice) before and after euthanasia.

146 ***In-vivo* pO_2 imaging for the mice with tail intravenous PtG4 injection**

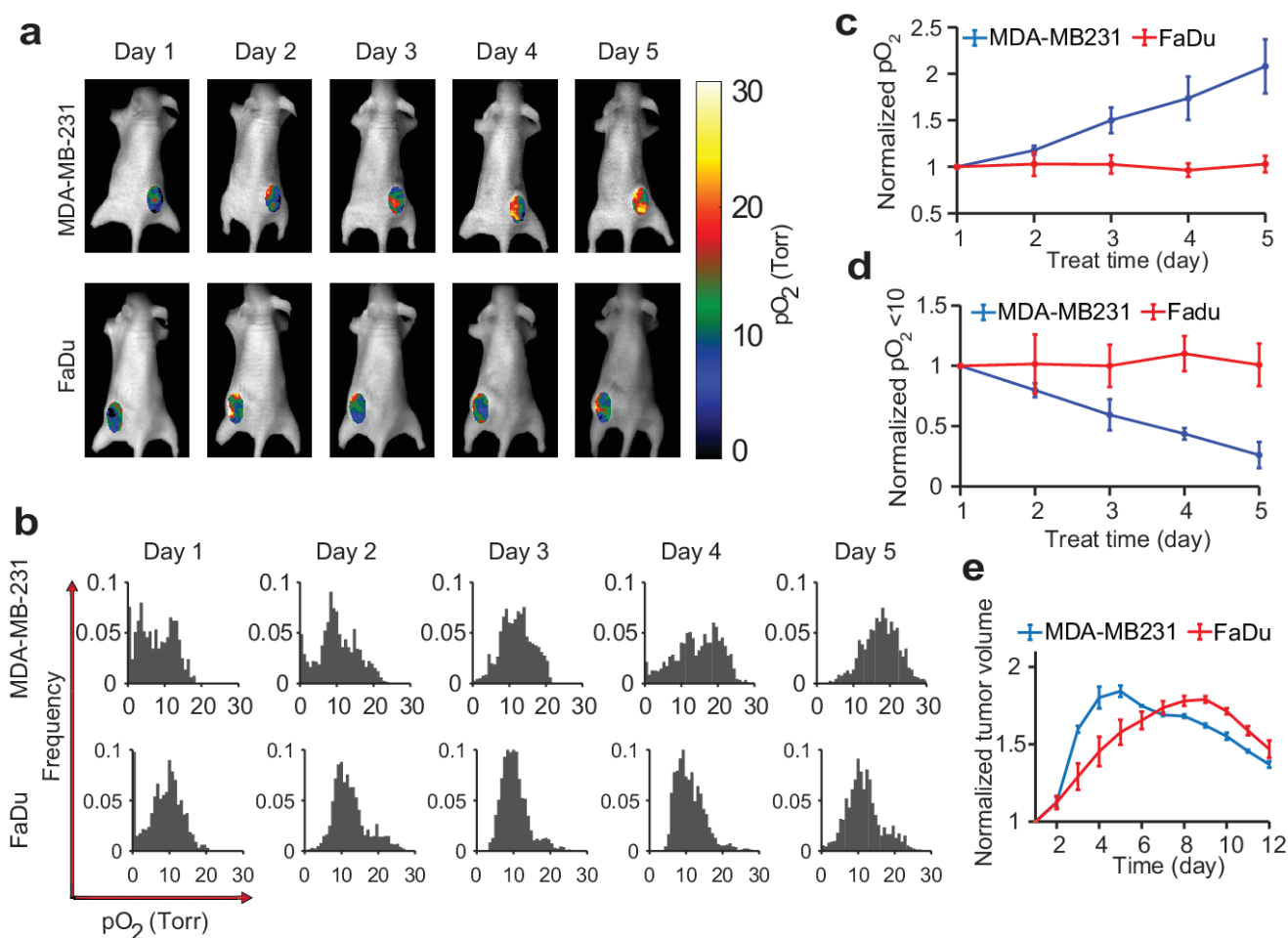
147 200 μL PtG4 with concentration of 200 μM was intravenously injected into a mouse tail vein, and then CEPLI images
 148 with different delay times were acquired 24 hours later (Fig. 4a). Phosphorescence signals of PtG4 in both tumor and
 149 surrounding normal tissue decreased while the delay time increased from 5 μs to 30 μs . The lower pO_2 value of tumor
 150 versus that of surrounding normal tissue indicated significant hypoxia existed in the tumor (Fig. 4b). Statistically
 151 significant differences (P < 0.005, n=3) are shown in Fig.4 (d) between median pO_2 values in tumor (11.3 \pm 0.8 Torr, mean
 152 \pm SE) and normal tissue (20.4 \pm 1.1 Torr, mean \pm SE). We also tested the possibility of CEPLI to *in-vivo* monitor pO_2
 153 responses to the promotion of oxygen consumption of tumor cell (**Supplementary Fig. 4**).



154 **Figure 4** In vivo pO₂ imaging of mice with MDA-MB-231 tumors 24 hours after intravenous injection of PtG4. (a) CEPLI
 155 images of a mouse are shown acquired with different delay times of 5, 10, 20, and 30 μ s as noted above. CEPLI images are overlaid
 156 on the white light image which was taken before CEPLI. In the first white light image in (a) the yellow and blue curves outline the
 157 regions of tumor and normal surrounding tissue, and (b) shows the tissue oxygen map and (c) the histogram of values. (d) shows
 158 box plots of oxygen in tumor and surrounding normal tissue (n=3 mice).

159 **In-vivo imaging of pO₂ during multiple-fractions of radiotherapy**

160 Six mice with subcutaneous MDA-MB-231 or FaDu tumors were imaged while undergoing 5-day multiple-fraction
 161 radiotherapy. The delivery included 6MV photon beams with 5 Gy/fraction daily, for 5 days, for a total radiation dose of
 162 25 Gy. PtG4 was IV injected 24 hours before the first treatment, and CEPLI images of PtG4 with different delay times
 163 were acquired during each fraction of radiation. The spatial and temporal heterogeneous pO₂ distributions of both MDA-
 164 MB-231 and FaDu tumors demonstrated high heterogeneity of the hypoxic areas within them^{29,30}, and the decrease in
 165 regions of the hypoxic tumor with progression of the fractionated radiotherapy was more obvious for the MDA-MB-231
 166 tumor line than for the FaDu line (Fig. 5a). The pO₂ values of the two tumor lines were distributed mainly below 20 torr
 167 on the first day, and increased into the range of 5 to 30 torr for MDA-MB-231 tumor line versus 0 to 25 torr for FaDu
 168 (Fig. 5b). The median pO₂ values of MDA-MB-231 increased with the progression of radiotherapy fractions, while no
 169 obvious change was seen for FaDu (Fig. 5c). The proportion of median pO₂ values <10 torr for MDA-MB-231 decreased
 170 during the multiple-fraction radiotherapy, but FaDu showed no obvious change, implying more hypoxic and
 171 radioresistant tumor with worse local control and overall survival³¹ (Fig. 5d). Tumor volumes responding to radiotherapy
 172 had less sensitivity as compared with pO₂ value changes, as tumor volumes started to decrease from day 5 for MDA-MB-
 173 231 tumors and day 9 for FaDu tumors respectively (Fig. 5e). These pO₂ and tumor volume changes in MDA-MB-231
 174 tumors suggested these tumors were more reactive to the radiation damage, as compared to FaDu tumors. The
 175 histological changes of tumors induced by radiation were evaluated by hematoxylin and eosin (H&E), HIF-1 α , TUNNEL
 176 and cleaved caspase-3 staining assays (Supplementary Fig. 5).



177

178

179

180

181

182

183

184

185

186

187

188

189

190

191

192

193

194

195

196

197

198

199

200

201

Figure 5 *In-vivo* longitudinal pO_2 imaging of mice with MDA-MB-231 or FaDu tumors, during 5-days of fractionated radiotherapy. (a, b) are example pO_2 images (a) and histograms (b), acquired during each day of radiotherapy treatment for both MDA-MB-231 and FaDu tumors. (c-d) shows pO_2 changes (c) and relative change of hypoxic fraction with $pO_2 < 10$ Torr during the 5-days of radiotherapy relative to the start of irradiation. The pO_2 and proportion of $pO_2 < 10$ were normalized by the first measurements during the fraction treatment on day 1. In (e) tumor volume changes during and after the radiotherapy are shown, normalized by the pre-treatment volume.

DISCUSSION

185

186

187

188

189

190

191

192

193

194

195

196

197

198

199

200

201

Incomplete response or lack of local control of tumor following radiotherapy is thought to be partially related to the hypoxic fraction of cells that have poor radiation sensitivity and promote escape signaling within their heterogeneous tumor environment. These hypoxic areas are known to be microscopically heterogeneous on a spatial scale dictated by the inter-capillary spacing, near hundreds of microns³². Methods to alter hypoxia via modification in combination with radiotherapy have been extensively investigated³²⁻³⁴, but all these approaches are limited incomplete methods to identify the individuals who would benefit from interventions or the inability to track if interventions are having the desired effect³³. There is a significant need to have tools to assess the distribution of pO_2 values across a tumor with the spatial resolution that matches the biology of the heterogeneity and therefore can be used to determine hypoxic fraction in situ³⁵⁻³⁷. The PtG4 based CEPLI for imaging pO_2 maps and detection of hypoxia demonstrated in this study could help to identify individual regions of hypoxia, and be used to understand whether increasing the radiation dose, either to the whole tumor or to a hypoxic sub-volume, improves clinical outcomes. The fact that it can be done as part of a fractionated radiotherapy scheme makes the approach particularly interesting for future clinical applications. Clearly, in this version, the limiting factor is the optical perspective of view which needs access to the tumor, and largely just senses the image from the first few mm of subcutaneous tissue, but future realizations of the technique could be adapted for intracavitary or near surface tumors. Alternatively, this technique might only be utilized in pre-clinical translational research studies, but it still provides unprecedented access to non-invasive sampling of pO_2 across a tumor surface, with near microscopic spatial resolution.

PtG4 was developed as a non-specific targeted phosphorescent probe that balances the right approach to bio-distribution with oxygen quenching sensitivity. In this work, it has been shown for the first time to localize within the tumor at a higher concentration than surrounding normal tissues and retain this localization for over a week. This preferential localization is presumably due to the tumor enhanced permeability and retention effect (EPR), and not likely due to chemical bonding. In addition, the strong luminescence quenching of PtG4 within higher oxygen concentration regions such as normal tissues, results in the phosphorescent signals from normal tissues being at least a factor of 2 lower than that from tumors (Fig. 1e), providing natural signal selection for hypoxic regions such as in solid tumors. Cellular localization studies (**Supplementary Fig. 6**) show that the agent is present across the cellular content of the tumor. There may be slightly higher sequestration into necrotic areas at longer time points, but there is also more necrosis at these time points, so this is hard to assay. Still cellular localization appears to be present throughout the time course studied here, in both tumor lines.

Since one injection of PtG4 allowed for imaging over multiple days, and possibly weeks, this can provide a very simple operational process to allow pO₂ imaging during fractionated radiotherapy. This observation alone makes this a strikingly strong value for the dye. Since the pO₂ was estimated from lifetime of PtG4, the decay of phosphorescent intensity signals from clearance of PtG4 during the treatment course will not affect the tissue oxygen mapping. Longer-term residence of PtG4 remains to be investigated as well as any long-term toxicity issues, while MTT results partially implied PtG4 have small effect to the physiological function of tumor cells (**Supplementary Fig. 7**). However, the dominant cause of the localization appears to be retention in the tumor, and the clearance of dye from the body seems to be equally contributed by both digestive and renal processes. These latter aspects of pharmacology remain to be studied.

Compared to other conventions of pO₂ measurement, the unique advantage of this CEPLI approach is in acquisition of whole pO₂ images at a spatial resolution that allows recovery of relevant biological pO₂ histograms of the tumor, and that this is acquired simultaneous with radiotherapy delivery in multiple fractions. The clear limitation of this approach is only 2D images of tissue oxygen can be obtained, yet there is no current method for volumetric histogram imaging at biologically relevant spatial resolution. Our previous studies showed the 3D tomographic imaging of PtG4 by using a light sheet excitation geometry with nonlinear diffuse optical tomographic reconstruction strategy to obtain sub-millimeter spatial resolutions in vivo²⁹. By using such imaging technology, 3D tomographic lifetime imaging of PtG4 could be acquired to reflect the heterogeneous pO₂ distributions inside tumor with high spatial resolutions in vivo. This is a technological area which could be examined in future work, requiring significant optimization of radiation dose, PtG4 dose and detection sensitivity.

METHODS

Molecular oxygen probe PtG4. Oxyphor PtG4 belongs to the family of dendritic oxygen probes.²⁴ It is a direct analog of the probe Oxyphor G4 (or PdG4),²¹ different only by the core dye atom, which was Platinum, as opposed to Palladium, within the tetrabenzoporphyrin molecule (**Supplementary Fig. 1a**). The porphyrin is responsible for the key optical properties of the probe, which include two highly intense absorption bands, one of which strongly overlaps with the Cherenkov spectrum ($\lambda_{\max}=435$ nm), and it has a strong phosphorescence ($\lambda_{\max}=780$ nm, QY~0.07 in deoxygenated aq. solutions), which is located optimally in the tissue near-infrared window where mammalian tissue has its minimum absorption (**Supplementary Fig. 1b**). The porphyrin molecule is encapsulated in a hydrophobic pocket, formed by folded aryl-glycine dendrimers. This dendrimer coating protects the porphyrin from interactions with various endogenous molecules and simultaneously brings the probe's sensitivity to the desired range by slowing down diffusion of oxygen in the vicinity of the excited state chromophore. In unprotected porphyrins, the rate of quenching is so high that even at low oxygen concentrations the phosphorescence signal is almost fully quenched. An additional essential feature of the probe is that its exterior is extensively modified with polyethyleneglycol (PEG) residues, making it hydrophilic but also highly inert with respect to biological macromolecules. It is due to this extensive PEGylation that the probe calibration parameters remain completely stable in biological environments. Whether PtG4 is dissolved in a buffered solution *in-vitro* or in blood plasma or interstitial fluid *in-vivo*, its phosphorescence lifetime can be unambiguously translated into local oxygen concentration. The molecular weight of PtG4 is ~35 kDa and the approximate diameter of the molecule in its folded state in aqueous medium is estimated at d~5-6 nm, based on molecular mechanic simulations. Therefore, PtG4 can easily diffuse into the tumor interstitial space from the leaky vasculature and remain there, a phenomenon known as enhanced permeability and retention (EPR) effect. However, the PEG coating prevents PtG4 from permeating cellular membranes, and also serves to reduce phototoxicity. The pO₂ readings, therefore, give average intratumoral tissue pO₂ at their site of extracellular localization, which should be in equilibrium with surrounding intracellular pO₂.

The native unquenched luminescent lifetime of PtG4 was measured as $\tau=44.6$ microseconds with a Stern-Volmer quenching constant of $k_q=366$ mmHg⁻¹ s⁻¹ and each batch was calibrated for oxygen pO₂ responsivity via an oxygen titration study, taking into account the temporal sampling of the emission signals after the excitation pulse. Using four time windows of acquisition in a 'stroboscopic' approach at 5, 10, 20, and 30 us varying delay times after the Linac pulse, with an integration time of 200 us. These temporal acquisition bands were used to acquire intensity for luminescence decay fitting, and calibration of known pO₂ versus observed emission lifetime, as captured in a custom set up. Data showed a high linearity between $1/\tau$ and pO₂ indicating the Stern-Volmer calibration quenching constant k_q and the lifetime τ were accurate (**Supplementary Fig. 1c**).

Tumor cell lines. The human breast cancer cell line MDA-MB-231 and human head neck cancer cell line FaDu cells were purchased directly from American Type Culture Collection (ATCC, Manassas Virginia). These are not listed in the ICLAC database of cross-contaminated or misidentified cell lines. Cells were grown in culture media in a humidified incubator at 37 °C and 5% CO₂ in MEM with 10% (v/v) fetal bovine serum (FBS), 100U/ml penicillin and 100ug/ml streptomycin. When ready for use, cells were trypsinized, counted, pelleted, and resuspended for injection.

Animal preparation. This study was approved by the Dartmouth Institutional Animal Care and Use Committee, and all procedures followed this approved protocol. Nude female mice at age of 6-8weeks (Charles River Labs, Wilmington, MA) were involved in this study. 10⁶ MDA-MB-231 or 10⁶ FaDu tumor cells were injected subcutaneously under the skin on the flank of each nude mouse. The mice were housed in the Dartmouth central animal facility and fed special diet- MP biomedical purified diet. After approximately 2 weeks of growth, animals were chosen for imaging when their tumor diameter was approximately 8 mm in size. On the day of initial use, mice were anesthetized and PtG4 was either injected into a tail vein (200 μ L PtG4 with the concentration of 200 μ M), or locally injected into the tumor or normal muscle directly for some experiments as noted (50 μ L PtG4 with the concentration of 200 μ M), right before the first *in-vivo* imaging session.

278 **In vitro phosphorescence imaging of biodistribution.** IVIS imaging was used to image the harvested organs (heart,
279 lung, liver, spleen, kidneys, brain, muscle, lymph node and tumor). Excitation and emission wavelengths were 620nm
280 and 790nm, respectively. In total 36 mice with MDA-MB-231 tumors were tail intravenously injected with 100 μ L PtG4
281 with concentration of 100 μ M per mice. At each of 12 time points of 0, 5min, 15min, 30min, 1h, 3h, 6h, 12h, 18h, 24h,
282 36h, and 48h, organs from three mice were imaged.

283
284 **Cherenkov-Excited Phosphorescence Lifetime Imaging (CEPLI) during Radiotherapy.** Cherenkov light was induced
285 in the tissue by irradiation from a linear accelerator (Varian Linac 2100CD, Varian Medical System), at the Norris Cotton
286 Cancer Center, Dartmouth-Hitchcock Medical Center. The beam size was adjusted to cover the entire tumor area for
287 treatment purposes. To minimize background light signals, the room lights were switched off, and all indicator lamps
288 masked with black cloth and black tape. The imaging system consisted of a time-gated intensified CCD camera (ICCD,
289 PI-MAX4 1024i, Princeton Instruments), a commercial lens (Canon EF 135mmf/2L USM) and an 750nm/100nm band
290 pass filter. The camera was put in a homemade lead box about 2 meters away from the imaging field, to shield it from
291 Compton scattered X-ray photons. The noise induced by X-ray photons was significantly suppressed, and the signal to
292 noise ratio (SNR) of CEPLI could be improved more than 7 times after shield (Supplementary Fig. 8). The time-gated
293 ICCD camera was synchronized to the radiation pulses (approximately of 3.25 μ s duration, 360Hz repetition rate) and
294 turned on at 5, 10, 20, and 30 us varying delay times for phosphorescence measurements. The intensifier gain was x100
295 and the luminescence signal generated during the 200 μ s gate width was integrated.

296
297 **Longitudinal imaging study.** The mice with PtG4 injected were continuously imaged for the 5 days during their
298 hypofractionated radiotherapy, using both the IVIS Spectrum CT system (Perkin Elmer) and with CEPLI during the
299 radiotherapy. All mice were under general anesthesia of inhaled isoflurane at 1-3% in flowing oxygen through a nose
300 cone, throughout imaging. For each of these five days, the CEPLI images were acquired during irradiation.

301
302 **Cytotoxicity assay.** In vitro cytotoxicity was measured by performing MTT assays on MDA-MB-231 cells. Different
303 concentrations of PtG4 (0, 10, 20 and 40 μ M diluted in PBS) were added to the wells. The samples were incubated for
304 24h in a cell culture incubator, and 10 μ L of 5 mg/mL MTT solution [3-(4,5-Dimethylthiazolyl-2)-2,5-diphenyl
305 Tetrazolium Bromide, MP Biomedical, Solon OH] was added to each well. After incubating the plate for another 6h in a
306 cell culture incubator, media is removed from all wells and 150 μ L of acidified isopropanol added to each well. Finally,
307 the percentage of living cells was determined based on the measured Optical Density (OD) at 540nm.

308
309 **Statistical analysis.** All statistical analyses testing for differences in pO₂ between treatment groups in this study were
310 done using Two-sample *t*-test with Matlab (Mathworks, Inc., Natick, MA)

ACKNOWLEDGMENTS

This work was funded by NIH grant R01 EB024498 as well as using shared irradiation resources from the Norris Cotton Cancer Center funded by P30 CA023108.

AUTHOR CONTRIBUTIONS

X.C. designed the experiments, analyzed all imaging data and wrote the paper. X.C., M.J.J., J.R.G., and C.Y. carried out the experiments and edited the manuscript. S.J. helped design the experiments and write of the paper. E.P.L., J.R.S. and P.B. provided advice on experimental design and data analysis and edited the manuscript. S. R. A. and S.A.V. provided the molecular probe PtG4 as well as edited the manuscript. D.J.G. and L.A.J. contributed advice on radiotherapy design and data interpretation and edited the manuscript. J.T. edited the manuscript. B.W.P. conceived the study, analyzed the data, provided full support for the work and edited the manuscript.

COMPETING FINANCIAL INTERESTS

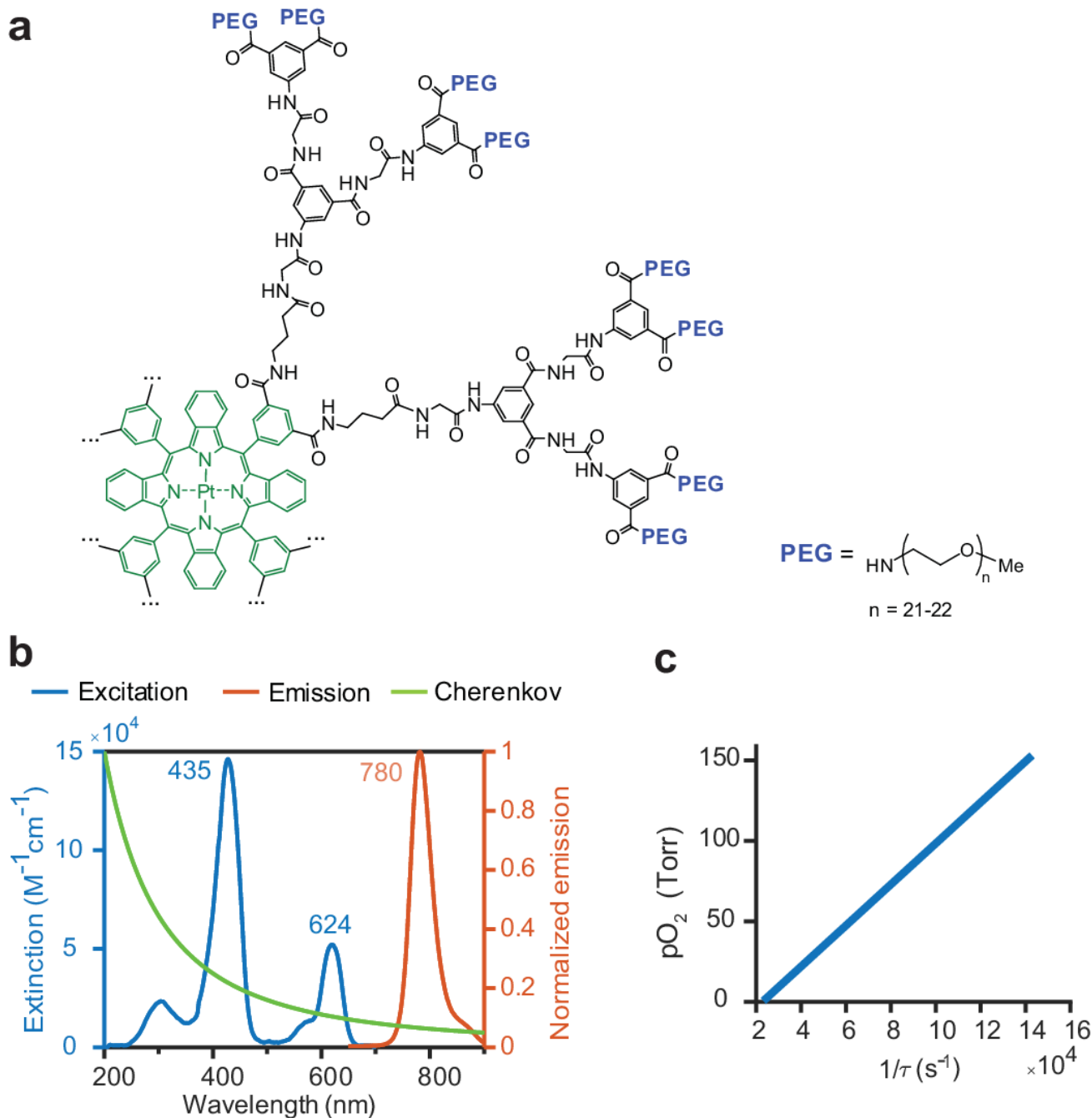
Brian Pogue declares that he is founder and president of DoseOptics LLC a company developing camera systems and software for radiotherapy imaging of Cherenkov light for dosimetry, a related application to the work presented here. The other authors declare no competing interests.

REFERENCES

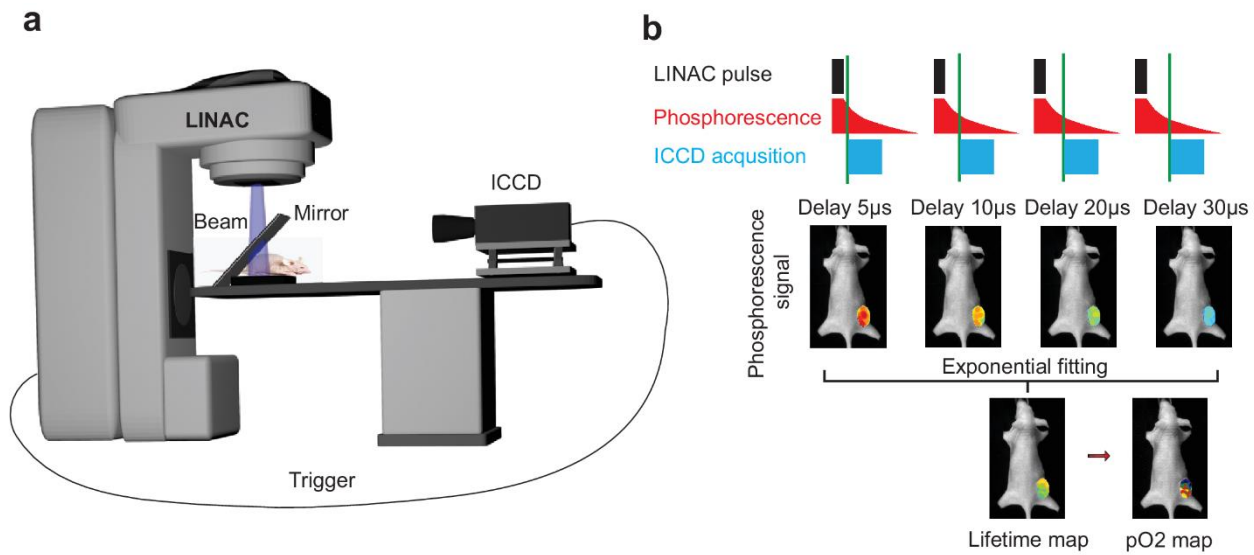
1. Oronsky, B.T., Knox, S.J. & Scicinski, J. Six degrees of separation: the oxygen effect in the development of radiosensitizers. *Transl Oncol* **4**, 189-198 (2011).
2. Shannon, A.M., Bouchier-Hayes, D.J., Condron, C.M. & Toomey, D. Tumour hypoxia, chemotherapeutic resistance and hypoxia-related therapies. *Cancer Treat Rev* **29**, 297-307 (2003).
3. Becker, A., *et al.* Oxygenation of squamous cell carcinoma of the head and neck: comparison of primary tumors, neck node metastases, and normal tissue. *Int J Radiat Oncol Biol Phys* **42**, 35-41 (1998).
4. Horsman, M.R., Nordsmark, M. & Overgaard, J. Techniques to assess the oxygenation of human tumors. State of the art. *Strahlenther Onkol* **174**, 2-5 (1998).
5. Nordsmark, M., *et al.* Hypoxia in human soft tissue sarcomas: adverse impact on survival and no association with p53 mutations. *Br J Cancer* **84**, 1070-1075 (2001).
6. Overgaard, J. Hypoxic modification of radiotherapy in squamous cell carcinoma of the head and neck - A systematic review and meta-analysis. *Radiother Oncol* **100**, 22-32 (2011).
7. Hoskin, P.J., Rojas, A.M., Saunders, M.I., Bentzen, S.M. & Motohashi, K.J. Carbogen and nicotinamide in locally advanced bladder cancer: early results of a phase-III randomized trial. *Radiother Oncol* **91**, 120-125 (2009).
8. Gaertner, F.C., Souvatzoglou, M., Brix, G. & Beer, A.J. Imaging of hypoxia using PET and MRI. *Curr Pharm Biotechnol* **13**, 552-570 (2012).
9. Nozue, M., *et al.* Interlaboratory variation in oxygen tension measurement by Eppendorf "Histogram" and comparison with hypoxic marker. *J Surg Oncol* **66**, 30-38 (1997).
10. Nordsmark, M., *et al.* The prognostic value of pimonidazole and tumour pO₂ in human cervix carcinomas after radiation therapy: a prospective international multi-center study. *Radiother Oncol* **80**, 123-131 (2006).
11. Hendrickson, K., *et al.* Hypoxia imaging with [F-18] FMISO-PET in head and neck cancer: potential for guiding intensity modulated radiation therapy in overcoming hypoxia-induced treatment resistance. *Radiother Oncol* **101**, 369-375 (2011).
12. Lock, S., *et al.* Residual tumour hypoxia in head-and-neck cancer patients undergoing primary radiochemotherapy, final results of a prospective trial on repeat FMISO-PET imaging. *Radiother Oncol* **124**, 533-540 (2017).
13. O'Connor, J.P.B., Robinson, S.P. & Waterton, J.C. Imaging tumour hypoxia with oxygen-enhanced MRI and BOLD MRI. *Br J Radiol* **92**, 20180642 (2019).
14. Baudelet, C. & Gallez, B. How does blood oxygen level-dependent (BOLD) contrast correlate with oxygen partial pressure (pO₂) inside tumors? *Magn Reson Med* **48**, 980-986 (2002).
15. Okunieff, P., Urano, M., Kallinowski, F., Vaupel, P. & Neuringer, L.J. Tumors growing in irradiated tissue: oxygenation, metabolic state, and pH. *Int J Radiat Oncol Biol Phys* **21**, 667-673 (1991).
16. Vanderkooi, J.M., Maniara, G., Green, T.J. & Wilson, D.F. An optical method for measurement of dioxygen concentration based

- 360 upon quenching of phosphorescence. *J Biol Chem* **262**, 5476-5482 (1987).
- 361 17. Rumsey, W.L., Abbott, B., Lo, L.W., Vinogradov, S.A. & Wilson, D.F. Imaging of oxygen distribution in the surface and deep
362 areas of the kidney. *Adv Exp Med Biol* **411**, 591-595 (1997).
- 363 18. Wilson, D.F. & Cerniglia, G.J.J.C.r. Localization of tumors and evaluation of their state of oxygenation by phosphorescence
364 imaging. *Cancer Res* **52**, 3988-3993 (1992).
- 365 19. Vinogradov, S.A., *et al.* Noninvasive imaging of the distribution in oxygen in tissue in vivo using near-infrared phosphors.
366 *Biophys J* **70**, 1609-1617 (1996).
- 367 20. Palmer, G.M., *et al.* Optical imaging of tumor hypoxia dynamics. *J Biomed Opt* **15**, 066021 (2010).
- 368 21. Esipova, T.V., *et al.* Two new "protected" oxyphors for biological oximetry: properties and application in tumor imaging. *Anal*
369 *Chem* **83**, 8756-8765 (2011).
- 370 22. Cerniglia, G.J., *et al.* Intravascular oxygen distribution in subcutaneous 9L tumors and radiation sensitivity. *J Appl Physiol* **82**,
371 1939-1945 (1997).
- 372 23. Erickson, K., *et al.* Effect of longitudinal oxygen gradients on effectiveness of manipulation of tumor oxygenation. *Cancer Res*
373 **63**, 4705-4712 (2003).
- 374 24. Lebedev, A.Y., *et al.* Dendritic phosphorescent probes for oxygen imaging in biological systems. *ACS Appl Mater Interfaces* **1**,
375 1292-1304 (2009).
- 376 25. Esipova, T.V., *et al.* Oxyphor 2P: A high-performance probe for deep-tissue longitudinal oxygen imaging. *Cell Metab* **29**, 736-
377 744 (2019).
- 378 26. Finikova, O.S., *et al.* Oxygen microscopy by two-photon-excited phosphorescence. *ChemPhysChem* **9**, 1673-1679 (2008).
- 379 27. Lecoq, J., *et al.* Simultaneous two-photon imaging of oxygen and blood flow in deep cerebral vessels. *Nat Med* **17**, 893 (2011).
- 380 28. Apreleva, S.V., Wilson, D.F. & Vinogradov, S.A. Tomographic imaging of oxygen by phosphorescence lifetime. *Appl Opt* **45**,
381 8547-8559 (2006).
- 382 29. Pogue, B.W., *et al.* Maps of in vivo oxygen pressure with submillimetre resolution and nanomolar sensitivity enabled by
383 Cherenkov-excited luminescence scanned imaging. *Nature Biomed Eng* **2**, 254-264 (2018).
- 384 30. Zhang, R., *et al.* Cherenkov-excited luminescence scanned imaging. *Opt Lett* **40**, 827-830 (2015).
- 385 31. LaRochelle, E.P.M., Shell, J.R., Gunn, J.R., Davis, S.C. & Pogue, B.W. Signal intensity analysis and optimization for in vivo
386 imaging of Cherenkov and excited luminescence. *Phys Med Biol* **63**, 085019 (2018).
- 387 32. Overgaard, J. Hypoxic radiosensitization: adored and ignored. *J Clin Oncol* **25**, 4066-4074 (2007).
- 388 33. Hoskin, P.J., Rojas, A.M., Bentzen, S.M. & Saunders, M.I. Radiotherapy with concurrent carbogen and nicotinamide in bladder
389 carcinoma. *J Clin Oncol* **28**, 4912-4918 (2010).
- 390 34. Janssens, G.O., *et al.* Accelerated radiotherapy with carbogen and nicotinamide for laryngeal cancer: results of a phase III
391 randomized trial. *J Clin Oncol* **30**, 1777-1783 (2012).
- 392 35. Lin, A. & Hahn, S.M. Hypoxia imaging markers and applications for radiation treatment planning. *Seminars in nuclear medicine*,
393 **42**, 343-352 (2012).
- 394 36. Horsman, M.R., Mortensen, L.S., Petersen, J.B., Busk, M. & Overgaard, J. Imaging hypoxia to improve radiotherapy outcome.
395 *Nat Rev Clin Oncol* **9**, 674-687 (2012).
- 396 37. Horsman, M.R. & Overgaard, J. The impact of hypoxia and its modification of the outcome of radiotherapy. *J Radiat Res* **57**, 90-
397 98 (2016).
- 398

Supplementary information

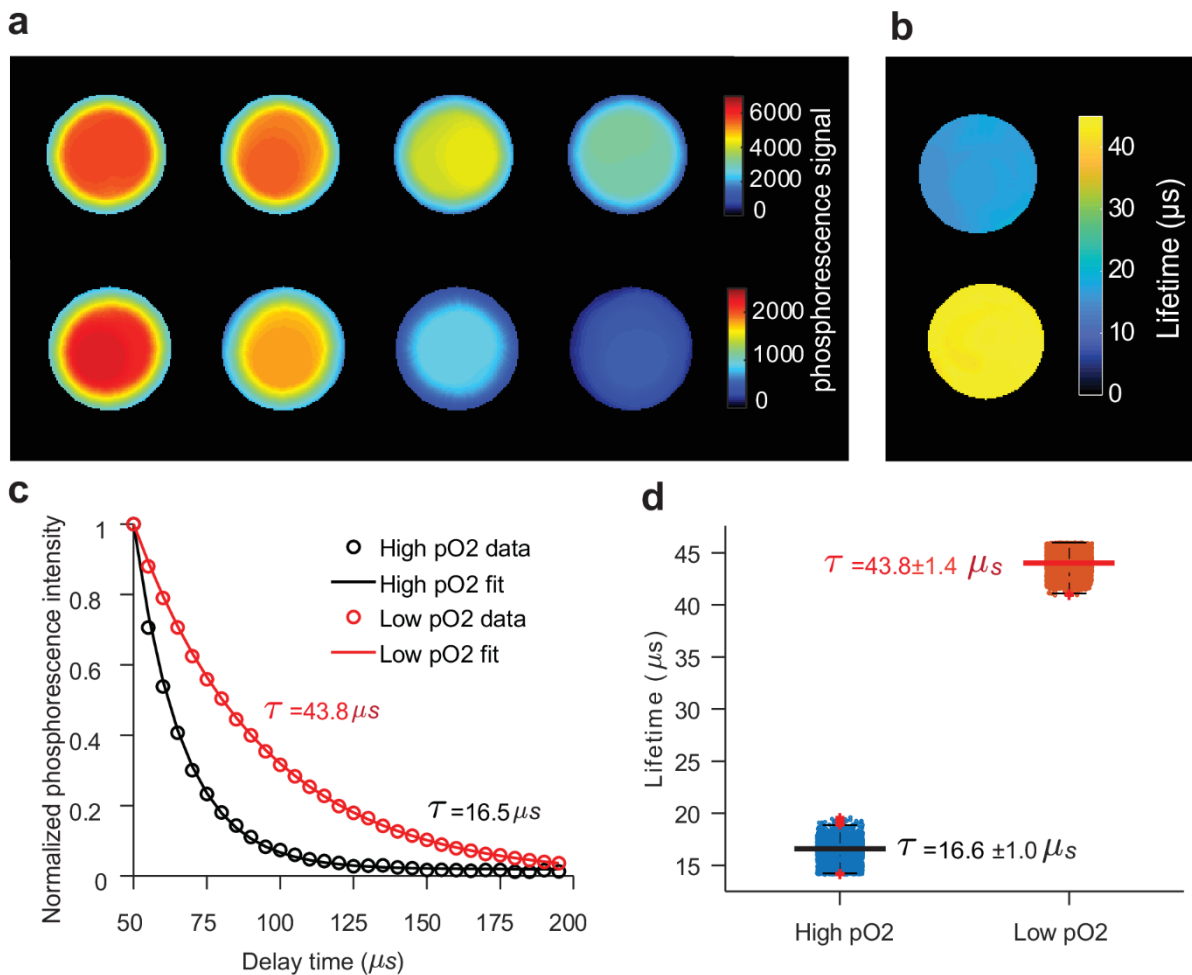


Supplementary figure 1 Properties of PtG4. (a) Structure and optical spectra of PtG4. (b) Excitation and emission spectrum of PtG4, and Cherenkov spectrum. The absorption band ($\lambda_{\text{max}}=435$ nm, $\epsilon \sim 140,000$ $\text{M}^{-1}\text{cm}^{-1}$) strongly overlaps with the Cherenkov spectrum, ensuring efficient excitation, while the phosphorescent photons ($\lambda_{\text{max}}=780$ nm) are minimally absorbed by the tissue and can easily diffuse from the depth and be detected by outside cameras. (c) Calibration curve of PtG4. The pO_2 values of a solution of PtG4 are plotted as a function of the inverse of phosphorescent lifetime.

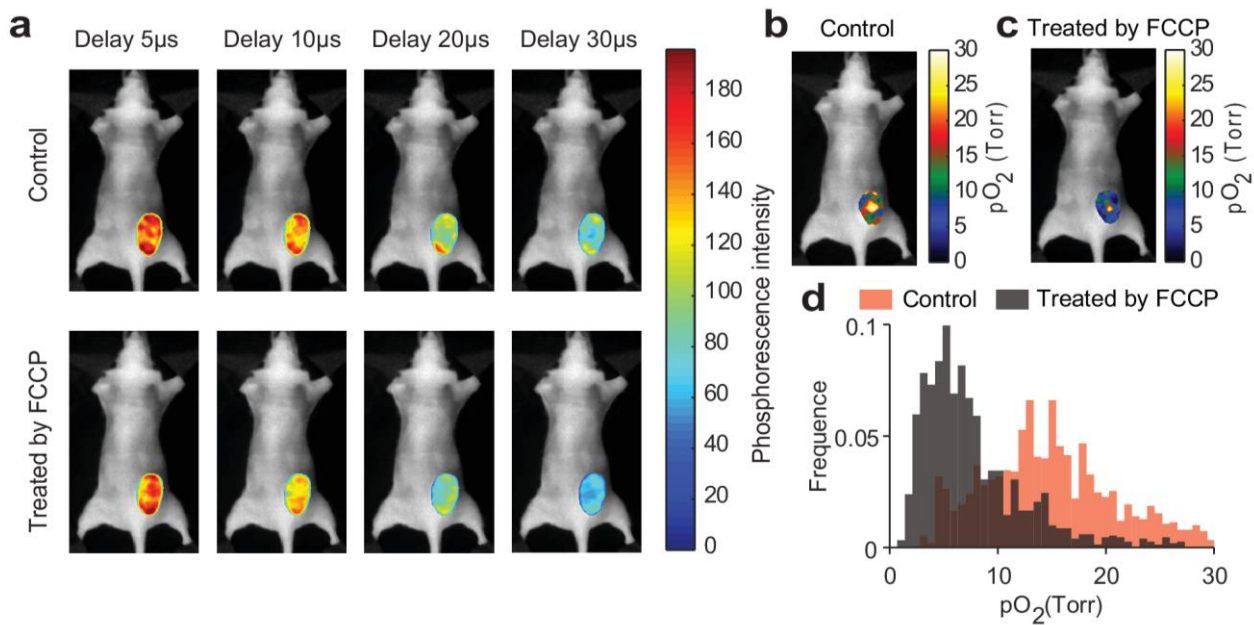


408
409
410
411
412
413
414

Supplementary figure 2 pO₂ mapping by Cherenkov-excited luminescence imaging. (a) A diagram of the experimental setup. The 6MV photon beam was delivered to generate Cherenkov light and excite phosphorescence probes. An intensified charge-coupled device (ICCD) camera was triggered by synchronized pulse from Linac to acquire luminescence signals of phosphorescence probes with different delay time. (b) Data acquisition and process. Four CEPLI images were acquired with the delay time of 5µs, 10µs, 20µs and 30µs, respectively. The lifetime of PtG4 was calculated by single exponential fitting pixel by pixel, and then pO₂ values could be calculated by Stern-Volmer equation.



415 **Supplementary figure 3** Lifetime estimation based on CEPLI. (a) CEPLI images with different delay time of PtG4 in
 416 low and high pO₂ environment. (b) The calculated lifetime map based on CEPLI images. (c) Lifetime measurement using
 417 a time-resolved fluorimeter FluoroMax4 (Horiba Scientific, Japan) (d) Boxplot of lifetime values obtained by CEPLI.



418

419

Supplementary figure 4 Imaging pO_2 responses to the change of tumor cell oxygen consumption on drug treatments.

420

(a) CEPLI images of a mouse acquired with different delay times for before and after treatment with FCCP (carbonyl

421

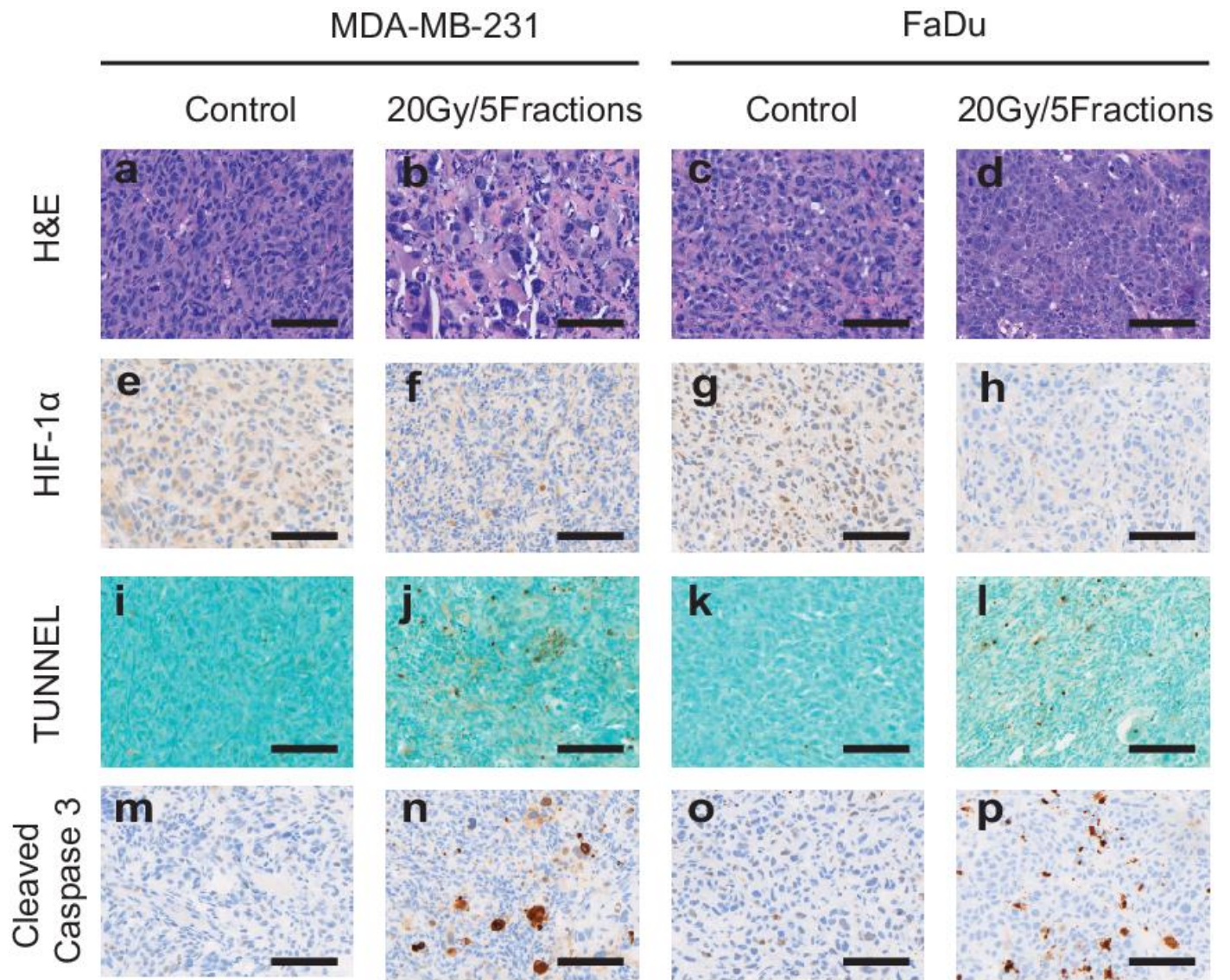
cyanide-4-(trifluoromethoxy) phenylhydrazine, an uncoupling agent which can promote the oxygen consumption of

422

cancer cells result in low pO_2). (b, c) pO_2 images for before (b) and after (c) treatment with FCCP. (d) pO_2 histogram

423

comparison for before and after treatment with FCCP.



424

425

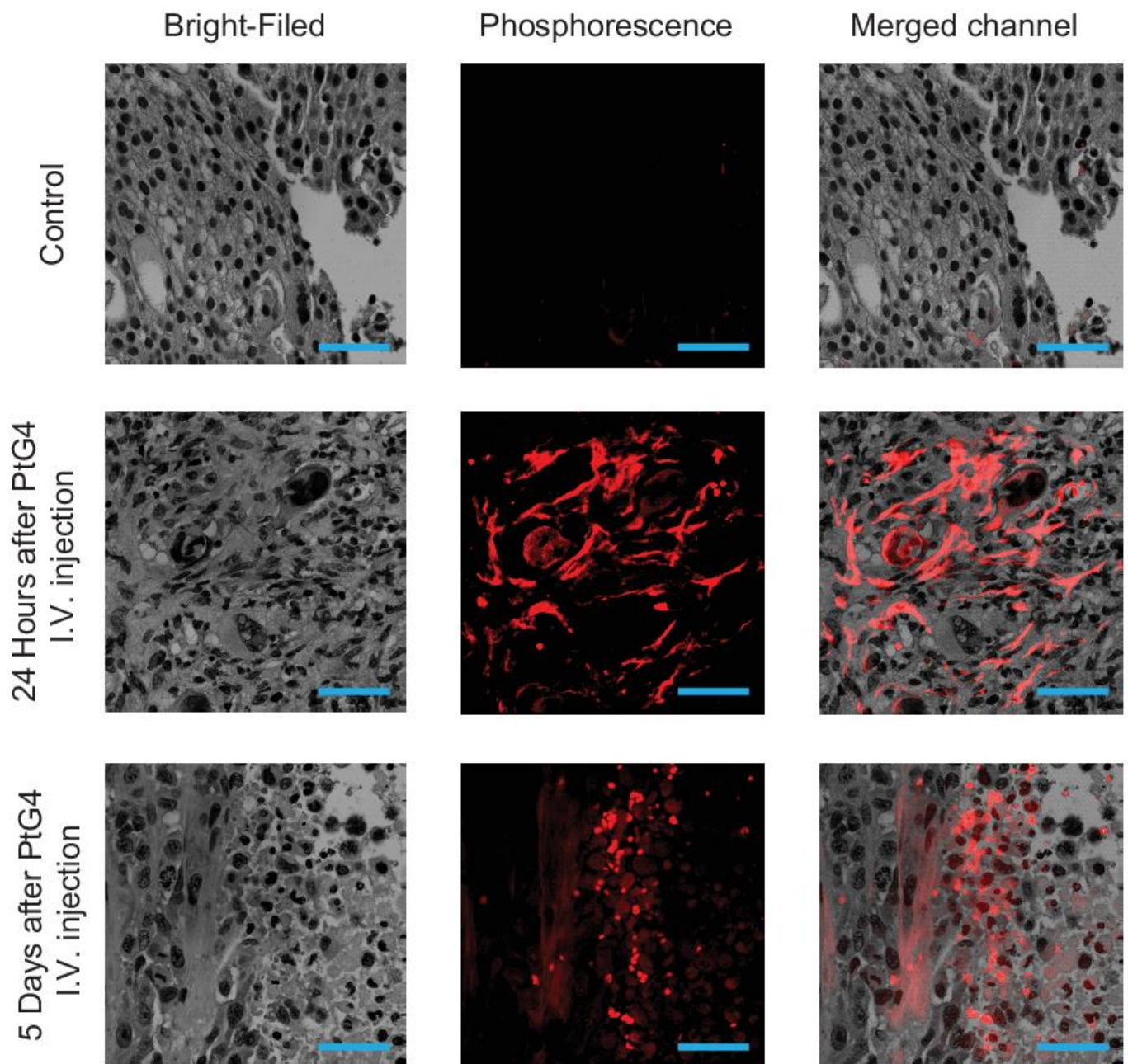
426

427

428

429

Supplementary figure 5 Histological analyses of tumor sections response to radiotherapy. (a-d) Representative hematoxylin and eosin (H&E) stained histopathologic tumor sections. (e-h) Expression of hypoxia-inducible factor 1 alpha (HIF-1 α) decreased in tumor cells when treated with radiotherapy compared to untreated tumors. (i-l) TUNEL staining of tumor sections, the brown stains indicate apoptotic cells. (m-p) Expression of cleaved caspase-3 activity in treated tumor sections. (scale bar: 100 μ m; Control: the mice without radiotherapy).



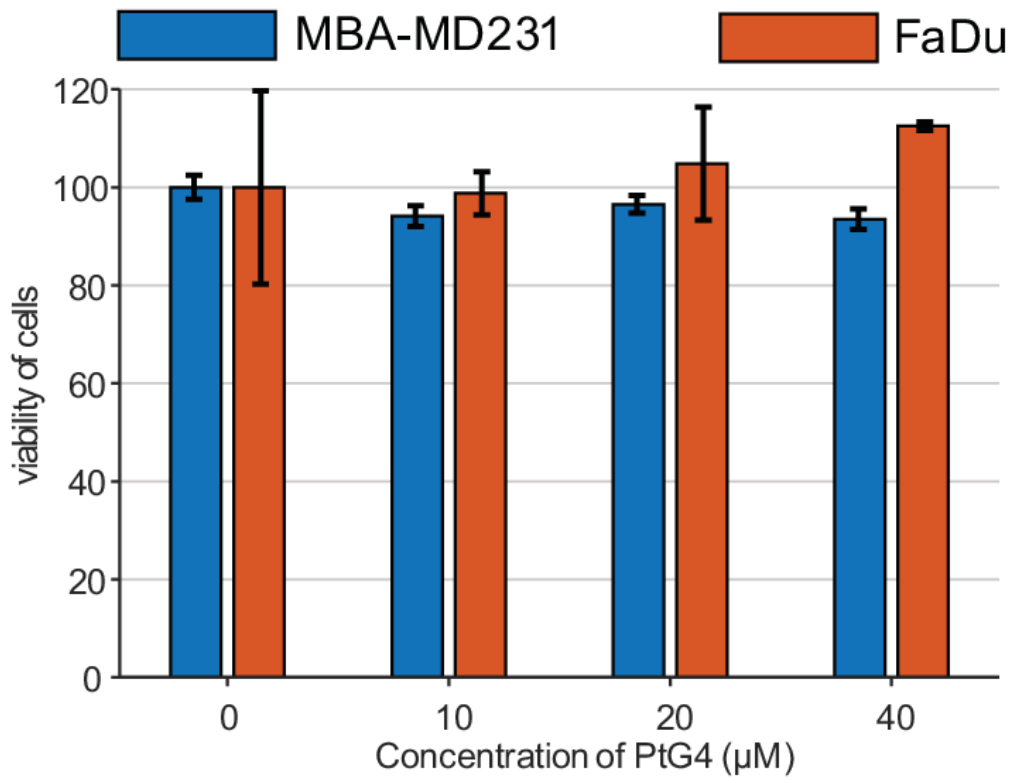
430

431

432

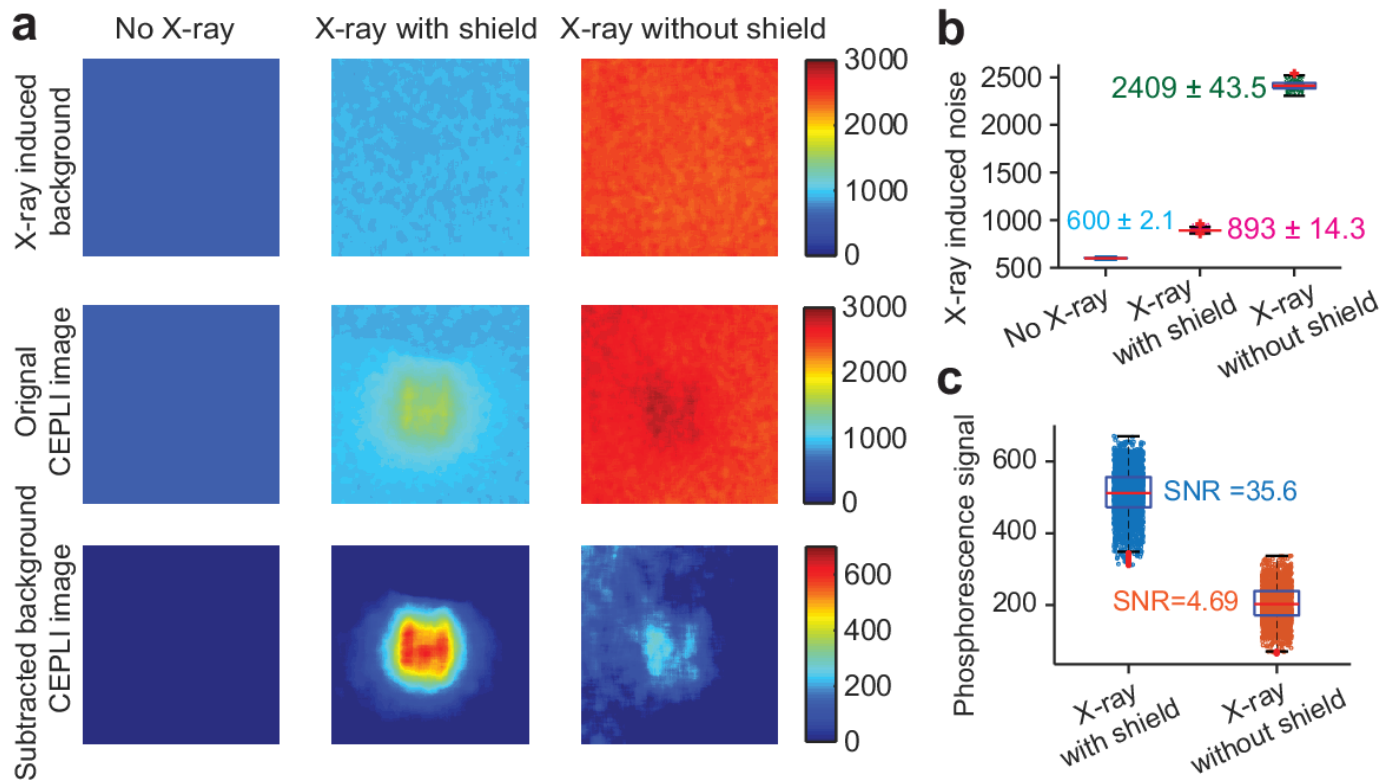
433

Supplementary figure 6 Fluorescence microscopy studies of PtG4 location in situ. Hematoxylin and eosin (H&E) stained slice of tumor without injection PtG4 (The first row), 24 hours after I.V. injection of PtG4 (The middle row), and 5 days after I.V. injection of PtG4(The third row). (scale bar: 50 μ m; Control: the mouse without injection of PtG4).



434

435 Supplementary figure 7 Toxicity evaluation using MTT assays of PtG4.



436

437

438

439

440

441

442

443

Supplementary figure 8 Noise suppression for CEPLI by X-ray block. (a) CEPLI images under different situations. The background of tissue like phantom (PBS with 1% intralipid and 1% porcine blood) reached to a high level when the X-ray was turned on, while background with X-ray block case was much lower than that without block (the up panel). Then a tube with PtG4 was put into the tissue like phantom with depth of 5mm, and the original CEPLI images were acquired (the middle panel). After subtracting the background, the CEPLI image for X-ray block case showed obvious phosphorescence signals of PtG4 (the below panel). (b) Comparison of X-ray induced background. Data was shown with mean \pm SD. (c) Comparison of SNR. The block case could significantly improve the SNR.